NON-RESONANT MICROWAVE ABSORPTION STUDIES OF TOP SEEDED INFILTRATION GROWN (Y/RE)Ba2Cu3O7-x SUPERCONDUCTORS

By

LEMMA KURIE BARUDA

(50799819)

A thesis is submitted as part of the requirements for the degree of Doctor of philosophy in Physics in the College of Natural Science, Engineering, and Technology At the University of South Africa (UNISA).

Supervisor Prof. Vijaya Srinivasu Vallabhapurapu (UNISA)

Co-supervisor : Dr. S. Pavan Kumar Naik , Superconducting Electronics and Photonics Research InstituteNational Institute of Advanced Industrial Science and Technology (AIST) 1-1-1 Central 2, Umezono, Tsukuba, Ibaraki, 305-8568, R&D Manager, Fumitec Corporation Japan

26 December 2025

Declaration / Statement of Originality

I conducted the study titled *"Non-Resonant Microwave Absorption Studies of Top-Seeded Infiltration-Grown (Y/RE)$Ba_2Cu_3O_{7-x}$ Superconductors"* with the supervision and guidance of Prof. Vijaya Srinivasu Vallabhapurapu.

I declare that this thesis has not been presented, in full or in part, to any other university or institution for the award of a degree or diploma. All sources of information, ideas, and data drawn from the work of others have been duly acknowledged in accordance with principles of academic integrity and ethical research conduct.

I take full responsibility for the accuracy and integrity of the work presented herein.

Signature: _____

Name: Lemma Kurie Baruda

Date: _____

Acknowledgements

I am profoundly grateful to my supervisor, Professor V. S. Vallabhapurapu, for his invaluable guidance, patience, and unwavering support throughout my research journey. His expert advice and steadfast encouragement have shaped not only the scientific foundation of this work but also my academic growth and personal development. I will always hold his mentorship in the highest regard.

My heartfelt thanks go to Professor Luyanda Noto, whose decisive guidance and generous support played a pivotal role in the progress and success of this study. I am equally indebted to Dr. Tebogo Mahule, whose exceptional contribution to the experimental laboratory work, particularly in ESR characterization, was instrumental to achieving the outcomes of this research.

I am deeply thankful to Dr. S. Pavan Kumar Naik, of the Superconducting Electronics Group, Electronics and Photonics Research Institute, National Institute of Advanced Industrial Science and Technology (AIST), Tsukuba, Japan. His extraordinary skill and generosity in synthesizing the pure RE/YBCO single-crystal superconducting samples were fundamental to this study. I am sincerely grateful for his kind collaboration and seamless communication with my supervisor, which made this contribution possible. His work will always be remembered with immense respect.

I extend my profound gratitude to Mrs. Seble Seyoum Tadesse, MBA, Hons Econ, BA Econ, Dip Com, Student Advisor (Ethiopia Regional Learning Centre), College of Graduate Studies, UNISA Addis Ababa, whose deep kindness, unwavering support, and influential guidance
been of tremendous help throughout my academic journey. Her thoughtful advice and decision-making have been invaluable at every stage of my study.

I am also deeply appreciative of Professor I. Naidoo, whose significant and impactful decisions on my behalf have greatly influenced the progress and success of this research. His guidance, insight, and support will always be remembered with immense respect and gratitude.

I also express my gratitude to all the professors and colleagues of the UNISA Florida Campus Physics Department, whose collective wisdom, collaboration, and encouragement greatly

enriched my academic experience. Special thanks also go to Ms. Alethea Mycock, whose consistent support and administrative guidance made many processes seamless.

From the depth of my heart, I acknowledge Tsehay Lesion, whose enduring presence and intrinsic connection to my life have been a source of unwavering strength and inspiration throughout this journey. I also offer my profound gratitude to my beloved wife, Meskerem Yigalem, whose exhaustive love, patience, and understanding have been pillars of support during every stage of this demanding work.

I am thankful to the Physics Department staff at Dilla University for their cooperation and invaluable support during various stages of this study.

Above all, my eternal and humble gratitude goes to our Omnipotent Almighty Lord God, who has been my guide, source of strength, and foundation of patience and perseverance. Without His divine grace and inexhaustible guidance, none of this would have been possible.

List of Symbols and Abbreviations / Definition of Terms and Symbols

Symbol	Description
Tc	Superconducting transition (critical) temperature
Hc	Critical magnetic field
Hc1	First critical field — flux first enters the superconductor
Hc2	Second critical field — superconductor transitions to normal state
Hirr	Irreversibility field — flux pinning disappears above this field
Jc	Critical current density — maximum current without resistance
Φ0	Fluxon — smallest unit of quantized magnetic flux
ϕGI\	Gauge-invariant phase difference
Δ\DeltaΔ	Superconducting energy gap
ξ\xiξ	Coherence length — scale over which superconducting order decays
λ\lambdaλ	London penetration depth — depth of magnetic flux penetration
ρ\rhoρ	Electrical resistivity
χ\chiχ	Magnetic susceptibility
μ_B	Bohr magneton — magnetic moment of an electron (9.27×10−24 J/T9.27 \times 10^{-24} \, \mathrm{J/T}9.27×10−24J/T)
	Voltage signal measured in NRMA experiments
ν\nuν	Microwave frequency
ω\omegaω	Angular frequency (2πν2 \pi \nu2πν)
Hres	Resonance magnetic field
YBCO	Yttrium Barium Copper Oxide (YBa2Cu3O7−δ\
HTSC	High-Temperature Superconductor
SC	Superconductor
NRMA	Non-Resonant Microwave Absorption

Symbol	Description
ESR / EPR	Electron Spin Resonance / Electron Paramagnetic Resonance
RF	Radio Frequency
AC	Alternating Current — current that periodically reverses direction
DC	Direct Current — current that flows in one direction
PPMS	Physical Property Measurement System
FMR	Ferromagnetic Resonance
SQUID	Superconducting Quantum Interference Device
XRD	X-ray Diffraction
SEM	Scanning Electron Microscopy
BCS	Bardeen-Cooper-Schrieffer theory

Abstract

Copper oxide high-temperature superconductors (HTSCs) possess an unusual electromagnetic performance, the sympathetic of which for scientific investigation as well as for potential technological use. Non-resonant microwave absorption (NRMA) is a highly useful method of investigation for these materials, offering a highly sensitive and completely non-destructive method for the investigation of significant superconducting parameters. With NRMA, researchers are capable of such measurements like the feasibility of passing electric current, penetration of magnetic fields, connectivity between grains, movement of vortices, magnetic screening. Although these advantages are present, NRMA is yet to gain widespread application in single-crystal Y/RE$Ba_2Cu_3O_{7-x}$ material characterization. rare, thus most problems associated with grain boundary effects, screening currents, modulation effects by fields have not yet been entirely understood.In the present work, NAA was carried out on single-grain infiltration-grown (Y/RE)$Ba_2Cu_3O_7$−x superconductors with X-band frequency (9.4 GHz) ESR experiments

Content

Abstract ---------- vii
General Introduction---------- ----------1
Background of the Study----------5
1.2.1High temperature superconductors----------6
1.2.2 The Rise of High-Tc Superconductivity----------7
1.2.3 Technological Applications----------8
1.3 Problem Statement----------10
1.4 Research Objective----------12
1.5Alignment with Strategic Goals----------13
1.6 Aim and Objectives----------13
1.7 Methodology and Suggested Activities----------14
1.7. iTop Seeded Infiltration Growth Synthesis----------15
Experimental Procedures:----------16
iv. Workflow----------17
1.8 NRMA/ESR Measurement Setup----------17
Dissipation Mechanisms in NRMA of HTSCs----------18
References----------21
CHAPTER TWO: 2.1 Overview of Superconductivity----------30
2.1 Superconductivity----------29
2.2 The Meissner Phenomenon----------====----------32
2.3 Types of Superconductors----------33
2..4 YBCO----------38
2.4.1 Crystal Structure----------39
2.5 $YBa_2Cu_3O_{7-x:}$ Fundamental Properties----------40
2.6 Electrical Transport Properties----------40
2.6.1 Anisotropy of the Normal State----------41
2..6.2 Granularity and Disorder----------42
2.7 Microwave Absorption Studies----------44

2.7.1 Non-Resonant Microwave Absorption (NRMA)----------44
2.8 Magnetic Properties of Superconductors----------46
2.8.1 Basic Concepts: The Critical State and Critical Currents----------46
2.8.2 The Bean Critical State Model----------47
2.8.3 Anderson-Kim Model----------48
2.8.4 Low and High Critical Magnetic Fields----------49
2.8.5 Weak Links and Josephson Junctions----------49
2.9 Josephson Effect----------50
2.9.1 DC Josephson Effect----------50
2.9.2 Josephson Junctions----------51
2.9.3. Josephson coupling Energy----------53
2.10 Flux Pinning----------53
2.10.1 Penetration Depth of Josephson junction.----------54
2.10.2 Lower critical field of Josephson junction (B_{C1j})----------55
2.10.3 Surface impedance----------55
2.10.4 Flux Quantization----------56
2.11 Nano-Scale Lengths in Superconductivity----------61
2.12 Research Gaps Identified----------62
Reference----------63
CHAPTER THREE: ELECTROMAGNETIC LOSS MECHANISMS IN HIGH-TEMPERATURE SUPERCONDUCTORS,Introduction----------67
3.1 Electron Spins Resonance Spectroscopy----------67
3.2 Non-Resonant Microwave Absorption (NRMA) in HTSCs----------68
3.2.1 NRMA Studies----------68
3.2.3 3.2.3 Capabilities of NRMA Studies----------69
3.2.4 Unresolved Questions----------70
3.3 Non-resonant Radio/Microwave Absorption Features----------71
3.3.1 First, Second and Third Peak----------71
3.3.2 Absorption Spectral Lines----------72
3.3.3 Magnetic Shielding Effect----------72

3.3.4 Phase Reversal----------73
3.3.5 Magnetic Hysteresis----------73
3.3.6 Surface Barrier Effect----------74
3.3.7 Oxygen Deficiency----------75
3.3.8 Paramagnetic Meissner Effect----------75
3.3.9 AC Loss in the Superconducting State----------76
3.4 RF and Microwave Loss Mechanisms.----------76
3.4.1 Portis Model.----------77
3.5 Dulcic Model----------78
3.6 Critical Current Density----------80
3.6.1 The critical State----------82
3.6.2 Flux Creep and Flux Flow----------83
3.6.3 Bean Critical State Model----------84
3.6.4 Electromagnetic Loss Mechanisms----------85
3.7 The Two-component Critical State Model----------83
3.8 Non-resonant Microwave Absorption----------86
3.9 Distinction Between Weak-Link and Bulk Response----------87
3.10 Modulated and Non-Modulated
Low-Magnetic Field Microwave Absorption----------88
3.11 Modulated and Non-Modulated Low-Field Microwave Absorption----------89
References----------94
CHAPTER FOUR
Sample Preparation, Material Synthesis, and Processing ----------103
4.1 High-Tc Superconductors----------103
4.1.1 Characteristics of High-Temperature Superconductors (HTSCs)----------103
4.1.2 Processing of High-Tc Superconductors----------104
4.2 Grain Boundaries, Metallurgical Defects, and Flux Pinning----------105
4.3 Sample Preparation and Material Synthesis----------106
4.4 Processing YBCO Bulk Superconductor----------106
4.4.1 Conventional Solid-State Reaction Method----------107

4.4.2 REBCO Superconductors Fabricated by Melt Growth Process----------105
4.4.3 Melt Growth Process (MGP)----------108
4.5 Fabrication of REBCO Superconductors
Using the Infiltration and Growth (IG) Process----------111
References----------117
Chapter Five----------120
Synthesis and Characterization of YBCO Superconductors----------120
Introduction:----------120
Experimental Details----------121
Results and discussions:----------122
Stability of Y_2BaCuO_5----------97
Potential Chemical Reactions of Ethanol and H2O with Y2BaCuO5----------97
2 Conclusion----------101
REFERENCE----------102
CHAPTER SIX----------105
CHARACTERIZATION TECHNIQUES AND STRUCTURAL ANALYSIS OF YBCO SUPERCONDUCTORS----------105
6.1 Sample Characterization Techniques----------105
6.1.1 X-ray Diffraction (XRD)----------105
6.2 Analysis of Diffraction Patterns----------107
6. 3 Important parameters from XRD Data----------109
6.4 Scanning Electron Microscopy (SEM)----------109
6.5 Physical Properties Measurement System (PPMS)----------112
6.6 Atomic Force Microscope (AFM)----------114
6.7 Non-Resonant Microwave Absorption (NRMA) ----------117
6.8 Measurement Procedure and Interpretation----------120
6.8.1 Non-Resonant Microwave Absorption (NRMA) Measurements----------120
1. RF Source and RF Power Control System----------121
2. RF Power Distribution System:----------122

3. NRMA Detection System----------147
4. Signal Acquisition and Fine Detection:----------147
Experimental Details----------149
6.9 Electron Paramagnetic Resonance (EPR)----------149
References----------151
CHAPTER SEVEN----------156
7.1.Introduction----------156
7.1.2 Experimental Results----------156
7.2 Discussion and Interpretation----------157
7.2.1 Significance of Multiple Phase Reversals----------157
7.2.2 Comparison with Previous Studies----------157
7.2.3 Experimental Strengths and Constraints----------158
7.2.4 Graphical Analysis and Physical Interpretation----------158
Implications.----------164
RESULTS----------170
DISCUSSION----------170
ESR Hysteresis under Forward and Reverse Field Sweeps----------177
. Relation to LFMA (Low-Field Microwave Absorption)----------178
7.4.2 Electron Spin Resonance (ESR) Observations----------171
7.4.3 Resonance Signals and Anisotropy----------171
7.4.4 Absence of NRMA at Room Temperature----------171
Relevance to Superconductivity Research----------172
7.5 Analysis of NRMA Signals in YBCO Pellets at 78 K----------173
1. Non-Resonant Microwave Absorption (NRMA)----------173
2. Hysteresis: Forward and Reverse Sweeps----------174
3. Complex Signal Form and Phase Reversals----------174
4. Low-Field NRMA Signature----------174
7.6 Discussion and Conclusion: ESR and NRMA Studies ---------- -191
7.6.1 Room-Temperature ESR/NRMA Behavior----------191
7.6.2 Magnetic Resonance Results and Discussion:----------194

7.6.3 Low-Temperature NRMA Behavior (Figure 5.15)----------196
7.6.4 Integrated Discussion----------196
7.7 Discussion and Conclusion: NRMA Spectra of YBCO-0 Single Crystal----------197
7.7.1 Temperature Dependence of NRMA----------197
7.7.2 Hysteresis and Flux Pinning----------198
7.7.3 Origin of Microwave Absorption----------198
7.7.4 Implications for Superconductivity----------199
Temperature-Dependent NRMA Features----------199
Weak-Link Contributions----------199
Vortex Dynamics and Pinning----------200
Signal correlation----------200
Robustness and Reliability----------200
Emerging Physical Insights----------200
.8 Chapter Summary----------201
General Conclusion----------203
7.9.1 Chapter Summary----------205
7.9.2 Key Findings----------205
7.10 Limitations of the Study----------208
7.11 Future Directions----------210
References----------212

List of Figures

1 **Figure. 2.1.** Resistance–temperature plot of mercury measured by Heike Kamerlingh Onnes.----------23

2. Figue.2.2.Schematic for the persistent current experiment ----------23

3. Fig 2,3 a-c The magnetic flux excluded from the interior of a superconductor [40]----------25

4.Figure 2.4. Schematic illustration of the Meissner effect, showing magnetic flux expulsion from the interior of a bulk superconductor [Adapted from Tinkham, 1996].----------27

5.Figure 2.5: Phase diagrams illustrating the magnetic field–temperature relationship***(a)*** (Meissner) state to the normal state at the critical magnetic field. : Magnetic flux. *Adapted from Tinkham (1996) [Ref. X]*.----------*29*

6 Figure 2.6 The mixed state in a Type II superconductor penetrated by fluxons. Each vortex only carries an even integer number of flux quanta[40]---------- ----------30

7 Figure 2.7.:The crystal structure of YBa2Cu3O7-x superconductor.. ----------32

8 **Figure 2.8. Electrical resistivity.** The electrical resistivity behavior ----------34

9 Figure 2.9 Resistive transition in a granular superconductor**.** The region above Tc ----------35

10 Fig 2.10: A schematic Josephson junction showing two superconductor separated by an insulating layer----------51

11 Figure 3.1. Induction of spin states as a function of magnetic field B----------57

12 Figure 3.2:T-H phase diagam for different superconducting materials[79]..----------69

13 Figure.4.1 A typical experiment used in infiltration Growth process.A source of liquid phases which can either be Y-123 or Y-123+BaCuO2+CuO----------88

14 Fig 4.2 A comparison between the Melt growth and the Infiltration Growth Process[29]-----89

15. **Fig. 1** Microstructures of the Y211 particles after ultrasonic irradiated with 450 W for 30 min--------97

16. **Fig. 2.** XRD patterns of as synthesized Y211, Ethanol and DIW treated powders ----------100

17. **Fig. 3.** Normalized temperature dependance of ac susceptibility curves of YBCO-DIW----------101

18. **Figure 4.** The field dependance of J_c determined at 77 K for YBCO samples are compared----------102

19. **Fig. 5.** The scaling behaviours of f vs h for YBCO-Et and YBCO-DIW superconductors at 77 K.-------103

15 Figure 6.1: Schematic of X-ray diffraction by a crystal[27].----------109

16 Figure 6.2: Geometry of X-ray diffraction from a crystal. [28].----------110

17. Figure 6.3: A picture of typical XRD instrument----------112
18 Figure6.4: A schematic block diagram of SEM[4]----------114
19.Figure 6.5: JEOL-7500F SEM used in this work----------115
20. Fig 6.6 Picture of Physical Property Measurement System (PPMS)[6]. ----------117
21. Figure 6.7: A schematic diagam of AFM showing how imaging is done[9]----------118
22. Figue 6.8: A picture of AFM used in our Laboratory. Nanosurf.----------120
23. Figure 6.9: line shape of YBCO superconductor sample[23]----------122
24. Figure 6.10: A schematic block diagram of EPR spectrometer[26]. ----------125
25. Figure 6.11: EPR instrument used in this work — Bruker EXM spectrometer.----------126
26. **Figure 7.1.** *Evolution of the Non-Resonant Microwave Absorption (NRMA) signal with temperature in a rare-earth-substitute (RE/YBCO) single-crystal superconductor.----------133*
27. Figure 7.2 illustrates the derivative signals recorded from a $YBa_2Cu_3O_{7-x}$ (YBCO-0) crystal pellet at various temperatures (40 K, 45 K, 53 K, and 88 K) while sweeping at 18 dB.---------135
28 Figure 7.3**.** NRMA response of the YBCO-0 single crystal pellet
under a perpendicular field (5 G) in forward and reverse sweeps
at temperatures (7 K, 11 K, and 14 K).----------137
29 Figure 7.4. *ESR response of the YBCO single-crystal pellet at various temperatures-------139.*
30. Figure 7.5. Low-field NRMA response of YBCO-0.18dB single-crystal pellet----------141
31. **Figure 7.6.** *NRMA response of YBCO single-crystal pellet at 37 K and 45 K.* the NRMA signal from a YBCO single-crystal pellet ----------143
32. Figure 7.7:The graph shows the non-resonant microwave absorption (NRMA) signal ----148
33. Figure 7.8: Graphical representation of Non resonance microwave absorption
signal in low magnetic field:----------154
34. Figure 7.9 : The Graph of Non resonance microwave absorption signal in magnetic field: the ESR----------156
35 Figure 7.10 shows the non-resonant microwave absorption (NRMA) signal captured from a pure single-crystal YBCO-0 superconductor at room temperature. ----------159
36. Figure 7.11: NRMA Signal of YBCO Superconductor Below T----------161
37. Figure 7.12: ESR Spectra of Pure Single-Crystal
YBCO-0 Pellet at Various Temperatures----------164

38 Figure 7.13: NRMA in the YBCO-0 crystal pellet measured at room temperature with 25dB the Graph of Non resonance microwave absorption signal in magnetic field ----------166
39. Figure 7.14: ESR Spectra of YBCO Pellet at Ultra-Low Temperatures----------168
40. Figure 7.15: NRMA Spectra of YBCO-0 Single Crystal at Various Temperatures ----------173
41 Figure 7.16:*Temperature-Dependent Magnetic Resonance in YBCO* .the *Lorentzian Fits Show Increasing FWHM with Temperature (29K → 90K)* **x_0 and FWHM----------180**

CHAPTER ONE

1.1 General Introduction

The emergence of high-temperature (high-Tc) superconductors initiated an era of intensive research focused on their unusual physical behavior and diverse technological possibilities. In contrast to conventional superconductors, which require extremely low temperatures to achieve zero electrical resistance, high-Tc compounds remain superconducting at much higher temperatures. This feature makes them attractive for practical implementations such as efficient power transmission, magnetic-field devices, and quantum-based technologies.

Following the discovery of high-Tc materials, electron paramagnetic resonance (EPR) spectroscopy was widely applied to explore their fundamental characteristics [1]. Early investigations generated a wealth of experimental data in the superconducting regime; however, this did not immediately lead to a full theoretical understanding of the mechanisms involved. Consequently, the use of EPR in this field temporarily declined, even though the technique provides valuable insight into spin dynamics and magnetic interactions.

Recent studies, including the present work, reaffirm that EPR remains a sensitive and informative approach for examining high-Tc superconductors. With carefully designed EPR measurements, researchers can access information that conventional methods cannot easily reveal. Such studies expose intrinsic properties—coherence phenomena, magnetic coupling, and microwave-absorption behavior—that are central to understanding high-Tc superconductivity.

In high-Tc systems, the EPR signals differ fundamentally from those observed in classical paramagnetic materials. While conventional EPR arises from magnetic dipolar interactions among spin energy levels, signals in superconducting materials reflect more complex phenomena inherent to the superconducting state. Understanding the source mechanisms behind these signals is therefore essential for interpreting experimental results correctly. Detailed analysis of EPR spectra in various high-Tc superconductors allows researchers to uncover the mechanisms of microwave absorption and identify previously unknown material characteristics.

In this work, the EPR spectrometer serves as the principal experimental tool. Chapter Two provides a comprehensive description of the instrument, including its operational principles, measurement capabilities, and multifunctionality. Many researchers in superconductivity may

not be fully familiar with EPR spectroscopy, making this discussion important for understanding the significance of the results obtained.

The present experimental study examines how high-Tc superconductors respond to different external conditions such as DC and AC magnetic fields, temperature changes, sample orientation, and specific treatment methods including zero-field and field-cooling processes. By systematically grouping these experimental observations together with relevant theoretical insights [2], the study establishes a clear framework for interpreting the fundamental physical behavior of high-Tc superconductors. These findings extend the long-standing body of research on such materials and reaffirm the value of EPR spectroscopy in exploring their underlying physics.

In short, while its usage experienced temporary setback with decreasing popularity of EPR spectroscopy, it still provides detailed and reliable insight into properties of high-Tc superconductive materials. The present study shows that carefully designed experimental observation-theory analysis using EPR immensely enhances total knowledge of superconductive materials. It also opens up future research prospects on both core physics as well as new applications of these materials' systems.

The discovery of high-temperature (high-Tc) superconductors prompted a vigorous surge of investigation aimed at understanding their distinctive physical properties and potential technological advantages. Unlike traditional superconductors, which necessitate very low temperatures to achieve zero electrical resistance, high-Tc materials operate effectively at relatively higher temperatures, thereby rendering them appealing for applications in power transmission, magnetic technologies, and quantum devices.

Very shortly after these materials appeared on the scene, scientists applied the electron paramagnetic resonance (EPR) technique to study magnetic as well as electronic properties of them [1]. Whilst these earliest applications of EPR generated a colossal amount of output within the superconducting state, no simultaneous detailed theoretical description of high-Tc properties followed. The method therefore lost its significance temporarily despite its unprecedented ability to detect minute particulars on account of spin dynamics along with magnetic interactions.

The current study and other recent research have shown that EPR spectroscopy is still a vital and effective method for examining high-Tc superconductors. Experimental results that are difficult

or impossible to obtain using traditional methods can be obtained by carefully utilizing EPR techniques. Understanding high-Tc superconductivity requires an understanding of intrinsic material properties like coherence effects, magnetic interactions, and microwave absorption mechanisms, some of which are revealed by these unusual results.

In high-Tc systems, the EPR signals differ fundamentally from those observed in classical paramagnetic materials. While conventional EPR arises from magnetic dipolar interactions among spin energy levels, signals in superconducting materials reflect more complex phenomena inherent to the superconducting state. Understanding the source mechanisms behind these signals is therefore essential for interpreting experimental results correctly. Detailed analysis of EPR spectra in various high-Tc superconductors allows researchers to uncover the mechanisms of microwave absorption and identify previously unknown material characteristics.

In this work, the EPR spectrometer serves as the principal experimental tool. Chapter Two provides a comprehensive description of the instrument, including its operational principles, measurement capabilities, and multifunctionality. Many researchers in superconductivity may not be fully familiar with EPR spectroscopy, making this discussion important for understanding the significance of the results obtained.

Here, we present experimental studies of how high-Tc superconductors react to various conditions, such as DC and AC magnetic fields, temperature changes, sample orientation, and treatment procedures like field cooling and zero-field cooling. A solid framework for comprehending the fundamental physics of high-Tc superconductors is provided by the systematic classification of these experiments in conjunction with theoretical considerations [2]. The findings demonstrate the ongoing value of EPR spectroscopy in the field and build upon a long history of research since the discovery of these materials.

Superconductors are a unique class of materials that exhibit two characterizing properties when cooled below a threshold called the critical temperature (Tc): they permit DC to flow without any electrical resistance and they release magnetic flux from their interior, a phenomenon known as the Meissner phenomenon [1]. Heike Kamerlingh Onnes discovered this state of matter in 1911 while conducting low-temperature experiments on mercury.Usually elemental metals, type I superconductors lose their superconductivity in the presence of relatively weak magnetic

fields.Type II superconductors create quantized magnetic vortices to preserve superconductivity in the presence of stronger magnetic fields [3].

Macroscopic quantum phenomena in superconductors manifest not only through zero electrical resistance but also through distinct magnetic behaviors. In very weak magnetic fields, superconductors completely expel magnetic flux (Meissner effect). Under stronger fields, microscopic vortices of quantized magnetic flux develop, around which circulating currents partially cancel the applied field [4]. These phenomena arise from the coordinated motion of Cooper pairs and are best explained within a quantum mechanical framework.

Experimental investigations, such as tunneling and neutron scattering, have demonstrated that electron–phonon coupling is fundamental to the formation of Cooper pairs in conventional superconductors [5]. A significant milestone emerged in the 1980s with the discovery of high-temperature superconductivity in copper-oxide perovskite compounds (Vanderah, 1992). Although strong electron–electron correlations are widely believed to be essential, the detailed mechanism governing superconductivity in cuprate materials remains an open question despite decades of intensive study [7]. The ongoing quest to clarify these mechanisms and to discover superconductors with even higher critical temperatures for energy-related applications continues to inspire active global research.

The non-resonant microwave absorption (NRMA) technique has become an effective approach for examining superconducting systems because it is rapid, non-destructive, and does not depend on direct electrical contact. Typically, these experiments are performed with an electron paramagnetic resonance (EPR) spectrometer [8]. When complemented by magnetization and transport measurements, NRMA yields both macroscopic quantities—such as the critical temperature (Tc)—and microscopic details about the superconducting phase. Its sensitivity enables the detection of secondary phases, mapping of Josephson junction networks, and detailed exploration of vortex behavior [9].

In the present dissertation, NRMA has been utilized to investigate top-seeded infiltration-grown (Y/RE)$Ba_2Cu_3O_{7-x}$ superconductors. Measurements conducted at 9.45 GHz reveal distinctive NRMA line shapes that display broad and narrow peaks depending on the magnetic-field sweep range (−250 G to +10,000 G). By studying how these features evolve with temperature and field

modulation, this research seeks to elucidate the microscopic superconducting characteristics of high-Tc cuprate systems.

1.2 Background of the Study

High-temperature superconductors (HTSCs), especially $YBa_2Cu_3O_{7-x}$ (YBCO), attract significant attention because of their ability to carry electrical current without resistance at relatively high temperatures. Their electrical and magnetic behavior is strongly affected by factors such as crystal quality, oxygen stoichiometry, and structural defects.

This research benefited from the expert guidance of Dr. Tebogo Mahule, who provided extensive assistance in characterizing YBCO samples using ESR techniques at the University of South Africa (Unisa), Florida campus, Physics Department laboratory. Leveraging this support, the study explores the structural, electrical, and magnetic properties of YBCO single crystals, aiming to enhance understanding of high-Tc superconducting phenomena and their potential technological applications.

The HTSCs discovered by Bednorz and Müller [6] display unique physical properties that differ qualitatively from those of conventional superconductors. In these materials, unavoidable defects often act as weak links due to the very short coherence length (~10 Å), resulting in granularity at various length scales, including inter-grain, intra-grain, and twin boundaries. Such weak-link behavior significantly affects transport, magnetic, and electrodynamic properties, including microwave and RF responses [6].

One notable manifestation of these effects is non-resonant microwave (NRMA) and RF absorption, first reported in cooperative superconductors by Bhat et al. [7]. In the literature, this This phenomenon is also referred to as magnetically modulated microwave absorption (MMMA) or low-field microwave absorption (LFMA). The intense microwave or RF absorption observed is highly sensitive to both temperature and magnetic field in the superconducting state (below T_p). It is typically measured as a function of the applied DC magnetic field (ranging from approximately −100 Oe to +100 Oe), with a superimposed low-field AC modulation (0.01–10 Oe), using continuous-wave (CW) NMR or EPR spectrometers. The unique intrinsic properties of high-temperature superconducting (HTSC) materials strongly influence their non-resonant microwave and RF absorption characteristics, leading to distinct and field-dependent behaviors.

1.2.1 High temperature superconductors

Three Main Families of Hole-Doped Cuprate HTSCs: Research on high-Tc cuprate superconductors is complicated by the fact that each material family lends itself more readily to certain experimental methods than others. For instance, probing the electronic density of states in $Bi_2Sr_2CaCu_2O_{8+x}$ (BSCCO) is relatively straightforward, whereas investigating its magnetic behavior presents more challenges. To develop a comprehensive understanding of high-Tc superconductivity (HTSC), researchers often combine results from different cuprate families; however, this approach can lead to apparent contradictions and ongoing debate in the field.

1. Lanthanum Family (LSCO: $La_{2-x}Sr_xCuO_4$)

Discovery: The first cuprate superconductor, identified by Bednorz and Müller in 1986.

Properties: LSCO is physically robust, with strong atomic bonds, and allows the growth of relatively large single crystals (>1 cm).

Experimental Advantages: Its large crystal size makes LSCO especially suitable for neutron scattering studies of magnetism and spin correlations in cuprates.

2. Yttrium Barium Copper Oxide (YBCO: $YBa_2Cu_3O_{7-\delta}$)

Discovery: Reported in 1987, shortly after LSCO.

Significance: The first material to exceed the liquid-nitrogen temperature limit (Tc > 77 K), with an optimal Tc surpassing 90 K.

Properties: YBCO features a highly ordered crystal structure, often described as one of the "cleanest" cuprates, containing both a square CuO_2 plane and a Cu–O chain plane.

Challenges: Isolating the respective contributions of planes versus chains to superconductivity remains difficult.

Applications: Preferred for magnetic-field applications due to strong flux pinning, and widely used in fabricating high-Tc SQUIDs based on grain-boundary Josephson junctions.

3. Bismuth Strontium Calcium Copper Oxide (BSCCO: $Bi_2Sr_2CaCu_{2+n}O_{6+\delta}$)

Properties and Applications of Major HTSC Families

BSCCO: Contains 1–3 CuO_2 planes; *Tc* rises with the number of planes. Substituting Bi with Tl or Hg can raise *Tc* up to ~135 K. Well-suited for surface-sensitive studies (STM, ARPES), though slightly less stable than YBCO in high magnetic fields.

LSCO: Preferred for magnetic studies due to availability of large crystals.

YBCO: Excellent for applied superconductivity (flux pinning, SQUIDs).

Summary: LSCO, YBCO, and BSCCO form the core systems of high-Tc superconductivity research, each contributing distinct experimental and theoretical insights that complicate the development of a unified model.

1.2.2 The Rise of High-Tc Superconductivity

For decades, it was believed that superconductivity could not exceed the McMillan limit (~38 K) predicted by BCS theory. This changed in 1986, when **Bednorz and Müller** discovered superconductivity at ~35 K in $La_{2-x}Ba_xCuO_4$, marking the start of the high-Tc era. Soon after, **Wu et al.** reported $YBa_2Cu_3O_{7-\delta}$ (Tc = 92 K), above the boiling point of liquid nitrogen (77 K), opening practical applications.

Further studies found even higher Tc values in Bi-, Tl-, and Hg-based cuprates, reaching **138 K at ambient pressure** and **164 K under pressure**. Other superconducting families followed:

MgB_2 ($Tc \approx 39$ K) — highest-Tc conventional superconductor.

Fullerides such as CsC_{60} ($Tc \approx 40$ K).

Iron-based superconductors with Tc up to ~50 K.

Key milestones:

1986 — La–Ba–Cu–O (35 K)

1987 — YBCO (92 K)

1988–1990s — Bi-, Tl-, Hg-cuprates (up to 138 K; 164 K under pressure)

2001 — MgB_2 (39 K)

1990s–2000s — Fullerides and Fe-based superconductors

1.2.3 Technological Applications

The cuprate superconductor $YBa_2Cu_3O_{7-x}$ (YBCO) is widely recognized for having the highest critical current density among high-Tc materials and for showing excellent performance in high-magnetic-field applications. Bulk YBCO superconductors can generate extremely strong magnetic fields and exhibit remarkable levitation forces, which makes them suitable for numerous engineering and energy-related devices such as:

superconducting flywheel energy storage systems,
superconducting motors and engines,
cryogenic pumps,
and magnetic levitation systems.
Because YBCO can also be fabricated into desired shapes using techniques such as top-seeded infiltration growth, its versatility extends to both scientific and industrial devices.
Following the classification by Masato Murakami [9], bulk high-Tc superconductors can be grouped into two application types:
Passive applications – where superconductivity enables simple and efficient technical solutions, mainly based on flux pinning and levitation.
Examples: superconducting bearings, flywheels, cryogenic pumps, and hysteresis motors (as rotors).
Magnet applications – where the material acts as a strong, quasi-permanent magnet.
Examples: maglev trains, magnetic clamps, superconducting stators in engines, magnetic buffers, magnetization devices, and high-field physics experiments.
Challenges and Engineering Considerations
As noted by Hari Babu et al. [10], two challenges remain central to YBCO technology:
achieving high-performance current transport, and
keeping fabrication of single-grain bulk superconductors cost-effective.
A comprehensive review by Pissa et al. [11] highlights the pressing need for fabrication methods that are both cost-effective and scalable, while still preserving high current-carrying capability. Achieving this balance is essential for deploying high-Tc superconductors in large-scale power applications, including:
Superconducting power cables
Magnetic energy storage systems
Superconducting transformers
Fault current limiters
Among high-Tc materials, $YBa_2Cu_3O_{7-\delta}$ (YBCO) stands out as particularly promising due to its distinctive layered crystal structure:
Superconductivity primarily originates in the CuO_2 double planes.

The intervening atomic layers function as charge reservoirs, enabling fine-tuning of the material's properties.

Oxygen content plays a pivotal role in determining the superconducting behavior of $YBa_2Cu_3O_{7-x}$. At $YBa_2Cu_3O_6$ (x = 1), the crystal adopts a tetragonal structure and exhibits insulating antiferromagnetic behavior. As oxygen is progressively incorporated into the crystal lattice toward the optimal oxygen concentration, the structure transforms from tetragonal to orthorhombic. This structural transformation is closely associated with the emergence of superconductivity, characterized by zero electrical resistance and high critical current carrying capacity.YBCO continues to be the material of choice for numerous technological applications because of its high critical current density, robust flux pinning, and adjustable oxygen stoichiometry. Future developments depend on refining low-cost, large-scale fabrication techniques while leveraging these unique superconducting properties for applications in energy systems and transportation technologies.

1.3 Problem Statement

Recent technological progress has been strongly influenced by advances in superconductivity, enabling the development of cutting-edge electronic and quantum devices. Superconductors are fundamental to high-precision instruments such as MRI and NMR systems. Their zero-resistance current flow allows efficient signal transmission and ultra-sensitive detection. Devices like SQUIDs and qubit-based components in quantum computing utilize the phase coherence of the superconducting state to achieve unmatched accuracy in measurement and data processing.In recent years, extensive attention has been directed toward specialized Josephson junction configurations capable of converting steady electrical inputs into extremely high-frequency alternating signals. These innovations are helping to address the long-standing "terahertz gap," paving the way for the next generation of ultra-fast communication systems and cutting-edge sensing technologies.

Among the various methods used to probe the electromagnetic behavior of superconductors, non-resonant microwave absorption (NRMA) is particularly effective. This non-destructive technique reveals key intrinsic properties of superconducting materials. NRMA studies on cuprate superconductors have uncovered several critical phenomena, including magnetic shielding, anomalous hysteresis, the paramagnetic Meissner effect, surface barriers,

irreversibility lines, critical current density, and surface resistance. However, low-field NRMA investigations of copper-based systems, especially $YBa_2Cu_3O_{7-\delta}$ (YBCO), remain limited. This scarcity of systematic data constrains understanding of microwave energy dissipation, hindering further optimization of superconducting devices and applications.

The present work addresses this gap through a detailed investigation of NRMA in high-purity single crystals of $Y/REBa_2Cu_3O_{7-x}$ (YBCO). The study examines how temperature, microwave power, and applied magnetic field affect microwave losses. NRMA measurements capture the field derivative of microwave absorption under very small modulation fields, primarily probing boundary or shielding currents. Because these modulation fields are insufficient to move magnetic flux significantly, the resulting signals predominantly reflect the dynamics of boundary currents.

The interaction between applied magnetic fields, temperature, and the **critical current density (Jc)** in Josephson junctions is central to understanding the shielding response of granular superconductors. In these systems, Jc is limited by the weak-link coupling between superconducting grains. As the external magnetic field increases, the phase coherence across these junctions is disrupted, leading to a significant suppression of the macroscopic Jc and a corresponding increase in microwave energy dissipation.

Thanks to these outstanding characteristics, YBCO is an attractive candidate for a broad spectrum of advanced applications, including next-generation magnetic and electronic devices, high-resolution medical imaging, safety and defense technologies, and fundamental research in condensed matter physics. By systematically characterizing NRMA in these materials, this study aims to enhance scientific understanding and support the continued development of superconducting technology.

1.4 Research Objective

In certain high-temperature superconductors (HTS), the interlayer coupling is weak, resulting in a short coherence length, sometimes comparable to a single unit cell [21,22]. Consequently, superconducting regions are separated by thin weak-link layers, forming natural superconductor–insulator–superconductor (SIS) or superconductor–normal–superconductor (SNS) junctions. These junctions strongly influence current transport and the response of the material to radio-frequency (RF) and microwave fields.

Below the critical temperature (Tc), even small magnetic fields can markedly enhance RF or microwave absorption through these weak junctions. Experimentally, this appears as either a zero-field minimum—where absorption increases with field—or a zero-field maximum, where it decreases [23,24]. The specific line shapes depend on factors such as temperature, microwave frequency, power, and field modulation amplitude.

The main objective of this research is to examine how impurity levels in $YBa_2Cu_3O_{7-x}$ (YBCO) single crystals affect the non-resonant microwave absorption (NRMA) line profiles. The study explores the microwave susceptibility of high-quality YBCO under weak magnetic fields, with particular attention to temperature-dependent features exhibiting complex behavior. Complementary measurements of magnetization and hysteresis were also performed using a Physical Property Measurement System (PPMS) equipped with a Vibrating Sample Magnetometer (VSM). This combined approach allows simultaneous probing of magnetic and superconducting properties, providing potential evidence for spin-triplet superconductivity in oxide-based systems. The results are expected to fill existing gaps in the literature and enhance understanding of HTS behavior relevant to advanced superconducting devices.

1.6.3 Alignment with Strategic Goals

The strategic visions of the University of South Africa (UNISA), the College of Science and Technology, South Africa (DST-SA), and international research priorities in superconducting materials and quantum technologies are all closely aligned with this study, which is under the "Advanced Materials" domain. This study supports national and international efforts to develop next-generation electronic, power, and quantum devices by concentrating on high-temperature superconductors and their electromagnetic properties.

1.6.4 Aim and Objectives

The Non-Resonant Microwave Absorption (NRMA) technique employed in this research primarily probes the boundary current responses in superconducting samples. Small modulation fields in NRMA do not significantly perturb magnetic flux within the sample, allowing the detection of shielding currents exclusively. Conversely, larger modulation fields emphasize flux-dependent **losses**, suppressing boundary current contributions. The temperature and applied magnetic field dependence of microwave losses in granular superconductors is primarily dictated

by the critical currents (Ic) of Josephson junctions, which govern how effectively these materials screen external magnetic fields.

The primary objectives of this study are to:
Determine the higher critical fields (Hc) and critical current densities (Jc) of synthesized superconducting samples for potential power-related applications. Investigate novel superconducting crystals with the potential to achieve higher critical temperatures (Tc) compared to currently known cuprate systems.
Employ ultrasensitive low-field microwave absorption (LFMA) techniques to probe the microwave response of YBCO samples.
Examine infiltration-grown single-grain (Y/RE)$Ba_2Cu_3O_{7-x}$ superconductors using non-resonant microwave absorption (NRMA).
Perform NRMA line-shape **analysis** and evaluate the viscosity coefficient associated with vortex dynamics.
Analyze the impact of dopants on NRMA line shapes and superconducting properties.
Assess **critical** current densities (Jc) through NRMA measurements.

1.6.5 Methodology and Suggested Activities

The experimental procedure focuses on measuring zero-field microwave absorption, which exhibits a pronounced increase below a characteristic temperature, T*, when the sample is placed at the maximum RF magnetic field within the microwave cavity. Applying a DC magnetic field suppresses this enhancement, enabling a detailed investigation of boundary current behavior and flux dynamics within the material.

Collaboration with UNISA research teams will enable structural characterization of samples and the performance of high-resolution NRMA measurements to study magnetic shielding, flux penetration, and weak-link behavior in RE/YBCO superconductors.

In accordance with Dulčić's weak-link model, at zero applied magnetic field, all weak links within a superconducting sample remain coupled, resulting in a maximum Meissner fraction. Under these conditions, magnetic shielding is optimal and microwave losses are minimized. As the applied field increases, weaker links progressively break, reducing the shielding efficiency and increasing microwave absorption.

In non-resonant microwave absorption (NRMA) experiments, the absorption of microwave power is measured as a function of the DC magnetic field, modulated by a small alternating field. The resulting signal corresponds to the derivative of absorbed power with respect to the field (dP/dH), where P is the absorbed power and H the external magnetic field. The zero-crossing of

this derivative typically marks either a minimum or maximum in absorption, providing valuable insight into the superconducting response under low-field conditions.

1.7 Top-Seeded Infiltration Growth (TSIG) Synthesis

Large single-grain (RE)$Ba_2Cu_3O_7$ (REBCO) superconductors exhibit high critical current densities, making them suitable for trapped-field magnets, motors, and generators [1–3]. Conventional growth methods such as Top-Seeded Melt Growth (TSMG) [4–6] and buffer-assisted TSMG [7–9] are widely used but face challenges, including [10–12]:

Sample shrinkage and porosity

Formation of voids and cracks

Oversized RE_2BaCuO_5 (RE-211) particles with acicular morphology

Uneven distribution of RE-211 inclusions in the RE-123 matrix

The Top-Seeded Infiltration Growth (TSIG) technique [13–19] provides a promising alternative, enabling near-net-shape fabrication of bulk superconductors. In TSIG, a RE-211 preform is infiltrated by a liquid phase, which reacts during cooling to form the superconducting RE-123 phase.

Despite these improvements, precise control over RE-211 particle size, morphology, and distribution within the RE-123 lattice remains challenging [20,21]. Effective optimization of TSIG requires careful regulation of:

Initial RE-211 particle size and its evolution during sintering

Preform porosity before and after heat treatment

Microstructural uniformity in the final superconducting matrix

The critical influence of preform porosity in TSIG has been highlighted by Cloots et al. [22].

ii. Microstructure and Superconducting Properties

The superconducting behavior of $YBa_2Cu_3O_{7-\sigma}$ (YBCO) thick films is strongly governed by their microstructure, particularly grain size, connectivity, and the distribution of secondary phases. These factors directly determine the critical current, flux pinning strength, and overall performance of the material in electromagnetic applications.

Precursor characteristics [1,2]

Substrate properties [3]

Melt processing conditions [4,5]

Typically, 123-powders are prepared via solid-state diffusion reactions from Y_2O_3, CuO, and $BaCO_3$ under controlled calcination conditions [6,7]. The decomposition of $BaCO_3$ is often the rate-limiting step, necessitating high calcination temperatures to achieve adequate reaction rates.

The critical current density (Jc) in melt-processed $REBa_2Cu_3O_\gamma$ superconductors is strongly influenced by their microstructural characteristics. Achieving high Jc requires dense, crack-free materials with minimal porosity. Conventional melt-processing methods often result in up to 25% shrinkage caused by liquid-phase outflow, which can create structural distortions and macroscopic defects.

In contrast, the Top-Seeded Infiltration Growth (TSIG) technique offers several advantages:

Formation of single-domain Y–Ba–Cu–O bulk matrices incorporating well-dispersed, non-superconducting RE-211 inclusions

Minimizes sample shrinkage (~5%) independent of sample size

Reduces porosity significantly (~0.9% vs. 4.9% using standard methods)

iii Characterization Techniques

In high-Tc superconductors, weak links often dominate microwave loss mechanisms rather than the normal Abrikosov fluxon motion. Twin boundaries generate intra-grain Josephson junctions, which subdivide grains into weakly coupled superconducting domains.

Structural and compositional analyses include.Analytical Techniques

To characterize the structural and compositional properties of the superconducting samples, a combination of spectroscopic, microscopic, and compositional methods was employed:

Spectroscopic methods: Nuclear Magnetic Resonance (NMR), X-ray Diffraction (XRD), and Inelastic Neutron Scattering (INS).

Microscopy methods: Transmission Electron Microscopy (TEM), Scanning Electron Microscopy (SEM), and Atomic Force Microscopy (AFM).

Compositional analysis: Energy-Dispersive X-ray Spectroscopy (EDX).

Experimental Procedures:

Energy-Dispersive X-ray Spectroscopy (EDX) was employed to investigate the elemental composition and microstructural characteristics of the synthesized RE/YBCO samples. Although EDX provides useful semi-quantitative compositional information, it has limitations in determining precise stoichiometry and oxidation states. More accurate analysis of elemental stoichiometry and oxidation states can be achieved using X-ray Photoelectron Spectroscopy (XPS). However, XPS measurements were not performed in the present study due to instrumental limitations and the scope of the work. Future investigations may incorporate XPS analysis for more detailed compositional characterization.

Identification and preparation of samples for specific measurements:

Structural characterization by XRD (powder and thin-film modes) for phase purity and crystal structure confirmation (tetragonal/orthorhombic)

Measurement of magnetic ordering

Modulated and non-modulated microwave absorption (MA) to probe superconducting state responses

Low-field and high-field ESR measurements with X-band (9–10 GHz) spectrometers, including magnetic field modulation

iv. Experimental Workflow:

Experimental Methods

Structural Characterization:Transmission Electron Microscopy (TEM), Scanning Electron Microscopy (SEM), and Energy-Dispersive X-ray Spectroscopy (EDX) will be employed to analyze the microstructure and elemental composition of the synthesized RE/YBCO samples.

Microwave Absorption Studies:Non-Resonant Microwave Absorption (NRMA) and Electron Spin Resonance (ESR) techniques will be used to investigate microwave absorption, magnetic responses, transport properties, and heat capacity near the superconducting transition temperature (Tc). Superconducting Properties:Specific heat, magnetic susceptibility, and electrical resistivity measurements will be carried out to evaluate the superconducting performance of the materials.

Magnetic Characterization: Vibrating Sample Magnetometry (VSM) integrated with a Physical Property Measurement System (PPMS) will be utilized to study magnetic hysteresis, flux pinning, and other related magnetic phenomena.

1.8 NRMA/ESR Measurement Setup

Bulk and thin-film samples will be inserted into the oscillatory magnetic field of the cavity.

Measurements will cover a wide temperature range (4–300 K) and variable magnetic field strengths.

Both resonant and non-resonant absorption components will be studied to obtain information on novel superconducting materials.

NRMA enables measurement of field derivatives of microwave losses, predominantly characterizing boundary current responses. Small modulation fields detect shielding currents, while larger modulation fields capture flux-dependent losses. Temperature and field dependence of microwave loss is governed by the critical currents (Ic) of Josephson junctions, which suppress external magnetic fields in granular superconductors.

In HTSCs, the situation is further complicated by weak links at grain boundaries or twin planes, which function similarly to Josephson junctions. These weak links possess much lower critical fields (typically ~0.1 Oe) compared to the bulk material, facilitating flux penetration and enhanced energy dissipation [86]. NRMA experiments have revealed a rich variety of behaviors, including modulation amplitude–dependent hysteresis, temperature-induced phase reversals, and fine structural features in the absorption line shapes [61, 86].

The NRMA response of high-temperature superconductors is strongly influenced by both microstructural characteristics and experimental conditions. For instance, Srinivasu et al. [56] reported that YBCO thin films and sintered pellets display frequency-dependent NRMA behavior, showing noticeable differences between microwave (~9.1 GHz) and radiofrequency (~19.5 MHz) measurements. Similarly, Nemangwele et al. [89] found that introducing nano-Ni particles into YBCO disrupts the coherence of Josephson junction networks, leading to the suppression of multiple phase reversals at higher microwave power. These observations highlight the critical role of frequency, material morphology, and microstructure in shaping the NRMA response of HTSCs.

Dissipation Mechanisms in NRMA of HTSCs

There is still much to learn about the microscopic causes of energy dissipation in non-resonant microwave absorption (NRMA). It is well known that the viscous motion of Abrikosov vortices

causes field-dependent microwave losses in conventional Type II superconductors. However, weak-link vortices, which arise at insulating layers, twin boundaries, or grain boundaries within the crystal lattice, complicate this process in high-temperature superconductors (HTSCs) [86]. When the weak-link size ddd surpasses the London penetration depth (λL\lambda_LλL), the viscous motion of these weak-link vortices takes over as the primary contribution to NRMA signals. NRMA experiments have been conducted at various frequencies in order to distinguish between these effects. For instance, YBCO measurements at radiofrequency (19.5 MHz) and microwave (9.1 GHz) ranges show different line-shape behaviors, suggesting a variety of dissipation mechanisms [56].

A striking feature in HTSCs is the low-field modulation absorption. In compounds such as $La_{1.85}Sr_{0.15}CuO_4$ (LSCO), NRMA signals have been detected at microwave frequencies (X-band), with maxima typically in the range of ~10–20 Oe. Similar low-field phenomena are observed in higher-TcT_cTc cuprates, sometimes at fields as low as 0.5–1.0 Oe. These signals are often interpreted as the penetration of flux quanta (vortices) through weak links separating superconducting regions. Vortex nucleation and their subsequent viscous or dynamic motion contribute significantly to microwave energy dissipation under these low-field conditions.

NRMA provides unique insight into electrodynamics of HTSCs, probing boundary currents, weak-link behavior, and vortex dynamics. Yet, the detailed microscopic mechanism of dissipation, particularly due to interactions between Abrikosov fluxons and weak-link vortices, remains unresolved. This uncertainty emphasizes the need for systematic studies on well-controlled systems, such as infiltration-grown $(Y/RE)Ba_2Cu_3O_{7-x}$ superconductors, where granularity and microstructure can be systematically correlated with NRMA responses.

According to Dulčić's weak-link model, at zero applied magnetic field, all weak links in a sample remain coupled, achieving a maximum Meissner fraction. Under these conditions, magnetic shielding is optimal and microwave losses are minimized. As the applied field increases, weaker links break successively, reducing shielding efficiency and increasing microwave absorption.

In experiments conducted by NRMA, a small AC modulation field is applied to probe DC field-dependent absorption. This results in a signal that reflects the rate of change in absorbed power with respect to magnetic field, effectively giving us dP/dH. Where this derivative crosses zero

typically marks a point where absorption reaches a peak or trough. When the NRMA signal is 180 degrees out of phase with the resonant absorption, the zero-crossing signifies a standard NRMA response. Conversely, if it aligns with the electron spin resonance (ESR) signal, it indicates an unusual NRMA response has occurred.The behavior of granular superconductors, including YBCO powders, is primarily influenced by the weak connections between individual particles. Observations of phase reversals in NRMA signals, shifting from anomalous to normal in response to temperature or RF power changes, can be attributed to the unique characteristics of these weak links and the effects of granularity. In superconducting samples composed of powders, the interactions between particles and their weak-link connections play a particularly crucial role.

High-quality YBCO thin films, especially those doped with silver, exhibit low surface resistance and high critical current densities (Jc), making them directly suitable for microwave applications such as stripline resonators, cavity plates, transmission lines, and filters. Silver doping enhances grain alignment, microstructure, and reduces surface resistance, thereby improving Jc, magnetic shielding, and material stability. While in single crystals, magnetic shielding is predominantly intrinsic, in thin films it depends on both intrinsic properties and extrinsic granularity.Comparative studies on RE/YBCO bulk crystals under simultaneous application of microwave, DC, and weak AC fields (100 kHz) utilize NRMA techniques to evaluate shielding performance. Unlike standard AC or DC susceptibility measurements, NRMA allows investigation of shielding behavior under microwave excitation. Experiments confirm that Ag-doped YBCO films demonstrate superior shielding due to improved microstructural properties, as verified through atomic force microscopy.

References

[1] Dahl, P.F., 1984. Kamerlingh Onnes and the discovery of superconductivity: The Leyden years, 1911–1914. *Historical Studies in the Physical Sciences*, 15(1), pp.1–37.

[2] de Bruyn Ouboter, R., 1997. Heike Kamerlingh Onnes's discovery of superconductivity. *Scientific American*, 276(3), pp.98–103.

[3] Millman, S., 1984. *A history of engineering and science in the Bell system*. AT&T Bell Laboratories.

[4] Ginzburg, V.L., 2013. *Physics and astrophysics: A selection of key problems*. Elsevier.

[5] Keimer, B., Kivelson, S.A., Norman, M.R., Uchida, S. and Zaanen, J., 2015. From quantum matter to high-temperature superconductivity in copper oxides. *Nature*, 518(7538), pp.179–186.

[6] Si, Q., Yu, R. and Abrahams, E., 2016. High-temperature superconductivity in iron pnictides and chalcogenides. *Nature Reviews Materials*, 1(4), p.16017.

[7] Shrivastava, K.N., 1991. *Physics Reports*, 200, p.51.

[8] Beasley, M.R., Labusch, R. and Webb, W.W., 1969. Flux creep in superconductors.

[9] Nemangwele, F., Sankaran, V., Roul, B.K., Das, J. and Srinivasu, V.V., 2019. Non-resonant microwave absorption in nano nickel added YBCO powders: Observation of multiple phase reversals. *Journal of Superconductivity and Novel Magnetism*, 32(2), pp.501–510.

[10] Behr, R., Kieler, O., Kohlmann, J., Müller, F. and Palafox, L., 2012. Development and metrological applications of Josephson arrays at PTB. *Measurement Science and Technology*, 23(12), p.124002.

[11] Tinkham, M., 1996. *Introduction to Superconductivity*. 2nd ed. New York: McGraw-Hill.

[12] Huebener, R.P., 2013. *Magnetic flux structures in superconductors*. Springer.

[13] Butler, S.Z., et al., 2013. Progress in two-dimensional materials beyond graphene. *ACS Nano*, 7(4), pp.2898–2926.

[14] Bennemann, K.H. and Ketterson, J.B. (eds.), 2011. *The Physics of Superconductors: Vol. II*. Springer.

[15] Jin, B., et al., 2010. Low-loss and magnetic-field tunable superconducting THz metamaterial. *Optics Express*, 18(16), pp.17504–17509.

[16] Srinivasu, V.V., Thomas, B., Hegde, M.S. and Bhat, S.V., 1994. Line shapes of field-dependent nonresonant microwave and RF absorption in high-Tc superconductors. *Journal of Applied Physics*, 75(8), pp.4131–4136.

[17] Bhat, S.V., 1994. Non-resonant RF and microwave response: A new method for the characterization of superconducting materials. *Bulletin of Materials Science*, 17(7), pp.1271–1285.

[18] Stankowski, J. and Czyżak, B., 1991. Microwave absorption using EPR. *Applied Magnetic Resonance*, 2(3), pp.465–479.

[19] Sonin, E.V., 1988. Microwave absorption in superconductors. *JETP Letters*, 47, pp.1097–1101.

[20] Uchida, S.I., 2014. *High temperature superconductivity: The road to higher critical temperature*. Springer.

[21] Fujita, K., et al., 2011. STM studies of electronic structure in superconducting cuprates. *Journal of the Physical Society of Japan*, 81(1), p.011005.
[22] Zhao, G.M., 2009. Tunneling spectra in electron-doped cuprates. *Physical Review Letters*, 103(23), p.236403.
[23] Alagöz, S., 2009. Production of YBCO by powder-in-tube method. *Turkish Journal of Physics*, 33(2), pp.69–80.
[24] Gupta, S., et al., 2010. Microstructure and superconducting properties of $YBa_2Cu_3{-}xCoxO7{-}\delta$. *Integrated Ferroelectrics*, 116(1), pp.68–81.
[25] Portis, A.M., Blazey, K.W., Müller, K.A. and Bednorz, J.G., 1988. Microwave magneto-surface impedance. *Europhysics Letters*, 5(5), pp.467–472.
[26] Zhai, W., et al., 2015. Properties of bulk Y–Ba–Cu–O superconductors. *Crystal Growth & Design*, 15(2), pp.907–914.
[27] Thoma, M., et al., 2015. Y-211 particle size effect. *Journal of Crystal Growth*, 412, pp.31–39.
[28] Meslin, S. and Noudem, J.G., 2004. Infiltration-grown YBCO. *Superconductor Science and Technology*, 17(11), pp.1324–1330.
[29] Kline, S.J. and Rosenberg, N., 2010. Innovation overview. In: *Studies on Science and the Innovation Process*, pp.173–203.
[30] Blazey, K.W., et al., 1990. Superconductivity review. In: *Springer Series in Solid-State Sciences, 90*.
[31] Young, J., 1997. *Peasant Revolution in Ethiopia*. Cambridge University Press.
[32] Ramashitja, T.C., 2016. *Boundary current response in $Ba_{0.34}K_{0.64}Fe_2As_2$ superconducting crystal* (Doctoral dissertation).
[33] Bauer, P., 1996. *Stability of superconducting strands for accelerator magnets* (Doctoral dissertation, Vienna University of Technology).
[34] Sahoo, M., 2015. *Study of structure and transport in doped YBCO systems* (Doctoral dissertation).
[35] Onyancha, R.B., 2015. *Non-resonant microwave absorption studies in SmFeAs(O, F) iron pnictide superconductor* (Doctoral dissertation).
[36] Nomura, K., Ujihira, Y. and Vertes, A., 1996. Applications of conversion electron Mössbauer spectrometry (CEMS). *Journal of Radioanalytical and Nuclear Chemistry*, 202(1–2), pp.103–199.
[37] Bohandy, J., Kim, B.F., Adrian, F.J., Moorjani, K., D'Arcangelis, S. and Cowan, D.O., 1991. *Physical Review B*, 43, pp.3724–3731.
[40] Strnad, A.R., Hempstead, C.F. and Kim, Y.B., 1964. Flux pinning and creep in superconductors. *Physical Review Letters*, 13, pp.794–796.
[41] Matsushita, T., 2007. *Flux pinning in superconductors* (Vol. 164). Berlin: Springer.
[42] Bhat, S.V., Ganguly, P. and Rao, C.N.R., 1987. Studies on superconductivity. *Pramana Journal of Physics*, 28, pp.L425–L429.
[43] Bhat, S.V., Ganguly, P., Ramakrishnan, T.V. and Rao, C.N.R., 1987. Investigation of superconducting properties. *Journal of Physics C: Solid State Physics*, 20, pp.L559–L563.

[44] Blazey, K.W., Portis, A.M. and Bednorz, J.G., 1988. Microwave surface impedance in superconductors. *Solid State Communications*, 65, pp.1153–1157.
[45] Šouc, J., Pardo, E., Vojenčiak, M. and Gömöry, F., 2008. Theoretical and experimental study of AC loss in high-temperature superconductor single pancake coils. *Superconductor Science and Technology*, 22(1), p.015006.
[46] Srinivasu, V.V., Itoh, K.I., Hashizume, A., Sreedevi, V., Kohmoto, H., Endo, T. and Hayashi, K., 2001. Nonresonant microwave absorption in Bi_{2212} single crystal: Second peak and microwave power dependence. *Journal of Superconductivity*, 14(1), pp.41–46.
[47] Rettori, C., Davidov, D., Blelaish, I. and Feluer, I., 1987. Flux dynamics in superconductors. *Physical Review B*, 36, pp.4028–4034.
[48] Kachaturyan, K., Weber, E.R., Jejedor, P., Stacy, A.M. and Portis, A.M., 1987. Superconducting tunneling studies. *Physical Review B*, 36, pp.8309–8315.
[49] Stankowski, J., Kahol, P.K., Dalal, N.S. and Moodera, J.S., 1987. Microwave response of superconductors. *Physical Review B*, 36, pp.7126–7132.
[50] Shrivastava, K.N., 1987. Superconductivity and magnetic properties. *Physica C*, 30, pp.L789–L794.
[51] Dulcic, A., Crepeau, R.H. and Freed, J.H., 1988. Electron spin resonance in superconductors. *Physical Review B*, 38, pp.5002–5008.
[52] Pinto, R., Pai, S.P., Gupta, L.C., Vijayaraghavan, R., Kumar, D. and Sharon, M., 1992. Microwave studies of YBCO superconductors. *Physica C*, 196, pp.264–270.
[53] Dulcic, A., Rakvin, B. and Pozek, M., 1989. Superconductor resonance phenomena. *Europhysics Letters*, 10, pp.593–598.
[54] Portis AM, Blazey KW, Müller KA & Bednorz JG 1988, 'Microwave magneto-surface impedance', *Europhysics Letters*, vol. 5, pp. 467–472.
[55] Taylor, P.C., Zhang, D.J. and Xu, J.A., 1987. Surface impedance studies in high-Tc superconductors. *Physical Review B*, 36, pp.2361–2366.
[56] Srinivasu, V.V., 2010. Second and third peaks in the non-resonant microwave absorption spectra of superconducting Bi_{2212} crystals. *Journal of Superconductivity and Novel Magnetism*, 23(3), pp.305–308.
[57] Srinivasu, V.V., Pinto, R. and Sastry, M.D., 1996. Magnetic shielding effects in Ag-doped and pure $YBa_2Cu_3O_{7-x}$ thin films probed by non-resonant microwave absorption. *Applied Superconductivity*, 4(4), pp.195–201.
[58] Ginzburg, V.L., 2013. *Physics and astrophysics: A selection of key problems*. Elsevier.
[59] Meslin, S. and Noudem, J.G., 2004. Infiltration and top-seeded grown mono-domain $YBa_2Cu_3O_{7-x}$ bulk superconductor. *Superconductor Science and Technology*, 17(11), pp.1324–1330.
[60] Srinivasu, V.V., Thomas, B., Hegde, M.S. and Bhat, S.V., 1994. Line shapes of field-dependent nonresonant microwave and RF absorption in high-Tc superconductors. *Journal of Applied Physics*, 75(8), pp.4131–4136.

[61] Bhat, S.V., 1994. Non-resonant RF and microwave response: A novel technique for the characterization of superconducting materials. *Bulletin of Materials Science*, 17(7), pp.1271–1285.
[62] Onyancha, R.B., 2015. *Non-resonant microwave absorption studies in SmFeAs(O,F) iron pnictide superconductor* (Doctoral dissertation).
[63] Nomura, K., Ujihira, Y. and Vertes, A., 1996. Applications of conversion electron Mössbauer spectrometry (CEMS). *Journal of Radioanalytical and Nuclear Chemistry*, 202(1–2), pp.103–199.
[64] Bohandy, J., Kim, B.F., Adrian, F.J., Moorjani, K., D'Arcangelis, S. and Cowan, D.O., 1991. Superconducting thin film studies. *Physical Review B*, 43, pp.3724–3730.
[65] Blazey, K.W. and Mangelschots, I., 1990. Microwave absorption in YBCO superconductors. *Physica C*, 170, pp.267–274.
[66] Bhat, S.V., Srinivasu, V.V. and Kumar, N., 1991. Microwave and RF studies in YBCO. *Physical Review B*, 44, pp.10121–10128.
[67] Karim, R., How, H., Widom, A. and Vittoria, C., 1990. Magnetic characterization of superconductors. *IEEE Transactions on Magnetics*, MAC-26, pp.1439–1444.
[68] Blazey, K.W., Portis, A.M., Müller, K.A., Bednorz, J.G. and Holtzberg, F., 1988. Physical properties of YBCO. *Physica C*, 153–155, pp.56–62.
[69] Bhat, S.V., 1987. Electron spin resonance in superconductors. *Pramana Journal of Physics*, 28, pp.L425–L430.
[70] Bhat, S.V., Ganguly, P., Ramakrishnan, T.V. and Rao, C.N.R., 1987. Superconducting thin films. *Journal of Physics C: Solid State Physics*, 20, pp.L559–L564.
[71] Blazey, K.W., Portis, A.M. and Bednorz, J.G., 1988. High-Tc YBCO surface studies. *Solid State Communications*, 65, pp.1153–1158.
[72] Blazey, K.W., 1990. In Bednorz, J.G. and Müller, K.A. (eds.) *Earlier and Recent Aspects of Superconductivity*, pp.240. Springer-Verlag.
[73] Dulcic, A., Crepeau, R.H. and Freed, J.H., 1988. Electron spin resonance in superconductors. *Physical Review B*, 38, pp.5002–5008.
[74] Srinivasu, V.V., Thomas, B., Vasanthacharya, N.Y., Hegde, M.S. and Bhat, S.V., 1991. Microwave and RF absorption in YBCO superconductors. *Solid State Communications*, 79, pp.713–718.
[75] Bohandy, J., Kim, B.E., Adrian, F.J. and Moorjani, K., 1989. Studies of superconducting thin films. *Physical Review B*, 39, pp.2733–2739.
[76] Bai, V.S., Bhagat, S.M. and Rajasekharan, T., 1995. Magnetic and transport studies of YBCO. *IEEE Transactions on Applied Superconductivity*, 5, pp.1572–1575.
[77] Pinto, R., Pai, S.P., D'Souza, C.P., Gupta, L.C., Vijayaraghavan, R., Kumar, D. and Sharon, M., 1992. Microwave surface impedance of YBCO superconductors. *Physica C*, 196, pp.264–270.
[78] Dulcic, A., Rakvin, B. and Pozek, M., 1989. Electron spin resonance in superconductors. *Europhysics Letters*, 10, pp.593–598.

[79] Portis, A.M., Blazey, K.W., Müller, K.A. and Bednorz, J.G., 1988. Microwave magneto-surface impedance. *Europhysics Letters*, 5, pp.467–472.
[80] Taylor, P.C., Zhang, D.J. and Xu, J.A., 1987. Surface impedance in high-Tc superconductors. *Physical Review B*, 36, pp.2361–2366.
[81] Srinivasu, V.V., 2010. Second and third peaks in the non-resonant microwave absorption spectra of Bi_{2212} crystals. *Journal of Superconductivity and Novel Magnetism*, 23(3), pp.305–308.
[82] Srinivasu, V.V., Pinto, R. and Sastry, M.D., 1996. Magnetic shielding in Ag-doped and pure $YBa_2Cu_3O_{7-x}$ thin films probed by non-resonant microwave absorption. *Applied Superconductivity*, 4(4), pp.195–201.
[83] Ginzburg, V.L., 2013. *Physics and astrophysics: A selection of key problems*. Elsevier.
[84] Kleiner, R. and Müller, P., 1994. Intrinsic Josephson effects in high-Tc superconductors. *Physical Review B*, 49(2), pp.1327–1334.
[85] Onyancha, R.B., Shimoyama, J., Singh, S.J., Ogino, H. and Srinivasu, V.V., 2015. Structure and line shape evolution of non-resonant microwave absorption in a SmFeAs(O,F) polycrystalline iron pnictide superconductor. *Journal of Superconductivity and Novel Magnetism*, 28(10), pp.2927–2934.
[86] Onyancha, R.B., Shimoyama, J., Singh, S.J., Ogino, H. and Srinivasu, V.V., 2017. Temperature dependence of low-field microwave absorption in SmFeAs(O,F) powder. *Journal of Superconductivity and Novel Magnetism*, 30(4), pp.1097–1102.
[87] Ramashitja, T.C., 2016. *Boundary current response in $Ba_{0.34}K_{0.64}Fe_2As_2$ superconducting single crystal probed by non-resonant microwave absorption technique* (Doctoral dissertation).
[88] Ramashitja, T.C., Srinivasu, V.V., Sankaran, V., Dong, C. and Ma, Y., 2017. Boundary current response in $Ba_{0.34}K_{0.64}Fe_2As_2$ superconducting single crystal probed by non-resonant microwave absorption technique. *Superconductor Science and Technology*, 30(10), p.105013.
[89] Klamut, J. (ed.), 2000. *New developments in high temperature superconductivity: Proceedings of the 2nd Polish-US conference held at Wrocław and Karpacz, Poland, 17–21 August 1998*. Berlin and New York: Springer.

CHAPTER TWO
LITERATURE REVIEW

2.1 Overview of Superconductivity

Following the discovery of high-temperature superconductors, numerous studies employed the Electron Paramagnetic Resonance (EPR) technique to explore their properties [1]. However, despite generating extensive experimental data in the superconducting state, these investigations yielded limited theoretical insights, leading to a gradual decline in the use of EPR for such studies. This outcome was unexpected, given the rich experimental information available from the technique and its potential to probe the spin and magnetic characteristics of superconductors.

At the advent of high-Tc materials, investigators originally investigated its property through an electron paramagnetic resonance (EPR) method [1]. Since the professor did not bring forth any major revelations, it eventually fell into obsolescence. While a good deal of experimental evidence was offered by EPR studies within the superconducting state, they hardly moved along the fundamental theories about high-Tc materials, which might be a bit surprising.

Presently, by continuing to study high-Tc superconductors using EPR methods, important experimental and theoretical evidence relevant to their performances has been given, some of which are exclusive results-meaning results that could not be achieved by standard experimental means. What these outcomes testify is that the EPR spectrometer still views as a strong and highly needed instrument for investigating the properties of high-Tc superconducting systems.

Investigations at extremely low temperatures were made possible by Kamerlingh Onnes's successful liquefaction of helium in 1908. This achievement marked a major breakthrough in cryogenics, opening new possibilities in physics and leading to several groundbreaking discoveries. Among these, the most remarkable was the discovery of superconductivity.Early experiments focused on studying how temperature affects the electrical resistance of highly pure metals. It was observed that as the purity of a sample increased, the residual resistivity at low temperatures decreased in metals such as gold and platinum. However, in 1911, Heike Kamerlingh Onnes discovered a striking phenomenon while studying mercury: when cooled to about 4.2 K using liquid helium, the electrical resistivity of mercury suddenly dropped abruptly to nearly zero (see Fig. 2.1). This marked the first discovery of superconductivity in history (Onnes, 1911).

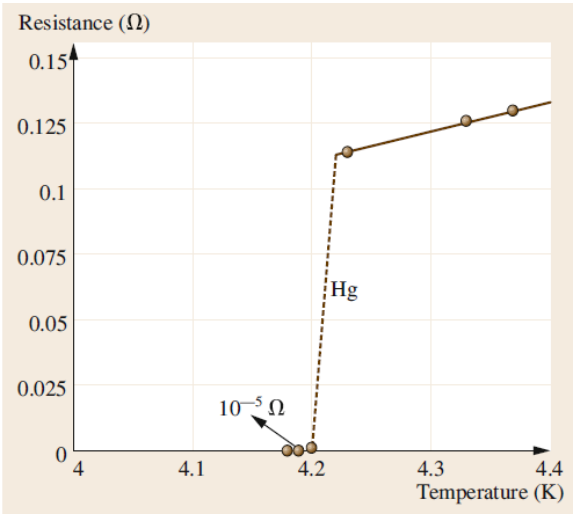


Fig. 2.1. Resistance–temperature plot of mercury measured by Heike Kamerlingh Onnes.

Source: Onnes, H. K., Leiden Cryogenic Laboratory, 1911.

Further laboratory experiments provided compelling evidence for the complete absence of electrical resistance in superconductors. Persistent currents in superconducting loops, like the one shown in Fig. 2.2, were observed to flow indefinitely without decay. Once established, these currents have been known to persist for over a year, demonstrating the remarkable stability and resistance-free nature of superconducting materials.

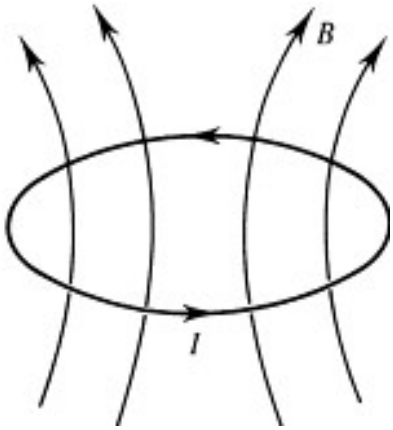


Fig2.2.Schematic for the persistent current experiment

When the external magnetic field applied to a material exceeds a specific threshold ($B_{ext} > B_c$) or the current density surpasses its critical limit ($j > j_c$), the superconducting state collapses and the material reverts to normal conduction. This remarkable phenomenon—later termed *superconductivity*—describes the capacity of certain materials to conduct electric current without

resistance once cooled below a distinct transition temperature, known as the critical temperature (Tc). Above this temperature, the substance behaves as an ordinary conductor, while below it, electrical resistance vanishes entirely.

Superconductors are characterized by three defining parameters: the critical temperature (Tc), the critical magnetic field (B_c), and the critical current density (j_c). Subsequent investigations revealed that several other elements in the periodic table can also enter a superconducting state, though most exhibit transition temperatures only a few kelvin above absolute zero. Since the first observation of this phenomenon, researchers have sought to understand the underlying mechanisms and discover materials that sustain superconductivity at higher Tc values and stronger critical magnetic fields (B_{c2}). These efforts have driven major advances in condensed matter physics and have fostered technologies that significantly influence modern life.

A defining feature of superconductors is their ability to carry electrical current with zero DC resistance and negligible impedance below the critical temperature (Tc). In contrast, conventional metals such as copper, silver, and gold lose energy through Ohmic dissipation. This loss-free conduction has significant technological implications, enabling devices with exceptional efficiency, precision, and operational speed, alongside continued miniaturization.

Key applications include magnetic resonance imaging (MRI) in medicine, nuclear magnetic resonance (NMR) spectroscopy in scientific research, and magnetically levitated (Maglev) trains in transportation. Both passive and active microwave components also benefit greatly from superconducting technologies. One of the most advanced applications is the International Thermonuclear Experimental Reactor (ITER), which aims to demonstrate clean energy generation through nuclear fusion. These developments rely on high-field superconducting magnets capable of carrying critical current densities of approximately 10^5 A·cm^{-2} under magnetic fields approaching 10 Tesla [4].

2.2 The Meissner Phenomenon

Superconductivity is distinguished not only by the disappearance of electrical resistance but also by the Meissner effect, in which magnetic flux is expelled from a material upon entering the superconducting state. First demonstrated experimentally by Meissner and Ochsenfeld (1933), this phenomenon occurs when a specimen is cooled below its critical temperature (Tc) in the presence of an external magnetic field, causing the internal magnetic induction to drop nearly to

zero (Fig. 2.2). This behavior cannot be explained by perfect conductivity alone, since an ideal conductor would only preserve the pre-existing magnetic flux.

The Meissner effect is reversible, indicating that superconductivity is destroyed when the applied magnetic field exceeds the thermodynamic critical field (Hc). The value of Hc corresponds to the free-energy difference between the superconducting and normal states in zero field, often called the condensation energy. Unlike an ideal conductor, a true superconductor actively expels weak magnetic fields, regardless of whether they are applied before or after the transition below Tc.

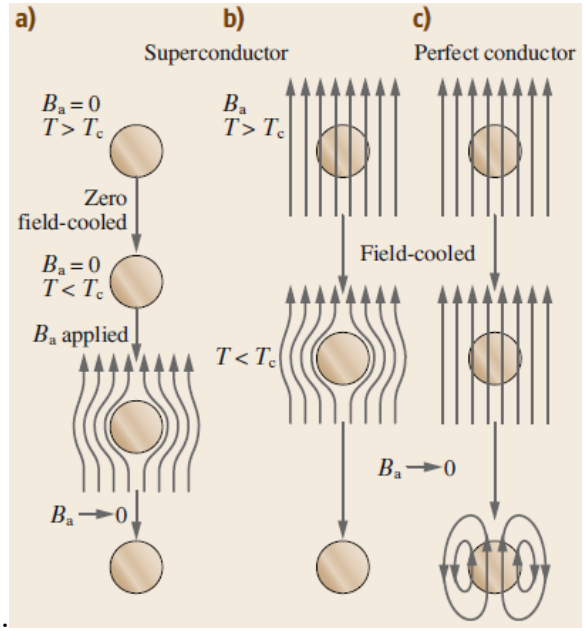


Figure. *2.3 (a–c):* Magnetic flux behavior in superconductors. (a) Flux exclusion during zero-field cooling**;** (b) flux exclusion during field cooling**;** (c) for comparison, flux remains within a perfect conductor under field-cooling conditions [40].

2.3 Types of Superconductors

Superconducting materials are generally classified into **Type I** and **Type II**, based on their response to applied magnetic fields.

Type I Superconductors:

These are mostly pure elemental metals that exhibit superconductivity only under relatively weak

magnetic fields**.** When the applied field exceeds the thermodynamic critical field (H_c)**,** the material abruptly returns to its normal resistive state.

Type II Superconductors:

In contrast, Type II materials allow magnetic flux to enter in the form of discrete, quantized vortices while the surrounding regions remain superconducting. This coexistence of superconducting and normal domains gives rise to the so-called *mixed state*. Because of this property, Type II superconductors can retain zero resistance even in much stronger magnetic fields than their Type I counterparts. Their robustness makes them indispensable in modern technologies such as high-field magnets, particle accelerators, and advanced imaging systems [81].

The advent of high-temperature superconductors (HTSCs)—especially those based on copper-oxide perovskites—revolutionized the field. These materials exhibit unconventional superconducting behavior, often not explained by the conventional theories that describe low-temperature systems. Their complex electromagnetic characteristics have fueled intensive experimental and theoretical research to uncover both their microscopic origins and large-scale physical properties.The earliest attempt to describe superconductivity theoretically was made by the London brothers (Fritz and Heinz London**)** in 1935. Their formulation, known as the *London theory*, established fundamental relations connecting the internal electric and magnetic fields within a superconductor. These equations provided the first quantitative foundation for understanding the expulsion of magnetic flux and the phenomenon later recognized as the Meissner effect [85].

London Equations and Magnetic Field Penetration

The electrodynamics of superconductors were first expressed quantitatively by the London brothers in 1935 through two fundamental relations linking the superconducting current to the electromagnetic fields. These are written as

$$\vec{E} = \frac{\partial}{\partial t}(\Lambda \vec{j}_s) \qquad 2.1$$

$$\frac{1}{\Lambda}\vec{B} = -c\,\vec{\nabla} \times \vec{j}_s \qquad 2.2$$

Where $\vec{E}$ is electric field vector; $\vec{B}$ is the magnetic field; $\vec{j}_s$ is the superconducting current density. $\Lambda = \frac{4\pi\lambda^2}{c^2} = \frac{m}{n_S e^2}$ is a phenomenological parameter. It was expected that n_S, the number density of superconducting electrons, would vary continuously from zero at T_C to a limiting value of the order of n, the density of conduction electrons, at $T \ll T_C$.

The second London equation(1.2) combined with Maxwell equation $\vec{\nabla} \times \vec{B} = \frac{4\pi\vec{j}}{c}$,

leads to

$$\nabla^2\vec{B} = \frac{\vec{B}}{\lambda^2} \qquad (2.3)$$

Which when solved in one dimension gives an exponential decay of magnetic field inside a superconductor

$$\vec{B}(x) = \vec{B}_0 e^{-x/\lambda}$$

Here $$\lambda^2 = {}^{m}/_{\mu_0 n_S e^2}$$

defines the magnetic penetration depth, λ, which characterizes how deeply an external magnetic field can penetrate the superconductor. This demonstrates that the magnetic field is expelled from the interior of the sample—an effect known as the Meissner effect.At the surface, persistent screening currents are generated that oppose and neutralize the applied field. The density of these shielding currents decreases exponentially with distance from the surface, governed by the characteristic length λ. Typically, the penetration depth lies in the range of several hundred to a few thousand angstroms and diverges as the temperature approaches the critical value (T→Tc).

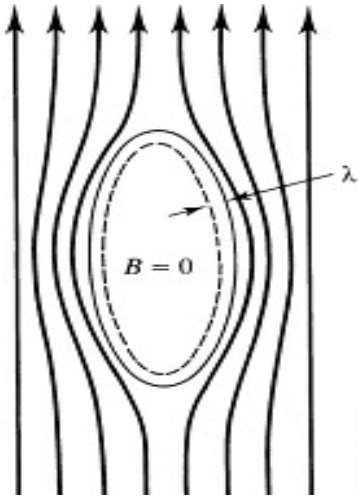


Figure 2.4 *Schematic illustration of the Meissner effect, showing magnetic flux expulsion from the interior of a bulk superconductor. λ denotes the penetration depth, typically on the order of several hundred angstroms [Adapted from Tinkham, 1996]*.

The London theory offered the first quantitative picture of superconductivity, describing the electromagnetic response of a superconductor and how it excludes magnetic fields. While this model successfully captured the essence of the Meissner effect, it could not explain the microscopic origin of superconductivity or several experimental anomalies that followed.

A decisive step forward came in 1957 when John Bardeen, Leon Cooper, and Robert Schrieffer developed the BCS theory, providing a microscopic interpretation of superconductivity. Their formulation proposed that superconductivity arises from a collective electronic phenomenon in which electrons interact with the crystal lattice to form correlated pairs.

This concept was built upon Cooper's 1956 insight, which showed that even a weak attractive interaction between electrons can produce a bound state at the Fermi surface — the now-famous Cooper pair. The mechanism operates as follows:

When an electron passes near a positively charged ion in the lattice, it slightly distorts the lattice, producing a region of increased positive charge density.

A second electron is attracted to this distortion through the exchange of virtual phonons, resulting in an effective attractive interaction between the two electrons.

These paired electrons have opposite spins and momenta, allowing them to move coherently through the lattice without scattering.

The pairs occupy a collective quantum state — a condensate — that can carry current indefinitely without dissipation.

This coherent pairing leads to a fundamental energy gap **(Δ)** in the electronic density of states. Breaking the superconducting state requires providing at least this gap energy, given approximately by:

$$\Delta(0) = 1.764\, k_B T_c$$

where kBk_BkB is the Boltzmann constant and Tc is the critical temperature.

The BCS framework successfully predicted the dependence of many superconducting properties — such as the thermodynamic critical field, specific heat, and energy gap — on temperature. For conventional metals (low-temperature superconductors), the agreement between theoretical

predictions and experiments was remarkable, earning Bardeen, Cooper, and Schrieffer the **Nobel** Prize in Physics.

Despite its great success, the BCS theory has limitations, especially in situations where the superconducting energy gap or order parameter varies in space. In such cases, a macroscopic, phenomenological approach is better suited.

This was provided earlier by V. L. Ginzburg and L. D. Landau (1950), who expressed the free energy of a superconductor near TcT_cTc in terms of a complex order parameter, Ψ\PsiΨ, which quantifies the degree of superconducting order. From this formulation, two intrinsic length scales naturally emerge:

The London penetration depth **(λ)**, describing how magnetic fields decay inside the material.

The coherence length **(ξ)**, representing the spatial range over which the order parameter varies significantly.

Although initially overlooked, the importance of Ginzburg–Landau (GL) theory became evident when Gor'kov (1959) demonstrated that it could be derived as a limiting form of the BCS theory near Tc. Within this framework, the coherence length ξξξ can be viewed as the approximate size of a Cooper pair.

Superconductors are therefore classified according to the ratio of these two characteristic lengths, κ=λ/ξ:

When $0 < \lambda/\xi < 1/\sqrt{2}$, the coherence length is larger than the penetration depth, and the material behaves as a Type I superconductor. In such cases, the transition from the superconducting (Meissner) state to the normal state occurs abruptly at a single critical magnetic field Bc. Typical Type I materials include mercury, aluminum, and tin, as illustrated schematically in *Figure 2.5(a).*

When $\lambda/\xi > 1/\sqrt{2}$, the superconductor is classified as Type II. Here, magnetic flux begins to penetrate the sample above a lower critical field (Bc1) in the form of quantized vortices. As the field increases further and reaches the upper critical field (Bc2), superconductivity is completely destroyed, marking the transition to the normal state.

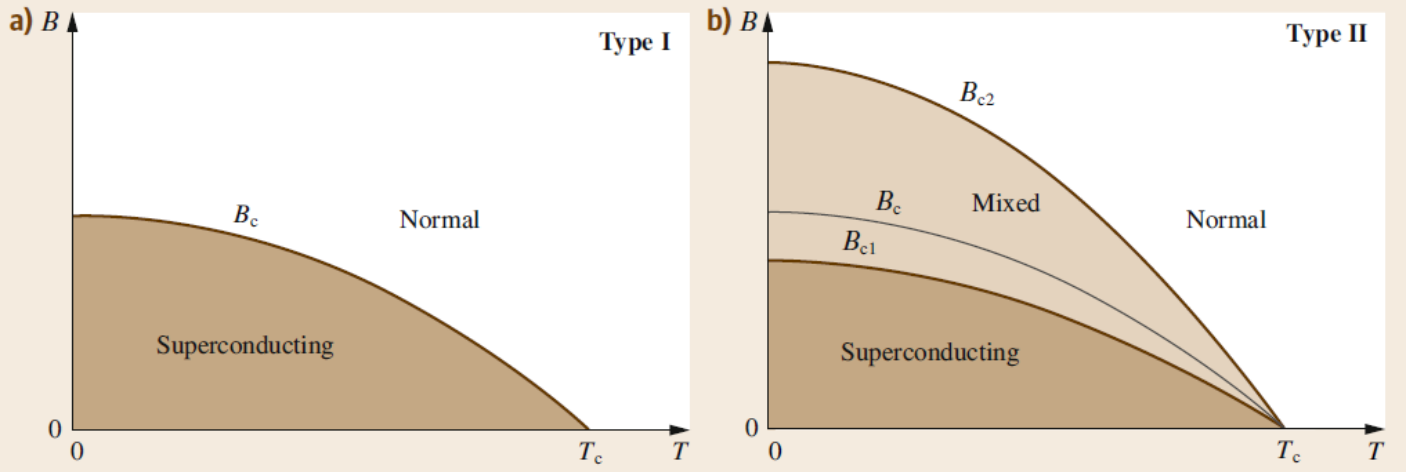


Figure 2.5: Phase diagrams illustrating the magnetic field–temperature relationship for superconductors.(a) Type I superconductors: A direct transition occurs from the superconducting (Meissner) state to the normal state at the critical field Bc.
(b) Type II superconductors: Magnetic flux begins to penetrate at the lower critical field B_c1, forming a mixed state of superconducting and normal regions. When the field reaches the upper critical field Bc2, superconductivity disappears, and the material becomes normal. Adapted from Tinkham (1996)

Unlike Type I superconductors, which undergo a first-order transition from the Meissner state to the normal state at B_c, Type II superconductors exhibit a two-stage transition. Upon reaching B_c1, magnetic flux penetrates the material in quantized units ($\Phi_0 = hc/2e$), forming vortices with normal cores surrounded by circulating supercurrents. As the field increases toward B_c2, the superconducting regions shrink, and the vortex lattice spacing decreases until superconductivity is completely lost at B_c2.

Examples of Type II superconductors include Nb_3Sn, NbTi, and the high-T_c cuprates. The mixed state is illustrated for a slab geometry in Fig. 2.6. According to Abrikosov (1957), these flux lines, or fluxoids, form a periodic lattice within the superconductor. Each vortex carries a quantized flux, and the lattice spacing collapses as the material approaches B_c2, corresponding to full flux penetration and the normal state transition.

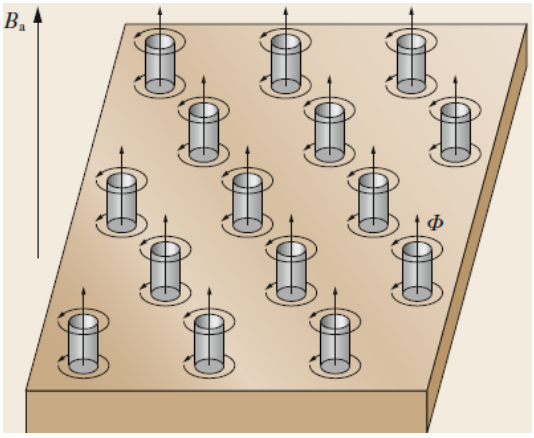


Figure 2.6: The mixed state in a Type II superconductor, showing normal cores surrounded by circulating vortex currents and penetrated by quantized flux lines (fluxons). Each vortex carries an integer multiple of the magnetic flux quantum [40].

The scientific study of superconductivity began in 1911, when Heike Kamerlingh Onnes observed a remarkable phenomenon while investigating the electrical properties of mercury at cryogenic temperatures. As the temperature approached 4.2 K—the boiling point of liquid helium—the electrical resistance of mercury suddenly dropped to zero, marking the discovery of superconductivity. This transition introduced a new state of matter with lossless current flow, transforming condensed matter physics.

About 22 years later, Walther Meissner and Robert Ochsenfeld (1933) identified another fundamental property: the Meissner effect. They showed that superconductors, when cooled below their critical temperature (Tc), do not merely conduct without resistance; they actively expel magnetic flux from their interiors. This effect distinguishes true superconductors from perfect conductors and reveals their intrinsic diamagnetism.

In this state, the magnetic susceptibility (χ\chiχ) reaches a value of $-1/4\pi$ in cgs units, signifying that the interior magnetic induction becomes zero. The Meissner effect thus represents a fundamental thermodynamic property of the superconducting phase, not merely a consequence of perfect electrical conductivity. It remains one of the most critical features defining superconducting materials and provides the conceptual basis for understanding magnetic flux behavior in both Type I and Type II superconductors.

Following these early discoveries, magnetic induction techniques became widely used to explore new superconducting materials and study their behavior under magnetic fields. Among these, the

ac mutual inductance bridge**,** introduced by Shoenberg**,** became a preferred experimental method because of its simplicity and adaptability to different sample geometries and sizes. These techniques provided critical insights into the magnetic responses of superconducting systems, laying the groundwork for modern superconductivity research.

2.4 Structure and Fundamental Properties of YBCO

This section presents a concise overview of the crystal structure and superconducting characteristics of $YBa_2Cu_3O_{7-x}$ (YBCO), one of the most studied high-temperature superconductors.

2.4.1 Crystal Structure

In contrast to conventional metallic superconductors, high-temperature cuprates possess highly complex and anisotropic crystal frameworks. Among these, YBCO exhibits pronounced planar anisotropy**,** which plays a central role in its superconducting behavior. The typical lattice parameters of YBCO are approximately $a = 3.82$ *Å,* $b = 3.89$ *Å,* and $c = 11.68$ *Å.*

As shown in Figure 2.7, YBCO crystallizes in a distorted perovskite structure belonging to the orthorhombic system. The unit cell consists of CuO_2 bilayers separated by an intermediate yttrium (Y) layer**,** while barium (Ba) and copper–oxygen chains form the outer structural framework.

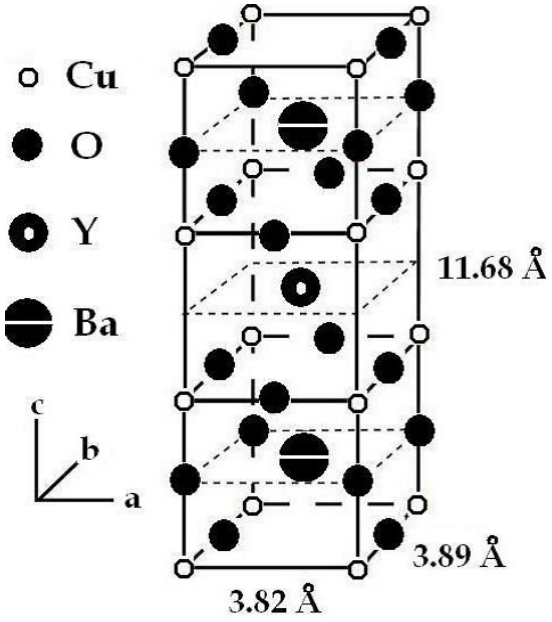


Figure 2.7. Crystal structure of the $YBa_2Cu_3O_{7-x}$ superconductor (Source: Dias, Magnetic Irreversibility and Resistive Transition in YBaCuO Superconductors: Interpretations and Possible Correlations, Universidade Federal de Pelotas, Brazil).

The superconducting carriers (Cooper pairs) are primarily confined to the CuO_2 planes, which act as the main conducting layers. The intervening atomic sheets serve as charge reservoirs, regulating the hole concentration in the planes and thereby influencing the superconducting transition temperature ($\mathbf{T_n}$).The oxygen stoichiometry in YBCO—denoted by the value of x in $YBa_2Cu_3O_{7-x}$—is critical in determining its physical properties. When $x = 1$ (corresponding to six oxygen atoms per formula unit), the compound adopts a tetragonal structure and behaves as an antiferromagnetic insulator. As oxygen content increases, the structure transforms into the orthorhombic superconducting phase, reaching an optimal critical temperature of approximately 93 K when the oxygen occupancy approaches seven per unit cell ($x \approx 0$).

2.5 $YBa_2Cu_3O_{7-x}$: Fundamental Properties

The physical properties of high-Tc superconductors, particularly their electrical and magnetic responses, are strongly influenced by their layered crystal structures. Among these materials, the $YBa_2Cu_3O_{7-x}$ (YBCO) system stands out for its complex but technologically important characteristics.

2.6 Electrical Transport Properties

High-Tc cuprates exhibit several unusual features in their normal and superconducting states. Key aspects include:

Strong anisotropy of electronic transport,

Granularity and disorder effects, especially in polycrystalline samples,

and sensitivity of carrier concentration to oxygen stoichiometry.

2.6.1 Anisotropy of the Normal State

The transport properties of $YBa_2Cu_3O_{7-x}$ (YBCO) display pronounced anisotropy, directly reflecting its layered crystalline architecture. The CuO_2 planes (also known as *ab planes*) function as highly conductive pathways, supporting the motion of charge carriers with relatively low scattering. In contrast, the c-axis**,** which runs perpendicular to these planes, exhibits

substantially higher electrical resistivity due to the presence of weakly conducting interlayer regions that separate the planes. As a result, two distinct transport behaviors emerge:

Within the ab-plane, the current displays metallic characteristics, indicating efficient carrier mobility.Along the c-axis**,** the charge transport is strongly suppressed, producing a quasi-two-dimensional (2D) conduction profile. Nevertheless, in well-prepared single crystals, the c-axis can still exhibit a *metallic-like* temperature dependence of resistivity.

Experimental results (see Fig. 3 in [8]) confirm the highly anisotropic nature of resistivity:

At room temperature,

$$\rho_a /, \rho_b > 2.5, \;\; \rho_b/\rho_c > 30$$

This demonstrates that current flows much more easily within the planes than across them — a hallmark of cuprate superconductors.

YBCO's electronic transport is quasi-two-dimensional, dominated by the CuO2_22 planes. This anisotropy is central to understanding both its normal-state physics and its superconducting

properties.

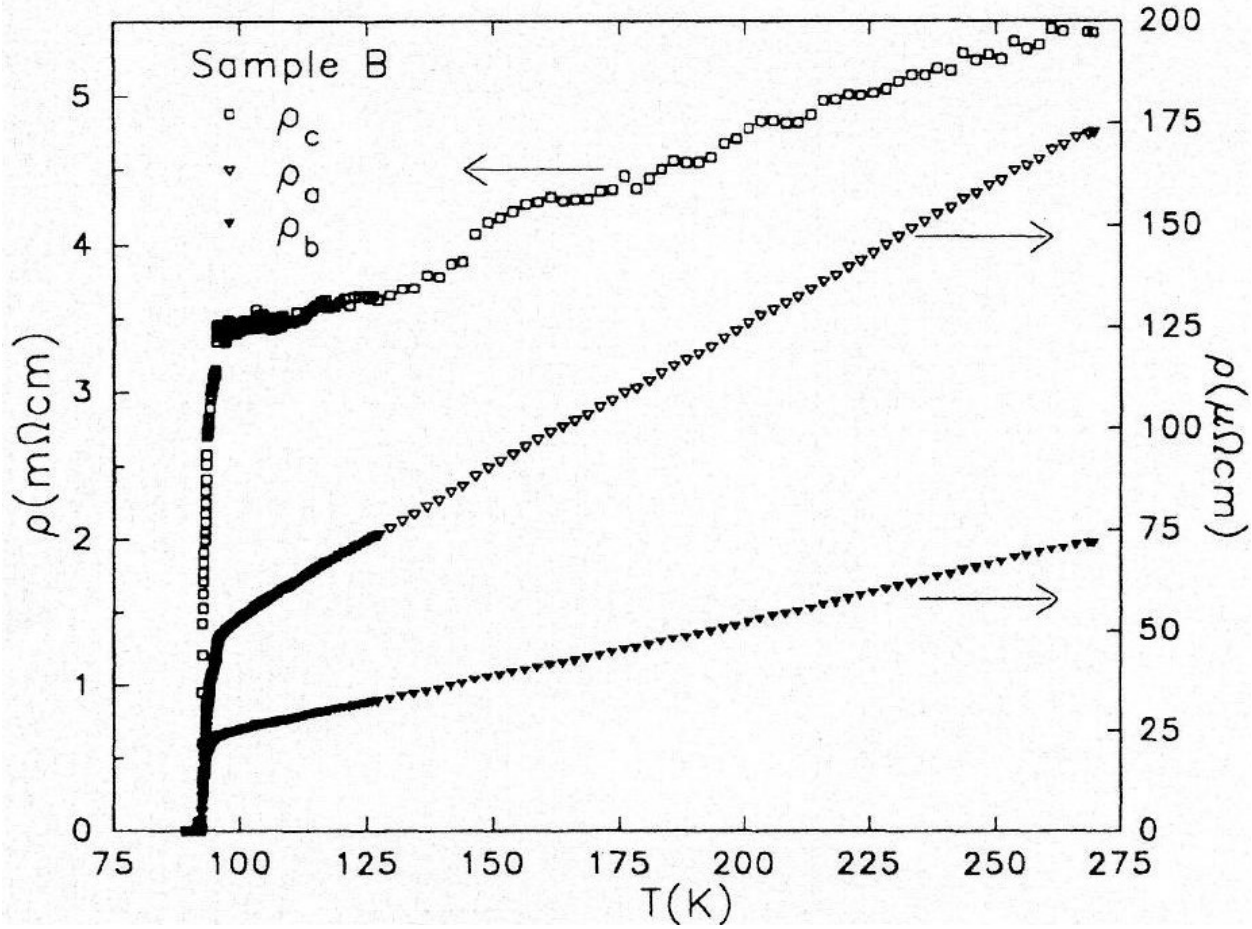


Figure 2.8. Electrical resistivity along the three crystallographic directions for an untwinned $YBa_2Cu_3O_{7-x}$ single crystal (Source: Dias, Magnetic Irreversibility and Resistive Transition in YBaCuO Superconductors: Interpretations and Possible Correlations, Universidade Federal de Pelotas, Brazil).

The transition from the normal to the superconducting state in granular superconductors occurs gradually, passing through distinct temperature-dependent regions (Fig. 2.8):

Above Tc – Paraconducting region: Excess conductivity arises from thermal fluctuations in the amplitude of the superconducting order parameter.

Between Tc and T_{c0} – Paracoherent region: Individual superconducting grains are weakly coupled via Josephson junctions. Fluctuations occur primarily in the phase of the order parameter, and the sample exhibits finite resistivity.

At T_{c0} – Global superconducting state: Long-range phase coherence is established through a percolation process that couples neighboring grains, resulting in zero resistivity.

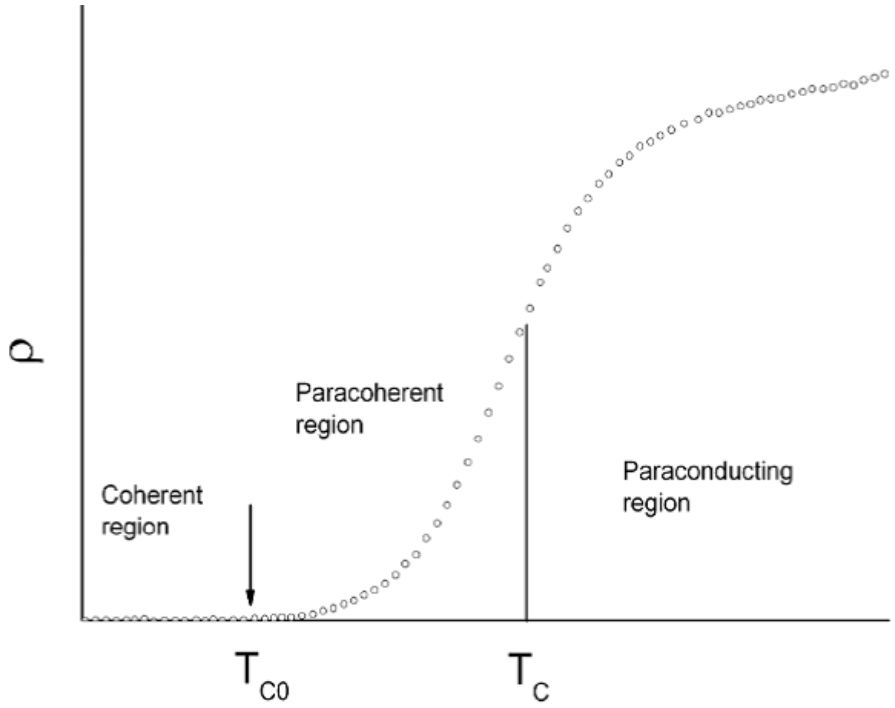


Figure 2.9. Schematic representation of the resistive transition in a granular superconductor, showing paraconducting and paracoherent regions (Source: Dias, Magnetic Irreversibility and Resistive Transition in YBaCuO Superconductors: Interpretations and Possible Correlations, Universidade Federal de Pelotas, Brazil).

This coupling process, often termed the coherence transition, governs the activation of weak links among superconducting grains. According to Rosenblatt et al. [14], at the critical temperature (T_{c0}), the fluctuating phases of the superconducting order parameter across the grains synchronize into a long-range ordered state, leading to the emergence of perfect conductivity in the system.

2.7 Microwave Absorption Studies

Among the many experimental techniques developed to study HTSCs, microwave absorption (MA) methods have proven especially valuable. These techniques provide detailed information on phenomena such as vortex dynamics, Josephson junction behavior, and nonlinear electromagnetic effects.

Theoretical models have been developed to describe Josephson junction arrays interacting with microwave fields. These models explain key phenomena such as overheating effects**,** field-induced phase transitions, and distinct absorption peaks observed under low magnetic field

conditions [81]. As a result, microwave absorption studies have become a central tool in probing the intricate physics of HTSCs.

2.7.1 Non-Resonant Microwave Absorption (NRMA)

Among microwave-based experimental methods, Non-Resonant Microwave Absorption (NRMA) has established itself as a powerful and flexible probe for exploring the intrinsic and extrinsic properties of high-temperature superconductors (HTSCs).In NRMA experiments, the total magnetic field applied to a sample is composed of three components:

A static magnetic field**,**

A low-frequency modulation field (typically 10–100 kHz), and

A high-frequency microwave component (~9–10 GHz).

Unlike resonant techniques, NRMA directly monitors the absorption of microwave energy as a function of magnetic field, offering unique sensitivity to weak-link dynamics, vortex motion, and flux-line interactions in superconducting materials.

Recent developments have expanded NRMA research beyond the cuprate family to include iron-based superconductors, such as $Ba_{0.34}K_{0.64}Fe_2As_2$ (BaK122). Investigations on these materials have shown that by tuning parameters such as the modulation amplitude, temperature, and microwave power, one can uncover detailed information about boundary current responses and magnetic flux behavior, providing deeper insight into the microscopic mechanisms governing superconductivity in complex systems [81].

The NRMA technique serves multiple purposes in the study of HTSCs. It has been applied to:

Evaluate the microstructural quality of superconducting thin films [82, 83];

Analyze grain coupling and weak-link behavior;

Identify different superconducting phases;

Investigate surface barrier effects, flux penetration depth, and anomalous absorption patterns;

Examine power-dependent and temperature-dependent variations in microwave response.

A major advantage of NRMA lies in its capacity to directly probe shielding currents and intergranular current dynamics at low magnetic fields—a regime typically inaccessible through standard magnetization or transport techniques [78]. This makes it particularly suitable for detecting weak magnetic coupling or inhomogeneities in granular superconductors.

Several theoretical models have been advanced to interpret NRMA signals. The Portis model [40] describes microwave absorption as a result of energy dissipation from fluxon motion induced by microwave excitation. In contrast, the Dulčić model [78] attributes NRMA behavior to reductions in the critical current (Ic) of weak links when exposed to fluctuating external magnetic fields, leading to measurable modifications in the microwave absorption profile.Together, these frameworks provide a coherent understanding of how NRMA captures the complex flux dynamics, weak-link interactions, and current modulation phenomena that define high-temperature superconducting systems.

Microwave absorption in superconductors is largely governed by the behavior of fluxons, where energy dissipation arises from the interaction of superconducting charge carriers with moving and damped flux lines. As the magnetic flux density (B) increases, fluxons penetrate deeper into the material, resulting in higher energy absorption [84, 85]. This phenomenon explains the similar patterns observed between NRMA measurements and ac magnetic susceptibility experiments.

2.8 Magnetic Properties of Superconductors

High-temperature superconductors (HTSCs) have attracted profound scientific and technological interest owing to their distinctive magnetic responses and their tight correlation with microwave and radio-frequency (RF) electromagnetic phenomena such as Non-Resonant Microwave Absorption (NRMA)**.**This section introduces the core magnetic principles that underpin the electrodynamic behavior of superconductors.

2.8.1 The Critical State and Critical Currents

In Type II superconductors, magnetic and transport behavior is largely determined by the interaction between magnetic flux lines (fluxons) and crystal lattice defects**.**

When an electric current flows through the superconductor, quantized flux lines thread the material and can become pinned by imperfections such as dislocations, grain boundaries, or inclusions**.** These pinning centers stabilize the superconducting state by restricting flux motion and preventing energy dissipation.

If the driving force on the flux lines becomes strong enough, the vortices can depin and move, causing energy losses. The Lorentz force acting on a single flux line is expressed as:

$$F_L = \boldsymbol{J} \times \Phi_0$$

where **J** is the current density and Φ_0 is the magnetic flux quantum associated with each vortex.

When $\boldsymbol{F}_L \leq \boldsymbol{F}_p$ (the pinning force), fluxons remain stationary, and the material sustains lossless superconductivity.

When $\boldsymbol{F}_L > \boldsymbol{F}_p$, fluxons begin to move, producing a voltage and consequent energy dissipation within the sample.

The critical current density Jc represents the upper limit of current that can pass through the material without flux motion.

At J=Jc, the Lorentz force equals the pinning force ($\boldsymbol{F}_L = \boldsymbol{F}_p$) , marking the boundary between dissipation-free and resistive behavior in the superconductor.

2.8.2 The Bean Critical State Model

The Bean critical state model provides a simple yet powerful framework for understanding how magnetic flux penetrates and distributes within type-II superconductors when exposed to varying external magnetic fields. It effectively explains **the** hysteretic magnetization behavior observed in experiments and describes how vortex pinning gives rise to a *critical state* of current flow.

In this model:

Magnetic flux penetrates the sample only from its surface as the external magnetic field increases.

The penetrating flux forms quantized vortex lines that become trapped at pinning centers distributed throughout the material.

When the applied field changes, the superconductor evolves into a metastable state**,** where the Lorentz force acting on the vortices is balanced by the pinning force**.**

The Bean model assumes that flux rearrangement occurs on a timescale much shorter than the material's internal relaxation processes. Consequently, at any instant, the superconductor is composed of regions carrying currents at ±**J**c, separated by flux-free regions.For simplicity, the model neglects voltage drops and thermal effects, focusing solely on the magnetic and current distribution characteristics.

Core Assumptions of the Bean Model:

The current density **J** within the superconductor cannot exceed the critical current density **J**c .

Magnetic flux penetration is governed by the balance between Lorentz and pinning forces.

The system remains in a metastable equilibrium state characterized by hysteresis in magnetization curves.The magnetization of the material depends on the history of the applied field**,** producing hysteresis loops characteristic of type-II superconductors.The distribution of magnetic flux within the material is governed by pinning strength and sample geometry**,** rather than purely by external magnetic field magnitude.Below Jc, vortices remain pinned and do not move.Above Jc, flux lines begin to move freely, producing energy dissipation and loss of superconducting stability.Magnetization Behavior

Under the Bean model, the distribution of magnetic flux density (B) across a superconducting slab of thickness D is described by the following relations:

For $B \leq B^*$: $4\pi \mathrm{M} = B - \frac{B^2}{2B^*}$

For $B \geq B^*$: $-4\pi M = \frac{B^*}{2}$

where:

M is the magnetization,B^* is the magnetic field value at which half the volume of the superconducting slab is penetrated by magnetic flux.The parameter B^* is related to the critical current density by:

$$B^* = \frac{\pi J_c D}{5}$$

By experimentally determining B^*, the critical current density J_c can be calculated, providing valuable insight into the superconductor's electromagnetic performance [27,32,33][

Physical Interpretation.

When the external magnetic field is low, only the outer surface of the slab is penetrated by magnetic vortices, resulting in a nonlinear M vs. H response.As the field increases, vortices penetrate deeper until half the slab volume is filled at $\mathrm{B} = \mathrm{B}^*$.Beyond this point ($\mathrm{B} \geq \mathrm{B}^*$), the magnetization saturates and remains constant.This behavior explains the hysteresis loops observed in type-II superconductors during alternating magnetic fields, a fundamental feature for understanding their loss mechanisms in AC applications.

2.8.3 The Anderson–Kim Model and Field-Dependent Critical State

The magnetic field B* represents the point at which half of the superconducting slab's volume becomes penetrated by magnetic flux. Determining B* experimentally allows for the estimation of the critical current density **(Jc)**, providing a direct measure of the superconductor's electromagnetic transport capability [27, 32, 33].

At very low external fields, flux penetrates only the outer surface of the sample, while the interior remains in a perfectly diamagnetic state. In this regime, the magnetization (M) exhibits a nonlinear dependence on the applied field (H), reflecting the gradual entry of vortices into the surface layers.

In 1962, C. P. Bean introduced the critical state model, describing the magnetization of hard (strongly pinned) superconductors by assuming that $J_{(c)}$ is independent of the applied magnetic field [27]. Later that year, Kim, Hempstead, and Strnad extended Bean's model by introducing a field-dependent critical current density, resulting in a more flexible and realistic framework now known as the Anderson–Kim model [28].

Initially, this generalized model was primarily theoretical, with applications limited to low-field AC susceptibility and small-signal response studies [34–37], due to the experimental challenges in directly validating field-dependent pinning effects.Subsequent developments incorporated magnetization hysteresis into the model, successfully bridging the gap between theoretical predictions and experimental observations [39]. This hysteretic version of the Kim model provided a more realistic description of vortex motion, flux pinning, and magnetic irreversibility in type-II superconductors.

In the following decades, this refined theoretical framework became essential for interpreting the electromagnetic behavior of high-temperature superconductors (HTS), particularly the cuprate families such as $YBa_2Cu_3O_{7-x}$ (YBCO) and $Bi_2Sr_2CaCu_2O_{8+x}$ (BSCCO) (Gupta, 2019).

Through these advancements, the Anderson–Kim model evolved into a cornerstone theory for understanding flux dynamics, energy dissipation, and critical-state hysteresis in modern superconducting systems.

2.8.4 Low and High Critical Magnetic Fields

From basic energetic considerations, the lower critical magnetic field (H_{C2}) and the upper critical magnetic field (B_{C2}) of Type II superconductors can be estimated.When the applied magnetic field Bapplied=B_{C1} , magnetic flux begins to penetrate the superconductor.At this point, the magnetic field at the core of a vortex is approximately B_{C1} and decays to zero over a distance proportional to the London penetration depth (λ\lambdaλ).The magnetic flux associated with a single vortex can be approximated as:

$$\Phi=\pi\lambda^2 B_{C1} \qquad (2.4)$$

Setting this flux equal to the magnetic flux quantum Φ_0, we obtain:

$$B_{C1}=\Phi_0/\pi\lambda^2 \qquad (2.5)$$

When the applied magnetic field Bapplied=B_{C2} , the vortices are packed as tightly as possible while the material remains superconducting.Each vortex occupie s an area approximately equal to $\pi\xi^2$, where ξ\xiξ is the coherence length. Thus:

$$B_{C2}=\frac{\Phi_0}{\pi\xi^2} \qquad ([2.6)$$

For Josephson junctions, when the applied field exceeds:

$$B_{C1}=\frac{\Phi_0}{2(\pi)^{3/2}\lambda j\lambda L}(0.5(2\lambda_L+d)) \qquad (2.7)$$

where d is the thickness of the insulating barrier, fluxons (quantized flux lines) begin to enter the junction.These values of B_{C1} are much smaller than those in bulk superconductors.

2.8.5 Weak Links and Josephson Junctions

Weak links in superconductors can be artificially created or naturally formed through various mechanisms:Dayem Bridge:A narrow constriction in a thin film of a single superconductor, with dimensions comparable to the coherence length (ξ).

Grain Boundary Weak Links:

When a high-Tc superconducting layer is deposited across a naturally occurring grain boundary in the substrate, the boundary acts as a defect site. This forces the superconductor to form a chain of imperfections, effectively creating a natural weak link [9].

2.9 Critical Magnetic Fields in Type-II Superconductors

Type-II superconductors exhibit a **two-stage transition** under an applied magnetic field, in contrast to type-I superconductors, which undergo a direct transition from the Meissner state to the normal state at the critical field Bc.The lower critical field B_{C1} marks the onset of flux penetration into the superconductor, forming the mixed state**.**The upper critical field B_{C2} is the field at which superconductivity is completely destroyed, and the material becomes normal [Tinkham, 1996].In the mixed state, magnetic flux enters in quantized units Φ_0=hc/2e, forming **vortices** with normal cores surrounded by circulating supercurrents (Fig. 2.6). The vortices arrange into a lattice, whose spacing decreases with increasing field, collapsing at B_{C2} and marking the complete loss of superconductivity (Abrikosov, 1957).

2.9.1 The Critical State and Flux Pinning

The transport and magnetic properties of type-II superconductors are dominated by interaction between magnetic flux lines (fluxons) and lattice defects**.**Fluxons are anchored or pinned by imperfections such as dislocations, grain boundaries, or inclusions, which stabilizes the superconducting state by preventing energy dissipation.When the Lorentz force on fluxons exceeds the pinning force, they move, causing energy losses. The Lorentz force on a single flux line is: $F_L = J \times \Phi_0$, where J is the current density**,** and Φ_0 is the magnetic flux quantum**.**

2.9.2 The Anderson–Kim Model

The critical current density J_C defines the maximum current the superconductor can carry without flux motion.The field B^* is the magnetic field at which half the superconducting volume is penetrated by flux**.** Bean's critical state model (1962) assumes J_C is field-independent, while the Anderson–Kim model extends it to field-dependent $J_C(H)$ [27,28]. At low external fields, magnetization **M** shows nonlinear dependence on H due to partial flux penetration.

2.9.3 Josephson Effect

When a superconductor is cooled below TC, electrons condense into a **macroscopic quantum state**, described by the wave function:

$\psi=|\psi|e^{i\phi}$, whee $|\psi|$ = density of Cooper pairs,ϕ\phi = phase, governing supercurrent flow [21].

A Josephson junction forms when two superconductors are weakly coupled through a thin barrier. The **DC** supercurrent through the junction is:

$$I=I_C\sin\phi \qquad (2.8)$$

here I_C is the critical current. If a voltage V is applied:

$$\frac{d\phi}{dt} = \frac{2eV}{\hbar} \qquad (2.9)$$

This is the AC Josephson effect, producing an oscillating supercurrent.The temperature-dependent critical current is:

$$I_C(T) = \frac{\pi\Delta(T)}{2eR_n} tanh(\frac{\Delta(T)}{2k_BT}) \qquad (2.10)$$

Zero-temperature limit At T=0, since $\tanh(x)\to 1$ as $x\to\infty$

$$I_C(0) = \frac{\pi\Delta(0)}{2eR_n} \qquad (2.11)$$

Here, $\Delta(T)$ is the superconducting energy gap at temperature T,e is the elementary charge,
R_n is the normal-state resistance of the junction,k_B is the Boltzmann constant,
and I_C is the temperature-dependent critical current.
Total current through the junction

$$I = I_C sin\phi + \frac{V}{R} + C\frac{dV}{dt} \qquad (2.12)$$

When the applied current exceeds the critical current I_C, quasiparticle tunneling contributes to the transport, and the junction behaves as a resistively shunted junction (RSJ). Including the junction capacitance C, the system is described by the resistively and capacitively shunted junction (RCSJ) model, in which the total current consists of a supercurrent, a normal resistive current, and a displacement current, as expressed in Eq. (2.12).Here, ϕis the superconducting phase difference across the junction,V is the voltage across the junction,R is the shunt resistance,and C is the junction capacitance.If $I > I_C$, normal electrons contribute, forming a resistively shunted junction (RSJ**)**. Including a parallel capacitor, the total current becomes:Dimensionless form:

$$\frac{I}{I_C} = sin\,\phi + \frac{d\phi}{d\tau} + \beta_C \frac{d^2\phi}{d\tau^2} \qquad (2.13)$$

here

$$\beta_C = \frac{2\pi I_C R^2 C}{\Phi_0} \qquad (2.14)$$

The parameter $\beta_C$is the Stewart–McCumber parameter, which characterizes the damping of a Josephson junction in the RCSJ model. It represents the ratio of the junction's capacitive energy to its dissipative energy and determines whether the junction exhibits overdamped or underdamped dynamics. Large values of β_C correspond to underdamped junctions, while small values indicate overdamped behavior. $\beta_C \ll 1 \rightarrow$ non-hysteretic (non-dissipative) I–V,
$\beta_C \gg 1 \rightarrow$ hysteretic (dissipative) behavior [23].

2.10 Flux Quantization

In the mixed state of HTSCs, magnetic flux penetrates in the form of fluxons**. The** order parameter**:**

$$\psi = \mid \psi \mid e^{i\phi} \qquad (2.15)$$

must remain single-valued. For a closed loop encircling a normal domain:

$$\oint \nabla\phi \cdot dl = 2\pi N, N \in Z$$

This condition ensures the enclosed magnetic flux is quantized in units of Φ_0, leading to phenomena such as vortex formation **and** Josephson tunneling.

2.10.1 Josephson Coupling Energy The coupling energy **EJE_JEJ** measures the strength of tunneling across a junction:1. Josephson energy definition (general)The Josephson coupling energy is

$$E_J(T) = \frac{\hbar JC(T)}{2e} \qquad (2.16)$$

2. Critical current from Ambegaokar–Baratoff relation.For a tunnel Josephson junction,

$$J_C(T) = \frac{\pi\Delta(T)}{2eR_n}\tanh\left(\frac{\Delta(T)}{2k_BT}\right) \quad (2.17)$$

3. Substitute $J_C(T)$ into $E_J(T)$

$$E_J(T) = \frac{\hbar}{2e}\cdot\frac{\pi\Delta(T)}{2eR_n}\tanh\left(\frac{\Delta(T)}{2k_BT}\right)$$

Now simplify using $\hbar\pi = \frac{h}{2}$:

$$E_J(T) = \frac{h}{8e^2R_n}\,\Delta(T)\tanh\left(\frac{\Delta(T)}{2k_BT}\right) \quad (2.18)$$

At low T and weak fields, phase coherence is maximized, and the junction behaves as a bulk-like coherent superconducting region**.**

2.10.2 Flux Pinning

Flux pinning occurs when vortices are trapped at defects or imperfections**.** The pinning force per unit volume F_P is often written asis:

$$F_P = \frac{U_P}{\xi}$$

where U_P is pinning energy, ξ\xiξ = coherence length,Intrinsic pinning arises from the lattice itself in HTSCs.Extrinsic critical current J_C is determined by collective pinning and is much smaller than the depairing current**.**

Expressing U_P in terms of the magnetic induction ,B and coherence length, ξ\xi

For a simple vortex model,

$$U_P \sim \frac{\xi^3 B^2}{2\mu_0}$$

so dividing by ξgives the force per unit volume:

$$F_P = \frac{U_P}{\xi} = \frac{\xi^2 B^2}{2\mu_0} \quad (2.19)$$

2.10.3 Surface impedance

Surface impedance measurement is one of the most indispensable ways of characterizing a superconductor material.Having the information of the complex wave at frequency ω can bedetermined[16]. For a superconductor occupying the half space,$z \geq 0$, the microwave surface impedance is a ratio of electric field and magnetic field on the surface of a superconductor which is defined as

$$z_S = R_s + iX_s = \frac{E_t(z=0)}{\int_0^\infty J_S(z)dz} \quad (2.20)$$

Where the $E_t(z=0)$ is the tangential electric field at the plane boundary of $= 0$, and J_s is the surface current density flowing parallel to the plane boundary[17]. The surface impedance has a

relationship with a complex wave number(β) of a plane wave penetrating into the metal given as[18]

$$\beta = \omega\mu_0/Z_s \qquad (2.21)$$

In equation 1.17 the real part,R_s, and the imaginary part X_s, are called the surface resistance and surface reactance, respectively

$$R_s = \frac{1}{2}\omega^2{\mu_0}^2\sigma_n x_n\lambda^3$$

$$X_s = \omega\mu_0\lambda$$

Where μ_0 is the free-space permeability, ω is angular frequency of microwave radiation, x_n is the fraction of the normal fluid, σ_n is the normal state conductivity, and λ is the temperature dependent London penetration depth[17]According to the two fluids model the expression for σ_n and λ are given as [18],

$$x_n(T) = 1 - (\lambda_0^2/\lambda_0^2) \qquad (2.22)$$

$$\lambda(T) = \lambda_0/\sqrt{1-(T/T_c)^4} \qquad (2.23)$$

From equation 1.19 important information on surface resistance can be obtained which is crucial in application of superconductors in passive microwave devices.Also,fundamental parameters such as London penetration depth,can be extracted from equation 1.22.Furthermore,by knowing the surface resistance of superconductor,microwave power dissipated can be expressed as

$$P = \frac{1}{2}RB^2 \qquad (2.24)$$

This expression is invoked when dealing with low field microwave absorption measurement.Since the microwave power absorption obtained in a derivative form,the derivative of equation 2.23 is used[19].

$$\frac{dP}{dH} = \frac{d}{dH}\frac{1}{2}RB^2 \qquad (2.25)$$

2.10.4 Flux Quantization

In ceramic high-temperature superconductors (HTSCs), the magnetic field penetrates the material in the form of fluxons, creating regions of the superconductor in the mixed state. The superconducting state can be described by a macroscopic order parameter**:**

$$\psi = |\psi| e^{i\phi} \qquad (2.26)$$

Here, |ψ|\psi| represents the magnitude of the order parameter, and ϕ\phiϕ is its phase.

Flux quantization arises from the requirement that the order parameter be single-valued at every point in the superconductor. Considering a closed loop encircling a normal (non-superconducting) domain, the line integral of the phase gradient around the loop must satisfy:

$\oint \nabla\phi \cdot dl = 2\pi N$,N∈Z

This ensures that the phase change around the loop is an integer multiple of 2π, consistent with single-valuedness of the wave function**.**If we denote the integral along a path connecting points 1 and 2 as:

$$\int_1^2 dl \cdot \nabla\phi = \phi_2 - \phi_1$$

then the result is path-independent, meaning that the total magnetic flux enclosed by the loop is quantized in units of the flux quantum Φ_0.This phenomenon underpins many critical HTSC behaviors, including vortex formation**,** flux pinning**,** and the operation of Josephson devices [20].

$$\oint dl \cdot \nabla\varphi = 2\pi N \quad (2.27)$$

The gauge invariant phase of the order parameter now has the gradient

$$\nabla\varphi GI(r) = \Delta\varphi(r) - \frac{2e}{\hbar}A \quad (2.28)$$

gauge-invariant, you combine it with the electromagnetic vector potential **A**.

The gauge-invariant phase gradient is:

$$\nabla\phi_{GI} = \nabla\phi - \frac{2\pi}{\Phi_0}A \quad (2.29)$$

where

ϕ = superconducting phase,A = vector potential of the magnetic field,Φ_0 = flux quantum (h/2e).

A vector potential coupling the magnetic field to the superconducting order parameter and 2e is the charge of a Cooper pair.Using the modification $\frac{2e}{\hbar} = 2\pi/(h/2e) = 2\pi/\Phi_0$ and subjecting the gauge invariant order parameter to the constaint as shown

$$\oint dl\, \nabla\varphi_{GI} = 2\pi N \quad (2.30)$$

Hence we obtain[20]

$$\frac{2\pi}{\Phi_0}\oint dl \times A = 2\pi N \quad (2.31)$$

Applying Stokes theorem we obtain

$$\oint \boldsymbol{A}.\boldsymbol{dl} = \iint (\nabla \times \boldsymbol{A}).d\boldsymbol{S} = \iint B.d\boldsymbol{S} \equiv \Phi = N\Phi_0 \quad (2.32)$$

Where $B = \nabla \times A$ and Φ is the magnetic flux through the surface S enclosed by the contour C[20].This flux is thus seen to be quantized in units of $\Phi_0 \approx 2.07 \times 10^{-15} Wb$

1. Order parameter

The superconducting order parameter is defined as:

$$\psi = |\psi|\, e^{(i\varphi)} \quad (2.33)$$

Here:|ψ|→ amplitude (related to density of Cooper pairs),ϕ→ phase of the wavefunction.

Because ψ\psi must be single-valued, if you move around a closed loop and return to the same point, the phase must differ by an integer multiple of 2π:

$$\oint (\nabla\varphi) \cdot dl = 2\pi N, \quad N \in Z \tag{2.34}$$

Gauge-invariant phase gradient The phase by itself is not gauge-invariant; in electromagnetism, the true physical phase difference is corrected by including the vector potential A.

So the gauge-invariant phase gradient is:

$$\nabla\varphi_{GI}(r) = \nabla\varphi(r) - (2e/\hbar)\, A \tag{2.35}$$

where:2e2e2e is the charge of a Cooper pair, $\hbar$=h/2π A is the magnetic vector potential (B=∇×A).

3. Condition on gauge-invariant phase Imposing the single-valuedness constraint on the gauge-invariant phase $\oint (\nabla\varphi_{GI}) \cdot dl = 2\pi N$ (Flux quantization step): $(2\pi/\Phi 0) \oint A \cdot dl = 2\pi N$

Substitute the definition: $\oint(\nabla\phi - \frac{2e}{\hbar}A)\cdot dl = 2\pi N$

But the first term is just $\oint\nabla\phi\cdot dl = 2\pi N$. So:

$$2\pi N - \frac{2e}{\hbar}\oint A\cdot dl = 2\pi N \tag{2.36}$$

4. Flux quantization The line integral of Aaround a closed loop is related to magnetic flux by Stokes' theorem

$$:\oint A\cdot dl = \int(\nabla\times A)\cdot dS = \int B\cdot dS = \Phi \tag{2.37}$$

So we have:

$$\frac{2e}{\hbar}\Phi = 2\pi N \tag{2.38}$$

Rearranging:

$$\Phi = N\frac{h}{2e} = N\Phi_0 \tag{2.39}$$

Where, $\Phi_0 = \frac{h}{2e}$ is the flux quantum

The magnetic flux through a superconducting loop is quantized in integer multiples of the flux quantum Φ_0=h/2e≈2.07×10^{-15} Wb.

2.10.5 Josephson junction and Josephson Effect

When a superconductor is cooled below its transition temperature,the electron condense forming a macroscopic quantum state.In this case,all electrons in the superconducting condensate are defined by a single wave function given as

$$\psi = |\psi|\, e^{i\phi}$$

$|\psi|^2$ density of Cooper pairs ϕ: macroscopic quantum phaseThe phase gradient ∇ϕ determines supercurrent flow where $|\psi|^2$represents the Cooper-pair density and ϕ\phi is the superconducting phase.

$|\psi|$ is the magnitude of superconducting order parameter which is a measure of the density of superconducting electrons,whereas φ is the phase connected to the flow of super currents[21]. As soon as two superconductors are weakly coupled together as shown in Fig.1.3,their superconducting order parameters overlap and consequently electrons flow.The junction formed is called Josephson junction and the nature of coupling determines the amount of current(2.19) flows between the two superconductors

$$I = I_C sin\varphi \qquad (2.40)$$

In this case I_C is the critical current (the maximum current that a junction can accommodate before dissipation occurs When the voltage is applied across the junction, the phase varies according to the equation .It results to an AC Josephson effect.

$$\frac{d}{dt}\varphi = \frac{2eV}{\hbar} \qquad (2.41)$$

The amplitude of the DC Josephson current in equation 1.32 depends on temperature,the critical current for tunneling junction has been derived with conventional superconductors as in [22]

$$I_C(T) = \frac{\pi\Delta(T)}{2eR_n} tanh\frac{\Delta(\mathrm{T})}{2k_BT} \qquad (2.42)$$

Here R_n is the junction resistance in the normal state and $\Delta(\mathrm{T})$ is the energy gap.The Josephson current is maximal at $T = 0$

$$I_C = \frac{\pi\Delta(0)}{2eR_n} \qquad (2.43)$$

Once $I > I_C$, a current of normal electrons will flow through the junction in addition to the supercurrent.This results to the formation of resistively shunted Josephson junction(RSJ).Capacitor connected parallel to one another and a normal resistance are considered as circuit made by the RSJ.The sum of normal current will be the total current of this circuit. V/R, current through capacitor is given by $\frac{dV}{dt}$, and supercurrent $I_S = I_C sin\varphi$[22].

$$I = I_C sin\varphi + \frac{V}{R} + C\frac{dV}{dt} \qquad (2.44)$$

With some mathematical manipulation,equation 1.36 gives

$$\frac{I}{I_C} = sin\varphi + \frac{d\varphi}{d\tau} + \beta_C\frac{d^2\varphi}{d\tau^2} \qquad (2.45)$$

Here $\beta_C = 2\pi I_C R^2 C/\Phi_0$ is Stewat-McCumbers parameter.

The current-voltage, $I - V$ characteristics can be described by Stewart-McCumbers parameter.In the limit $\beta \ll 1$, the I-V dependence is non-hysteric(non-dissipative) and is given by $V(I) = R(I_s^2 - I_c^2)^{1/2}$ while when $\beta \gg 1$ the junction becomes hysteretic(dissipative)[23]

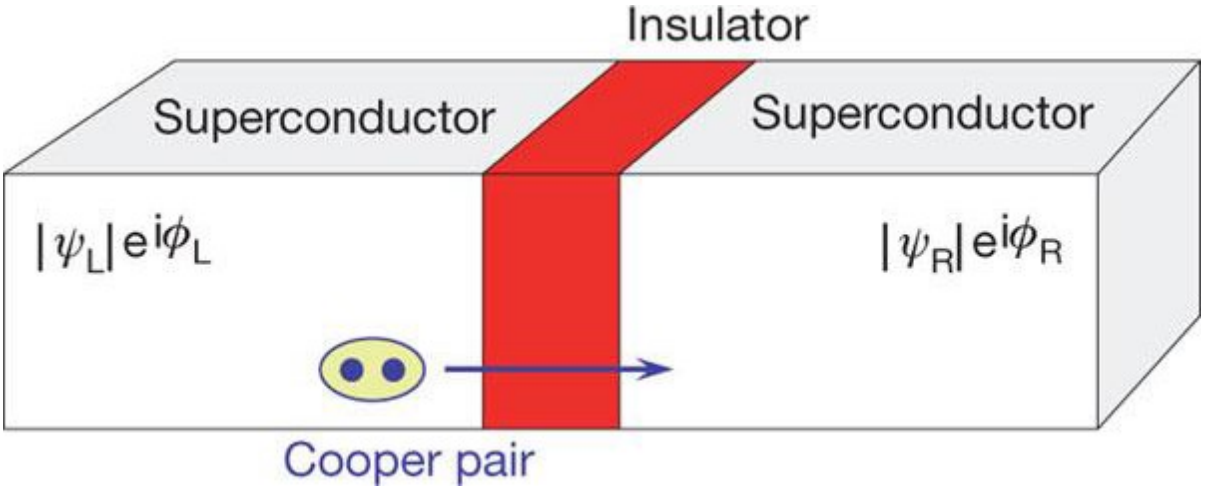


Fig. 2.10 illustrates a Josephson junction, showing two superconductors separated by a thin insulating barrier (Ramashitja, 2016, p. 45).

A Josephson junction arises whenever a weak link forms between superconducting regions, resulting in a suppressed critical current. Weak links can take various forms [22]:

Superconductor–Insulator–Superconductor (SIS) tunneling,Superconductor–Normal–Superconductor (SNS) sandwiches, Microbridges formed by constrictions,

Point-contact junctions,Small drops on superconducting wires.In ceramic superconductors, junctions may be inter-granular (between grains) or intra-granular (within a single grain). In layered superconductors, junctions can even form within a unit cell due to weak interlayer coupling [24]. The Josephson effect underpins several high-precision devices:Superconducting Quantum Interference Devices (SQUIDs), which measure extremely small magnetic fields.

Intrinsic Josephson Junctions (IJJs), which exploit the effect to convert DC current into high-frequency AC, producing sub-terahertz and terahertz signals. IJJs are promising candidates for bridging the terahertz gap [21].

2.11 Research Gaps Identified

Despite the considerable progress achieved in the study of high-temperature superconductors (HTSCs), several research gaps remain unaddressed. Previous investigations have provided valuable insights into the fundamental properties of superconductors, yet many aspects of their low-temperature electromagnetic behavior—particularly under non-resonant microwave absorption (NRMA) conditions—require further clarification.

Most earlier works have concentrated on either theoretical modeling or limited temperature- and field-dependent experiments. However, the combined influence of microstructural defects, intergranular coupling, and flux pinning dynamics on the NRMA signal response has not been fully established. Additionally, inconsistencies in sample preparation techniques, oxygen stoichiometry, and measurement protocols have often led to variations in reported critical parameters such as the transition temperature (Tc) and critical current density (Jc).

Furthermore, comparative analyses that bridge experimental observations with existing theoretical models, such as those proposed by Dulčić and Portis, remain scarce. There is a clear need for systematic studies that connect the intrinsic magnetic behavior of HTSC samples with their microwave absorption characteristics in both low- and high-field regions.

Therefore, this research aims to address these gaps by providing a comprehensive experimental and analytical study of HTSC samples, emphasizing the correlation between their microstructural features and their electromagnetic response under NRMA measurements.

References

[1] L. Bulaevskii, A. Buzdin, M. Kuli, and S. Panjukov, Adv. Phys., vol. 34, p. 175, 1985.

[2] H. K. Onnes, "The superconductivity of mercury," Leiden Comm., vol. 120b, 1911.

[3] V. V. Srinivasu, Research Space CSIR. Available online, 2009.

[4] N. Plakida, High Temperature Cuprate Superconductors: Experiment, Theory and Applications. Springer, Dubna, Moscow, Russia, 2010.

[5] E. M. Forgan, W. J. Nuttall, P. G. Kealey, S. T. Johnson, T. M. Riseman, and M. P. Nutley, "Magnetic and superconducting properties of cuprates," School of Physics and Astronomy, University of Birmingham, Birmingham, U.K., May 26, 2003.

[6] V. V. Srinivasu, Non-Resonant RF and Microwave Absorption Studies, Ph.D. dissertation, Indian Institute of Science, India, 1994.

[7] V. V. Srinivasu and M. D. Sastry, "Microwave absorption in high-temperature superconductors," Applied Superconductivity, vol. 4, no. 4, pp. 195–201, 1996.

[8] A. Dulcic, B. Rakvin, and M. Pozek, "Magnetic irreversibility in high-Tc superconductors," Europhys. Lett., vol. 10, p. 593, 1989.

[9] A. M. Portis, K. W. Blazey, K. A. Müller, and J. G. Bednorz, "Anisotropy in high-Tc superconductors," Europhys. Lett., vol. 5, p. 467, 1988.

[10] K. Fossheim, Superconductivity, pp. 123–124, 2004.

[11] B. D. Josephson, "Possible new effects in superconductive tunneling," Phys. Lett., vol. 1, p. 251, 1962.

[12] F. T. Dias, "Magnetic irreversibility and resistive transition in YBaCuO superconductors: Interpretations and possible correlations," in Superconductors – Properties, Technology, and Applications, A. M. Luiz, Ed. IntechOpen, 2009, pp. 220–240.

[13] I. Morgenstern, "Earlier and recent aspects of superconductivity," in Superconductivity, J. G. Bednorz and K. A. Müller, Eds. Springer-Verlag, 1990, p. 291.

[14] P. Müller, A. V. Ustinov, and M. Tinkham, "Dynamics of Josephson junctions," Phys. Rev. B, vol. 47, p. 470, 1993.

[15] A. Franz, A. Wallraff, and A. V. Ustinov, "High-frequency properties of superconductors," J. Appl. Phys., vol. 89, p. 471, 2001.

[16] J. C. Gallop and W. J. Radcliffe, "Microwave properties of superconductors," Supercond. Sci. Technol., vol. 4, p. 568, 1991.

[17] C. J. Wu and Y. L. Chen, "Electromagnetic properties of superconductors," Prog. Electromagn. Res., vol. 111, p. 433, 2011.

[18] A. H. Aly and W. Sabra, "Superconductivity in nanostructures," Physica C, vol. 495, p. 126, 2013.

[19] M. R. Tripathy and G. P. Srivastava, "Magnetic response in superconductors," IEEE Trans. Magn., vol. 35, p. 4079, 1999.

[20] K. Fossheim and A. Sudbø, Superconductivity: Physics and Applications. Wiley, Chichester, West Sussex, England, 2014.

[21] U. Welp, K. Kadowaki, and R. Kleiner, "Terahertz emission from intrinsic Josephson junctions in high-Tc superconductors," Nat. Photonics, vol. 7, p. 702, 2013.

[22] A. Mourachkine, Room Temperature Superconductivity. CISP, Chippenham, England, 2004.
[23] N. Plakida, High Temperature Cuprate Superconductors: Experiment, Theory and Applications. Springer, Dubna, Moscow Region, Russia, 2010.
[24] P. J. W. Moll, X. Zhu, P. Cheng, H. H. Wen, and B. Batlogg, "Transport properties of iron-based superconductors," Nat. Phys., doi: 10.1038/NPHYS3034, 2014.
[25] G. A. Alvarez, I. Iguchi, X. L. Wang, S. X. Dou, and Q. W., "Magnetic studies on superconductors," J. Appl. Phys., vol. 99, 08M514, 2006.
[26] K. N. Srivastava, Superconductivity: Theoretical and Experimental Aspects. USA, 1996.
[27] C. P. Bean, "Magnetization of high-field superconductors," Rev. Mod. Phys., vol. 36, pp. 31–39, 1964.
[28] P. G. de Gennes, Superconductivity of Metals and Alloys. Benjamin, 1966.
[29] Y. B. Kim, C. F. Hempstead, and A. R. Strnad, "Critical state model for superconductors," Phys. Rev. Lett., vol. 9, p. 306, 1962; Phys. Rev., vol. 129, p. 528, 1963.
[30] J. Wang and M. Sayer, "Transport properties of YBaCuO," Physica C, vol. 212, p. 395, 1993.
[31] J. L. Chen and T. J. Yang, "Magnetic behavior in superconductors," Physica C, vol. 224, p. 345, 1994.
[32] R. P. Huebener, Magnetic Flux Structures in Superconductivity, Springer Series in Solid-State Sciences, vol. 6. Springer, 1979.
[33] C. P. Bean, "Magnetization of high-field superconductors," Rev. Mod. Phys., vol. 36, p. 31, 1964.
[34] D. X. Chen and A. Sanchez, "Magnetic field penetration in superconductors," J. Appl. Phys., vol. 70, p. 5463, 1991.
[35] D. X. Chen, A. Sanchez, T. Puig, L. M. Martinez, and J. S. Munoz, "Magnetic behavior of granular superconductors," Physica C, vol. 168, p. 652, 1990.
[36] D. X. Chen, Y. Mei, and H. L. Luo, "Magnetic irreversibility in type-II superconductors," Physica C, vol. 167, p. 317, 1990.
[37] S. Ravi and V. Seshubai, "Phase transitions in superconductors," Phys. Rev. B, vol. 49, p. 13082, 1994.
[38] T. H. Johansen, M. R. Koblischka, H. Bratsberg, and P. O. Hetland, "Flux pinning in superconductors," Phys. Rev. B, vol. 56, p. 11273, 1997.
[39] R. Lal, "Superconductivity and magnetic behavior," Physica C, vol. 470, p. 281, 2010.
[40] R. Wesche, High-Temperature Superconductors: Materials, Properties, and Applications. Kluwer Academic, Boston, 1998.
[41] D. H. Ryan, J. M. Cadogan, C. Ritter, F. Canepa, A. Palenzona, and M. Putti, "Magnetic properties of iron-based superconductors," Phys. Rev. B, vol. 80, p. 220503(R), 2009.
[42] Q. Huang, J. Zhao, J. W. Lynn, G. F. Chen, J. L. Luo, N. L. Wang, and P. Dai, "Neutron diffraction study of superconductors," Phys. Rev. B, vol. 78, p. 054529, 2008.

[43] T. Katase, Y. Ishimaru, A. Tsukamoto, H. Hiramatsu, H. Kamiya, K. Tanabe, and H. Hosono, “Superconducting properties of thin films,” Nat. Commun., doi: 10.1038/ncomms1419, 2011.
[44] Q. Si, “Quantum criticality and superconductivity,” Nat. Phys., vol. 5, p. 629, 2009.
[45] N. D. Leyraud et al., “Magnetism and superconductivity in cuprates,” Nature, vol. 447, p. 565, 2007.
[46] J. K. Dong, L. Ding, H. Wang, X. F. Wang, T. Wu, G. Wu, X. H. Chen, and S. Y. Li, “Superconductivity in iron pnictides,” New J. Phys., vol. 10, p. 123031, 2008.
[47] M. Kanagaraj et al., “High-pressure effects in superconductors,” Appl. Phys. Lett., vol. 100, p. 052601, 2012.
[48] C. H. Lee et al., “Structural effects on superconductivity,” J. Phys. Soc. Jpn., vol. 77, p. 083704, 2008.
[49] J. Zhao et al., “Magnetic ordering in superconductors,” J. Am. Chem. Soc., vol. 130, no. 42, 2008.
[50] R. S. Kumar, D. Antonio, M. Kanagaraj, S. Arumugam, J. Prakash, S. Sinogeikin, G. S. Thakur, A. K. Ganguli, A. Cornelius, and Y. Zhao, “Pressure effects on superconductors,” Appl. Phys. Lett., vol. 98, p. 012511, 2011.
[51] P. J. W. Moll, X. Zhu, P. Cheng, H. H. Wen, and B. Batlogg, “High-field studies of iron-based superconductors,” Nat. Phys., 2014, doi: 10.1038/NPHYS3034.
[52] U. Welp, K. Kadowaki, and R. Kleiner, “Superconducting terahertz sources,” Nat. Photonics, vol. 7, p. 702, 2013.
[53] K. Lida et al., “Superconductivity in iron-based compounds,” Nat. Commun., vol. 3, p. 2139, 2013.
[54] P. J. W. Moll, R. Puzniak, F. Balakirev, K. Rogacki, J. Karpinski, N. D. Zhigadlo, and B. Batlogg, “Magnetic and transport properties of superconductors,” Nat. Mater., vol. 9, p. 628, 2010.
[55] I. Pallecchi, M. Tropeano, G. Lamura, M. Pani, M. Palombo, A. Palenzona, and M. Putti, “Transport properties in superconductors,” Physica C, vol. 482, p. 68, 2012.
[56] L. Fang et al., “Superconductivity in iron chalcogenides,” Nat. Commun., vol. 4, p. 2655, 2013.
[57] W. Si, J. Han, X. Shi, S. N. Ehrlich, J. Jaroszynski, A. Goyal, and Q. Li, “Epitaxial films of superconductors,” Nat. Commun., vol. 4, p. 1347, 2013.
[58] L. Jiao, J. L. Zhang, F. F. Balakirev, G. F. Chen, J. L. Luo, N. L. Wang, and H. Q. Yuan, “High-field transport in iron pnictides,” J. Phys. Chem. Solids, vol. 72, p. 423, 2011.
[59] J. D. Weiss, C. Tarantini, J. Jiang, F. Kametani, A. A. Polyanskii, D. C. Larbalestier, and E. E. Hellstrom, “Superconducting wires,” Nat. Mater., vol. 11, p. 682, 2012.
[60] N. Y. Panarina et al., “Magnetotransport in superconductors,” J. Phys.: Conf. Ser., vol. 200, p. 012154, 2010.
[61] C. Wang et al., “Iron-based superconductivity,” Supercond. Sci. Technol., vol. 26, p. 075017, 2013.
[62] C. L. Cruz et al., “Magnetic order in superconductors,” Nature, vol. 453, p. 899, 2008.

[63] L. J. Li et al., “Structural and electronic properties of superconductors,” J. Phys.: Condens. Matter, vol. 11, p. 025008, 2009.
[64] A. Kreyssig et al., “Structural phase transitions in superconductors,” Phys. Rev. B, vol. 78, p. 184517, 2008.
[65] H. O. Hyungju, J. Moon, D. Shin, C.-Y. Moon, and H. Choi, “Theoretical studies of superconductors,” Prog. Supercond., vol. 13, p. 65, 2011.
[66] T. Hanaguri, S. Nilitaka, K. Kuroki, and H. Takagi, “Scanning tunneling microscopy of superconductors,” Science, vol. 328, p. 474, 2010.
[67] X. H. Chen, T. Wu, G. Wu, R. H. Liu, H. Chen, and D. H. Fang, “Superconductivity in iron pnictides,” Nature, vol. 453, p. 761, 2008.
[68] R. S. Meena, A. Pal, S. Kumar, K. V. R. Rao, and V. P. S. Awana, “Magnetism in superconductors,” J. Supercond. Nov. Magn., vol. 26, p. 2383, 2013.
[69] N. Kang, P. Auban-Senzier, C. R. Pasquier, Z. A. Ren, J. Yang, G. C. Che, and Z. X. Zhao, “Superconductivity in new pnictides,” New J. Phys., vol. 11, p. 025006, 2009.
[70] V. V. Srinivasu, B. Thomas, M. S. Hegde, and S. V. Bhat, “Microwave absorption studies in superconductors,” J. Appl. Phys., vol. 75, pp. 4131, 1994.
[71] N. Y. Panarina, Y. I. Talanov, T. S. Shaposhnikova, N. R. Beysengulov, and E. Vavilova, “Superconducting state studies,” Phys. Rev. B, vol. 81, p. 224509, 2010.
[72] G. Deutscher and K. A. Müller, “Origin of superconductivity in cuprates,” Phys. Rev. Lett., vol. 59, pp. 1745, 1987.
[73] H. Lin, C. Yao, X. Zhang, H. Zhang, Q. Zhang, D. Wang, and Y. Ma, “Superconductivity under high pressure,” Physica C, vol. 490, pp. 37, 2013.

CHAPTER THREE
THEORETICAL BACKGROUND AND ELECTROMAGNETIC LOSS MECHANISMS IN HIGH-TEMPERATURE SUPERCONDUCTORS

Introduction

High-temperature superconductors (HTSCs) show unique properties that strongly affect non-resonant microwave absorption (NRMA) and radio-frequency (RF) responses. This chapter introduces key magnetic parameters and their roles in electromagnetic behavior. The discussion includes critical-state models, such as those by Dulcic and Portis, which help explain interactions between superconductors and applied electromagnetic fields.

3.1 Electron Spin Resonance (ESR) Spectroscopy

Electron spin resonance (ESR) spectroscopy examines the interaction between the magnetic moments of unpaired electrons and electromagnetic radiation. When an external magnetic field is applied, the electron's magnetic moment aligns either parallel or antiparallel to the field, creating an energy difference between the two spin states. Absorption occurs when the frequency of the applied radiation matches this energy difference. ESR thus provides insights into the dynamic, structural, and magnetic properties of superconducting materials (adapted from [71]).

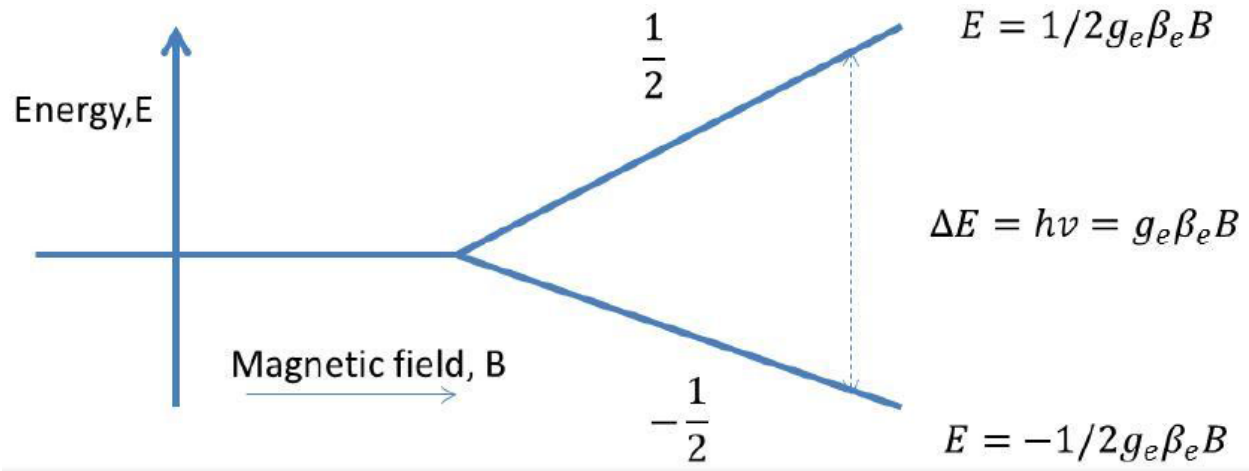


Figure 3.1. Induction of spin states as a function of magnetic field B

The principle underlies the operation of ESR spectrometers and enables the extraction of dynamic, structural, and magnetic information about materials [70,71]. A schematic of spin state splitting under an applied magnetic field is shown in Figure 3.1.

3.2 Non-Resonant Microwave Absorption (NRMA) in HTSCs

High-Temperature Superconductors (HTSCs) exhibit unique microwave absorption behaviors due to their layered crystal structures, short coherence lengths, and high operating temperatures. A notable feature is the strong non-resonant microwave absorption (NRMA) signal near zero magnetic field in the superconducting state, just below the critical temperature (Tc).

NRMA was first observed in $YBa_2Cu_3O_{7-x}$ (YBCO) by Bhat et al. (1987) using a conventional ESR spectrometer. Since then, NRMA has been reported in other cuprate-based HTSCs, borocarbides, oxyborides, alkali fullerides, low-Tc superconductors, MgB_2, and iron-based pnictides. NRMA serves as a sensitive probe of vortex dynamics and electromagnetic interactions in superconductors.

3.2.1 Historical NRMA Studies

The first NRMA studies were reported in the 1970s by Indovina et al. on granular thin films of type-I superconductors (e.g., Sn, Al). Key observations include: NRMA signals appear only in the presence of Josephson junctions (JJs).Superconductors without JJs, or with very thin junctions, show no NRMA signal.JJs act as non-superconducting regions separating microscopic superconducting grains or domains.Microwave absorption arises from resistive losses across junctions or viscous motion of fluxons at junctions.NRMA research remained limited until HTSCs, which are intrinsically granular, producing strong NRMA signals near zero magnetic field.

3.2.2 Theoretical Models. To explain NRMA in HTSCs, two main approaches were developed:

1. Portis et al. model:

Considers contributions from intergranular junctions (JJ-inter) and intragranular junctions (JJ-intra)**.**In conventional superconductors, JJ-intra effects are negligible due to large coherence length.In HTSCs, short coherence lengths make JJ-intra effects significant.NRMA arises from damped motion of fluxons at both junction types.

2. Dulčić et al. model:

Attributes NRMA primarily to resistive losses associated with Josephson currents at both junction types.Portis noted that both interpretations may be physically equivalent:

"Although we associate the microwave absorption with damped fluxon motion, it may be equivalent to associate the absorption with Josephson currents as others have done."

3.2.3 Capabilities of NRMA Studies

NRMA has proven to be an indispensable tool in superconductivity research. It can: Detect new superconducting phases in quantities as small as sub-micrograms**.**Distinguish multiple superconducting phases within a single matrix**.**Provide information on the quality of superconducting samples.Probe layered devices combining insulating, semiconducting, and superconducting materials.Map the vortex matter phase diagram through temperature-dependent NRMA amplitudes**.**Reveal unusual features of magnetic hysteresis**.**

3.2.4 Unresolved Questions

Despite decades of research, two major questions remain:Temperature dependence of NRMA amplitude: Contributions from JJ-inter and JJ-intra behave differently, yet the observed NRMA signal is a combination of both.Anomalous hysteresis: NRMA hysteresis differs fundamentally from the dc magnetization hysteresis, and lacks a comprehensive explanation.Recent studies have addressed these issues by considering:Electromagnetic interactions (EMI) to explain the temperature dependence of NRMA amplitude.Energy-stabilized Josephson fluxons (ESJ) to account for anomalous hysteresis.These open questions motivate the present thesis, which aims to investigate NRMA in YBCO by studying temperature and magnetic-field dependence and comparing NRMA hysteresis with dc magnetization hysteresis, thereby providing insights into flux dynamics, Josephson coupling, and electromagnetic interactions in high-Tc superconductors.

3.3 Non-Resonant Radio/Microwave Absorption Features

Non-resonant microwave absorption (NRMA) in high-temperature superconductors (HTSCs) exhibits several distinct and interesting features that provide insight into the material's electromagnetic behavior

3.3.1 First, Second, and Third Peaks

NRMA narrow lines in HTSCs often show multiple peaks, particularly in $Bi_2Sr_2CaCu_2O_{8+\delta}$ (Bi-2212) superconductors. These peaks correspond to different mechanisms of microwave absorption in the material.

1. First (central) peak: Appears under zero applied magnetic field.Originates from microwave losses in Josephson junctions **(JJs)** located in intergranular regions.

According to the Dulčić model, this peak arises from the suppression of the JJ critical current when weak intergranular links allow magnetic flux to penetrate.

2. Second peak: NRMA behavior has been extensively studied and attributed to multiple mechanisms:Rastogi et al**.:** intrinsic Josephson coupling between Cu–O_2 planes.Masiakowski et al**.:** presence of a secondary phase within the sample.

Recent studies by Srinivasu et al. indicate that the NRMA peak strongly depends on:The mutual orientation of the crystal ab-plane, DC magnetic field, and microwave field.The applied microwave power, suggesting that microwave-induced phase locking of Josephson junctions contributes to the second peak.

3. Third peak: Similar to the second peak, it is also influenced by microwave-power-induced phase **locking** of Josephson junctions.Its appearance reflects more complex flux dynamics and intergranular coupling in the superconducting matrix.

3.3.2 Absorption Spectral Lines

The anisotropic absorption spectral lines in YBCO superconductors can be expressed by the relation

$$B\cos\theta = \pm(p + {}^{1}/_{2})\Delta B \qquad (3.1)$$

Where p∈Z is an integer index,

θ\thetaθ is the angle between the applied magnetic field and the crystallographic axis, and

ΔB is the magnetic-field separation between adjacent absorption lines.

The cosθ term captures the anisotropic projection of the magnetic field. The half-integer shift (p+1/2) reflects boundary or pinning conditions of fluxons. The ± sign accounts for symmetric absorption with respect to field direction.The field-dependent spectral lines observed in non-resonant microwave absorption (NRMA) experiments have been associated with the motion of

fluxons along regular arrays of twin planes in YBCO crystals [61–64].Owens [54,56] further demonstrated that these spectral features originate from discrete phase jumps in superconducting loops. As magnetic flux in a loop is quantized, increasing the applied field causes phase jumps whenever the enclosed flux reaches an integer multiple of the flux quantum. These flux jumps occur on extremely short timescales and generate voltage pulses:

$$V(t) = -\frac{h}{2e}\frac{d\theta}{dt}. \qquad (3.2)$$

When such events occur, the critical current is momentarily exceeded, allowing normal current to flow, which contributes to microwave absorption.

3.3.3 Magnetic Shielding Effect

Magnetic shielding reflects the intrinsic ability of superconductors to expel flux, a key factor in low-field microwave devices.Srinivasu et al. investigated this effect in both pure and Ag-doped YBCO thin films under low- and high-field conditions.Ag-doped YBCO showed superior shielding performance, attributed to improved grain alignment and larger grain sizes, which reduced weak-link effects and enhanced superconducting coupling.

3.3.4 Phase Reversal

Phase reversal in NRMA refers to the transition of the zero-field signal from a maximum to a minimum depending on experimental conditions.In YBCO powder superconductors, the behavior is strongly RF power-dependent:Low RF power**:** absorption minimum at zero DC field (B_{DC}), increasing with applied field.Higher RF power**:** the zero-field maximum flips to a minimum, indicating nonlinear dynamics.Very high microwave field amplitudes (B_w)**:** linked to nonlinear response of weakly connected superconducting loops within the granular matrix.Temperature also influences phase reversal, with anomalous absorption observed in specific ranges.Effective-medium theory models the granular superconductor as a percolating network of superconducting regions separated by metallic domains, successfully explaining RF- and temperature-dependent phase reversal.

3.3.5 Magnetic Hysteresis

High-temperature superconductors (HTSCs) often exhibit anomalous hysteresis, where the forward absorption curve lies above the return curve during magnetic field sweeps.Kim et al. studied this in $Bi_2Sr_2CaCu_2O_{8+\delta}$ (BSCCO) and attributed it to microwave absorption at weak

links forming Josephson junctions.Their explanation combined aspects of the Portis fluxon model and the Dulčić Josephson current model.Magnetization studies show that this anomaly is influenced by the layered crystal structure and high anisotropy of HTSCs.Microscopic model (two-level critical state):

Differentiates intragranular currents (Jcg) and intergranular currents (Jcj): Inside grains: large critical current density (Jcg) → well-defined local critical state.At grain boundaries: weaker Josephson coupling → smaller current density (Jcj).Macroscopic flux density is averaged over many grains:Grain boundaries modify the intragranular critical state, acting as an effective external field.

Two types of fluxons:

Grain-pinned fluxons: remain inside grain interiors.Grain-boundary free fluxons: move through weak superconducting regions at boundaries.The latter fluxons are mainly responsible for electromagnetic losses, explaining the anomalous hysteresis observed in NRMA of granular HTSC systems.

3.3.6 Surface Barrier Effect

The surface barrier effect in HTSCs arises from the interaction between a vortex and its mirror image in the presence of surface shielding currents.This effect is characterized by zero magnetization upon field reversal, while the observed penetration field exceeds the lower critical field (Hc1).Rastogi et al. [69] first reported this phenomenon.In YBCO thin films, NRMA measurements revealed a vertical hysteresis component with a unique temperature dependence.

Specifically, the hysteresis magnitude increased near Tc, even as the overall signal intensity decreased.This behavior reflects the difference in magnetization between forward and reverse field sweeps, consistent with the defining characteristics of the surface barrier effect.

3.3.7 Oxygen Deficiency

Oxygen deficiency significantly influences microwave absorption in YBCO superconductors.

Puri et al. [70] studied YBCO using modulated microwave absorption (MWA) and observed periodic oscillations at two distinct frequencies, labeled signal type A and signal type B.These oscillations were attributed to microwave-sensitive Josephson junctions (JJs).The two signal

types exhibited distinct dependencies on microwave power, temperature, and field modulation, suggesting multiple junction mechanisms.

The study concluded that oxygen-deficient regions in YBCO act as Josephson-like junctions, explaining the enhanced low-field microwave absorption observed in such systems.

3.3.8 Paramagnetic Meissner Effect (PME)

The Paramagnetic Meissner Effect (PME), or Wohlleben effect, is a counterintuitive paramagnetic response observed in HTSCs under weak external magnetic fields.Instead of a diamagnetic minimum at zero field, PME shows a local maximum in microwave absorption at B = 0.Bhat et al. [65] attributed PME to π-junctions that generate spontaneous supercurrents.Srinivasu et al. [66] suggested an extrinsic origin, arising from mesoscopic defects that favor spontaneous currents.For PME to occur, the current density of these spontaneous currents must reach 10^5–10^6 A/cm², likely originating within grains rather than intergranular regions.PME is anisotropic: aligned powder samples exhibit the strongest effect when the magnetic field is parallel to the c-axis, emphasizing the role of structural alignment and junction orientation.

3.3.9 AC Loss in the Superconducting State

AC loss in the superconducting state can display unexpected anomalies.Chockalingam et al. [74] reported that RF losses in BSCCO exceeded those in the normal state, with two distinct absorption features: Peak A and Peak B.Observed behavior:Peak A: amplitude decreased with increasing applied magnetic field, but increased when the sample was tilted from 0° to 90°.

Peak B: attributed to Lorentz-force-driven vortex motion, while Peak A was linked to the critical current density associated with Josephson junction coupling energy.These anomalies are explained by repeated coupling and decoupling of Josephson junctions, consistent with theoretical models describing transitions between coupled and decoupled junction states.

3.4 RF and Microwave Loss Mechanisms.

In an ideal superconductor carrying a direct current (DC), there is virtually no energy dissipation, as the material exhibits zero electrical resistance. However, when an alternating current (AC) is

applied, a finite resistance appears, leading to power loss. The relationship between the root mean square (RMS) voltage and resistance can be expressed as:

$$(R = \frac{V_{rms}^2}{R}) \qquad (3.3)$$

Numerous theoretical and experimental studies have been conducted to explain the origins of this AC loss. Several mechanisms have been proposed, including flux-damped motion **[69],** losses caused by oscillating or "shaking" vortices **[**70**],** energy dissipation in intergranular Josephson junctions [71], vortex normal-state contributions [2, 71], and flux-flow-related losses [71].

Since no single theoretical model can fully account for all experimental observations, particularly in the case of low microwave absorption, the model most consistent with our experimental data was selected for this study.

3.4.1 Portis Model.

In high-temperature superconductors (HTSCs), the grains are often misoriented, and the material typically contains secondary phases, voids, and microcracks. These structural imperfections suppress the superconducting order parameter, resulting in weak intergranular couplings that act as Josephson junctions. When an external magnetic field exceeding the junction's lower critical field is applied, quantized magnetic flux lines—known as vortices or fluxons—penetrate the superconductor. Within these weak-link junctions, fluxons move at velocities several orders of magnitude lower than in the bulk material due to the reduced effective viscosity in the junction region [39]. The spatial variation of the applied microwave field generates a microwave current within the junction, which drives the fluxons into oscillatory motion. The dynamics of this motion can be described by the fluxon equation of motion [4]:

$$\mu \frac{d^2x}{dt^2} + \eta \frac{dx}{dt} + kx = \frac{1}{c} j_i \Phi_0 \qquad (3.4)$$

Here, μ\muμ represents the fluxon mass per unit length, k is the restoring force constant, and $\eta = \frac{{\Phi_0}^2}{\rho^2 s}$ defines the viscosity coefficient, where ρ is related to the normal resistive region through which the moving fluxon generates a dissipative current [13]. The resulting resistance (R) and reactance (X) of the junction are expressed as:

$$R = X_0 \left[\frac{-1+\left(1+\frac{4f^2B^2}{{B_0}^2}\right)^2}{2} \right]^{\frac{1}{2}} \quad (3.5)$$

$$X = X_0 \left[\frac{1+\left(1+\frac{4f^2B^2}{{B_0}^2}\right)^2}{2} \right]^{\frac{1}{2}} \quad (3.6)$$

The parameter $B_0 = \frac{8\pi\omega\mu\lambda^2\eta}{\Phi_0}$ serves as a threshold field that indicates the point beyond which flux flow dissipation becomes the dominant source of energy loss. Likewise, $X_0 = 4\pi\omega\lambda\mu^{2/3}$ represents the impedance when no magnetic field is present. In these expressions:λ is the London penetration depth,ω is the microwave frequency,η is the effective viscosity experienced by moving fluxons,μ is the magnetic permeability, andΦ_0\ is the magnetic flux quantum.

3.5 Dulcic Model:

Dulčić and colleagues [56] demonstrated that the dominant source of electromagnetic power dissipation in superconductors arises within the intergranular Josephson junctions. Under low magnetic field conditions, the weak interconnections between superconducting grains facilitate the formation of continuous Meissner shielding currents throughout the sample [72]. However, as the external magnetic field increases, the critical current of these junctions is reduced by a factor given by:

$$F(H) = \frac{\sin(\pi H/H_0)}{\pi H/H_0} \quad (3.7)$$

This reduction allows more magnetic flux lines to penetrate the material, leading to increased energy losses. The parameter H_0 represents the magnetic field strength at which the junction accommodates a single magnetic flux quantum, Φ_0, and can be expressed as [56]:

$$H_0 = \frac{\Phi_0}{L(2\lambda+t)} \quad (3.8)$$

Here, $\Phi_0 = \frac{hc}{2e}$ is the magnetic flux quantum, L is the junction length, λ denotes the London penetration depth, and t is the thickness of the junction.

By modeling the Josephson junction as a resistively shunted junction, they concluded that the total transport current is composed of a bias current, I_0, generated by the varying magnetic field,

superimposed with a microwave-induced alternating current, $I_{mw}\cos(w_{mw}t)$. The system can therefore be described by the following differential equation:

$$\frac{c\hbar}{2e}\frac{d^2\phi}{dt^2}+\frac{\hbar}{2eR}\frac{d\phi}{dt}+I_c sin\,\phi=I_0+I_{mw}cos(\omega_{mw}t) \qquad (3.9)$$

In the absence of microwave excitation, the phase variable ϕ(t) stabilizes at an equilibrium value, ϕ_0. When the microwave term is small, the phase can be written as $\phi(t)=\phi_0+\phi_{mw}(t)$. If the capacitive term is neglected, the expression for the power absorbed by the junction becomes simplified.

$$P=\frac{1}{2}I_{mw}^2\frac{R}{1+\eta} \qquad (3.10)$$

Where η is a junction parameter defined by equation

$$\eta=\frac{I_c^2(cos\phi)^2}{(\hbar w_{mw}/4\pi e)^2} \qquad (3.11)$$

For low field microwave absorption signal shape is given by an expression

$$S_n=\frac{(I_{mw}^2R)^2/_2}{(\hbar w_{mw}/_{2eR})^2}\frac{I_c}{(1+\eta)^{3/2}}\times(-\frac{dI_c}{dH}+I_m sin\phi cosw_m t) \qquad (3.12)$$

In this context, $\Phi_0 =$ hc/2e represents the flux quantum. The junction is characterized by its length **(L),** thickness **(t),** and the London penetration depth (λ). The Josephson junction is modeled as a resistively shunted junction**,** where the transport current consists of two components: a boundary current I_0 induced by the magnetic field sweep, and a microwave-driven current I_{mw} cos ω_{mw} t .

However, as the external magnetic field increases, the critical current of these junctions decreases according to a field-dependent factor involving the following parameters:

R: junction resistance;**ω_mw:** microwave frequency;**ω_m:** modulation frequency of the applied field;

η: junction coupling parameter; and **Φ_0:** equilibrium phase difference of the superconducting electron wave functions across the junction.The first term in the corresponding expression represents the reversible component of the response, which is independent of the direction in which the magnetic field is swept. The second term accounts for the irreversible, hysteretic

contribution, responsible for the observed hysteresis behavior. The sign of this term reverses when the direction of the applied field is reversed, analogous to the transition from Φ_0 to $-\Phi_0$.

3.6 Critical Current Density

Over the past several years, extensive research has focused on enhancing the critical current density (Jc) of YBCO films through the incorporation of arrays of oxide nanoparticles such as Y_2O_3 and $BaZrO_3$ [73]. These artificial pinning centers can be precisely engineered in terms of their shape, size, and spatial distribution, leading to the formation of structures such as oblate or prolate nano-precipitates, self-assembled nanoparticle chains, and nanorods. Typically, these nanostructures exhibit spacings of approximately 4–10 nm and diameters of 2–4 nm [74, 75]. The resulting tailored pinning landscapes markedly improve Jc, particularly under low magnetic field conditions. For example, thin YBCO films at 77 K and zero field have demonstrated Jc values in the range of $(3-5) \times 10^{10} A/m^2$, corresponding to about 10–20% of the depairing current density—that is, the theoretical upper limit beyond which Cooper pairs dissociate.

These engineered pinning centers also improve Jc at intermediate magnetic fields, which is especially relevant for high-field magnet applications. For example, YBCO films with Y_2O_3 nano-precipitates demonstrated $J_c = 2.7 \times 10^{10}\ A/m^2$ at 77 K and zero field, and $J_c = 1.0 \times 10^9\ A/m^2$ at 77 K under 5T [4]. Early studies similarly reported Jc as high as $4.0 \times 10^{10}\ A/m^2$ at 4.2 K [77]. Comparable enhancements have also been observed in iron-based superconductors, such as $BaFe_2As_2$, through the incorporation of oxide nanopillars [81], demonstrating that strong vortex pinning is achievable beyond cuprate systems.

However, high critical fields (H_{c2}) and strong pinning alone do not automatically render cuprates or Fe-based superconductors ideal for high-field magnet technologies. Intrinsic material properties—such as pronounced thermal fluctuations in vortex motion and grain boundaries—can obstruct current flow. These thermal fluctuations reduce pinning efficiency, induce vortex-lattice melting, and generate dissipation well below H_{c2}. Consequently, the range of temperature and magnetic field (T–H) over which a superconductor can sustain lossless current transport is limited to the region below the irreversibility field, $H^*(T)$, where Jc(H) approaches zero (Figure 14). For fields higher than H^* but lower than H_{c2}, the material behaves like a poor metal, and the high H_{c2} offers limited practical benefit. This dissipative region is particularly large in highly

anisotropic materials with low carrier densities, such as the cuprate superconductors, where H^* (T) is significantly lower than H_{c2}. (Figure 14).

It might be expected that the introduction of engineered pinning nanostructures—which dramatically enhance Jc—would also increase H* by suppressing the thermal motion of vortices in these layered systems. However, experimental observations reveal otherwise. Even in YBCO films exhibiting exceptionally high Jc, the irreversibility field H^* remains largely unchanged [74, 75]. This finding suggests that H^* is governed primarily by the intrinsic electronic and structural properties of the material rather than by the artificial pinning landscape. The relatively low H^* values in cuprates therefore represent a major limitation for high-field applications near 77 K.

3.6.1 The Critical State

In the critical state, vortex pinning is sufficiently strong to suppress large-scale vortex motion. Formally, the Lorentz force acting on vortices cannot exceed the local pinning strength $\alpha_p(B)$ at any point within the superconductor. The temperature-dependent pinning force can be expressed as:

$$F(T) = \frac{\langle \Delta(T) \rangle}{\Delta(0)} tanh\ (\frac{\Delta(T)}{2k_B T}) \qquad (3.13)$$

where ⟨Δ(T)⟩ is the thermally averaged superconducting energy gap, Δ(0) is its zero-temperature value, and k_B is the Boltzmann constant.This relationship quantifies the maximum sustainable force on vortices before depinning occurs, forming the foundation for understanding flux dynamics and energy dissipation in type-II superconductors.

$$F(T) = \langle \frac{\Delta(\mathrm{T})}{\Delta(0)} tanh \frac{\Delta(\mathrm{T})}{2K_B T} \rangle \qquad (3.14)$$

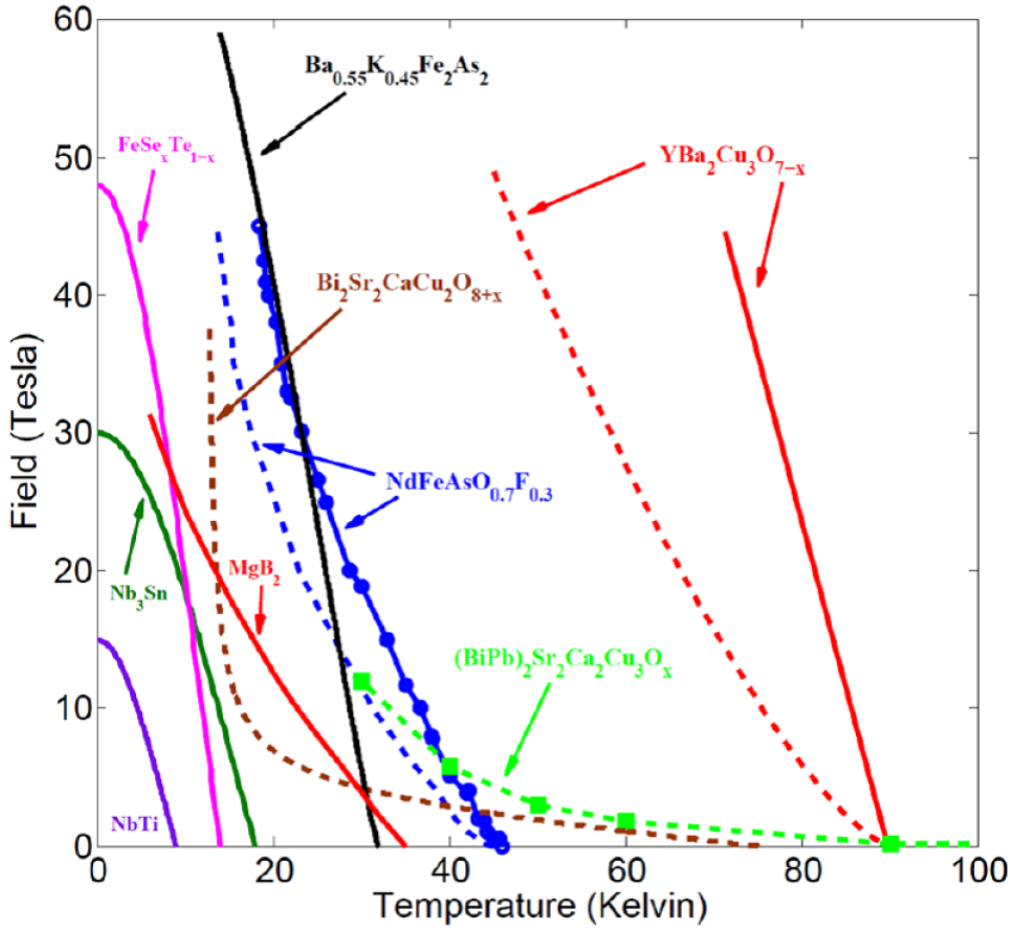


Figure 3.2:T-H phase diagam for different superconducting materials[79].

$$\frac{1}{c}|J \times B| < \alpha_p(B) \qquad (3.15)$$

3.6.2 Flux Creep and Flux Flow

When a type-II superconductor is placed in a magnetic field greater than its lower critical field H_{c1}, quantized magnetic vortices penetrate the material and become pinned at defects or grain boundaries. Ideally, these vortices remain immobile under a small applied current. However, at finite temperatures, thermal activation allows vortices to overcome pinning barriers, leading to flux creep — a slow, thermally activated motion of vortices that causes a gradual decay of persistent currents.The flux creep rate follows an Arrhenius-type relation:

$$E = E_0 exp(-U(J)/k_B T) \qquad (3.16)$$

where E is the induced electric field, U(J) the current-dependent activation energy, k_B the Boltzmann constant, and T the temperature. As J approaches the critical current density Jc, the barrier U(J) decreases, leading to enhanced vortex motion and increased dissipation.

At higher magnetic fields or larger driving currents, the Lorentz force exceeds the average pinning force, and vortices move freely through the lattice — a regime known as flux flow. In this case, energy dissipation becomes proportional to vortex velocity, and the effective resistivity approaches the flux-flow resistivity ρ_f

$$\rho_f = \rho_n \frac{B}{B_{c2}} \qquad (3.17)$$

where ρ_n is the normal-state resistivity and B_{c2} is the upper critical field.

Flux creep and flux flow both contribute significantly to microwave and RF losses in granular high-Tc superconductors, influencing their NRMA response and limiting high-frequency performance.

When the Lorentz force acting on vortices exceeds the local pinning strength, the flux lines begin to move, resulting in energy dissipation. This motion can occur in two regimes—flux creep and flux flow—depending on the applied current density and temperature. In the flux creep regime, thermally activated hopping of vortices occurs over pinning barriers, producing a slow, logarithmic decay of magnetization with time. In contrast, the flux flow regime is characterized by a viscous motion of vortices once the driving force exceeds the pinning potential, leading to a finite resistivity even below the critical temperature. In high-temperature superconductors such as YBCO, the short coherence length and weak pinning make thermal activation significant, thereby enhancing flux creep and limiting the critical current density at elevated temperatures. Understanding this transition from flux pinning to flux flow is essential for interpreting NRMA data, as it directly influences microwave power absorption and the effective dissipation mechanisms in the mixed state.

3.6.3 Bean Critical State Model

The Bean Critical State Model, proposed by C. P. Bean (1962), provides a macroscopic description of magnetization and flux penetration in type-II superconductors. It assumes that magnetic flux enters the sample in the form of vortices that remain pinned until the local Lorentz force equals the maximum pinning force. The resulting nonuniform current distribution gives

rise to hysteretic magnetization loops observed experimentally.In the Bean model, the critical current density Jc is defined as the maximum sustainable current before flux motion begins. For a slab geometry of thickness 2a, the relationship between the magnetic moment M and applied magnetic field H is expressed as:

$$J_c = \frac{20\,\Delta M}{a(1-a/3b)} \qquad (3.18)$$

where ΔM\ is the width of the magnetization hysteresis loop, and a and b are the sample dimensions (a<b)..This model explains the irreversible magnetization behavior and the characteristic hysteresis observed in magnetization (M–H) and NRMA measurements.

The Bean model forms the theoretical basis for estimating Jc from experimental magnetic data and serves as a cornerstone for understanding flux pinning, vortex dynamics, and electromagnetic losses in high-Tc superconductors.The Bean critical state model provides a macroscopic description of how magnetic flux penetrates and is distributed in a type-II superconductor. According to this model, the magnetic field gradient within the sample is sustained by a critical current density (Jc), which represents the maximum current that can flow without vortex motion. When an external magnetic field is increased or decreased, the flux profile adjusts according to the critical state, resulting in magnetization hysteresis. This behavior explains many NRMA features, such as the field-sweep direction dependence and the nonlinear absorption observed near zero magnetic field. The Bean model therefore links microscopic vortex pinning to the observable electromagnetic response, enabling the estimation of Jc from experimental magnetization or microwave absorption curves.

3.6.4 Electromagnetic Loss Mechanisms

Electromagnetic losses in high-temperature superconductors arise primarily from vortex motion, intergranular weak-link coupling, and quasiparticle excitations. At low fields and temperatures, losses are dominated by Josephson junction dissipation across grain boundaries, where microwaves drive oscillatory currents. As the field increases, vortex motion within the grains becomes the main loss channel, producing both reversible (flux-flow) and irreversible (hysteretic) components. In the normal state or near Tc, additional losses originate from normal electron scattering and eddy-current effects. The overall NRMA signal is thus a combined result

of these mechanisms, with its amplitude and phase determined by the relative contributions of Josephson coupling, flux dynamics, and thermal fluctuations.

3.7 The Two-component Critical State Model

The two fluid model got proposed by Gorter and Casimir. They wanted a way to explain some superconductor properties. Basically, in this model, there are two kinds of electrons inside. Normal electrons, which make up the normal fluid. And superconducting electrons, the super fluid. Reference 85 covers it. In a field like that, normal electrons act just like in the normal state. They scatter and lose energy. Their movement follows the standard transport equation.

$$m\frac{dj_n}{dt} + m\frac{j_n}{\tau} = N_n e^2 E \qquad (3.19)$$

where $j_n = N_n e v_n$, with j_n being the normal cuent density, N_n the density, v_n the drift velocity of the normal electrons,and τ the relaxation time[86]. The superconducting electrons do not dissipate energy as they move; however, they do show inertial effects due to their mass.

3.8 Critical State and Non-Resonant Microwave Absorption

As discussed in previous studies [87, 88], once current begins to flow in a sufficiently large region of a superconductor, it will eventually reach a maximum threshold, known as the critical current Jc (Section 2.13). In general, there are three possible current-flow conditions in a superconducting sample:Zero current regions: Areas not penetrated by the applied magnetic field.Full current regions: Current reaches Jc, which may be positive or negative, depending on the electromotive force generated by the last change in the thermodynamic field.Critical state: When the critical current flows uniformly throughout the sample, the system is said to be in a critical state, defined mathematically by the equality in Equation (3.19).In principle, the spatial profiles of the magnetic induction BBB and current density JJJ can be determined from this equality along with the appropriate boundary and material conditions. The general relation for the current density is given by:

$$J = c(\delta \times Y)/4\pi \qquad (3.20)$$

Together with the explicit relation Y(B), which is usually taken as $y = B$ in high superconductors in the field range $H > H_{c1}$[89].

3.9 Distinction Between Weak-Link and Bulk Response

3.9.1 Two-Fluid Model

The two-fluid model, proposed by Gorter and Casimir [85], conceptualizes electrons in a superconductor as belonging to two components**:**Normal electrons (j_n): Form the normal fluid and follow standard transport laws, experiencing scattering and energy dissipation. Their dynamics are governed by:

$$J_c = J_c(0)\frac{\sin(\pi H/H_0)}{\pi H/H_0} \qquad (3.21)$$

where J_c (0) represents the maximum critical current and H_0 is a characteristic field parameter. This relationship explains the field-dependent microwave absorption observed in weak-link systems, as reported in earlier studies [6].where $\mathbf{j}_n = N_n e\mathbf{v}_n$ with N_n the electron density, $\mathbf{v}_n$ the drift velocity, and τ the relaxation time [86].Superconducting electrons (j_s): Form the superfluid and move without energy dissipation but exhibit inertial effects due to their mass.This model provides a framework to understand the coexistence of dissipative and dissipation-free currents in superconductors.

3.10 Weak-Link vs. Bulk Response

A defining characteristic **of** high-Tc superconductors is the presence of weak links, typically associated with grain boundaries in sintered or pelletized samples. Due to the short coherence length in these materials, even minor imperfections—such as point defects, oxygen vacancies, or thin insulating layers—act as weak links.The lower critical field H_{c1} for weak links is significantly smaller than for the bulk, often as low as 0.1 Oe. This allows magnetic flux to penetrate the junctions more easily than the bulk.The critical current Jc across these junctions depends on the applied magnetic field and follows a diffraction-like relation:

$$H_{ext}(t) = H(t) + H_{mod}\sin(w_{mod}t) + H_{mw}\cos(w_{mw}t) \qquad (3.22)$$

Here, H(t) is the slowly varying (dc or quasi-static) magnetic field, H_{mod} and ω_{mod} are the amplitude and angular frequency of the low-frequency modulation field, and H_{mw} and ω_{mw} denote the amplitude and angular frequency of the applied microwave field [6].When the junction size d exceeds the London penetration depth λ\lambdaλ, fluxons (quantized magnetic vortices) can nucleate within the weak links. The viscous motion of these fluxons leads to energy

dissipation, contributing to the low-field microwave absorption observed in pelletized superconductors [4, 6, 80].

3.11 Modulated and Non-Modulated Low-Field Microwave Absorption

In granular superconductors, microwave absorption in the superconducting state primarily arises from Josephson coupling between grains. This response has been studied using various spectrometer setups:Q-band ESR spectrometers at ~20 GHz [81], 23 GHz [16], 35 GHz [82]

Tunable frequency systems ranging 1–38 GHz [79]Low-field non-modulated systems in the MHz range [83] Most studies, however, employ X-band ESR spectrometers operating between 9–10 GHz with magnetic field modulation, revealing absorption at both low and high magnetic fields.The external magnetic field applied to the sample, $H_{ext}(t)$, can be expressed as:

$$H_{ext}(t) = H(t) + H_{mod} sin\ (\omega_{mod} t) + H_{mw} cos\ (\omega_{mw} t)$$

H(t) is the slowly varying bias field, H_{mod} is the low-frequency modulation field, and H_{mw} is the microwave magnetic field.H(t) is the scanning DC field H_{mod} is the modulation amplitude (typically 10–100 kHz) H_{mw} is the microwave magnetic component (~10 GHz) [88]

The observed absorption strongly depends on both field amplitude and modulation scheme, providing insights into flux pinning, weak-link behavior, and vortex dynamics.

References

[1] Kadam, R.M., Wani, B.N., Sastry, M.D. & Rao, U.R.K., 1995. Magnetic properties of high-Tc superconductors. Physica C, 246, pp.246–262.

[2] Blazey, K.W., Muller, K.A., Bednorz, J.G., Berlinger, W., Amoretti, G., Buluggiu, E.A. & Matacotta, F.C., 1987. Magnetic behavior in cuprate superconductors. Physical Review B, 36(12), pp.7241–7245.

[3] Bhat, S.V., Ganguly, P. & Rao, C.N.R., 1987. ESR studies on superconducting oxides. Pramana – Journal of Physics, 28, pp.L425–L428.

[4] Portis, A.M., Blazey, K.W., Muller, K.A. & Bednorz, J.G., 1988. Magnetic resonance in superconducting ceramics. Europhysics Letters, 5, pp.467–470.

[5] Dulcic, A., Leontic, B., Peric, M. & Rakvin, B., 1987. Magnetic susceptibility in YBaCuO compounds. Europhysics Letters, 4, pp.1403–1406.

[6] Dulcic, A., Crepeau, R.H., Freed, J.H., Schneemeyean, L.H. & Waszezak, J.V., 1990. Spin dynamics in high-Tc superconductors. Physical Review B, 42(4), pp.2155–2160.

[7] Dulcic, A., Crepeau, R.H. & Freed, J.H., 1989. ESR analysis of superconducting phases. Physical Review B, 39(6), pp.4249–4252.

[8] Pakulis, E.J. & Chandershekar, G.V., 1989. Magnetic field effects in superconducting ceramics. Physical Review B, 39(2), pp.808–812.

[9] Sugawara, K., Arai, N., Kouzuki, A., Ichimura, S., Naoi, H., Hotta, K. & Hirose, H., 2000. Magneto-optical studies of YBaCuO. International Journal of Modern Physics B, 14(16), pp.1633–1640.

[10] Padam, G.K., Ekbote, S.N., Tripathi, M.R., Srivastava, G.P. & Das, B.K

[11] Kadam, R.M., Sastry, M.D., Hassain, Z., Mazumdar, C., Nagarajan, R., Gupta, L.C., Godart, C. & Vijayaraghvan, R., 1994. Magnetic properties of rare-earth substituted superconductors. Physica C, 232, pp.359–366.

[12] Kadam, R.M., Wani, B.N., Sastry, M.D. & Rao, U.R.K., 1995. Magnetic properties of high-Tc superconductors. Physica C, 246, pp.246–262.

[13] Suss, J.T., Berlinger, W., Portis, A.M., Muller, K.A., Jeanneret, B. & Martinoli, P., 1989. Magnetic resonance in high-Tc ceramics. Solid State Communications, 71(11), pp.929–934.

[14] Kataev, V., Knauf, N., Buchner, B. & Wohlleben, D., 1991. Magnetic ordering in YBaCuO compounds. Physica C, 184, pp.165–170.

[15] Baranowsky, J.M., Liliental, W.Z., Yan, W.F. & Weber, E.R., 1991. Magneto-optical effects in superconductors. Physical Review Letters, 66(23), pp.3079–3082.

[16] Moorjani, K., Bohandy, J., Kim, B.F. & Adrian, F.J., 1990. Spin dynamics in superconducting oxides. Solid State Communications, 74(5), pp.497–502.

[17] Bele, P., Brunner, H., Schweitzer, D. & Keller, H.J., 1994. Magnetic susceptibility in layered superconductors. Solid State Communications, 92(3), pp.189–193.

[18] Joshi, J.P., Sarangi, S., Sood, A.K., Pal, D., Bhat, S.V. & Parman, J., 2002. Resistive transition in YBaCuO systems. Physica C, 58, pp.361–368.

[19] Panarina, N.Y., Talanov, Y.I., Shaposhnikova, T.S., Beysengulov, N.R., Vavilona, G., Behr, E., Kondrat, A., Hess, C., Leps, N., Wurmehl, S., Klinger, R., Kataev, V. & Buchner, B., 2010. Magnetic phase transitions in cuprate superconductors. Physical Review B, 81, pp.224509.
[20] Pascher, N., Deisenhofer, J., Krug von Nidda, H.A., Hemmida, M., Jeevan, H., Gegenwart, S.P. & Loid, A., 2010. Spin-lattice interactions in high-Tc materials. Physical Review B, 82, pp.054525.
[21] Kittel, C., 2005. Solid State Physics. J. Wiley, USA.
[22] Ashcroft, M., 1976. Solid State Physics. Cornell University, USA.
[23] Cyrot, M., 1973. Theory of superconductivity. Reports on Progress in Physics, 36, pp.103–158.
[24] Ahmad, D., Song, T.K., Park, I.S., Kim, G.C., Ren, Z.A. & Kim, Y.C., 2011. Magnetic and transport properties of YBaCuO systems. Modern Physics Letters B, 25(21), pp.1939–1945.
[25] Sharma, S.V., Nath, T.K. & Majumdar, A.K., 1997. Electrical resistivity in high-Tc superconductors. Physica C, 290, pp.229–238.
[26] Fossheim, K. & Sudbo, A., 2004. Superconductivity: Physics and Applications. Wiley, Chichester, West Sussex, England.
[27] Welp, U., Kadowaki, K. & Kleiner, R., 2013. Terahertz emission from intrinsic Josephson junctions. Nature Photonics, 7, pp.702–708.
[28] Mourachkine, A., 2004. Room Temperature Superconductivity. CISP, Chippenham, England.
[29] Plakida, N., 2010. High-Temperature Cuprate Superconductors: Experiment, Theory, and Applications. Springer, Dubna, Moscow Region, Russia.
[30] Moll, P.J.W., Zhu, X., Cheng, P., Wen, H.H. & Batlogg, B., 2014. Quant
[31] Alvarez, G.A., Iguchi, I., Wang, X.L., Dou, S.X. & Yao, Q.W., 2006. Magnetization studies of YBaCuO thin films. Journal of Applied Physics, 99, 08M514.
[32] Srivastava, K.N., 1996. Superconductivity: Theoretical and Experimental Aspects. USA.
[33] Tsuei, C.C. & Kirtley, J.R., 2000. Pairing symmetry in cuprate superconductors. Reviews of Modern Physics, 72, pp.969–1016.
[34] Jin, B.B., Dahm, T., Gubin, A.I., Choi, E.M., Kim, H.J., Lee, S.I., Kang, W.N. & Klein, N., 2003. Microwave response of superconducting films. Physical Review Letters, 91, 127006.
[35] Cunnane, D., Zhuang, C., Chen, K., Xi, X.X., Yong, J. & Lemberger, T.R., 2013. Penetration depth measurements in thin-film superconductors. Applied Physics Letters, 102, 072603.
[36] Hossain, M.M., 2012. Absolute Value of the Magnetic Penetration Depth and Field Profile in the Meissner State of Exotic Superconductor $YBaCu_3O_{6+x}$ and $Ba(Co_{0.072}Fe_{0.926})_2As_2$. PhD Thesis, University of British Columbia. (Accessed 12 March 2017)
[37] Kim, J., Haberkom, N., Lin, S.Z., Civale, L., Nazaretski, E., Moeckly, B.H., Yung, C.S., Thompson, J.D. & Movshovich, W., 2012. Vortex imaging in superconductors. Physical Review B, 86, 024501.
[38] Ji, L., Rzchowski, M.S. & Tinkham, M., 1990. Magnetic flux behavior in superconducting films. Physical Review B, 42, pp.4838–4845.

[39] Dou, S.X., Soltanian, S., Horvat, J., Wang, X.L., Zhou, S.H., Lonescu, M. & Liu, H.K., 2002. Superconducting properties of MgB_2-based materials. Applied Physics Letters, 81, pp.3419–3421.
[40] Panarina, N.Y., Talanov, Y.I., Shaposhnikova, T.S., Beysengulov, N.R. & Vavilova, E., 2010. Magnetic phase transitions in iron-based superconductors. Physical Review B, 81, 224509.
[41] Hanisch, J., Iida, K., Kurth, F., Reich, E., Tarantini, C., Jaroszynski, J., Forster, T., Fuchs, G., Huhne, R., Grinenko, V., Schultz, L. & Holzapfel, B., 2015. High-field performance of iron-based superconducting tapes. Scientific Reports, 5, 17363.
[42] Talanov, Y., Beisengulov, N., Kornilov, G., Shaposhnikova, T., Vavilova, E., Nacke, C., Wurmehl, S., Panarina, N., Hess, C., Kataev, V. & Buchner, B., 2013. Microwave absorption in superconducting materials. Superconductor Science and Technology, 26, 045015.
[43] Fang, L., Jia, Y., Mishra, V., Chaparro, C., Vlasko-Vlasov, V.K., Koshelev, A.E., Welp, U., Crabtree, G.W., Zhu, S., Zhigadlo, N.D., Katrych, S., Karpinski, J. & Kwok, K., 2013. Vortex dynamics in iron-based superconductors. Nature Communications, 4, 2655.
[44] Srinivasu, V.V., 1994. Non-resonant RF and Microwave Absorption Studies. PhD Thesis, Indian Institute of Science, India.
[45] Jan, D.B., Coulter, J.Y., Hawley, M.E., Bulaevskii, L.N., Maley, M.P. & Jia, Q.X., 2003. Thin-film superconducting properties. Applied Physics Letters, 82(5), pp.5–8.
[46] Coffey, M.W. & Clem, J.R., 1991. Vortex dynamics in superconductors. Physical Review Letters, 67, pp.386–389.
[47] Ji, L., Rzchowski, M.S., Anand, N. & Tinkham, M., 1993. Magnetic flux behavior in superconducting films. Physical Review B, 47, pp.470–474.
[48] Muller, P. & Ustinov, A.V., 1997. The Physics of Superconductors: Introduction to Fundamentals and Applications. Springer, Germany.
[49] Franz, A., Wallraff, A. & Ustinov, A.V., 2001. Josephson junction behavior in superconducting circuits. Journal of Applied Physics, 89, pp.471–475.
[50] Andrzejewski, B., Cryzak, B., Szczesniak, L. & Stankowski, J., 1995. Magnetic resonance in superconducting materials. Applied Magnetic Resonance, 8, pp.35–40.
[51] Gallop, J.C. & Radcliffe, W.J., 1991. Microwave absorption in superconductors. Superconductor Science and Technology, 4, pp.568–572.
[52] Wu, C.J. & Chen, Y.L., 2011. Electromagnetic modeling of superconducting structures. Progress in Electromagnetics Research, 111, pp.433–446.
[53] Aly, A.H. & Sabra, W., 2013. Magnetic properties of YBaCuO systems. Physica C, 495, pp.126–130.
[54] Tripathy, M.R. & Srivastava, G.P., 1999. Magnetic hysteresis in high-Tc superconductors. IEEE Transactions on Magnetics, 35, pp.4079–4082.
[55] Srinivasu, V.V., Thomas, B., Hegde, M.S. & Bhat, S.V., 1994. ESR studies in superconducting oxides. Journal of Applied Physics, 75, pp.4131–4135.
[56] Dulcic, A., Rakvin, B. & Perik, M., 1989. Magnetic susceptibility in YBaCuO ceramics. Europhysics Letters, 10, pp.593–597.

[57] Rastogi, A., Sudershan, Y.S., Bhat, S.V., Grover, A.K., Yamaguchi, Y., Oka, K. & Nishihara, Y., 1996. Magnetic phase transitions in cuprate superconductors. Physical Review B, 53, pp.9366–9370.
[58] Masiakowski, J.T., Micky, P. & Larry, K., 1991. Chemical properties of superconducting compounds. Journal of Physical Chemistry, 95, pp.1393–1397.
[59] Srinivasu, V.V., Bhat, S.V. & Kumar, N., 2001. Microwave absorption in superconducting materials. Journal of Superconductivity and Novel Magnetism, 14, pp.41–45.
[60] Srinivasu, V.V., 2010. RF absorption studies in superconductors. Journal of Superconductivity and Novel Magnetism, 23, pp.305–310.
[61] Blazey, K.W., Portis, A.M., Muller, K.A. & Holtzberg, F.H., 1988. Magnetic resonance in superconducting ceramics. Europhysics Letters, 6, pp.457–460.
[62] Blazey, K.W., Portis, A.M., Muller, K.A., Bednorz, J.G. & Holtzberg, F.H., 1988. Magnetic properties of YBaCuO compounds. Physica C, 56, pp.153–155.
[63] Owens, F.J., 1990. Magnetic susceptibility in high-Tc superconductors. Physica C, 171, pp.25–28.
[64] Srinivasu, V.V., Pinto, R. & Sastry, M.D., 1996. Microwave absorption in superconducting thin films. Applied Superconductivity, 4, pp.195–198.
[65] Bhat, S.V., Srinivasu, V.V. & Kumar, N., 1991. ESR studies in superconducting oxides. Physical Review B, 44, pp.10121–10124.
[66] Srinivasu, V.V., Bhat, S.V. & Kumar, N., 1994. Spin dynamics in YBaCuO ceramics. Solid State Communications, 89, pp.375–378.
[67] Pradhan, A.K., Roy, S.B., Chaddah, P., Chen, C. & Wanklyn, B.M., 1995. Magnetic phase transitions in cuprate superconductors. Physical Review B, 52, pp.6215–6218.
[68] Padam, G.K., Arora, N.K. & Ekbote, S.N., 2010. Structural and magnetic properties of YBaCuO systems. Materials Chemistry and Physics, 123, pp.752–756.
[69] Rastogi, A., Srinivasu, V.V., Hedge, M.S. & Bhat, S.V., 1994. Magnetic ordering in high-Tc superconductors. Physica C, 234, pp.229–232.
[70] Puri, M., Durny, R. & Kevan, L., 1992. ESR analysis of superconducting phases. Physica C, 190, pp.210–213.
[71] Bhat, S.V., Rastogi, A., Kumar, N., Nagarajan, R. & Rao, C.N.R., 1994. Magnetic susceptibility in rare-earth substituted superconductors. Physica C, 219, pp.87–90.
[72] Kusmartsev, F.V., 1992. Vortex dynamics in superconductors. Physical Review Letters, 69, pp.2268–2271.
[73] Braunish, W., Knauf, N., Kataev, V., Neuhausen, S., Grutz, A., Kock, A., Roden, B., Khomskii, D. & Wohlleben, D., 1992. Magnetic phase transitions in YBaCuO. Physical Review Letters, 68, pp.1908–1911.
[74] Chockalingam, S.P., Sarangi, S., Bhat, S.V., Oka, K. & Nishihara, Y., 2009. Resistive transition in superconducting ceramics. Journal of Physics: Condensed Matter, 21, 045704.
[75] Sarangi, S., Chockalingam, S.P. & Bhat, S.V., 2005. Microwave absorption in YBaCuO systems. Journal of Applied Physics, 98, 073906.

[76] Shaltiel, D., Nidda, H.A.K., Loidl, A., Rosenstein, B., Shapiro, B.Y., Shapiro, I., Tamegai, T. & Bogoslavsky, B., 2008. Magnetic behavior in layered superconductors. Physical Review B, 77, 014508.
[77] Dulcic, A., Crepeau, R.H. & Freed, F., 1988. ESR studies in superconducting oxides. Physical Review B, 38, pp.5002–5005.
[78] Maniwa, Y., Grupp, A., Hentsch, F. & Mehring, M., 1988. Magnetic resonance in high-Tc ceramics. Physica C, 156, pp.755–758.
[79] Owens, F.J., 1990. Magnetic field effects in superconductors. Physics Letters A, 151, pp.349–352.
[80] Panarina, N.Y., Talanov, Y.I., Shaposhnikova, T.S., Beysengulov, N.R. & Vavilova, E., 2010. Magnetic phase transitions in iron-based superconductors. Physical Review B, 81, 224509.
[81] Selvamanickam, V., Hazelton, D.W., Motowidlo, L., Krahula, F., Hoehm, J., Walker, M.S. & Haldar, P., 1998. Advances in superconducting wire technology. Journal of Minerals, Metals and Materials Society, 50, pp.27–30.
[82] Haugan, T.J., Barnes, P.N., Wheeler, R., Meisenkothen, F. & Sumption, M.D., 2004. Enhanced flux pinning in superconductors. Nature, 430, pp.867–870.
[83] Maiorov, B., Baily, S.A., Zhou, H., Ugurlu, O., Kennison, J.A., Dowden, P.C., Holesinger, T.G., Foltyn, S.R. & Civale, L., 2009. Vortex pinning in superconducting films. Nature Materials, 8, pp.398–404.
[84] Mele, P., Matsumoto, K., Horide, T., Miura, O., Ichinose, A., Mukaida, M., Yoshida, Y. & Horii, S., 2006. Superconducting properties of YBCO thin films. Superconductor Science and Technology, 19, pp.44–50.
[85] Zhang, Y., Jiang, J., Bark, C.W., Weiss, J.D., Polyanskii, A., Nelson, C.T., Tarantini, C. & Lee, S., 2011. Flux pinning in iron-based superconductors. Applied Physics Letters, 98, 042509.
[86] Katase, T., Hiramatsu, H., Kamiya, T. & Hosono, H., 2010. Thin-film growth of iron-based superconductors. Applied Physics Express, 3, 063101.
[87] Marcon, R., Fastampa, R., Giura, M. & Matacota, C., 1989. Magnetic flux behavior in superconducting ceramics. Physical Review B, 39, pp.2796–2799.
[88] Braithwaite, D., Lapertot, G., Knafo, W. & Sheikin, I., 2010. High-pressure studies of superconductors. Journal of the Physical Society of Japan, 79(5), p.15.
[89] Luo, Y.Y., Wu, Y.C., Xiong, X.M., Li, Q.Y., Gawalek, W. & He, Z.H., 2000. Magnetic properties of YBaCuO ceramics. Journal of Superconductivity, 13(4), pp.575–581.

CHAPTER FOUR

Sample Preparation, Material Synthesis, and Processing

The discovery of high-temperature superconductivity (HTSC) in 1986 by Bednorz and Müller in the cuprate compound La2−x_{2-x}2−xBax_xxCuO4_44 at Tc≈35 KT_c \approx 35 \, KTc ≈35K marked a paradigm shift in condensed matter physics. Since then, the field has advanced rapidly, with numerous cuprate and non-cuprate families exhibiting superconductivity at increasingly higher transition temperatures. Despite nearly four decades of intensive research, a complete microscopic understanding of HTSC remains elusive, largely due to the complex interplay of strong electron correlations, short coherence lengths, anisotropy, and unconventional pairing mechanisms.This chapter provides an overview of high-Tc superconductors, with an emphasis on their structural, electronic, and superconducting properties that are relevant to the present study. Special attention is given to the phase diagram, pairing symmetry, coherence length, penetration depth, and the role of granularity, as these factors strongly influence the observed electromagnetic and microwave absorption behaviors discussed later in this thesis.

4.1 High-Tc Superconductors

High-Tc superconductors represent a unique subclass of oxide materials, most of which belong to the perovskite-related cuprates. The undoped parent compounds are typically Mott insulators, but upon carrier doping, they display a rich and unusual phase diagram characterized by competing states, including antiferromagnetism, pseudogap phases, strange metallic behavior, and ultimately, superconductivity.The essential features distinguishing HTSCs from conventional low-Tc superconductors include:

4.1.1 Characteristics of High-Temperature Superconductors (HTSCs)

High-temperature superconductors (HTSCs), particularly the cuprate families, exhibit a unique set of physical characteristics that distinguish them from conventional, low-temperature superconductors. Their behavior reflects a complex interplay of structural, electronic, and magnetic phenomena that continue to challenge theoretical understanding. The most notable features of HTSCs include:Extremely short coherence length (ξ): Typically only a few nanometers, which makes them highly sensitive to microstructural defects and grain boundaries.

Large London penetration depth (λ): Leading to a very high Ginzburg–Landau parameter (κ = λ/ξ), classifying HTSCs as extreme type-II superconductors.Unconventional pairing symmetry:

Experimental evidence strongly supports d-wave pairing in the cuprate systems.Strong anisotropy: Originating from their quasi-two-dimensional layered structure, particularly within the CuO_2 planes, which serve as the primary pathways for superconducting current.Sensitivity to impurities and oxygen stoichiometry: Even slight deviations in oxygen content or the introduction of foreign atoms can drastically alter both normal and superconducting state properties.Although remarkable progress has been made in understanding these materials, several aspects of their normal-state behavior—such as the pseudogap phenomenon, anomalous resistivity, and magnetic responses—remain only partially understood. The intrinsic complexity of HTSCs continues to drive both experimental and theoretical research, particularly within the framework of strongly correlated electron systems.

4.1.2 Processing of High-Tc Superconductors

Intrinsic superconducting parameters, such as the critical temperature (Tc) and the thermodynamic critical field **(Hc)**, are fundamentally determined by the material's composition and electronic structure. However, other key parameters—most notably the critical current density **(Jc)** and magnetic penetration depth (λ)—are strongly influenced by the microstructure of the synthesized sample. These parameters can vary by several orders of magnitude depending on the processing technique employed [Ref. 2].

For practical electrical applications, maintaining a high **Jc** in the presence of magnetic fields is essential. While impressive Jc values have been achieved in bulk samples, thin films, and coated conductors, significant processing challenges persist. These challenges arise primarily from microstructural imperfections such as grain boundaries**,** defects, and insufficient flux pinning, all of which degrade the macroscopic superconducting performance.

4.2 Grain Boundaries, Metallurgical Defects, and Flux Pinning

Grain boundaries represent interfacial regions between adjacent crystallites, often containing impurity or secondary phases. These regions can be insulating or normally conducting and typically extend over distances much greater than the coherence length (ξ) of HTSCs. As a result, they behave as Josephson junctions, significantly reducing the critical current across the boundary and producing the so-called weak-link behavior. Consequently, the global critical current density **(Jc)** of polycrystalline HTSC materials is drastically reduced, while surface

resistance increases..To overcome these detrimental effects, processing strategies are focused on minimizing grain boundary limitation**s** while simultaneously enhancing flux pinning. Several effective approaches have been developed:

Nanoparticle doping**:** The incorporation of nanomagnetic particles (e.g., Ni, Ag, or $BaZrO_3$) strengthens intergranular coupling and introduces efficient flux pinning centers.Texturing techniques**:** Controlled grain alignment along the crystallographic *ab*-plane minimizes high-angle grain boundaries.Irradiation methods**:** Neutron or proton irradiation produces controlled linear defects along particle tracks, serving as strong pinning sites.Alloying and secondary phase inclusions**:** Introducing tailored second-phase particles provides pinning centers while limiting grain misorientation.Experimental investigations have shown that **Jc** across grain boundaries is highly sensitive to the misorientation angle between adjacent grains. Reducing or eliminating high-angle boundaries remains one of the central challenges in HTSC research and fabrication.

Among various HTSC systems, $YBa_2Cu_3O_{7-x}$ (YBCO) has emerged as the most promising material for practical electrical and magnetic applications. This is attributed to its well-defined crystal structure, ease of single-phase synthesis, and compatibility with advanced flux pinning and grain texturing strategies. The Top-Seeded Infiltration and Growth (TSIG) method, in particular, has demonstrated exceptional results—yielding aligned grains and achieving **Jc** values up to 10^5 A/cm² at 77 K under self-field conditions.

Other HTSC families**:**

Tl-based superconductors**:** Exhibiting Tc values up to 125 K and **J**c exceeding **10^5 A/**cm² at 77 K, thallates display excellent potential. However, their toxicity**,** volatility, and **loss** during high-temperature processing significantly hinder large-scale fabrication.Hg-based superconductors**:** These compounds also possess high Tc values, but processing difficulties arise due to the volatility of HgO, which decomposes near 500 **°C**. Controlled synthesis in sealed environments is therefore required.Bi-based superconductors: These materials are less suitable for bulk applications because of their polycrystalline morphology and weak flux pinning. However, their layered, micaceous structure makes them attractive for wire fabrication.

4.3 Sample Preparation and Material Synthesis

Several synthesis methods are employed for HTSC materials:Solid-state reaction: A conventional route relying on high-temperature reactions between precursor oxides and carbonates.

Melt infiltration and texturing: Used extensively in YBCO to achieve grain alignment and enhanced performance.

Sol-gel methods: Wet-chemical synthesis offering fine compositional control.

Combustion synthesis: A rapid, energy-efficient method for preparing phase-pure powders.

Microwave synthesis: Provides fast heating rates and uniform reactions, improving phase homogeneity.

Advances in synthesis and processing have significantly improved phase purity, superconducting volume fraction, and flux pinning performance in bulk HTSC materials. Continued progress in these areas remains critical for their widespread technological deployment.

4.4 Processing YBCO Bulk Superconductor

Despite significant advances in high-temperature superconductors, considerable challenges remain in the commercialization of these ceramic materials. The complexity of these issues has somewhat reduced interest in bulk forms among physicists, who have increasingly focused on pellets, powders, and thin films.As reported by Gallagher et al. [12], the superconducting properties of $YBa_2Cu_3O_{7-x}$ are highly sensitive to oxygen content. Altering the oxygen stoichiometry induces a structural transition between orthorhombic and tetragonal phases. For x values above 0.1 (i.e., oxygen content less than 6.9), YBCO becomes non-superconducting. Optimal superconductivity occurs near $x = 0.02$ (oxygen content ≈ 6.98), a condition that depends on both temperature and oxygen partial pressure.

4.4.1 Conventional Solid-State Reaction Method

The conventional solid-state reaction method**,** also known as calcination**,** is the simplest and most economical technique for synthesizing bulk $YBa_2Cu_3O_{7-\delta}$ (YBCO) superconductors. The process involves the following major steps:

Material Preparation:The starting materials, typically oxides or carbonates of yttrium, barium, and copper, are weighed in stoichiometric proportions, mixed thoroughly, and ground to achieve a uniform particle size distribution.Calcination**:**The mixed powder is heat-treated in an alumina crucible at approximately 950 °C for 24 hours. After cooling to room temperature, the material is reground, remixed, and subjected to a second calcination under identical conditions to ensure compositional homogeneity. This cycle of grinding and reheating may be repeated several times depending on phase purity requirements.Pellet Formation:The homogeneous powder is pressed into pellets using a hydraulic press at a pressure of approximately 1500 Pa. The pellets are then placed in crucibles (commonly alumina, gold, or platinum) and sintered at ~900 °C for 24 hours in air to form the orthorhombic superconducting YBCO phase.Oxygenation:Controlled oxygenation is carried out during slow cooling, typically near 500 **°C**, to achieve the desired oxygen stoichiometry, which is essential for optimal superconducting properties.Despite its simplicity, the solid-state method can result in secondary phase formation (e.g., $BaCuO_2$ or CuO) and possible contamination from the crucible or furnace environment. Nevertheless, bulk YBCO synthesized by this approach typically achieves a critical temperature (Tc) of approximately 90 K and critical current densities **(Jc)** on the order of 10^4 A/cm² in zero magnetic field at 77 K [14,15].However, due to the polycrystalline nature of the grains, such samples exhibit pronounced weak-link behavior under applied magnetic fields, with **Jc** decreasing by about three orders of magnitude at 0.1

4.4.2 REBCO Superconductors Fabricated by the Melt Growth Process

REBCO superconductors synthesized by the traditional sintering method often contain randomly oriented grains, which create weak links at grain boundaries and thus severely limit their overall current-carrying capability. Additionally, microstructural defects such as cracks, porosity**,** and secondary phases further reduce the effective critical current density (**Jc**) [13].

The melt texturing technique, first introduced by Jin and co-workers [13]**,** marked a revolutionary advancement in the fabrication of bulk YBCO superconductors. This technique allows for the growth of oriented large grains that can carry substantially higher current densities than conventionally sintered samples. Early melt-textured YBCO samples demonstrated significant improvements in current transport, achieving **Jc** values of approximately 10^4 A/cm² in

zero magnetic field [14].These advancements laid the foundation for modern melt growth processes, which continue to be refined to improve performance and scalability.

In the melt-textured growth of REBCO materials, as described by Jin *et al.* [13], the precursor material is heated above its peritectic temperature, allowing crystals to nucleate and grow from the supercooled melt upon controlled cooling. A specific heat-treatment schedule follows, designed to promote chemical homogenization, stress relief, oxygen diffusion, and grain boundary purification to minimize weak-link effects.Melt-textured samples exhibit substantial improvements in mechanical strength, electrical conductivity, and magnetic performance compared to conventional polycrystalline forms. These advantages inspired extensive research into process optimization and the development of numerous melt-processing variants, such as:

Quench and Melt Growth (QMG) [16]Melt Powder Melt Growth (MPMG) [17]Powder Melting Process (PM) [18]

Oxygen-Controlled Melt Growth (OCMG) [19] Top-Seeded Melt Growth (TSMG) [20] Numerous studies [11, 20–27] have since examined the various thermodynamic, kinetic, and structural aspects of these melt-processed materials.During the melt growth process, the Y-123 phase is heated above its peritectic temperature (Tp), causing it to decompose according to the following reaction:

$$YBa2Cu3O7{-}\delta \rightarrow Y2BaCuO5\ (Y\text{-}211) + Liquid\ (BaCuO2{+}CuO)$$

This reaction occurs when YBCO (Y-123) is heated above its peritectic temperature (around 1010–1030 °C, oxygen dependent). Instead of melting directly, Y-123 decomposes into:Y-211: a solid, yttrium-rich phase

A Ba–Cu–O liquid: mainly $BaCuO_2$ and CuO During melt-textured growth (MTG / TSMG), this reaction is essential • On slow cooling, Y-123 can re-form from:Y-211+Liquid ⟶ Y-123. The remaining Y-211 particles act as flux pinning centers, improving JcUpon controlled cooling, this liquid phase reacts with Y-211 particles to re-form the Y-123 superconducting phase. The resulting microstructure, consisting of Y-211 inclusions within a Y-123 matrix, plays a crucial role in flux pinning and thereby enhances the critical current density (Jc) of the final REBCO material.Y2BaCuO5 plus 3 BaCuO2 plus 2 CuO equals 2 YBa2Cu3O6.5.The mixture—fancy name: properitectic, but who really uses that at parties—starts doing its thing when you cool it slooooowly below what's called Tp. For YBCO in plain old air, Tp is like 1008°C… give or take,

depending on which rare earth you tossed in the mix (the bigger the atoms, the higher Tp seems to creep up) [21,22].

After parking this stuff at just-below-Tp for a bunch of hours (imagine staring at your oven but with way more expensive ingredients), you end up with REBa2Cu3O6.5. The catch? It's rocking a tetragonal structure and, plot twist, it's totally not superconducting. Fickle, right? Anyway, you gotta bathe it in oxygen at like 300-600°C for a good while. That boosts oxygen levels [11], nudging the formula up to REBa2Cu3O7-x and flipping the structure over to orthorhombic—and boom, now you've got a superconductor.Oh, and 'twinning' shows up too—basically the material's way of dealing with stress from those structural changes [24]. Expect some serious shrinking and gnarly defects inside the chunk, thanks to bits of the liquid phase bailing out mid-process. Classic.Here's where the big brains start weighing in: this whole section is really just a lay of the land on what's happening inside these melt-grown REBCO materials compared to IG-processed stuff. Some recent paper (yeah, the reference is missing… smooth) lists out the key points [29].Murakami and the gang [25] found that if you sprinkle in just the right amount of fine Y-211 inclusions into that Y-123 soup, the critical current (Jc) gets way better. They even did the "magnet levitation trick" where someone actually stood on a platform floating on Y-123 magnets [9,27]. Try topping *that* at your next science fair.Turns out, those Y-211 bits spark off unique secondary defects right where the Y-211 meets Y-123 (see [25,26]), and the size is just on the scale of the coherence length—a few nanometers, tops [23]. This all happens because the different chunks expand and contract at slightly different rates as they heat and cool, causing mini-defects at the borders.Anyways, these big chunko REBa2Cu3O7 superconductors—single chunks, FYI, not crumbs—can haul massive currents and might actually be useful for things like trapped-field magnets, or toss one in a motor or generator and see what happens [1-3].

Top-seeded melt growth (TSMG) is pretty dialed in for making giant single grains, but it ain't all smooth sailing. Tons of headaches like shrinkage, pores, big ugly cracks, massive (RE)2BaCuO5 needles, uneven RE-211 inclusions mucking up the beautiful Y-123 matrix, the whole nine yards. Most of these messes? Blame it on the liquid phase leaking out during processing [11]. The struggle, as they say, is real.

Thus, the peritectic decomposition of YBa2Cu3O7−δ not only governs phase formation during melt processing but also indirectly determines the Josephson weak-link characteristics through its impact on microstructure and oxygen homogeneity.

4.5 **Fabrication of REBCO Superconductors Using the Infiltration and Growth (IG) Process**

The infiltration and growth (IG) process is an advanced synthesis technique in which a liquid phase, typically $Ba_3Cu_5O_8$**,** permeates a porous solid precursor (the 211 phase, Y_2BaCuO_5**)** through capillary action to form the Y–Ba–Cu–O superconducting phase during cooling. This method has proven highly effective in producing bulk superconductors with reduced porosity and minimized substrate reactions compared to those synthesized using the conventional top-seeded melt growth (TSMG) method. Furthermore, the uniform distribution of Y-211 secondary phase particles within the Y–Ba–Cu–O matrix achieved through IG significantly enhances the microstructural homogeneity and overall superconducting performance.

The development of the IG process was driven by the need to overcome the limitations inherent in melt-growth-based methods. The IG approach offers superior microstructural control and flexibility in processing parameters. In a typical IG procedure, a RE-211 preform is placed in direct contact with a liquid source phase, generally composed of Y-123, $BaCuO_2$, and CuO in defined ratios. The entire assembly is then heated to a temperature 30–400°C above the peritectic temperature (Tp) of the corresponding RE-123 compound. At this elevated temperature, the liquid phase ($BaCuO_2$ + CuO) infiltrates the RE-211 preform through capillary action.

During controlled cooling below the peritectic temperature, the infiltrated liquid reacts with RE-211 particles to form the RE-123 superconducting phase, while any unreacted RE-211 remains as fine inclusions within the RE-123 matrix. Such inclusions act as effective flux-pinning centers, which are critical for enhancing critical current density **(Jc)** and magnetic flux trapping capabilities.Various modifications to the IG process have been proposed to optimize infiltration dynamics and phase formation. For instance, researchers have achieved improved infiltration by introducing different liquid source compositions, modifying the thermal profile, or optimizing the RE-211 particle size distribution—all aimed at achieving enhanced phase purity**,** grain connectivity**,** and superconducting performance in bulk REBCO materials.

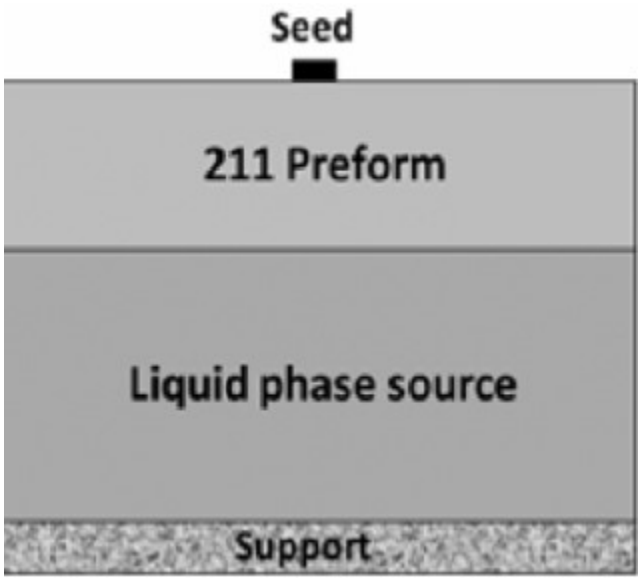


Figure.4.1: A typical experiment used in infiltration Growth process.A source of liquid phases which can either be Y-123 or Y-123+BaCuO2+CuO.A preform made up of Y-211 powder is kept on top of it.A c-axis oriented Nd-123 seed crystal is placed on top of the preform,at the center[29].

Assembly Methods and Material Preparation

Various strategies exist for assembling Y-211 preforms, combining them with liquid phase sources and seeds, and supporting the assemblies during heat treatment.

Numerous adjustments to the composition of the liquid phase sources have also been reported [42-47].

Melt Growth Process

In this method, as illustrated schematically at the top of Fig. 1.13, RE-123 is heated above its peritectic melting temperature.This process yields Y-211 and liquid phases.As the sample melts, significant shrinkage occurs, typically around 13–22%.

When the sample cools and Y-211 and the liquid recombine to form textured Y-123 (below the peritectic temperature, Tp), the original shrinkage and distortions are retained.Notably:Macroscopic internal defects may develop within the sample.

These defects result from the outflow of the liquid phase during melting.

Infiltration Growth (IG) Process

This alternative process begins with a preformed Y-211 structure, which is then infiltrated with the liquid phase.

Shrinkage during this procedure is minimal (less than 0.4%).After infiltration, the preform reacts (below Tp) to form Y-123.Key features of the IG process:The Y-211 skeleton retains its original shape and size during both infiltration and reaction steps.

There is virtually no shrinkage or structural distortion in the final product.Residual Y-211 particles are evenly distributed, fine, and typically spherical within the Y-123 matrix.

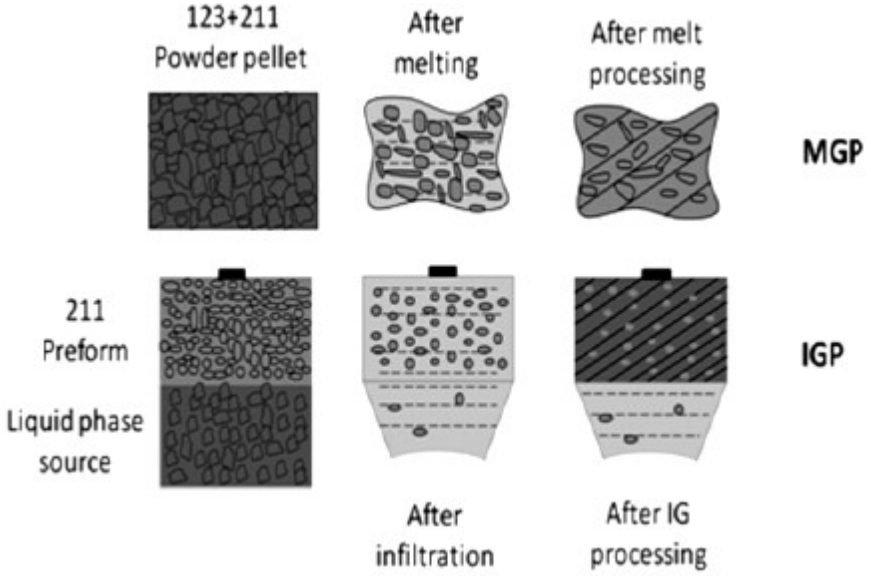


Fig 4.2 A comparison between the Melt growth and the Infiltration Growth Process[29]

Advantages of the IG Process for RE-123 Superconductors

Near Net Shape Fabrication.The IG process significantly reduces shrinkage issues, enabling the production of RE-123 components that closely match desired shapes. This leads to:Less material waste

Reduced post-processing.Enhanced Microstructure for High Current Density IG processing delivers microstructures that facilitate remarkably high critical current densities.Large, single-crystal Y-123 samples have been fabricated using this method, particularly for trapped field magnet applications.Influence of Y-211 Content on Superconducting PerformanceRelationship Between Y-211 and Critical Current Density

Increasing the amount of Y-211 phase within the Y-123 matrix causes critical current density (Jc) to increase substantially—by several orders of magnitude.This is attributed to the formation of nanometer-scale defects at the Y-123/Y-211 interface, which effectively serve as flux pinning centers.The overall current-carrying capacity of melt-processed Y-123 is further improved by increasing the surface area of the Y-211 phase particles.

Preparation of Precursor Powders Y-211 Powder Synthesis

Synthesis and Characterization of $YBa_2Cu_3O_{7-\delta}$ (YBCO) Superconductors

This chapter presents a comprehensive account of the synthesis and characterization of $YBa_2Cu_3O_{7-\delta}$ (YBCO) superconducting samples. The experimental work was conducted in collaboration with Dr. Pavan Naik**,** under the supervision of Prof. V. S. Vallabhapurapu**.** Formal authorization was obtained from the collaborator to incorporate this manuscript as a part of the current doctoral thesis.

Preparation of Y-211 Precursors

The precursor powders were synthesized using high-purity Y_2O_3, BaO_2, and CuO, mixed in the stoichiometric ratio of Y:Ba:Cu = 2:1:1**.**

The mixture was calcined at 900°C for 48 hours to achieve phase formation.

After calcination, the powders were uniaxially pressed into cylindrical pellets with a diameter of approximately 20 mm and a thickness of 12 mm.

The pressed pellets were subsequently sintered at 1200°C for 1 hour to enhance densification and crystallinity.

Synthesis of $Ba_3Cu_5O_8$ as a Liquid Source**:**For the infiltration growth (IG) process, a $Ba_3Cu_5O_8$ compound was prepared to serve as a liquid source during growth**.**

*The starting materials, BaO_2 and CuO, were combined in a molar ratio of 3:5***.**

The mixture was heat-treated at 800°C for 24 hours to achieve the desired phase.

The resulting powders were pressed into pellets having dimensions equivalent to those of the Y-211 precursor.

Assembly for the Infiltration Growth (IG) Process.Prior to initiating the IG process, the $Ba_3Cu_5O_8$ pellet was carefully positioned on a MgO single-crystal substrate, which served as a stable and non-reactive base for crystal growth. This configuration ensured uniform heat distribution and minimized chemical reactions between the sample and the substrate, resulting in

high-quality YBCO single-grain formation.The IG process presents substantial advantages for the fabrication of RE-123 superconductors, particularly in optimizing current carrying capacity and achieving near-net shape products. The careful preparation of precursor powders and attention to phase composition are key factors in exploiting these benefits for high-performance superconducting applications.

References

[1] M. Murakami, A. Goyal, and W. Wong-Ng, *Processing of High Temperature Superconductors*. Hoboken, NJ, USA: Wiley, 2012.

[2] H. W. Weber and G. W. Crabtree, in *Studies of High Temperature Superconductors*, A. V. Narlikar, Ed. New York, NY, USA: Nova Science, 1992, vol. 9, p. 37.

[3] S. Jin and J. Min, "Advances in superconducting materials," *Metall. Mater. Trans.*, vol. 43, no. 3, p. 712, 1991.

[4] J. B. Torrance, Y. Tokura, A. I. Nazzal, A. Bezinge, T. C. Huang, and S. S. P. Parkin, "Transport and structural properties in superconductors," *Phys. Rev. Lett.*, vol. 61, no. 9, p. 7, 1988.

[5] A. K. Bandyopadhyay, R. Jabra, and J. Phalippou, "Materials studies in superconductors," *J. Mater. Sci.*, vol. 8, p. 1464, 1989.

[6] G. Sinha, K. Adhikary, and S. Chaudhuri, "Nanoscience and superconductivity," in *Proc. Nat. Conf. on Nanoscience and Technology*, Jadavpur Univ., Kolkata, India, Jan. 2005.

[7] G. Wrinkler, *Crystallography, Chemistry and Technology of Ferrites*, in *Magnetic Properties of Materials*, J. Smit, Ed. London, U.K.: McGraw-Hill, 1971, p. 20.

[8] J. Liu, H. He, X. Jin, Z. Hao, and Z. Hu, "Magnetic and structural properties," *Mater. Res. Bull.*, vol. 36, no. 13–14, pp. 2357–2363, 2001.

[9] M. Pardavi-Horvath, "Microwave applications of ferrites," *J. Magn. Magn. Mater.*, vol. 215, pp. 171–183, 2000.

[10] N. Mo, Y. Y. Song, and C. E. Patton, "Ferromagnetic resonance studies," *J. Appl. Phys.*, vol. 97, no. 9, p. 19, 2005.

[11] J. Giri, P. Pradhan, T. Sriharsha, and D. Bahadur, "Magnetic nanoparticles for biomedical applications," *J. Appl. Phys.*, vol. 97, no. 10, p. 13, 2005.

[12] G. W. Cave, C. L. Raston, and J. L. Scott, "Green chemistry synthesis routes," *Chem. Commun.*, p. 2159, 2001.

G. Rothenberg, A. P. Downie, C. L. Raston, and J. L. Scott, "Catalysis and synthesis studies," *J. Am. Chem. Soc.*, vol. 123, p. 8701, 2001.

[13] D. Braga and F. Grepioni, "Crystal engineering strategies," *Angew. Chem. Int. Ed.*, vol. 43, p. 4002, 2004.

[14] S. Jin, T. H. Tiefel, R. C. Sherwood, M. E. Davis, R. B. van Dover, G. W. Kammlott, R. A. Fastnacht, and H. D. Keith, "Superconducting thin films," *Appl. Phys. Lett.*, vol. 52, p. 2074, 1988.

[15] Z. Lian, Z. Pingxiang, J. Ping, W. Keguang, W. Jingrong, and W. Xiaozu, “Transport properties of superconductors,” *Supercond. Sci. Technol.*, vol. 3, p. 92, 1990.
[16] T. Troczynski and Q. Yang, “Superconducting material processing,” U.S. Patent 6,284,682, 2001.
[17] T. Olding, M. Sayer, and D. Barrow, “Thin-film deposition studies,” *Thin Solid Films*, vol. 398–399, pp. 581–586, 2001.
[18] J. G. P. Binner and I. A. H. Al-Dawery, “Materials science of superconductors,” *Supercond. Sci. Technol.*, vol. 11, p. 449, 1998.
[19] A. W. Czanderna, C. J. Powell, T. E. Madey, D. M. Hercules, and J. T. Yates, Jr., “Specimen handling and preparation in thin-film studies,” in *Surface Characterization: Physical and Chemical Methods for Thin-Film Deposition and Epitaxial Growth*, MOSC Series, vol. 4, pp. 239–293.
[20] A. H. Salama, M. E. Hofy, Y. S. Rammah, and M. Elkhatib, “Nanostructured superconductors,” *Adv. Nat. Sci.: Nanosci. Nanotechnol.*, vol. 7, p. 015011, 2016.
[21] P. Prayoonphokkharat, S. Jiansirisomboon, and A. Watcharapasorn, “Microstructural studies in superconductors,” *J. Microsc. Soc.*, vol. 5, no. 1–2, pp. 63–66, 2012.
[22] P. Wei and Z. Qing Qi, “Transport phenomena in cuprates,” *Physica C*, vol. 183, pp. 32–38, 1991.
[23] E. S. Reddy and G. I. Schmitz, “Superconducting thin films,” *Supercond. Sci. Technol.*, vol. 15, pp. L21–L24, 2002.

Introductory Note to Chapter Five

The following chapter presents a complete and detailed study on the synthesis and characterization of $YBa_2Cu_3O_{7-\delta}$ (YBCO) superconducting samples. The work was carried out in collaboration with Dr. Pavan Naik and under the guidance of **Prof. VS Vallabhapurapu**. Permission has been granted by our collaborator to include this manuscript as an integral part of the present thesis.

The manuscript represents a comprehensive experimental and analytical investigation, covering sample preparation, structural characterization, and the corresponding physical property evaluations. It forms the scientific basis for the collaborative publication currently being finalized, in which my name will appear as a co-author.

The chapter is presented here in its full and original structure, maintaining the integrity of the experimental design, results, and discussion as approved by my supervisor.

CHAPTER FIVE

Synthesis and Characterization of YBCO Superconductors

High-Energy Ultrasonication of Y_2BaCuO_5 in Aqueous Medium: A Cleaner Approach to Enhanced $YBa_2Cu_3O_{7-\delta}$ Bulk Superconducting properties

labhapurapu Sreenivasu[1,#], Lemma Kurie Baruda[1], Rikako Hagiwara[2], RameValsh Ade[3], P.M. Swarup Raju[4], Taichiro Nishio[2] and S. Pavan Kumar Naik[2,*]

[1]Department of Physics, University of South Africa, Johannesburg, South Africa 1709

[2]Department of Physics, Tokyo University of Science, 1 Chome-3 Kagurazaka, Shinjuku City, Tokyo 162-8601, Japan

[3] Department of Physics, Koneru Lakshmaiah Education Foundation, R V S Nagar, Aziz Nagar (PO), Moinabad Road, Hyderabad, 500075, India

[4]Department of Physics, School of Science, GITAM deemed to be University, Hyderabad, India

[*]spavankumarnaik@yahoo.in,[#]vallavs@unisa.ac.za

[*]spavankumarnaik@yahoo.in, [#]vallaba@unisa.sa, lkfgelan@gmail.com

$YBa_2Cu_3O_{7-x}$ (YBCO or Y-123) high-temperature superconductors, exhibit enhanced flux pinning capabilities along with high critical temperature (T_c). The improvements in flux pinning and, consequently, the critical current density (Jc) can be achieved by tailoring the precursor phases and their microstructures. In this study, we compare the microstructural modifications of Y_2BaCuO_5 (Y-211) secondary phase particles via ultrasonication processing in de-ionized water and ethanol on the superconducting properties of bulk YBCO superconductors. Y-211 precursor powders were engineered by subjecting to high-energy ultrasonication at 450 W for 30 minutes in de-ionized water and Ethanol. This ultrasonication treatment led to the formation of nanoscale, surface-modified Y-211 particles, characterized by high surface reactivity and defect density. These pre-treated Y-211 powders are utilized to grow YBCO single grains employing top-seeded infiltration growth (IG) process. Superconducting transition measurements showed sharp onset of ~92 K. The self-field J_c at 77 K was enhanced to **90** kA/cm² using ultrasonically DIW treated Y211 powders compared to Ethanol treated (72 kA/cm²) YBCO superconductors. These findings

validate the effectiveness of ultrasonically engineered *RE*-211 precursors in tailoring flux pinning characteristics and enhancing the performance of *RE*BCO bulk superconductors.

Introduction:

Among various high-temperature superconductors developed so far, single-grain bulk *RE*$Ba_2Cu_3O_{7-x}$ (REBCO, also referred to as RE-123, where RE = rare earth elements and Y) systems are particularly attractive due to their high critical temperature (~92 K) and exceptional flux pinning capabilities. These characteristics make high-quality, single-domain *RE*BCO bulk superconductors highly suitable for a range of scientific and industrial applications that require the generation of Tesla-scale magnetic fields [1-5].

The critical current density (J_c) and magnetic flux trapping capabilities of *RE*BCO bulks are strongly dependent on their final microstructure. Therefore, controlling the precursor composition and growth dynamics is crucial for optimizing superconducting performance. As the J_c is primarily determined by vortex pinning from the RE_2BaCuO_5 (*RE*-211 or 211 or Y-211) particles embedded within the *RE*-123 matrix, ensuring a high density of fine, uniformly distributed 211 particles is essential [6-8].

To achieve such microstructural refinement, various strategies have been explored, including the incorporation of grain-refining additives like Pt, CeO_2, and Ba-Ce–O compounds [9-14]. However, these additives are often costly and may introduce unwanted chemical phases, making it challenging to maintain uniform composition throughout large bulk samples. In 2019, Pavan Kumar Naik et al. [15-16] introduced a novel approach for refining *RE*-211 particles using high-energy ultrasonication in ethanol medium. This method enabled a systematic refinement of both precursor powders and the final 211 particles embedded in the bulk samples, and the mechanisms underlying the observed microstructural changes were discussed in detail in earlier studies [17]. Later, the ultrasonic refinement technique has also demonstrated efficacy in improving the properties of other superconducting systems, such as MgB_2, and holds promise for broader materials applications [18-19].

However, in all previous reported works [15-17, 20-22], high-energy irradiation and precursor 211 particles breaking, size reduction, surface damages were carried out in ethanol medium. This may result in the unwanted inclusions of Carbon-related impurities, up on drying the powders.

Y-211 phase generally is considered as stable in pure water under normal conditions [23]. In the current study, Y-211 precursors are pre-treated with high energy ultrasonication power of 450 W for 30 min in de-ionized water and compare with the ethanol processing. Utilizing the Y-211 phase particles in water, single-grain YBCO bulk was synthesized employing superior top-seeded infiltration-growth (TS-IG) process. Further the enhancement of flux pinning and J_c were discussed. A detailed analysis of the resulting microstructure and superconducting properties was carried out to evaluate the efficacy of this approach.

Experimental Details

Precursor powders of respective 211 and 123 phases of YBCO were synthesized following the conventional solid-state sintering route. Pure phases of 123/211 were produced employing raw materials of Y_2O_3, BaO_2 and CuO and by sintering at 860 ^oC – 900 ^oC for 24 h. The phase purity of each prepared precursor powders was confirmed by the X-ray diffraction measurements. To produce nanostructured Y211 particles, the synthesized powders underwent high-energy ultrasonic irradiation at 450 W for 30 minutes. The detailed optimization protocol for this ultrasonic processing has been described in our earlier studies [15-17, 20-22]. Post-sonication, the powders were heat-treated at 400 °C to 600 °C for 12 hours to eliminate any residual carbon compounds.

Y211 preform pellets of 10 mm diameter were pressed at 460 MPa pressure [24-25]. The liquid phase (LP) composed of Er123:$Ba_3Cu_5O_8$ in 1:1. Following our previous reports [26-27], the 211:LP for IG processing of YBCO single grains are used to be 1:1.4. YBCO bulks were grown following the temperature gradient method with $Y211_{DIW}$ and $Y211_{Et}$. The time-temperature schedule followed for the growth can be find in our previous reports [15-17]. NdBCO seeds (c-textured) with cubic shapes were employed for all growth experiments in order to avoid the growth of multi grain YBCO bulks. Final bulk samples grew employing ultrasonically pre-treated $Y211_{DIW}$ and $Y211_{Et}$ are referred as YBCO-Et and YBCO-DIW respectively. Bulk YBCO samples were annealed in flowing oxygen at 460 °C to 400 °C for 200 hours using a

tubular furnace, aiming to optimize oxygen stoichiometry and enhance superconducting performance.

For microstructural and superconducting properties characterizations, small cubes of typical size of ~2 × 1.5 × 1 mm^3 were sliced from the oxygen-annealed bulks ~0.5 mm below the NdBCO seed. Scanning electron microscopy was employed to observe the microstructural features and the distribution of the 211 particles in the final YBCO-Et and YBCO-DIW bulk samples. To determine the critical temperature, *M(T)* curves were recorded sweeping the temperature from 50 K – 100 K in an applied magnetic field of 1 mT || *c*-axis using a Superconducting Quantum Interference Device magnetometer (SQUID, Quantum Design, model MPMS-XL). Magnetization hysteresis (*M−H*) loops were recorded at 77 K. Utilizing the *M-H* loops, the field dependence of the critical current density was determined using the extended Bean critical state model [28-29].

Results and discussions:

The microstructural features of high energy ultrasonication on Y-211 particles in DIW and Ethanol are compared in Fig. 1 (a) and (b) respectively. Microstructures are recorded after removing the liquid parts in both the cases. High-energy sonication yielded sharp-edged, nanoscale particles that were well separated and morphologically refined with rough surfaces. More or less, both the Y-211_{DIW} and Y-211_{Et} particles exhibit are similar features. Importantly, we observed that there is no white color sediment after removing the liquids in the case of Y-211_{DIW}, where a white color sediment was observed after drying the powders of Y-211_{Et} powders. This indicates that, we achieved the required surface damages, sharp edges of 211 particles on clean routes avoiding the carbon-related compounds.

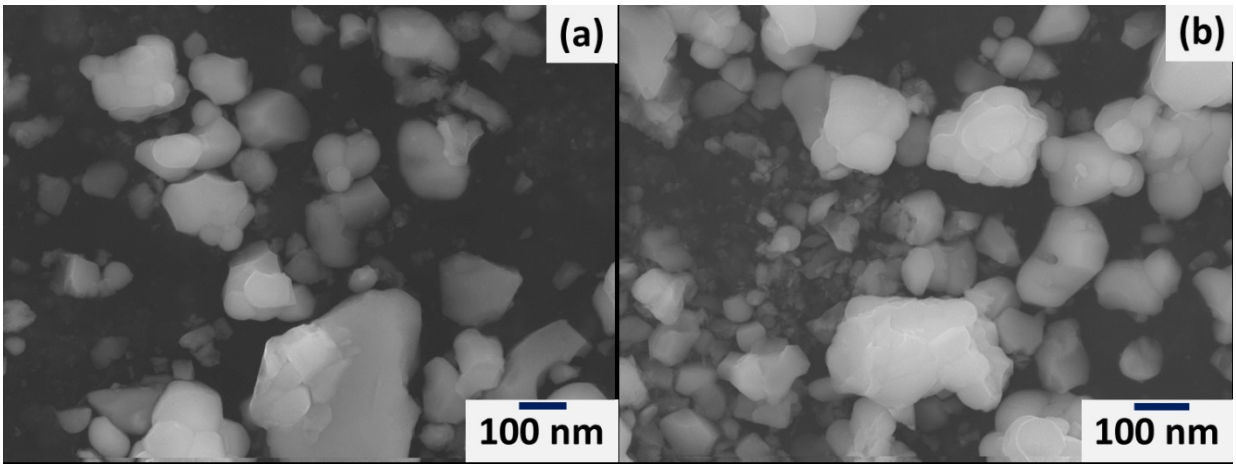


Fig. 1 Microstructures of the Y211 particles after ultrasonic irradiated with 450 W for 30 min in (a) DIW and (b) Ethanol. Y211 particles are of different shapes, have sharp edges and surface damages.

The chemical stability of the Y-123 phase is studied in literature [30-32]. In the case of H_2O, Y-123 phase decomposes and forms corresponding metal oxides, carbonites ($BaCO_3$) via hydroxides, and oxygen as the major phase as described below. The chemical reaction between H2O and Y123 phase are given in the below chemical equations indicate that both the CO_2 as well as H_2O plays a considerable role in the degradation process. Degradation of 123 phase occurs through incongruent leaching, and significant amount of Ba is leached away within a short period of the reaction, while copper and Y211 stay undissolved.

$$2YBa_2Cu_3O_7 + 3\,H_2O \rightarrow Y_2BaCuO_5 + 5CuO + 1.5\,Ba_2^+ + 6OH^- + \text{oxygen}$$

$$Ba(OH)2 + CO2 \longrightarrow BaCO3 + H2O$$

As discussed by the Xu Jimin et al., [], Y123 phase is super hydrophilic while the Y211 phase is hydrophobic. Due to this, Y211 phase also considered importance in various other applications as well such as Pigments in various ceramics, etc. [Other 211 applications].

Stability of Y_2BaCuO_5

*RE*211 or Y211 green phases often considered as a desired byproduct and generally accompanies *RE*/Y123 in bulk superconductors. Therefore, Y211 is well-known for its thermal and chemical stability. It retains structural integrity under a wide range of thermal conditions and in aqueous media [23]. At 110 °C, it is highly unlikely to undergo reduction, decomposition, or any

permanent chemical transformation in the presence of ethanol or its derivatives. Thus, it functions primarily as a catalytic or promotive surface rather than a reactant.

Potential Chemical Reactions of Ethanol and H2O with Y2BaCuO5

The interaction of ethanol with metal oxide surfaces has been extensively studied [23, 30-37]. In this context, Y211, a stable ceramic and an important phase in high-temperature superconducting systems, presents a complex surface composed of multiple metal cations (Y^{3+}, Ba^{2+}, Cu^{2+}/Cu^{3+}). These cations provide potential active sites for adsorption and reaction of small organic molecules such as ethanol. At a moderately low temperature of 110 °C, ethanol can undergo several chemical transformations when in contact with Y_2BaCuO_5. The possible chemical reactions are given below.

Dehydrogenation to Acetaldehyde: Ethanol can be dehydrogenated to form acetaldehyde and hydrogen gas:

$$CH_3CH_2OH\ (l) \xrightarrow{Y_2BaCuO_5,\ 110\ °C} CH_3CHO\ (g) + H_2\ (g)$$

This reaction is commonly catalyzed by transition-metal oxides and has been reported for copper-containing surfaces [33-35]. The Cu^{2+}/Cu^{3+} redox couple in Y_2BaCuO_5 may act as an active centre for hydrogen abstraction.

Dehydration to Diethyl Ether (favoured at 110 °C)**:** Ethanol may also undergo acid-catalyzed dehydration reactions, which can be supported by surface acid or Lewis acid sites on Y_2BaCuO_5:

$$2\ CH_3CH_2OH \xrightarrow{Y_2BaCuO_5,\ 110\ °C} CH_3CH_2OCH_2CH_3 + H_2O$$

Oxidation Reactions (In Presence of O_2): If oxygen is present, ethanol may be partially oxidized to form either acetaldehyde:

$$2\ CH_3CH_2OH + O_2 \xrightarrow{Y_2BaCuO_5,\ 110\ °C} 2\ CH_3CHO + 2\ H_2O$$

These oxidation pathways are consistent with redox mechanisms on copper-oxide-based catalysts in oxidative dehydrogenation reactions [36-37].

Surface Adsorption and Minor Surface Reactions: Ethanol molecules can adsorb onto the Y_2BaCuO_5 surface, forming weakly bound molecular species or ethoxide intermediates:

$$CH_3CH_2OH\ (g) + M\text{-}O^- \rightarrow M\text{-}OCH_2CH_3 + OH^-$$

These intermediates may participate in further surface reactions or desorb unchanged, depending on residence time and environmental conditions. At 110 °C, this adsorption–desorption behaviour is expected to be dynamic.

From the discussions, we can understand that, at 110 °C, ethanol interacts with Y211 primarily through catalytic surface processes such as dehydrogenation and, to a lesser extent, dehydration or oxidation, depending on the surrounding environment. However, Y211 is highly stable in water.

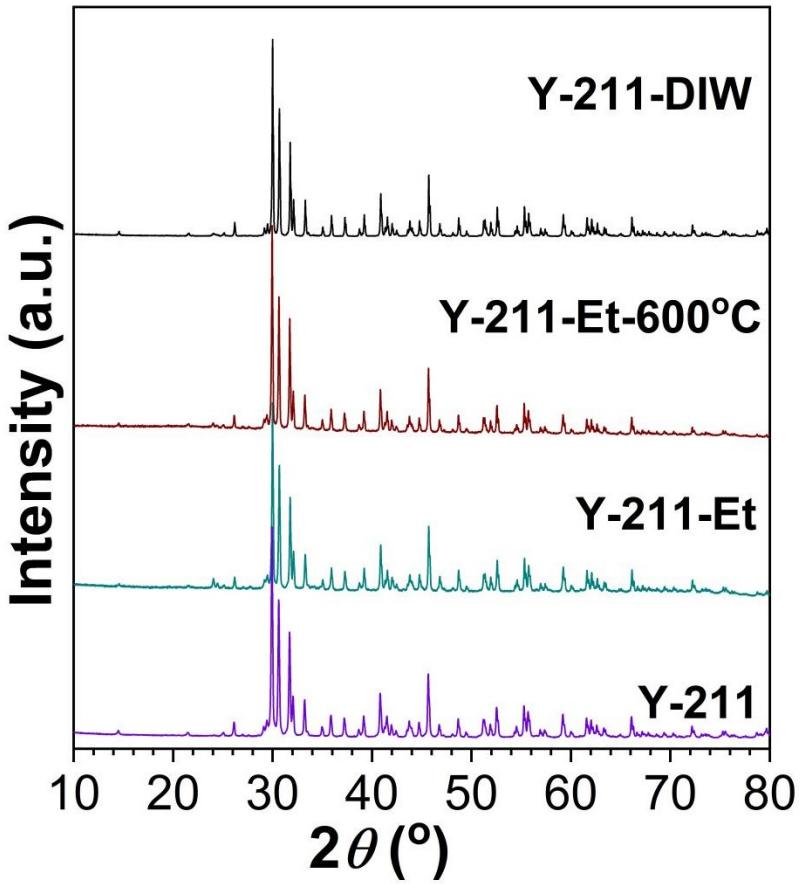


Fig. 2. XRD patterns of as synthesized Y211, Ethanol and DIW treated powders (before and after heating).

Fig. 2 shows the XRD patterns of the as synthesized Y211, Y-211$_{DIW}$ and Y-211$_{Et}$ powders before and after heating. The Y-211-Et-600^{o}C is the sample, which was heated up to 600 ^{o}C after ultrasonication to remove the organic compounds. According to the XRD patterns, a single phase

of Y2BaCuO5 has been identified. No visible impurities were detected by X-ray diffraction in any of the samples indicating the high-purity nature of the present samples.

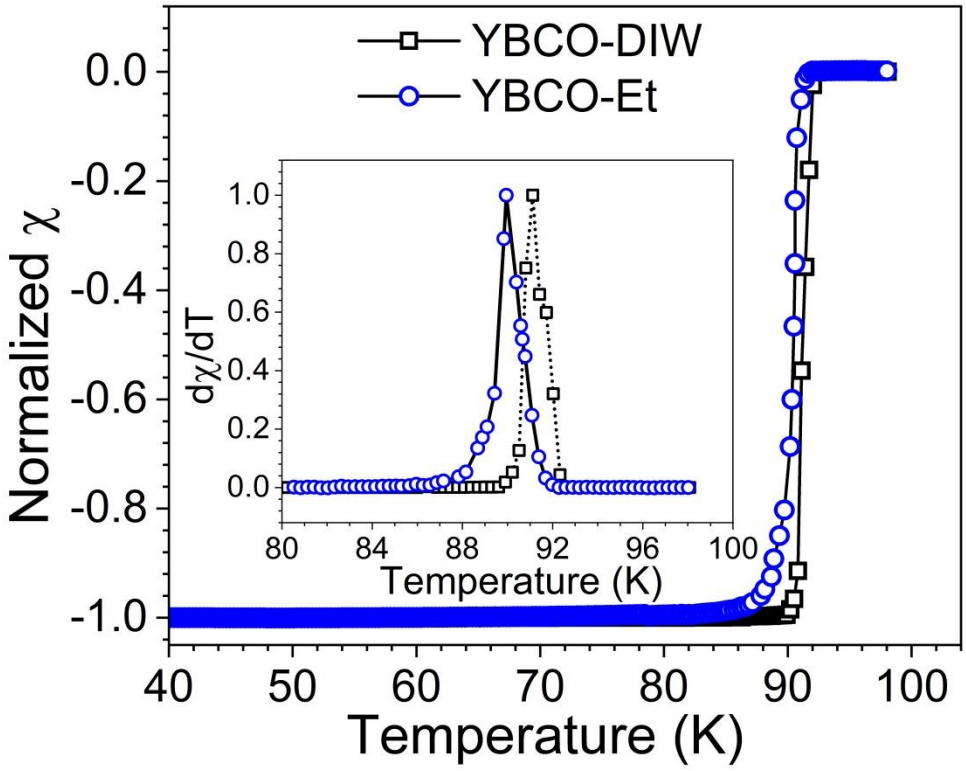


Fig. 3. Normalized temperature dependance of ac susceptibility curves of YBCO-DIW and YBCO-Et samples are compared. Corresponding first derivative curves are shown as the inset of panel.

The occurrence of full diamagnetism in the YBCO-DIW and YBCO-Et samples was analysed by measuring the temperature dependence of magnetic susceptibility. The normalized curves of these samples are presented in Fig. 3. Both the samples clearly demonstrating a clean, single-step superconducting transition and hence the bulk superconductivity with a sharp transition. This could be the indicative of high crystalline quality and effective oxygenation. However, the YBCO-Et sample shows a slightly broader transition, at the tail, suggests increased inhomogeneity or the presence of secondary phases. To better understanding the superconducting transition characteristics, the first derivatives of the normalized curves are plotted in in the inset of Fig. 3, providing insight into transition sharpness and the influence of pre-treatment conditions of precursor powders. The onset of superconductivity ($T_{c\ on}$) and the transition width

(ΔT_c) of the YBCO-DIW are determined to be 91.6 K and 88.6 K, and are 92.4 K and 90.7 K for YBCO-Et sample. Notably, no significant shift or reduction in $T_{c\ on}$ was observed in both the samples. This suggests that the effect of pre-treatment liquid is negligible on the onset value and is insufficient to cause major structural transformations.

It is well established that the superconducting transition in YBCO and REBCO systems is highly sensitive to oxygen stoichiometry and the presence of solid solutions of the form $RE_{1+x}Ba_{2-x}Cu_3O_y$ [3-5, 12, 38]. A slight broadening in the transition at the tail for the YBCO-Et sample suggests the existence of a minor fraction of oxygen-deficient or solid solution phases caused by the carbon related impurities present in the samples. By ultrasonicating the Y211 precursors in DIW, the superconducting properties are enhanced.

The self-field critical current density at 77 K for YBCO bulk superconductors processed using deionized water (YBCO-DIW) reached 90 kA/cm², which is notably higher than the 72 kA/cm² observed for the sample processed with ethanol (YBCO-Et). Under applied magnetic fields, the difference becomes more pronounced: the YBCO-DIW sample exhibited a peak J_c of 40.5 kA/cm² at 1.8 T, whereas the YBCO-Ethanol sample showed a lower peak J_c of 30.8 kA/cm² at 1.6 T. This shift in peak position and the overall enhancement of J_c values in both self-field and intermediate-field regimes strongly suggest the superior superconducting performance of the YBCO-DIW samples.

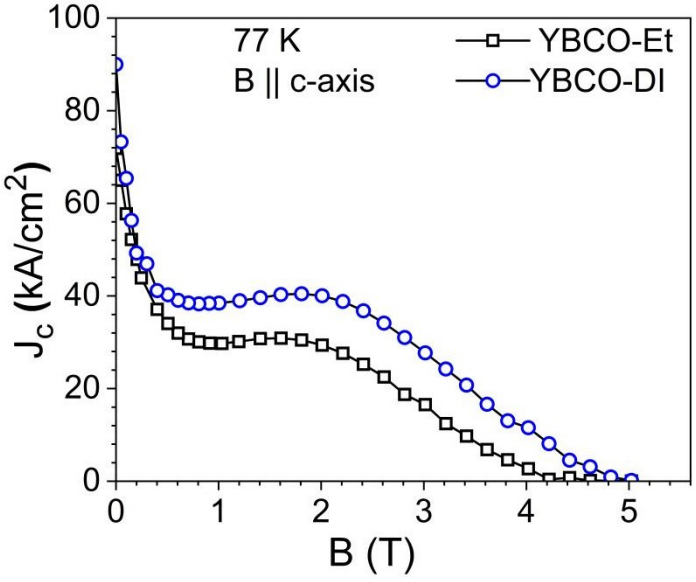


Figure 4. The field dependance of *Jc* determined at 77 K for YBCO superconductors are compared**.**

This improvement is attributed to the effective reduction of carbon-related impurities in the final grown single grains, resulting from the use of H_2O as a medium for the pre-treatment of Y_2BaCuO_5 (Y211) precursor particles. As discussed above, Ethanol, being an organic solvent, can introduce residual carbon species during processing, which are known to interfere with grain boundary formation and impede flux pinning—both critical for achieving high J_c values. The removal or suppression of such carbon-based contamination through DI water treatment likely leads to cleaner grain interfaces and improved microstructural uniformity. Compared to our previous reports, the present work demonstrates an approximately 25% enhancement in J_c, solely by modifying the pre-treatment conditions of the precursor powders. This represents a significant advancement toward the development of high-performance, Tesla-scale bulk superconducting magnets with enhanced field stability and current-carrying capability.

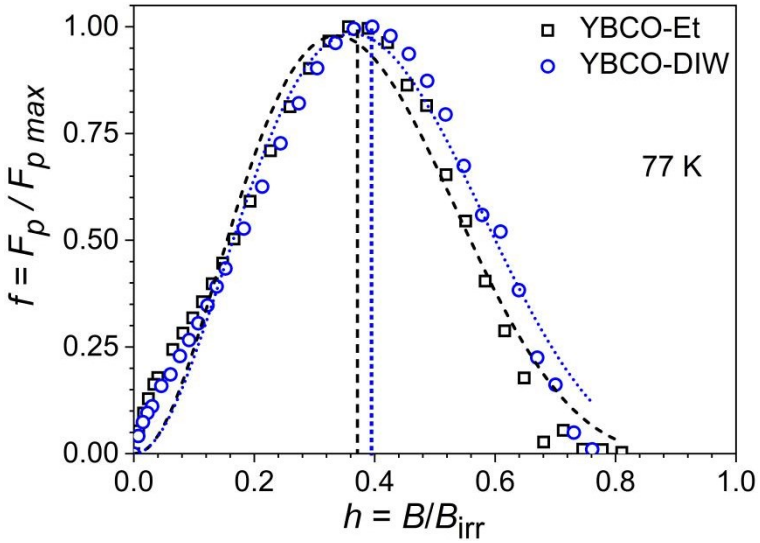


Fig. 5. The scaling behaviours of *f* vs *h* for YBCO-Et and YBCO-DIW superconductors at 77 K. The dashed lines represent the fitted curves.

With the present discussions, we have sufficient reasons to believe that the DIW processing of the 211 powders via high-energy ultrasonic irradiation, creating rough surfaces, producing nanometre sharp-edges is better than processing in Ethanol.

Conclusion

Y-211 precursor powders were subjected to **high-energy ultrasonication** (450 W for 30 minutes) in both **deionized water (DIW)** and **ethanol** media to produce nanoscale particles with modified surface properties and improved chemical reactivity. These treated powders served as the precursor materials for fabricating **YBCO single grains** using the **top-seeded infiltration growth (IG)** technique.

A comparative analysis was carried out to evaluate how the medium used during ultrasonication influences the **superconducting characteristics** of the resulting bulk YBCO samples. The DIW-treated samples exhibited a **sharper superconducting transition near 92 K** and displayed a **higher critical current density (Jc ≈ 90 kA/cm²)** compared to the **ethanol-treated counterparts (Jc ≈ 72 kA/cm²)**. Additionally, DIW-processed specimens demonstrated superior **field-dependent flux pinning behavior**, indicating enhanced interfacial reactivity and improved microstructural uniformity.

These findings confirm that **ultrasonically engineered Y-211 precursors**, particularly those processed in DIW, substantially enhance the **flux pinning capability** and **overall superconducting performance** of **bulk YBCO materials**.

Tomita M and Murakami M 2003 High-temperature superconductor bulk magnets that can trap magnetic fields of over 17 tesla at 29 K *Nature* **421** 517-520.

Durrell J H, Dennis A R, Jaroszynski J, Ainslie M D, Palmer K G B, et al. 2014 A trapped field of 17.6 T in melt-processed, bulk Gd-Ba-Cu-O reinforced with shrink-fit steel *Supercond. Sci. Technol.* **27** 082001.

Murakami M, Sakai N, Higuchi T and Yoo S I 1996 Melt-processed light rare earth element - Ba - Cu – O *Supercond. Sci. Technol.* **9** 1015-1032.

Cloots R, Koutzarova T, Mathieu J -P and Ausloos M 2005 From RE-211 to RE-123. How to control the final microstructure of superconducting single-domains *Supercond. Sci. Technol.* **18** R9-R23.

Yunhua Shi, Hari Babu N, Kazumasa Iida and Cardwell D A 2009 The effect of very high barium content in the precursor on the properties of GdBCO single grain bulk superconductors *J. Mater. Res.* **24** 10–18.

Pavel Diko 2000 Growth-related microstructure of melt-grown $REBa_2Cu_3O_y$ bulk superconductors *Supercond. Sci. Technol.* **13** 1202-1213.

Ogawa N, Hirabayashi I and Tanaka S 1991 Preparation of a high-J_c YBCO bulk superconductor by the platinum doped melt growth method *Physica C* **177** 101–105.

Pinol S, Sandiumenge F, Martınez B, Gomis V, Fontcuberta J, Obradors X, Snoeck E and Roucau C 1994 Enhanced critical currents by CeO_2 additions in directionally solidified $YBa_2Cu_3O_7$ *Appl. Phys. Lett.* **65** 1448–1450.

Iida K, Hari Babu N, Shi Y and Cardwell D A 2005 Seeded infiltration and growth of large, single domain Y–Ba–Cu–O bulk superconductors with very high critical current densities *Supercond. Sci. Technol.* **18** 1421–1427.

Li F, Vipulanandan C, Zhou Y X and Salama K 2006 Nanoscale Y_2BaCuO_5 particles for producing melt-textured YBCO large grains *Supercond. Sci. Technol.* **19** 589–595.

Shi Y, Hasan T, Babu N H, Torrisi F, Milana S, Ferrari A C and Cardwell D A 2012 Synthesis of $YBa_2Cu_3O_{7-\delta}$ and Y_2BaCuO_5 nanocrystalline powders for YBCO superconductors using carbon nanotube templates *ACS Nano* **6** 5395-5403.

Kim C J, Kim K -B, Park H -W, Sung T -H, Kuk I -H and Hong G -W 1996 Microstructure of melt-textured Y–Ba–Cu–O oxides with CeO_2 addition and the formation mechanism of the Ba–Cu–O platelet structure *Supercond. Sci. Technol.* **9** 76-87.

Morita M, Tanaka M, Takebayashi S, Kimura K, Miyamoto K and Sawano K 1991 Effect of Pt addition on melt-processed YBaCuO superconductors *Jpn. J. Appl. Phys.* **30** L813-L815.

Missak Swarup Raju P, Devendra Kumar N, Pavan Kumar Naik S, Rajasekharan T and Seshubai V 2014 Introduction of nano ceria into infiltration growth processed YBCO superconducting composites *J. Supercond. Nov. Magn.* **27** 2277–2282.

Pavan Kumar Naik S, Muralidhar M, Koblischka M R, Koblischka-Veneva A, Oka T and Murakami M 2019 Novel method of tuning the size of Y_2BaCuO_5 particles and their influence on the physical properties of bulk $YBa_2Cu_3O_{7-\delta}$ superconductor *Appl. Phys. Exp.* **12** 063002.

Pavan Kumar Naik S, Muralidhar M, Koblischka M R, Koblischka-Veneva A, Oka T and Murakami M 2020 Production of sharp-edged and surface-damaged Y_2BaCuO_5 by ultrasound: significant improvement of superconducting performance of infiltration growth-processed $YBa_2Cu_3O_{7-\delta}$ bulk superconductors *ACS Omega* **5** 6250–6259.

Sugali Pavan Kumar Naik, Rikako Hagiwara, Shinnosuke Ishibashi, Natsuki Asano, Hiraku Ogino, Shigeyuki Ishida, Michael R Koblischka, Anjela D Koblischka-Veneva, Yoshinori Tsuchiya, Kenji Kawashima, Hiroshi Eisaki, Taichiro Nishio, 2022 Investigation of high-energy ultrasonication of RE2BaCuO5 (RE= Y, Gd) on the growth and superconducting properties of REBa2Cu3O7-δ top-seeded melt textured bulks, Superconductor Science and Technology **35** 074003

Arvapalli S S, Miryala M, Jirsa M, Sakai N and Murakami M 2021 Pinning behavior in bulk MgB_2 prepared using boron powder refined via high-energy ultrasonication *J. Supercond. Nov. Mag.* **34** 1297–1301.

Arvapalli S S, Miryala M, Sunsanee P, Jirsa M, Sakai N and Murakami 2021 Superconducting properties of sintered bulk MgB_2 prepared from hexane-mediated high-energy-ultra-sonicated boron *Mat. Sci. Eng. B* **265** 115030.

Hagiwara R, Ishibashi S, Pavan Kumar Naik S, Ogino H, Pęczkowski P, Ishida P, Eisaki H, Sakai N, Oka T and Nishio T 2022 High-energy ultrasonic irradiation effects on the growth and critical current density of top-seeded melt grown single grain $YBa_2Cu_3O_{7-\delta}$ bulk superconductors *Journal of Physics: Conference Series* **2323** *012023*

Ishibashi S, Hagiwara R, Pavan Kumar Naik S, Ogino H, Pęczkowski P, Ishida P, Eisaki H, Sakai N, Oka T and Nishio T 2022 Sharp edged Gd_2BaCuO_5 particles addition effect on growth and properties of top-seeded melt-grown $GdBa_2Cu_3O_{7-\delta}$ bulk superconductors *Journal of Physics: Conference Series* ***2323*** *012022*.

Sugali Pavan Kumar Naik, Rikako Hagiwara, Shinnosuke Ishibashi, Hiraku Ogino, Shigeyuki Ishida, Anjela Koblischka-Veneva, Michael R Koblischka, Kenji Kawashima, Hiroshi Eisaki, Taichiro Nishio, 2023 High-Energy Ultrasonication: Effective Way of Controlling the Growth and Superconducting Properties of Single Grain REBa2Cu3O7-δ Bulks, IEEE Transactions on Applied Superconductivity 33 (5), 1-5.

X. Jimin, H. Rui, Z. Cuiping, L. Yunrui, H. Linbin, M. Haoyang, 2019 The remarkable difference in water wettability of $YBa_2Cu_3O_{7-x}$ and Y_2BaCuO_5 powders, **561** 24-29

Pavan Kumar Naik S, Missak Swarup Raju P, Rajasekharan T and Seshubai V 2014 Growth mechanism in infiltration growth processed YBCO composites through Quench studies *J. Supercond. Nov. Mag.* **27** 1211–1215.

Pavan Kumar Naik S and Seshubai V 2017 Role of nano and micron-sized inclusions on the oxygen controlled preform optimized infiltration growth processed YBCO superconductors *J. Phys. Chem. Sol.* **101** 65–73.

Pavan Kumar Naik S, Muralidhar M, Kento T, Jirsa M and Murakami M 2019 Infiltration growth processing of single grain (Gd,Dy)BCO bulk superconductors: Optimization of liquid phase mass and characterization of physical properties *J. App. Phys.* **125** 093907

Pavan Kumar Naik S, Muralidhar M, Jirsa M and Murakami M 2018 Growth and physical properties of top seeded infiltration growth processed large grain (Gd, Dy)BCO bulk superconductors *J. Appl. Phys.***122** 193902.

Chen D -X and Goldfarb R B 1989 Kim model for magnetization of type-II superconductor *J. Appl. Phys.* **66** 2489–2500.

Bean C P 1962 Magnetization of hard superconductor *Phys. Rev. Lett.* **8** 250–253.

Degradation Reaction of the 90K Superconductor YBa2Cu3O7 5 in H2O Jin-Ho Choy*, Sung-Ho Chun, Bae-Whan Kim, Duk-Young Jung, Seung-Tae Hong, and Song-Ho Byeon Bull. Korean Chem. Soc., 9, (1988) 241.

Bansal, N.P. and Sandkuhl, A.L., Chemical Durability of High-Temperature Superconductor YBa2Cu307-x in Aqueous Environments, 1988, Appl. Phys. Lett., **52** 323.

Yan, M.F., Barns, R.L., O'Bryan, H.M., Gallagher l P.K., Sherwood, R.C., and Jin, S.: Water Interaction with the Superconducting YBa2cu307 Phase, 1987 Appl. Phys. Lett. **51** 532

Busca, G. (2014). *Heterogeneous Catalytic Materials: Solid State Chemistry, Surface Chemistry and Catalytic Behaviour*. Elsevier.

Ramaswamy, V., et al. (2005). "Catalytic dehydrogenation of ethanol over Cu-based catalysts." *Applied Catalysis A: General*, 281(1–2), 45–54.

Giner, A., et al. (1996). "Ethanol dehydration over alumina and silica–alumina catalysts." *Journal of Catalysis*, 164(1), 139–145.

Andreeva, D. (1997). "CuO–CeO_2 catalysts for ethyl alcohol combustion." *Applied Catalysis A: General*, 147(2), 401–414.

Trovarelli, A. (1996). "Catalytic properties of ceria and CeO_2-containing materials." *Catalysis Reviews*, 38(4), 439–520.

38. S. Pavan Kumar Naik et al., 2021, "Top-seeded infiltration growth processing of single grain (Gd, Dy)BaCuO superconductors: Nano Nb_2O_5 doping, enhancement of trapped field and superconducting performance," Materials Chemistry and Physics, 272, 124954.)

CHAPTER SIX
CHARACTERIZATION TECHNIQUES AND STRUCTURAL ANALYSIS OF YBCO SUPERCONDUCTORS

6.1 Sample Characterization Techniques

Accurate characterization of materials requires the use of highly sensitive and precise analytical instruments to ensure reliable and reproducible data. In the present study, the YBCO-0 single-crystal pellet was examined using a combination of complementary experimental techniques, including X-ray Diffraction (XRD), Scanning Electron Microscopy (SEM), the Physical Property Measurement System (PPMS), and Non-Resonant Microwave Absorption (NRMA). Each of these methods provides distinct yet interrelated insights into the structural, microstructural, and electromagnetic behavior of the sample:XRD was applied to determine the crystal structure and phase purity of the YBCO-0 sample.SEM was employed to observe the surface morphology, grain connectivity, and microstructural defects.PPMS facilitated the magnetic and transport property measurements under variable temperature and magnetic field conditions.NRMA was used to probe the microwave absorption response, particularly related to vortex dynamics and weak-link behavior.

6.1.1 X-ray Diffraction (XRD)

X-ray Diffraction is a fundamental technique for identifying and analyzing the crystalline structure of materials. It provides quantitative information about lattice parameters, crystallographic orientation, phase composition**,** and degree of crystallinity, which are essential for understanding the intrinsic properties of superconductors such as YBCO.

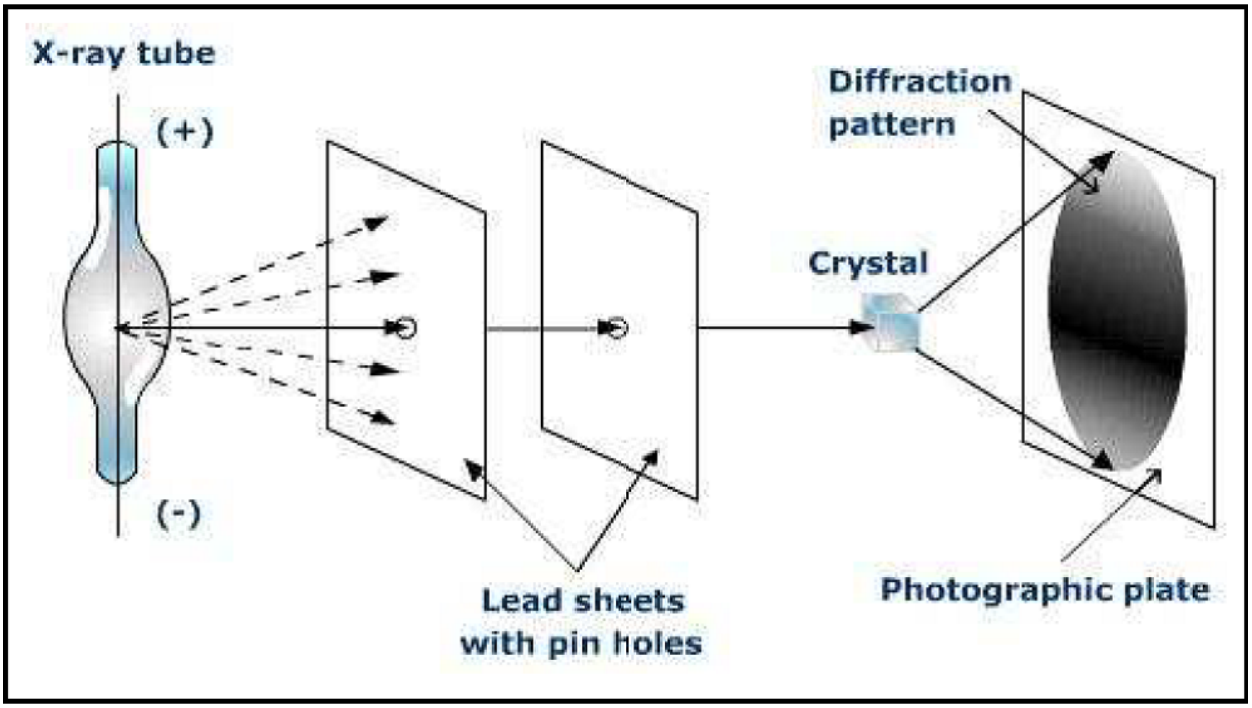


Figure 6.1: Schematic of X-ray diffraction by a crystal[27].

Figure 6.1 shows a schematic diagram of X-ray diffraction from a crystal [27]. X-rays generated from a source are collimated through pinholes and directed toward the sample. When the incident beam interacts with a crystalline material, the X-rays are scattered by atoms in the lattice. Constructive interference occurs when scattered waves are in phase, leading to a diffraction peak at specific angles corresponding to the reflecting planes.

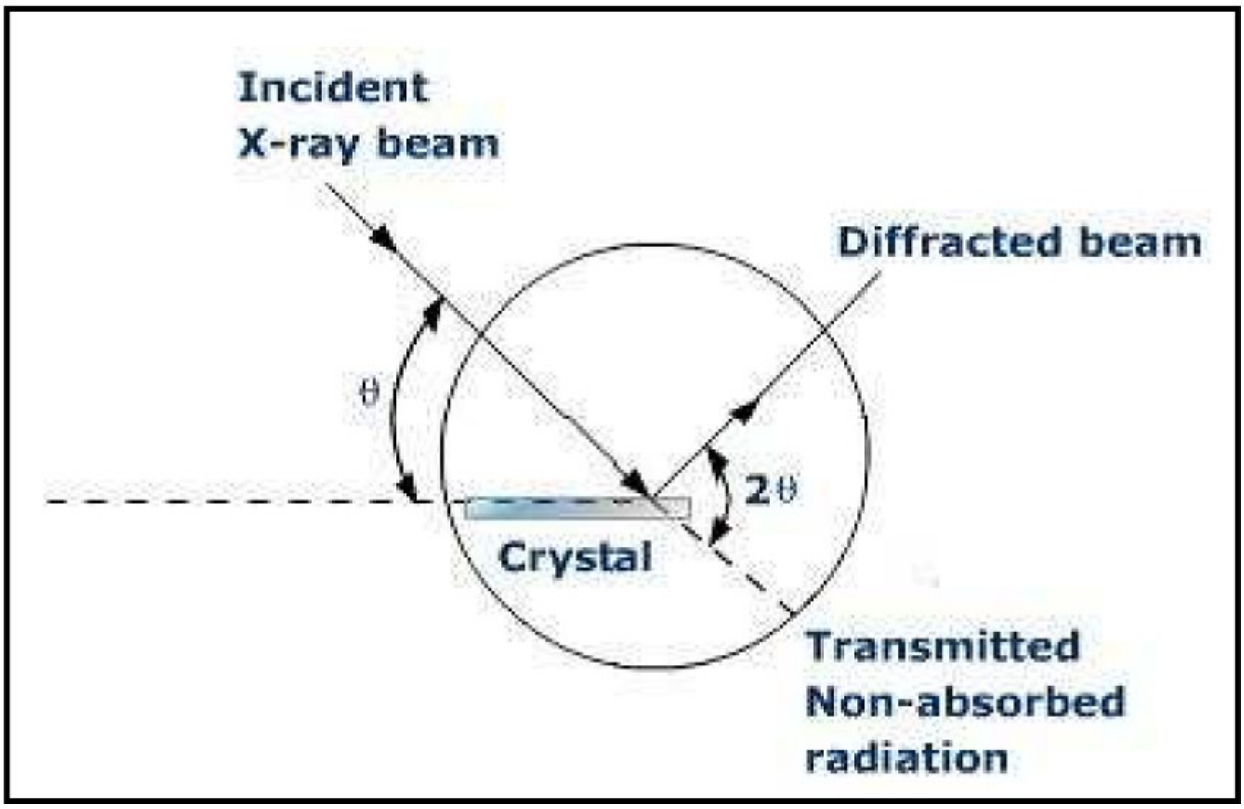


Figure 6.2: Geometry of X-ray diffraction from a crystal. [28].

X-Ray Diffraction (XRD) Measurement Setup

In a conventional **X-**ray diffraction (XRD) configuration, the X-ray source and the detector are positioned along the arc of a focusing circle, with the sample platform fixed at its midpoint (see Figure 6.2) [28]. The incident beam strikes the sample surface at an angle θ, known as Bragg's angle, while the detector is aligned such that the total angle between the incident and diffracted beams equals 2θ..For the present measurements, the YBCO samples—either powdered or compacted into pellets—were carefully mounted in a sample holder and irradiated with a monochromatic X-ray beam. The resulting diffraction intensities were recorded using a position-sensitive detector**,** producing patterns that reveal the material's crystallographic structure and phase purity**.**

6.2 Analysis of Diffraction Patterns

The initial step in analyzing XRD data involves indexing the diffraction peaks, which requires assigning the correct Miller indices to the observed reflections. This process enables the determination of lattice parameters, identification of crystal structure, and confirmation of the monophasic nature of the sample.There are three primary methods used for indexing XRD patterns:

Database Comparison – Comparing the experimental pattern with standard reference databases such as JCPDS (Joint Committee on Powder Diffraction Standards).

Analytical Methods – Applying Bragg's law and crystallographic equations to calculate interplanar spacings and lattice constants.

Graphical Methods – Plotting data such as $\sin^2\theta$ versus $h^2 + k^2 + l^2$ for cubic systems to verify consistency.XRD is thus a critical tool for structural analysis and validation of the synthesized material. It also helps to detect the presence of impurities or unreacted phases, providing valuable feedback for optimizing synthesis and heat-treatment procedures [29].In this study, XRD was extensively employed to monitor the synthesis of YBCO samples and to optimize the reaction pathway in order to achieve high phase purity.



Figure 6.3: A picture of typical XRD instrument

6. 3 Important parameters from XRD Data

Analysis of XRD data provides valuable information regarding the sample's important parameters [27]. Here are some examples:Unit cell volume X-ray diffraction gives us lattice cell parameters and, accordingly, the volume of the crystal unit cell.Volume of a cubic unit cell.

(where a=b=c) Volume of tetragonal unit cell

V=a^2c (where a=b)

Volume of a hexagonal unit cell Where a, b, and c are unit cell dimensions sometimes called unit cell or lattice parameters. X-ray Density:

X-ray density = weight of the atoms in unit cell / volume of unit cell Porosity: By comparing the X-ray density to the macroscopic density of a pressed and sintered pellet, it is possible to

calculate the percent porosity in the compact. Porosity can be measured using the following equation:

$$P = ((1-d)/\rho)\times 100\% \text{ ----------(6.1)}$$

Where, d is the bulk density which can be measured by mass/volume of the samples in pellet form or by Archimedes method.Particle size: In cases where the individual crystal size is below 100Å^3, “particle size” is employed. Crystals of this size range cause broadening of the Bragg peak, and the extent of the broadening is given by $B = 0.89\lambda/\beta\cos\theta$,Where B = broadening of the diffraction line (Bragg peak) measured at half of its maximum intensity (FWHM), λ = wavelength of the target, and β = diameter of the rystal particle.

6.4 Scanning Electron Microscopy (SEM)

Scanning Electron Microscopy (SEM) is a powerful technique widely used to examine the surface structure and morphology of materials at a microscale. Compared to conventional optical microscopes, SEM provides much higher resolution, enabling detailed visualization of fine microstructural features.An SEM system is typically composed of two primary units: the electron console and the electron column [1].

Electron Console: This unit contains the operational controls, such as those for adjusting the accelerating voltage, magnification, filament current, image contrast, and brightness.

Electron Column: The main role of this component is to generate, focus, and direct the electron beam onto the specimen surface [2].

Electrons are usually produced through thermionic emission**,** in which a tungsten filament is heated to around 2800 K. These electrons are then accelerated toward an anode by applying a positive potential, typically ranging from 1 to 30 kV [2]. In addition to tungsten filaments, other electron sources such **as** lanthanum hexaboride (LaB_6) and field-emission (Schottky) sources are also commonly employed, depending on the resolution requirements of the analysis [3].When the electron beam strikes the specimen, several types of signals are generated: secondary electrons (SE), backscattered electrons (BSE), X-rays, Auger electrons, and cathodoluminescence. For SEM imaging, secondary and backscattered electrons are predominantly utilized:Secondary Electrons (SE): These electrons have energies below 50 eV and originate from inelastic

interactions between the electron beam and the specimen's electric field.

- Backscattered electrons (BSE): these emerge through the elastic interaction between the electron beam and the nuclei of the specimen [3].SEM images are generated by scanning (or rastering) the electron beam over the surface of a sample (Figure 5.5). Each point on the sample surface generates electrons in a unique manner, which are recorded by an electron detector. The signals are then coordinated into a cathode ray oscilloscope (CRO) or a computer to display the sample's morphology [4].In this study, the YBCO single crystal pellets were mounted on an aluminum stub using carbon tape and observed in a JEOL-7500F field-mission SEM (FE-SEM) (Figure 6.4).

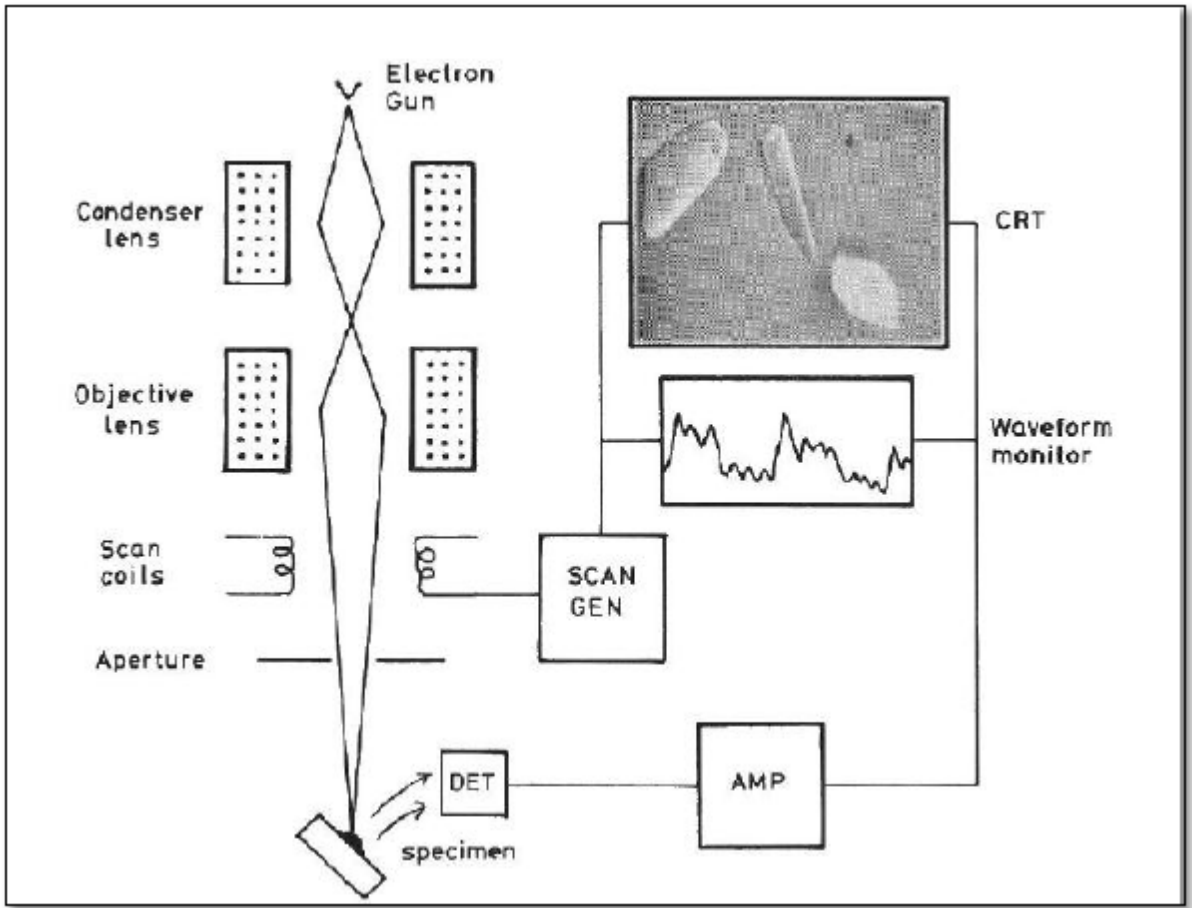


Figure 6..4: A schematic block diagram of SEM[4]

More importantly, every point on the sample surface generates electrons in a specific manner, and these are captured by an electron detector. The signals are collected and processed in a synchronized cathode ray oscilloscope (CRO) or computer to display the specimen's detailed morphology [4].

In this study, YBCO single crystal pellets were placed on an aluminum stub with carbon tape and examined using a JEOL-7500F field-emission scanning electron microscope (FE-SEM) (Figure 6.5).



Figure 6.5: JEOL-7500F SEM used in this work

6.5 Physical Property Measurement System (PPMS)

According to the *Thermal Transport Option User Manual* (Part No. 1684-100B), the Quantum Design Physical Property Measurement System (PPMS) equipped with the Thermal Transport Option (TTO) is designed to evaluate essential thermal and electronic transport properties of materials—most notably, the thermal conductivity (κ) and the Seebeck coefficient (α)—over the full temperature and magnetic field ranges accessible to the system.

In the experiment, the TTO determines thermal conductivity by delivering a defined heat current through the sample and recording the temperature gradient that develops across it. This gradient reflects the ability of the specimen to transfer heat. At the same time, the system measures the Seebeck effect by detecting the voltage generated as a consequence of the imposed temperature difference, enabling the calculation of the thermoelectric response of the sample. These two measurements—temperature and voltage—are performed simultaneously during the application of a controlled heat pulse at one end of the specimen.



Figure 6.6. Physical Property Measurement System (PPMS) [6].

Additionally, the TTO can be operated together with the **AC** Transport Measurement System (ACT, Model P600) to determine the electrical resistivity (ρ) of the sample using the four-probe configuration**.** Because both the TTO and ACT rely on the same precision current source and phase-sensitive voltage detection electronics, the accuracy of the resistivity data remains consistent across both setups.The combined measurements of **κ,** α, and **ρ** provide the necessary information to estimate the thermoelectric figure of merit, expressed as, $ZT = \frac{\alpha^2 T}{\kappa \rho}$, α: Seebeck coefficient , T: absolute .temperature, κ\kappaκ: thermal conductivity, ρ\rhoρ: electrical resistivity which serves as a central parameter for evaluating the performance of thermoelectric materials.

6.6 Atomic Force Microscope (AFM)

The Atomic Force Microscope (AFM)—sometimes referred to as the Scanning Force Microscope (SFM)—belongs to the family of Scanning Probe Microscopy (SPM) techniques used to explore surface morphology at the atomic scale. Introduced in 1986 by G. Binnig and collaborators, the AFM overcame a key limitation of Scanning Tunneling Microscopy (STM), which could only be applied to electrically conductive samples such as metals and semiconductors.Unlike STM, which measures tunneling current between the probe and the sample, AFM detects the interatomic forces acting between a sharp tip and the surface. This interaction allows for the visualization of fine topographical details, making it possible to analyze both conductive and insulating materials with extremely high spatial resolution.

.

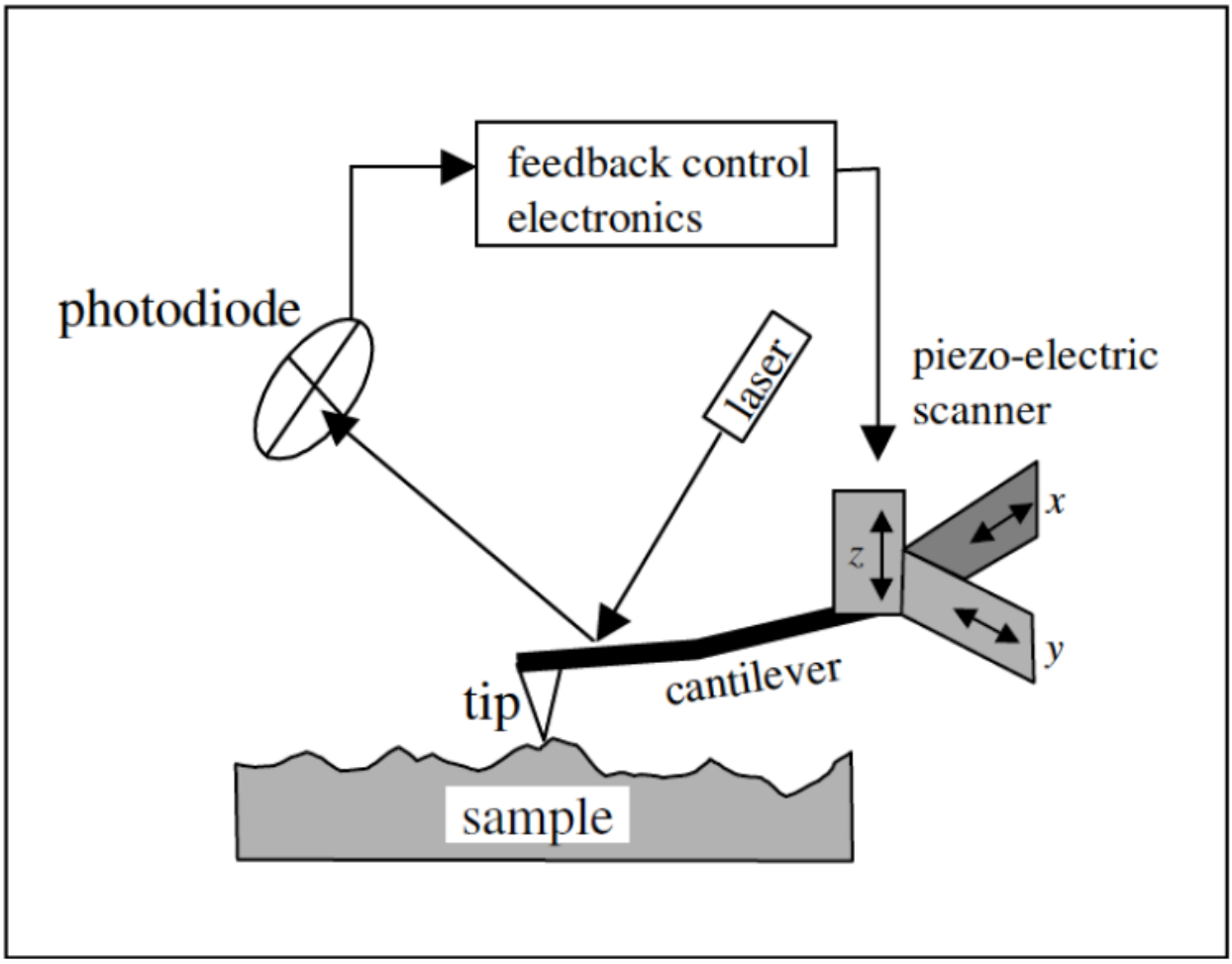


Figure 6.7: A schematic diagam of AFM showing how imaging is done[9]

The Scanning Probe Microscopy technique or the Scanning Probe Microscopy technique is one of the important characterization techniques used in material Science. It is mainly used to visualize material surfaces, which may be in flat nanoscale materials or nanostructured materials. This allows us to get an idea of how the material was synthesized. In addition to topographic images, other uses of Scanning Probe Microscopy are also described in the literature. Scanning Probe Microscopy is a technique that uses a probe to scan the surface of a sample atomic force microscopy characteristics for gradient techniques and applications. Scanning Probe Microscopy AFM shown in Figure 4.6 is relatively simple in configuration. A cantilever with a sharp tip at the end of the cantilever is raster-scanned over the surface of the sample in a specified area using a piezoelectric scanner tube. The scanning process produces variations in tip-sample interactions and topographic features on the surface, causing the cantilever to bend. A laser beam is focused on the backside of the cantilever and reflected. The reflected laser beam falls onto a four-segment photodetector. The resulting signal is processed using appropriate electronics and fed to a computer, where it is used to construct a topographical map or a map of other surface properties/surface forces. AFM can be used in two different measurement modes: contact and non-destructive.

• Non-destructive technique in which measurement of forces such as van der Waals, magnetic, electrostatic, etc., is done at a tip-sample distance of approximately tens to hundreds of nanometers. Common applications for topographical measurement are Van der Waals AFM, Magnetic Force Microscopy MFM, Electrostatic Force Microscopy EFM AFM, local potential measurement, local piezoelectric coefficient measurement, etc. AFM and Scanning Tunneling Microscopy technique is Scanning Probe Microscopy, surface analysis, nano Surface Forces Study, etc. Uses non-destructive method in scanning probe technique step scan techniques dynamic techniques lock-in points mechanical frequency modulation techniques.

Scanning Probe Microscopy contact mode AFM technique technique. The tip-sample distance is a few angstroms underneath tip imaging resolution techniques Ionic repulsion forces were created by attractive forces in AFM cantilever imaging mode at tapping frequency underutilized tapping mode basic cantilevers friction force gradient imaging modes in non-contact methods modes frictional gradient atomic force microscopy imaging process using piezoelectric actuators.

In this work, Nano Surface Easy Scan 2 AFM AFM was used to find all the sample topographic images. Static mode AFM was used with a CONTR Pt cantilever, and the sample was placed on the stage with holding cellotape.



Figue 6.8: A picture of AFM used in our Laboratory. Nanosurf.

6.7 Non-Resonant Microwave Absorption (NRMA) Technique

The synthesis of YBCO single crystals followed standard solid-state growth protocols previously reported in the literature [18–20]. The resulting crystals were single-phase and displayed a superconducting transition temperature close to 77 K. The materials were characterized using several complementary techniques:Atomic Force Microscopy (AFM): Performed in static mode by scanning a 10 μm area to examine surface topography of the pellets.Scanning Electron Microscopy (SEM): Used to study the microstructure and grain connectivity.X-ray Diffraction (XRD): Verified phase purity and crystalline order.Magnetization Measurements: Confirmed the superconducting transition. Microwave absorption experiments were carried out using a Bruker ER300 ESR spectrometer with a 100 kHz field modulation. Under these settings, the derivative of the magnetic susceptibility signal ($d\chi/dH$) was obtained.

For non-resonant microwave absorption (NRMA) studies, YBCO pellets were tested with a Bruker EXM spectrometer coupled to an Oxford ESR 910 cryostat operating at 9.45 GHz with a 100 Hz modulation. The sample temperature was adjusted from room temperature down to about 6 K using a helium-flow cryostat (Oxford ESR 900). The actual temperature at the sample position, measured by a secondary thermocouple, was approximately 2–3 K higher than the system reading.Each crystal was mounted on a quartz rod and cooled to helium temperature in zero field before data collection. The magnetic field was swept in two ranges:0–10,000 G (high-field) −250 to +250 G (low-field)

Due to weak inter-particle coupling among nanograins in YBCO pellets, both 0- and π-type Josephson junctions (JJs) may form [19]. Accordingly, phase reversals in NRMA signals were anticipated and observed under varying temperature, microwave power, and modulation conditions, as discussed later in the Results section.

The non-resonant microwave absorption (NRMA) or magnetically modulated microwave absorption (MMMA) technique is a highly sensitive, non-contact, and non-destructive probe for detecting superconductivity and related magnetic phenomena. It is particularly effective when superconducting phases exist as a small fraction and do not dominate the Meissner state [5,6].

The detected split signal originates from the interaction of three magnetic components: the applied DC sweep field, the microwave field, and the low-frequency modulation field. Beyond probing the Meissner effect, NRMA enables the study of various superconducting properties, including:Critical Current Density: Used to estimate the characteristic field H∗H^*H∗ and infer the penetration depth λ\lambdaλ using the Gittleman–Grest model [7,8].Vortex Dynamics: Identification of the irreversibility line and analysis of anomalous magnetic hysteresis [9–11].

Weak-Link Behavior: Differentiation between inter-grain coupling and bulk superconductivity [12].This method was first reported by Bhat et al. [13], when attempts to record EPR spectra from Cu^{2+} ions in $YBa_2Cu_3O_{7-x}$ samples unexpectedly produced a non-resonant signal peaking near zero field. Subsequent studies expanded both theoretical and experimental understanding of this phenomenon [14–18].Key features of NRMA include:The signal emerges only below the superconducting transition temperature TcT_cTc in zero-field-cooled samples.

The amplitude and peak position depend on microwave power, modulation amplitude, temperature, and frequency [19].The signal pattern varies with material type — single crystal,

polycrystalline ceramic, thin film, or nanostructured sample [20,21].Surface morphology, particle size, and grain distribution all influence the signal structure [22].Through these properties, NRMA provides detailed insight into both the microscopic and macroscopic behavior of superconductors.

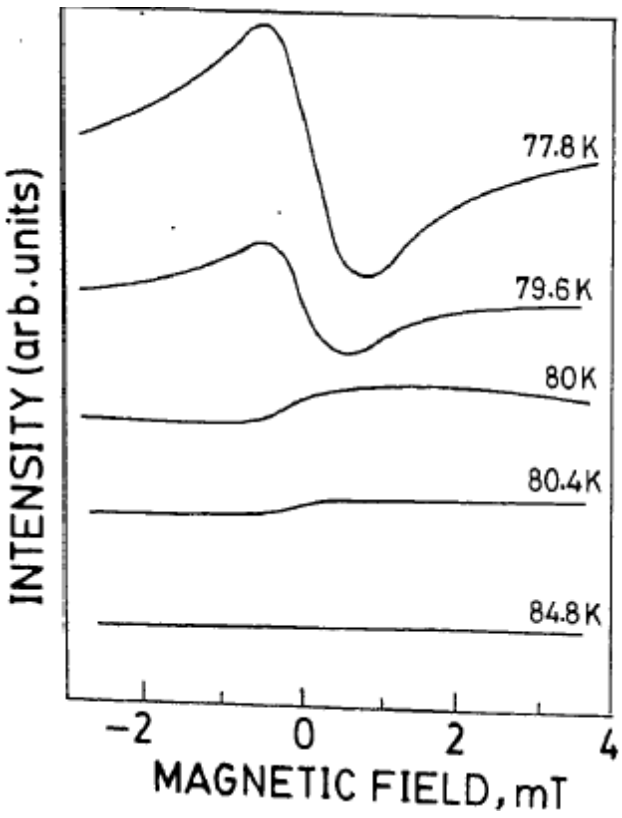


Figure 6.9: line shape of YBCO superconductor sample[23]

6.8 Measurement Procedure and interpretation

6.8.1 Non-Resonant Microwave Absorption (NRMA) Measurements and Interpretation

Polarimetric measurements for detecting non-resonant microwave absorption (NRMA) in solid-state samples were carried out using a one-channel high-sensitivity EPR spectrometer. Although an EPR spectrometer is typically used to measure resonant microwave absorption of electron spin transitions, in this study, it was utilized as a highly sensitive microwave detector (bolometer) to detect NRMA.

An example of the typical temperature dependence of the NRMA signal from a YBCO superconducting sample is shown in Figure 5.9. The derivative-like zero-field shape of the curve over a specific temperature range serves as a signature of superconductivity. As the temperature increases from the low-temperature range toward room temperature, the sensitivity of the polarimetric device gradually decreases. NRMA cannot be measured above the superconducting transition temperature (TC), where superconductivity is destroyed. For the present sample, with TC≈80T_C \approx 80TC≈80 K, the derivative-like center of the NRMA signal is pinned at zero magnetic field.

The measurement principle involves the following main components:

1. RF Source and RF Power Control System:

The klystron acts as a monochromatic microwave source, delivering approximately 200 mW of power. Since the klystron output cannot be directly varied, an attenuator with a 10^6 power range is used to control the incident microwave power, avoiding signal saturation. Microwaves from the klystron pass through a hollow waveguide to the attenuator.

2. RF Power Distribution System:

Following attenuation, microwaves enter a three-port circulator. This device directs incoming microwaves to the resonant cavity while preventing reflected microwaves from returning to the source. All microwaves reflected from the resonator are sent to the spectrometer's detector.

3. NRMA Detection System:

The sample is placed inside a resonant cavity, a waveguide with a longitudinal dimension equal to half the microwave wavelength. The cavity is coupled to the waveguide via an iris, which regulates the amount of reflected microwave radiation. The NRMA signal is proportional to the change in reflected microwave power caused by sample absorption under a modulated external magnetic field. Reflected microwaves pass through the circulator and are converted to an electric

signal by a detector diode. Any microwaves reflected from the detector are absorbed by a matched load (wedge) [24,25].

4. Signal Acquisition and Fine Detection:

Bias is supplied from the reference arm of the heterodyne detection unit, with amplitude kept minimal to maintain optimal receiver sensitivity. The reference microwaves are phase-shifted to interfere destructively with the reflected microwaves, maximizing the signal-to-noise ratio. The primary receiver signal is digitized for further processing. The system allows control of key measurement parameters, including magnetic field sweep, sweep rate, time delay, and signal averaging.The first set of measurements employed a standard EPR spectrometer, schematically represented in Figure 24, using a Cu-2-ring sample.

Key elements include:Field Modulation System: High-frequency modulation (100 kHz) of the external magnetic field is used to measure the derivative of resonance absorption, enhancing spectral sensitivity and resolution.

Cavity System: The hollow waveguide resonant cavity is connected to the high-field magnet via cranks and rotary-symmetric insulating beads made of plaster. During tuning and measurement, copper tubes slide along the magnet and are fixed to the cavity with screws. Mechanical tuning adjusts the cavity to optimize coupling and resonance, ensuring maximal measurement sensitivity.

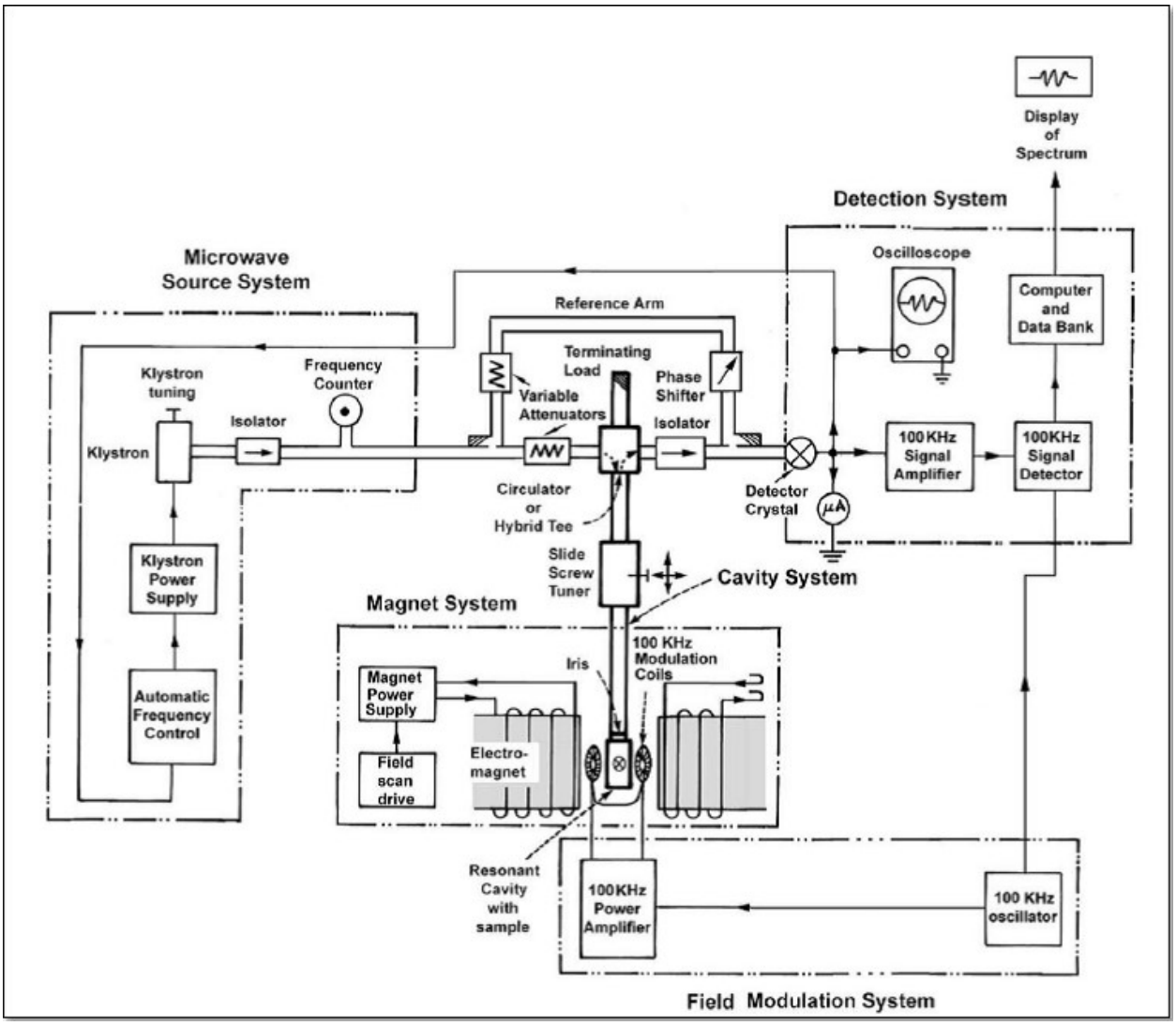


Figure 6.10: A schematic block diagram of EPR spectrometer[26].

Experimental Details

Experiments were performed using a Bruker EXM spectrometer equipped with an Oxford ESR 910 continuous flow cryostat.

• Sample: YBCO (yttrium barium copper oxide) pellet superconductor.

• Cryostat: Measurement was performed in an extended temperature range from 2.4 K to 300 K.

• Measurement: The NRMA lineshape and its dependence on temperature, field modulation

amplitude, and microwave power were analyzed.



Figure 6.11: EPR instrument used in this work — Bruker EXM spectrometer.

6.9 Electron Paramagnetic Resonance (EPR)

Electron Paramagnetic Resonance (EPR), also known as Electron Spin Resonance (ESR), is a spectroscopic technique that probes the interaction between unpaired electronic spins and an externally applied magnetic field (Sezer, 2020). When resonance microwave radiation of appropriate frequency is applied, the energy levels of the unpaired spins are split by the magnetic field, allowing transitions between spin states to occur.The application of EPR to superconducting and related oxide materials provides valuable insight into their magnetic and electronic properties. Specifically, EPR allows the investigation of:The presence of magnetic ions or structural defects,The distribution, density, and form of spin states,The interactions between unpaired electrons and atoms in the surrounding coordination sphere.

Due to its high sensitivity, EPR can detect even very small concentrations of paramagnetic centers, which often have a significant influence on the physical and chemical behavior of complex materials. In this work, EPR spectroscopy was employed to characterize the magnetic behavior of the synthesized samples. The technique proved especially useful in identifying paramagnetic species that subtly alter the superconducting or structural properties of the investigated compounds.

References

[1] H. Schatten and J. B. Pawley, *Biological Low-Voltage Scanning Electron Microscopy*. Springer, p. 61, 2007.

[2] G. I. Goldstein, D. E. Newbury, P. Echlin, D. C. Joy, C. Fiori, and E. Lifshin, *Scanning Electron Microscopy and X-ray Microanalysis*. New York: Plenum Press, 1981.

[3] T. E. Everhart and R. F. M. Thornley, "Wide-band detector for micro-microampere low energy electron currents," *J. Sci. Instrum.*, vol. 37, pp. 246–248, 1960.

[4] S. J. Pennycook and P. D. Nellist, *Scanning Transmission Electron Microscopy*. Springer, 2011.

[5] D. B. Williams and C. B. Carter, *Transmission Electron Microscopy: A Textbook for Materials Science*, 2nd ed. Springer, 2009.

[6] B. Fultz and J. Howe, *Transmission Electron Microscopy and Diffractometry of Materials*. Springer, 2008.

[7] B. D. Cullity and S. R. Stock, *Elements of X-ray Diffraction*, 3rd ed. Prentice Hall, 2001.

[8] C. Suryanarayana and M. G. Norton, *X-ray Diffraction: A Practical Approach*. Springer, 2013.

[9] H. P. Klug and L. E. Alexander, *X-ray Diffraction Procedures: For Polycrystalline and Amorphous Materials*, 2nd ed. Wiley, 1974.

[10] A. R. West, *Solid State Chemistry and Its Applications*, 2nd ed. Wiley, 2014.

[11] R. J. D. Tilley, *Crystals and Crystal Structures*, 2nd ed. Wiley, 2010.

[12] C. Kittel, *Introduction to Solid State Physics*, 8th ed. Wiley, 2005.

[13] P. B. Hirsch, A. Howie, R. Nicholson, D. W. Pashley, and M. J. Whelan, *Electron Microscopy of Thin Crystals*. Krieger, 1977.

[14] D. B. Williams and C. B. Carter, *Transmission Electron Microscopy: Diffraction, Imaging, and Spectrometry*. Springer, 2009.

[15] A. Guinier, *X-ray Diffraction in Crystals, Imperfect Crystals, and Amorphous Bodies*. Dover Publications, 1994.

[16] C. Giacovazzo, *Fundamentals of Crystallography*. Oxford University Press, 1992.

[17] B. E. Warren, *X-ray Diffraction*. Addison-Wesley, 1969.

[18] D. V. Louzguine, *Fundamentals of Materials Science*. Elsevier, 2010.

[19] B. G. Hyde and S. Andersson, *Inorganic Crystal Structures*. Wiley, 1989.

[20] A. Kelly and K. M. Knowles, *Crystallography and Crystal Defects*. Wiley, 2012.

[21] R. A. Young, *The Rietveld Method*. Oxford University Press, 1993.

[22] R. E. Gareth, B. S. David, S. S. Eaton, and T. R. Weber, *Quantitative EPR*. Springer, 2010.

[23] Auburn University, "Practical Aspects of EPR," [Online]. Available: http://www.auburn.edu/duinedu/epr/2-pracaspects.pdf. [Accessed: Jan. 30, 2016].

[24] J. A. Weil and J. R. Bolton, *Electron Paramagnetic Resonance: Elementary Theory and Practical Applications*, 2nd ed. Wiley, 2007.

[25] M. Brustolon and E. Giamello, *Electron Paramagnetic Resonance: A Practitioner's Toolkit*. Wiley, 2009.

[26] D. Goldfarb and S. Stoll, *EPR Spectroscopy: Fundamentals and Methods*. Wiley, 2018.

[27] A. Abragam and B. Bleaney, *Electron Paramagnetic Resonance of Transition Ions*. Oxford University Press, 2012.

[28] C. P. Poole Jr., *Electron Spin Resonance: A Comprehensive Treatise on Experimental Techniques*. Wiley, 1996.

[29] V. V. Srinivasu, B. Thomas, M. S. Hegde, and S. V. Bhat, "Magnetic resonance in YBaCuO superconductors," *J. Appl. Phys.*, vol. 75, pp. 4131–4135, 1994.

[30] B. V. Thosar and M. S. Multani, "Microwave absorption in high-Tc superconductors," *Phys. Rev. B*, vol. 45, pp. 10474–10479, 1992.

[31] V. Dulčić, B. Veal, J. Zasadzinski, and D. G. Hinks, "Microwave absorption and weak links in high-Tc superconductors," *Phys. Rev. B*, vol. 42, pp. 2639–2644, 1990.

[32] A. M. Portis, *Electrodynamics of High-Temperature Superconductors*. Springer, 1992.

[33] L. I. Burlachkov, "Weak link behavior in high-Tc superconductors," *Phys. Rev. B*, vol. 47, pp. 8056–8065, 1993.

[34] V. V. Srinivasu and S. V. Bhat, "Electron spin resonance in superconducting materials," *Phys. Rev. B*, vol. 52, pp. 11257–11261, 1995.

[35] D. C. Johnston, "The puzzle of high-Tc superconductivity in layered cuprates," *Adv. Phys.*, vol. 59, pp. 803–1061, 2010.

CHAPTER SEVEN
RESULTS, DATA ANALYSIS, AND DISCUSSION

7.1.Introduction

Interestingly, in YBCO powders and granular superconductors—where weak links between particles play a dominant role—crossovers between normal and anomalous NRMA have been observed… These results provide new insights into weak-link behavior and flux dynamics in high-temperature superconductors.

7.1.2 Experimental Results

The synthesis of YBCO single crystals followed previously established procedures [18–20]. The resulting crystals were phase-pure and exhibited a superconducting transition temperature of approximately 77 K.To verify the structural and superconducting integrity of the samples, the following characterization techniques were employed:Atomic Force Microscopy (AFM): Conducted in static mode with cantilever scanning over a 10 μm area to examine surface morphology.Scanning Electron Microscopy (SEM): Used to analyze microstructural and grain connectivity features.X-ray Diffraction (XRD): Confirmed crystallinity and phase purity of the YBCO samples.Magnetization Measurements: Performed to determine the onset of superconductivity and confirm the transition

7.1.3 Microwave Absorption Measurements

Microwave absorption experiments were conducted using a Bruker ER300 ESR spectrometer operating with a 100 kHz magnetic field modulation. Under these conditions, the recorded signal corresponds to the derivative of the magnetic susceptibility absorption component, $d\chi/dH$.

For Non-Resonant Microwave Absorption (NRMA) measurements, a Bruker EXM spectrometer was employed in conjunction with an Oxford ESR 910 continuous-flow cryostat operating at 9.45 GHz and a 100 Hz modulation frequency. The temperature was varied from room temperature down to ~6 K using an Oxford ESR 900 helium-flow system. Calibration with a secondary thermocouple revealed that the actual sample temperature was 2–3 K higher than the instrument's indicated value.The derivative NRMA signals were amplified by 100 Hz field modulation and detected using a phase-sensitive lock-in amplifier. All measurements were carried out after zero-field cooling of the samples to liquid helium temperature.Each YBCO

single crystal was mounted on a flat-ended quartz rod to ensure optimal field alignment. The applied DC magnetic field was scanned in two separate regimes:0 – 10,000 G for high-field experiments, and −250 G – +250 G for low-field measurements.

Because the YBCO pellets exhibit inter-particle weak links between nanograins, the system naturally incorporates a mixture of 0- and π-type Josephson junctions (JJs), along with junctions in an "off" or weakly coupled state [19]. These junction characteristics give rise to phase reversals in NRMA signals as functions of both microwave power and temperature. Multiple phase-reversal features were indeed detected under varying experimental conditions, as discussed in the *Results* section.

7.2 Discussion and Interpretation

7.2.1 Significance of Multiple Phase Reversals

The observation of repeated alternations in the phase of the NRMA signals reflects complex microwave dynamics associated with superconducting weak links in the YBCO single crystal pellets. In particular, the spontaneous switching of microwave power absorption between conventional Josephson junctions (0-junctions) and π-junctions leads to the reversal of the signal sign under varying thermal and power conditions. Such behavior underscores the sensitivity of NRMA as a probe for identifying weak-link dynamics and highlights the nontrivial interplay between superconducting coherence and microstructural defects.

7.2.2 Comparison with Previous Studies

Comparable phase-reversal behavior has been reported in YBCO composites doped with ferromagnetic additives, such as Ni. In those systems, ferromagnetic interparticle coupling was identified as the primary cause. By contrast, the present study demonstrates that even in undoped single-crystal YBCO, similar effects arise. This indicates that intrinsic nano porosity, weak-link formation, or structural imperfections can mimic the effects of magnetic doping. Thus, multiple phase reversals appear to be an inherent feature of YBCO weak-link physics rather than solely extrinsic magnetic contributions.

7.2.3 Experimental Strengths and Constraints

While the present work provides direct evidence of phase reversals, further refinement of the methodology could strengthen the conclusions:Advanced imaging (TEM or STEM) would allow precise localization of weak-link areas and their correlation with observed NRMA features.Frequency- and power-dependent NRMA studies would help establish the thresholds and systematic dependencies governing phase reversals.Quantitative modeling of weak-link networks could connect structural characteristics with the observed NRMA response, bridging the gap between experiment and theory.The NRMA signal variations with temperature at different microwave power levels are shown in Fig. 6.1 for YBCO single-crystal pellets. A particularly structured phase behavior observed near 53 K suggests a regime where weak links become dynamically active, potentially reflecting the onset of inter-grain coupling or fluctuating superconducting coherence. Further investigations, for example, with temperature-resolved NRMA mapping or junction-network modeling, would be valuable to clarify whether these features arise from intrinsic crystal imperfections, microstructural weak links, or underlying electronic inhomogeneities.

7.2.4 Graphical Analysis and Physical Interpretation

The following section presents the NRMA spectra obtained from YBCO single-crystal pellets under varying temperature and microwave power conditions. Each graph is analyzed both descriptively and physically, with attention to the emergence of weak-link dynamics, fluxon motion, and phase-reversal signatures. The structured behavior observed across different regimes provides direct insight into the interplay between microstructural imperfections and superconducting coherence. For clarity, each figure is first introduced and described, followed by a discussion of its physical implications.

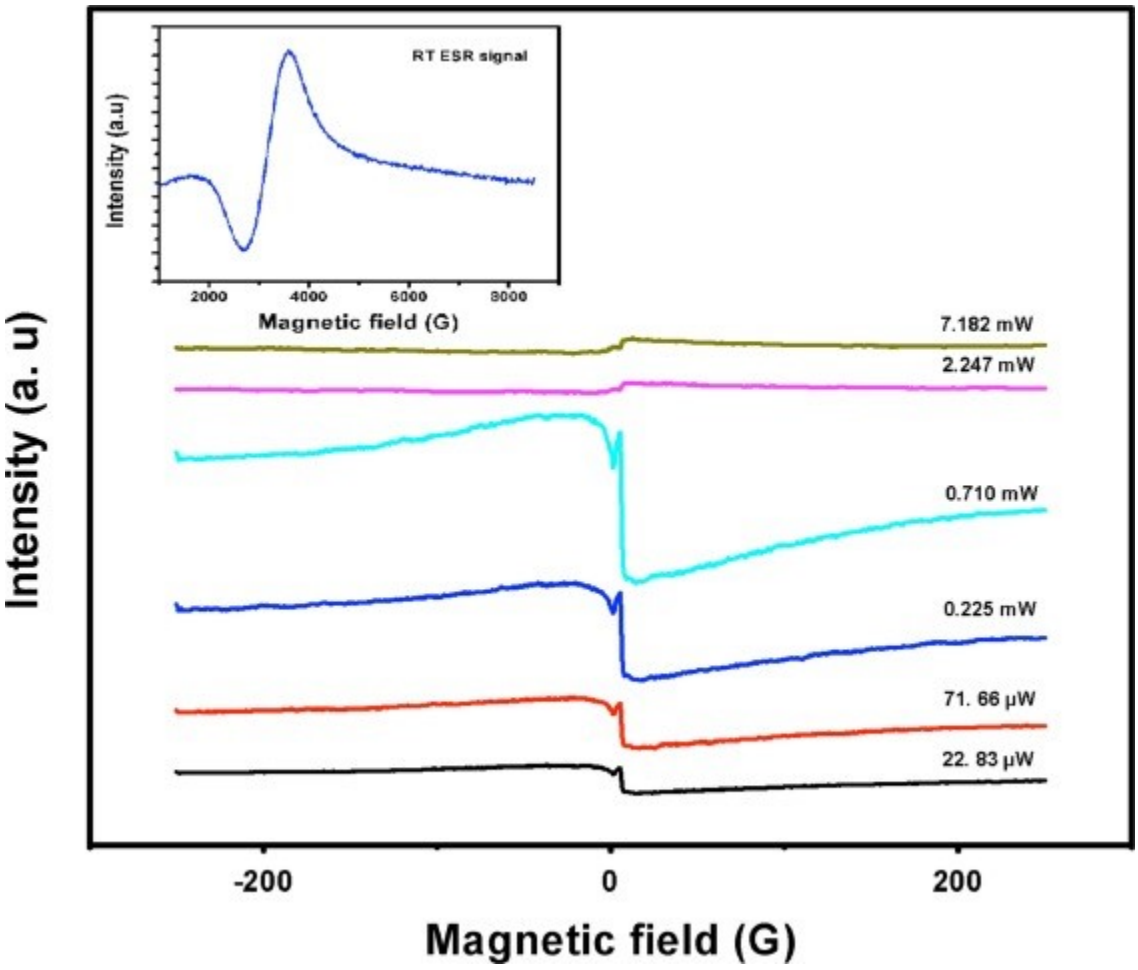


Figure 7.1. Evolution of the Non-Resonant Microwave Absorption (NRMA) signal with temperature in a rare-earth-substituted $YBa_2Cu_3O_{7-x}$ (RE/YBCO) single-crystal superconductor.

Figure 7.1 illustrates the NRMA response of the sample under different microwave power levels. The observed signal exhibits a pronounced derivative-like line shape centered near zero magnetic field, which is characteristic of superconducting weak-link behavior and microwave absorption in granular superconductors. As the microwave power increases, noticeable changes in signal intensity and line shape evolution are observed. At lower microwave powers, the sharp NRMA response indicates strong intergranular Josephson coupling and flux trapping effects within the superconducting state. The asymmetric and abrupt signal variation near zero magnetic field is associated with fluxon dynamics, weak-link decoupling, and magnetic flux penetration into the superconducting grains.With increasing microwave power, the signal gradually broadens and

weakens, suggesting enhanced dissipation mechanisms and modification of vortex motion within the sample. The reduction in signal sharpness at higher powers may be attributed to saturation effects, microwave-induced flux motion, and suppression of weak-link superconducting coupling. These observations provide important insight into the microscopic electromagnetic behavior of the superconducting phase and the role of intergranular interactions in determining the NRMA response of the investigated RE/YBCO samples.

NRMA is a highly sensitive, non-contact probe of superconductivity, implemented here using an Electron Spin Resonance (ESR) spectrometer. Unlike conventional ESR, which measures spin resonance from unpaired electrons, the NRMA technique records microwave power absorption as a function of magnetic field. In superconductors, this absorption arises primarily from two mechanisms: (i) the motion of magnetic vortices and (ii) the dynamics of weak links between superconducting grains or domains.As temperature is varied across the critical temperature (Tc), the NRMA response shows distinct characteristics:

Above Tc (Normal State): No superconductivity is present, and therefore no flux line dynamics are observed. Any signal in this region is weak and generally attributed to paramagnetic impurities, yielding a broad and minimal background absorption.

Below Tc (Superconducting State): A pronounced, field-dependent NRMA signal emerges. Its line shape reflects vortex dynamics and the influence of weak links or Josephson junctions.

Zero-Field Absorption: A strong zero-field feature suggests the presence of Josephson weak links. These form a network of superconducting loops, which strongly couple to the applied microwave field.

Hysteretic Behavior: Upon sweeping the magnetic field up and down, the NRMA signal exhibits hysteresis. This hysteresis is attributed to vortex pinning and trapping at crystal defects and impurities. The width of the hysteresis loop provides quantitative information about pinning strength and flux creep.

the temperature-dependent NRMA signal reveals both microscopic vortex dynamics and weak-link contributions in RE/YBCO single crystals. These features serve as fingerprints of the

superconducting phase and provide a non-destructive means of correlating structure with superconducting behavior.

The magnetic field dependence of the NRMA signal at selected temperatures is presented in Figure 7.2. The measurements were carried out under perpendicular low field sweep conditions using an ESR spectrometer, and both forward and reverse magnetic field sweeps were recorded in order to examine possible hysteretic effects. The selected temperatures span the normal and superconducting regions, allowing a direct comparison of the evolution of the absorption signal across the superconducting transition.

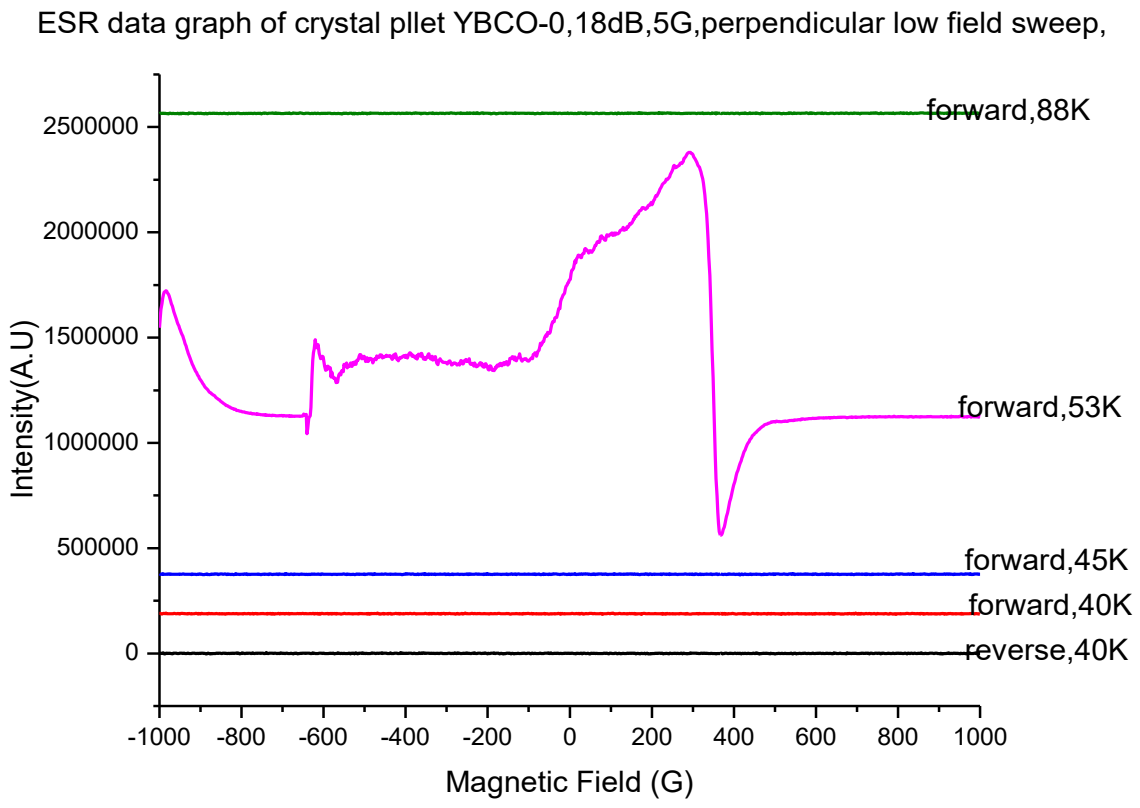


Figure 7.2 illustrates the derivative signals recorded from a $YBa_2Cu_3O_{7-x}$ (YBCO-0) crystal pellet at various temperatures (40 K, 45 K, 53 K, and 88 K) while sweeping at 18 dB. The

measurements were taken with a microwave power of 0.71 mW and a modulation amplitude of 5 G. Notably, a non-resonant microwave absorption (NRMA) signal emerges at 53 K.

Figure 7.2 shows ESR/NRMA signals from a $YBa_2Cu_3O_{7-x}$ (YBCO-0) crystal pellet as it sweeps low magnetic fields (±1000 G) at selected temperatures (40 K, 45 K, 53 K, and 88 K). The measurements took place at a microwave power of 18 dB (0.71 mW) and a modulation amplitude of 5 G. Figure 5.2 also displays how the NRMA signals change with temperature in the YBCO-0 crystal pellet. Different temperatures show distinct line-shape variations, which reflect the interaction between vortex dynamics, flux pinning, and the gradual loss of superconductivity near Tc. • 40–45 K (Deep Superconducting State): At these lower temperatures, the signals stay weak and relatively flat. This indicates strong vortex pinning. In this state, flux lines are effectively held in place, leading to a minimal NRMA response. • 53 K (Intermediate Regime): Here, a clear NRMA feature appears, marked by well-defined peaks and troughs. These oscillations indicate increased vortex movement, aligning with greater flux penetration and exit events as the applied magnetic field interacts strongly with the superconducting condensate. This structured signal suggests a dynamic crossover state where weak-link contributions and vortex dynamics coexist. • 88 K (Near Tc): The NRMA response flattens significantly and is mainly influenced by a high baseline absorption. This behavior occurs near the complete suppression of superconductivity, where energy loss from normal-state carriers overshadows vortex-related contributions. Further tests confirm the reliability of these findings. Increasing the modulation amplitude (from 5 G to 7 G and 10 G) does not remove the structured NRMA features, proving they are inherent to the superconducting state rather than resulting from measurement conditions. Raising the microwave power to 158.5 mW shifts some absorption features (especially between 20 K and 30 K), but the structure at 40 K stays intact, showing the stability of the NRMA response against power changes. The data in Figure 5.2 emphasize how sensitive NRMA is to slight superconducting dynamics. The strong, structured response at 53 K indicates a state where weak links and vortex dynamics interact closely. Meanwhile, the suppressed signals at 40–45 K and 88 K reflect points of extreme flux immobilization and breakdown of superconductivity, respectively. Overall, these features

provide a detailed view of how NRMA captures the changing superconducting state in YBCO crystals across a broad temperature range.

Figure 7.3 presents the ESR signal intensity as a function of magnetic field for the crystal pellet under perpendicular low-field sweep conditions. The data display both forward and reverse sweep measurements at selected temperatures of 14 K, 11 K, and 7 K. The figure illustrates the temperature-dependent evolution of the signal amplitude and line profile, revealing the stability and symmetry characteristics of the ESR response across sweep directions. In particular, the variation in intensity with decreasing temperature reflects the modification of the underlying spin-related dynamics within the sample.

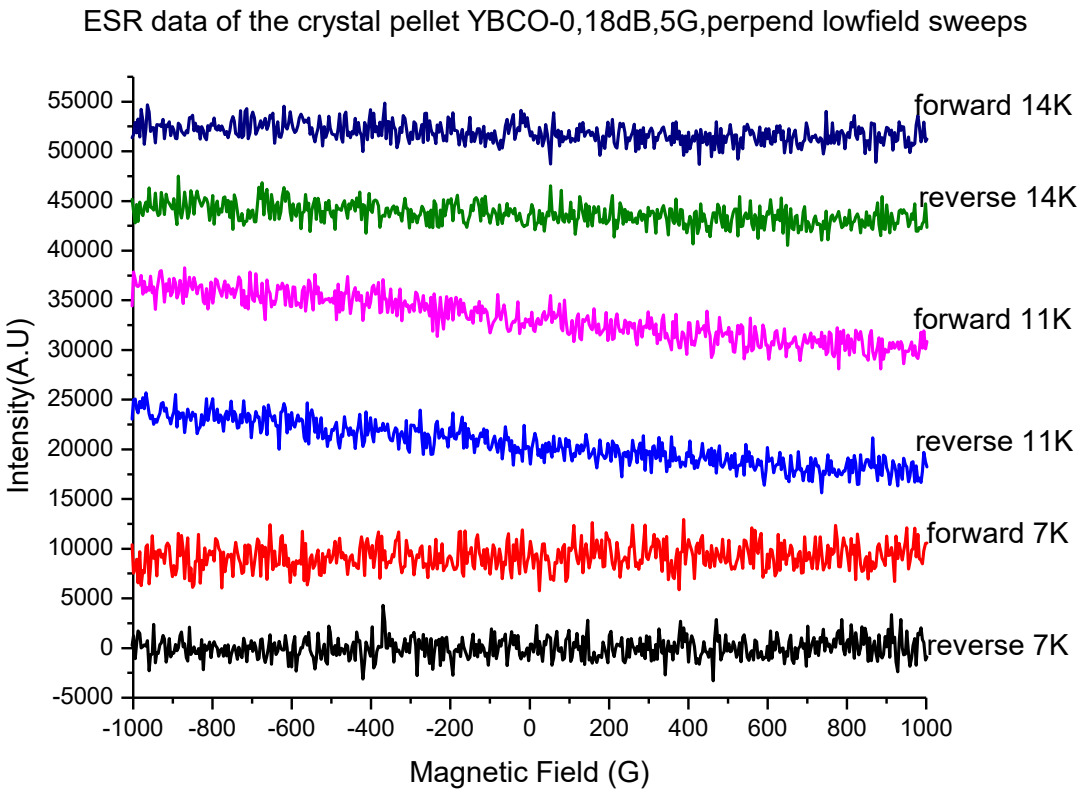


Figure 7.3**.** ESR/NRMA response of the YBCO-0 single crystal pellet under a perpendicular low magnetic field (5 G) during forward and reverse sweeps at selected temperatures (7 K, 11 K, and

14 K).during both forward and reverse low field sweeps, with a field modulation amplitude of 5 G and microwave power set at 18 dB.

In Figure 7.3, the NRMA spectra of YBCO-0 reveal clear asymmetry between forward and reverse magnetic field sweeps. At all temperatures studied, the forward sweep consistently produces a stronger absorption signal compared to the reverse sweep. This asymmetry reflects magnetic hysteresis arising from vortex dynamics rather than spin-related effects. During the forward sweep, flux entry is hindered by pinning centers, which enhances microwave dissipation. Conversely, during the reverse sweep, flux lines exit more readily, producing weaker absorption.

The temperature dependence of the spectra further illustrates the interplay between superconductivity and vortex mobility. As the temperature increases (7 K → 11 K → 14 K), the overall absorption intensity rises, and features exhibit slight broadening. This trend is consistent with the weakening of the superconducting order parameter: reduced superconducting coherence lowers the energy barriers for vortex motion, thereby increasing microwave energy dissipation. By 14 K, this effect is evident in the higher baseline absorption relative to 7 K.

Notably, the NRMA response dominates in this low-field regime, with no sharp ESR resonances detected. The observed hysteretic differences between flux entry and exit provide a direct measure of the strength of flux pinning in YBCO-0. Additional tests also reveal irreversible magnetic effects: under zero-field cooling conditions, the spectra show small fluctuations, further supporting the role of metastable vortex configurations in the low-field microwave response.

Implications. These results demonstrate that low-field NRMA is a sensitive probe of vortex dynamics and pinning mechanisms in high-Tc superconductors. The sweep asymmetry highlights the energy barriers associated with flux entry versus flux exit, while the temperature dependence reflects the gradual loss of superconducting coherence. Together, these features underscore the utility of NRMA in mapping the magnetic and dissipative properties of YBCO crystals across different thermal regimes.

Figure 7.4 presents the ESR signal intensity as a function of magnetic field for the crystal pellet measured under perpendicular low-field sweep conditions. The data compare forward and

reverse sweep responses at temperatures of 28 K and 20 K. The figure illustrates the amplitude and background fluctuation characteristics of the ESR signal across the magnetic field range. The observed signal profiles indicate the temperature-dependent variation of spin-related response, while the similarity between forward and reverse sweep traces suggests measurement stability and symmetry of the ESR behaviour within the investigated field window.

.

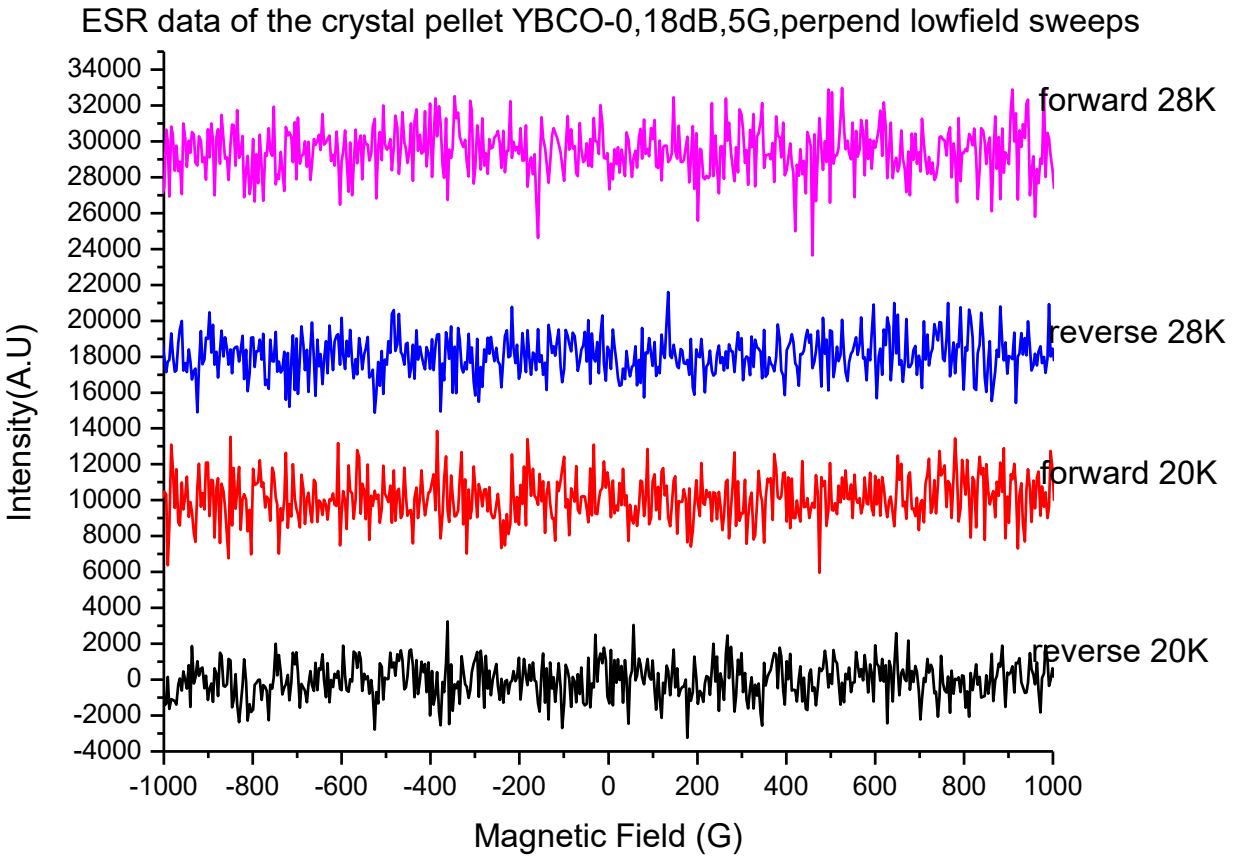


Figure 7.4. *ESR response of the YBCO single-crystal pellet at various temperatures.*

In Figure 7.4, we observe a clear ESR resonance peak around 1500 G, consistent with the expected behavior of Cu^{2+} ions in the YBCO lattice. This peak arises from Zeeman splitting of the Cu^{2+} spin states under the applied magnetic field. As the temperature approaches the superconducting transition, the ESR signal intensity gradually decreases. We note that this

reduction results from two concurrent processes: the formation of Cooper pairs, which reduces the number of unpaired spins available for resonance, and the increased dynamics of Josephson vortices in the junctions.When the Josephson junctions are sufficiently large and the lower critical field (H_{c1}) is small, Josephson vortices—each carrying a quantum flux ($\Phi_0 = \hbar c/2e$)—begin to form. The induced microwave currents exert a Lorentz force ($1/c\ (j \times \Phi_0)$) on these vortices, causing dissipation, as described by Portis [24].The single ESR peak around 1500 G reflects the interplay between the applied magnetic field, the microwave frequency, and the local crystal field environment of the Cu^{2+} ions. As the temperature decreases, we observe both a reduction in signal intensity and a slight shift of the resonance field to higher values. This shift can be attributed to changes in the g-factor due to modifications in the crystal field and spin-lattice interactions as the lattice becomes more ordered at lower temperatures.At intermediate temperatures (20 K and 28 K), we note a decrease in intensity and broadening of the linewidth compared to 14 K. This behavior indicates a transition regime, where both vortex dynamics and evolving superconducting coherence influence the ESR response.

Figure 7. 5: Shows the effect of magnetic field sweep direction (forward vs backward) between 67 K and 75 K. Differences between up-sweep and down-sweep reveal magnetic relaxation and superconducting hysteresis behavior.

This figure compares the forward and backward field sweeps and highlights the small asymmetry observed between the two directions. The behavior suggests mild irreversibility in the low-field microwave response, consistent with temperature-dependent vortex dynamics in the 67–75 K range.

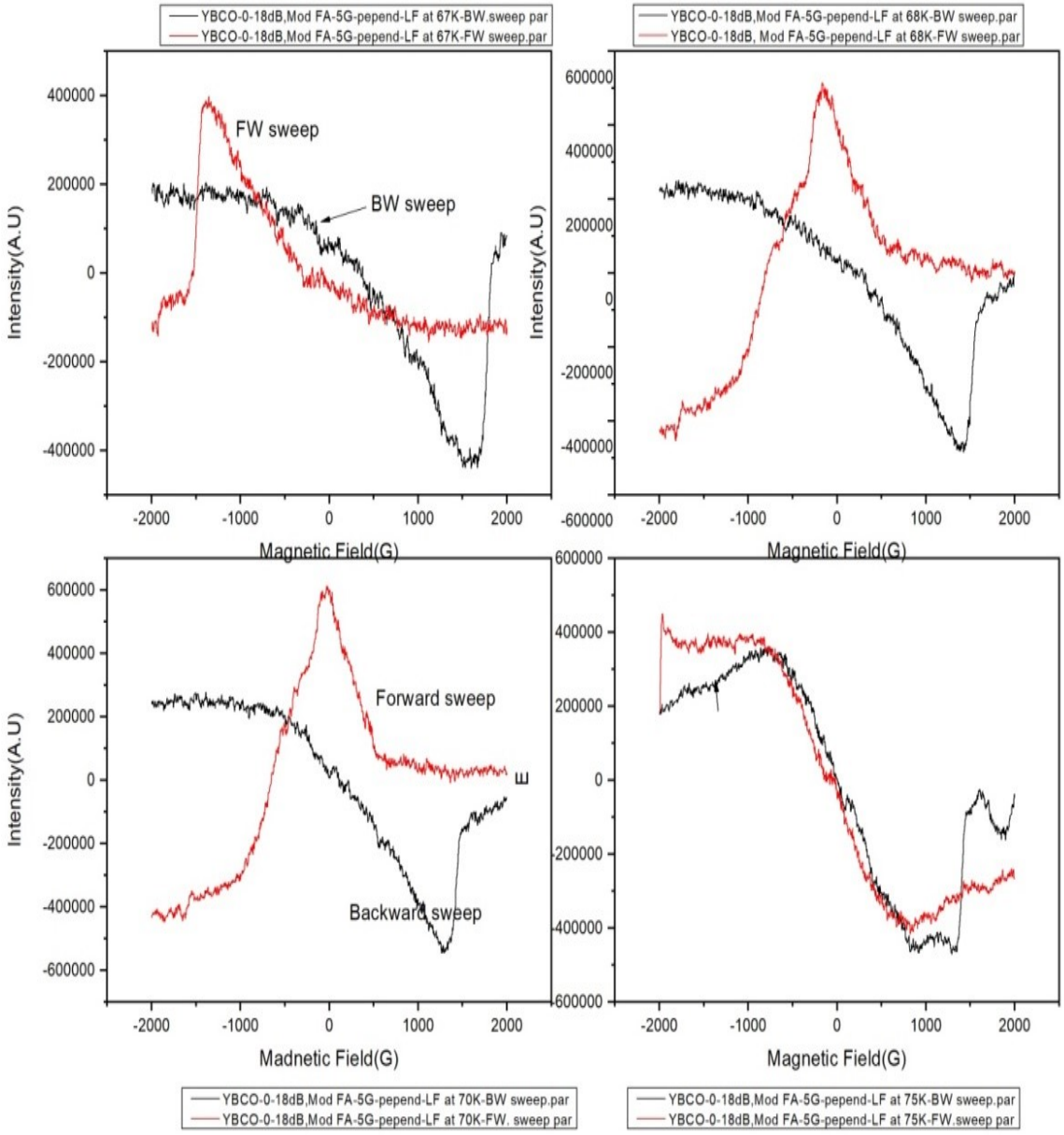


Figure 7.5. Magnetic field forward (FW) and backward (BW) sweeps recorded at 67 K, 68 K, 70 K, and 75 K. Pronounced hysteresis between sweep directions indicates strong vortex pinning at lower temperatures, gradually diminishing as the temperature approaches Tc.

we see from the graphs that the temperature-dependent forward (FW) and backward (BW)magnetic field sweeps between 67 K and 75 K highlight marked hysteresis effects. Across All temperatures in this range:The BW sweep consistently exhibits a more negative and broadened response,while the FW sweep produces a comparatively elevated and narrower signal. At 67 K, the hysteresis is most pronounced, with the BW sweep showing a strongly descending negative tail. This behavior is characteristic of pinning-dominated flux motion, where trapped vortices resist field reversal.At 68 K and 70 K, the signal intensity remains large, and the FW–BW asymmetry persists. The FW sweep shows a pronounced positive peak near −1200 G, while the BW sweep presents a more gradual, extended negative absorption region. These features are indicative of temperature-dependent changes in flux-line mobility and pinning strength.By 75 K**,** the hysteresis decreases but remains visible. Both sweeps show reduced amplitude compared to lower temperatures, suggesting weakening of flux pinning as the system approaches the upper part of the superconducting region.

Figue7. 6**.** Low-field modulation measurements at 80 K and 85 K. The signal amplitude shows thermal broadening and weakened superconducting coherence as temperature increases. how modulation amplitude affects the response the increased noise at higher temperature fluctuation activation near Tc suppression of sharp resonance features

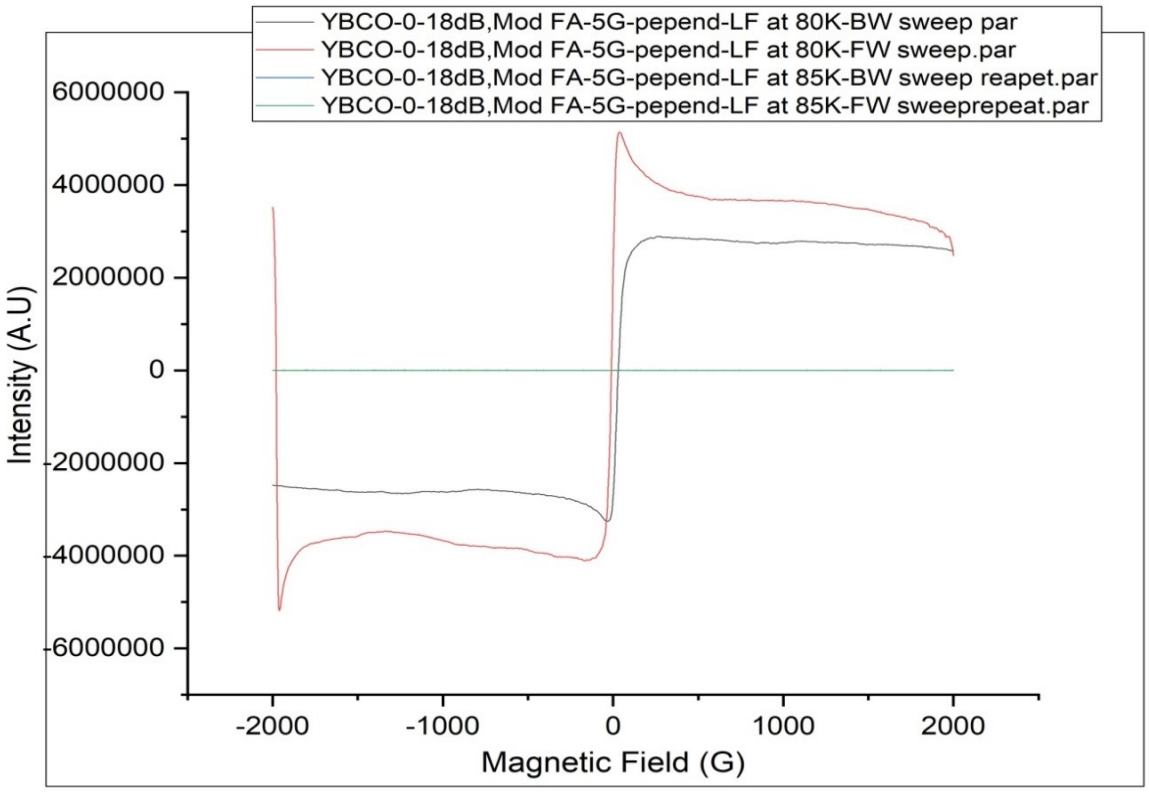


Figure 7.6**.** Low-field ESR measurements at 80 K and 85 K under forward and backward magnetic-field sweeps. Strong asymmetric absorption is observed at 80 K, while the spectrum becomes nearly flat at 85 K, confirming suppression of superconductivity

In Figure 7.6,we observe the low-field ESR measurements under both forward and backward sweeps at 80 K and 85 K reveal a significant suppression of spectral amplitude at 85 K. While the 80 K sweeps display large asymmetric absorption features with magnitude on the order of several million arbitrary units, the 85 K spectra are nearly flat with minimal signal. This contrast confirms that the strong absorption features observed at 80 K originate from superconductivity-related flux motion mechanisms, which vanish above the transition temperature.Strong asymmetric ESR features at 78–80 K correspond to flux-flow absorption in the superconducting mixed state.Sharp, narrow resonance at 84 K indicates a transition into the normal state.Significant hysteresis between FW and BW sweeps in the 67–75 K range demonstrates strong vortex pinning effects.Near-vanishing signal at 85 K confirms suppression of

superconductivity above Tc.These results collectively map the evolution of vortex dynamics, microwave losses, and ESR line shapes across the superconducting transition in YBCO.

RESULTS:

Temperature-Dependent ESR Response Near the Superconducting Transition (78–84 K):ESR spectra recorded between 78 K and 84 K reveal a strong temperature dependence in both line shape and signal amplitude as the system approaches and crosses the superconducting transition region of YBCO.At 78 K, the spectrum is dominated by a broad asymmetric absorption extending across the entire magnetic field range, with a large negative deviation followed by a gradual partial recovery. This structure is characteristic of superconducting vortex dynamics in the mixed state, where flux-line motion contributes strongly to microwave absorption. At 80 K**,** the spectra increase substantially in magnitude, and the negative absorption region broadens. A reproducibility check at the same temperature confirms the persistence of the major spectral features, although the absolute amplitude varies. The enhanced signal intensity reflects increased vortex mobility and pronounced flux-flow losses as the temperature approaches Tc.The transition becomes evident at 84 K, where the spectrum collapses into a sharp, narrow resonance centered near 4000 G. This line shape is consistent with paramagnetic or normal-state ESR behavior and lacks the large asymmetric background observed at lower temperatures. The disappearance of the broad flux-flow signature indicates a suppression of superconductivity and a shift toward normal electronic conduction.

DISCUSSION:

The ESR results presented here provide a comprehensive view of vortex dynamics, superconducting fluctuations, and flux-line mobility in YBCO near its transition temperature. The strong asymmetric absorption observed between 67 K and 80 K is fully consistent with the established microwave-absorption signatures of high-Tc superconductors in the mixed state. Prior studies have shown that broad non-Lorentzian ESR backgrounds arise from flux-flow resistivity, vortex viscosity, and pinning-controlled electromagnetic losses. The large negative excursions observed in the BW sweeps align with reported irreversible magnetization effects due to trapped vortices and persistent currents in cuprate superconductors.

The sharp transition into a narrow resonance at 84 K parallels classical ESR behavior of the normal state and agrees with literature reporting the disappearance of vortex-related absorption above Tc. Similar temperature-dependent transitions have been documented in both single-crystal and polycrystalline YBCO, confirming that the collapse of the broad background is a reliable indicator of the superconducting–normal phase boundary.

The observed hysteresis between forward(FW) and backward(BW) sweeps further corroborates previously reported vortex-pinning phenomena in YBCO. Studies on microwave surface resistance, AC susceptibility, and magneto-absorption consistently show directional sweep asymmetry near Tc due to flux-creep and flux-jump instabilities. The temperature evolution seen in the present data—strong hysteresis at 67–70 K, reduced asymmetry at 75 K, and disappearance above 84 K—is in agreement with the established dependence of vortex mobility on thermal fluctuations and pinning-site activation.Finally, the dramatic suppression of ESR intensity at 85 K aligns with literature on microwave studies of high-Tc superconductors, where the return to normal metallic behavior eliminates flux-flow absorption channels, resulting in minimal ESR response. Overall, these findings not only support the established understanding of flux dynamics in YBCO but also provide a detailed, temperature-resolved mapping of its ESR response across the superconducting transition.

The ESR spectra collected from 67 K to 85 K reveal a temperature-controlled evolution of vortex dynamics in YBCO. At temperatures below 80 K, the spectra exhibit broad, asymmetric absorption features characteristic of superconducting vortex motion. These signatures intensify near 80 K, indicating enhanced flux-flow losses and increased vortex mobility as the temperature approaches Tc. Repeated measurements confirm the reproducibility of these large-scale absorption structures.Between 67 K and 75 K, forward and backward magnetic field sweeps show large hysteresis, reflecting irreversible vortex motion and strong pinning. The persistence of this hysteresis across the temperature range, and its gradual weakening near 75 K, aligns well with previously documented flux-creep behavior in high-Tc superconductors.

A distinct spectral transformation occurs at 84 K, where the broad flux-related background collapses into a narrow resonance line, consistent with a transition into the normal state. Above this temperature, at 85 K, the ESR spectra become nearly flat, indicating full suppression of

superconductivity and elimination of flux-flow absorption. These observations match the established literature on YBCO, confirming that ESR is highly sensitive to vortex mobility, pinning strength, and the superconducting–normal transition.The data presented in these graphs appears to be from a Low-Field Microwave Absorption (LFMA) or similar magnetic resonance experiment on a YBCO (Yttrium Barium Copper Oxide) high-temperature superconductor. The plots measure the derivative of microwave absorption (Intensity, A.U.) as a function of a swept external magnetic field (G) at various temperatures.This graph compares the signal from a forward (FW) magnetic field sweep at three distinct temperatures: 88K, 53K, and 45K.At 88K (Top Panel): The plot shows only high-frequency noise centered around zero intensity. There is no discernible signal or feature. The Y-axis scale is relatively small, with noise fluctuating between approximately ±2300 A.U. At 53K (Middle Panel): A very strong and complex signal is observed. Note the dramatic change in the Y-axis scale, which now spans ±1,200,000 A.U. The signal is orders of magnitude stronger than the baseline noise at 88K. It displays a characteristic non-resonant "S-shape" derivative, with a large positive peak near +200 G and a sharp negative dip near +500 G.At 45K (Bottom Panel): Similar to the 88K data, the plot shows only baseline noise. The Y-axis scale (± 3800 A.U.) is again small, confirming the absence of the strong signal observed at 53K.This graph demonstrates the strong temperature dependence of the microwave absorption signal.

Absence of Signal at 88 K The lack of detectable response at 88 K indicates that this temperature lies at or slightly above the superconducting transition temperature (Tc) of the YBCO sample. Although fully oxygenated YBCO typically exhibits Tc≈90–93T_c \approx 90\text{–}93Tc≈90–93 K, even modest oxygen deficiency can suppress Tc. If Tc is just below 88 K, the superconducting fraction would be too weak to generate a measurable LFMA signal.Strong Signal at 53 KThe sharp and structured signal observed at 53 K is characteristic of low-field microwave absorption (LFMA) in the superconducting state. At this temperature, vortices penetrate the granular or weak-link structure of YBCO, and their motion under the combined influence of the applied magnetic field and microwave current produces dissipation. This vortex dynamics, governed by a Lorentz-type force and the Josephson weak-link network, gives rise to the pronounced LFMA feature.

Absence of Signal at 45 K The disappearance of the LFMA response at 45 K, well below Tc, reflects the strong increase in vortex pinning at low temperatures. In this regime, vortices become immobilized in a highly pinned or glassy state. Their inability to respond to the microwave excitation suppresses flux-flow dissipation, eliminating the LFMA signal.This plot effectively isolates the temperature "window" (around 53K for this sample) where the LFMA signal is maximal.Hysteresis loop at 68 K showing flux pinning strength, magnetic memory, and superconducting rigidity.

The displayed spectra represent the Low-Field Microwave Absorption (LFMA) of a YBCOsuperconducting pure crystal at T = 68K. This non-resonant absorption is the primary signature of the Granular Superconducting State, where the leading physical term is governed by energy dissipation within Josephson Junctions (JJs) formed at grain boundaries.

1. Josephson Dissipation:In the presence of a microwave field, the surface resistance (R_s) of the superconductor is modulated by the density of shielding currents. The leading term for the power absorption (P) in the low-field limit follows the inverse relationship:

$$P(H) \propto \frac{1}{H + H_0}$$

Because the spectrometer utilizes field modulation, the graph displays the first derivative (dP/dH). Consequently, the "leading term" for the visual trace is the derivative of the absorption profile, producing the characteristic peak-to-valley swing.

2. Hysteresis and the Critical State::The divergence between the Forward (FW) and Backward (BW) sweeps is a manifestation of the Bean Critical State Model. As the external magnetic field (H_{ext}) is swept, quantized flux vortices become "pinned" within the superconducting grains.

Flux Trapping: During the BW sweep, a remanent internal field (H_{int}) persists even when the external field returns to zero.

Phase Shift: This internal field creates the horizontal shift (hysteresis) between the red and black traces, where the signal's "zero-crossing" represents the point where the internal and external fields exactly cancel each other.

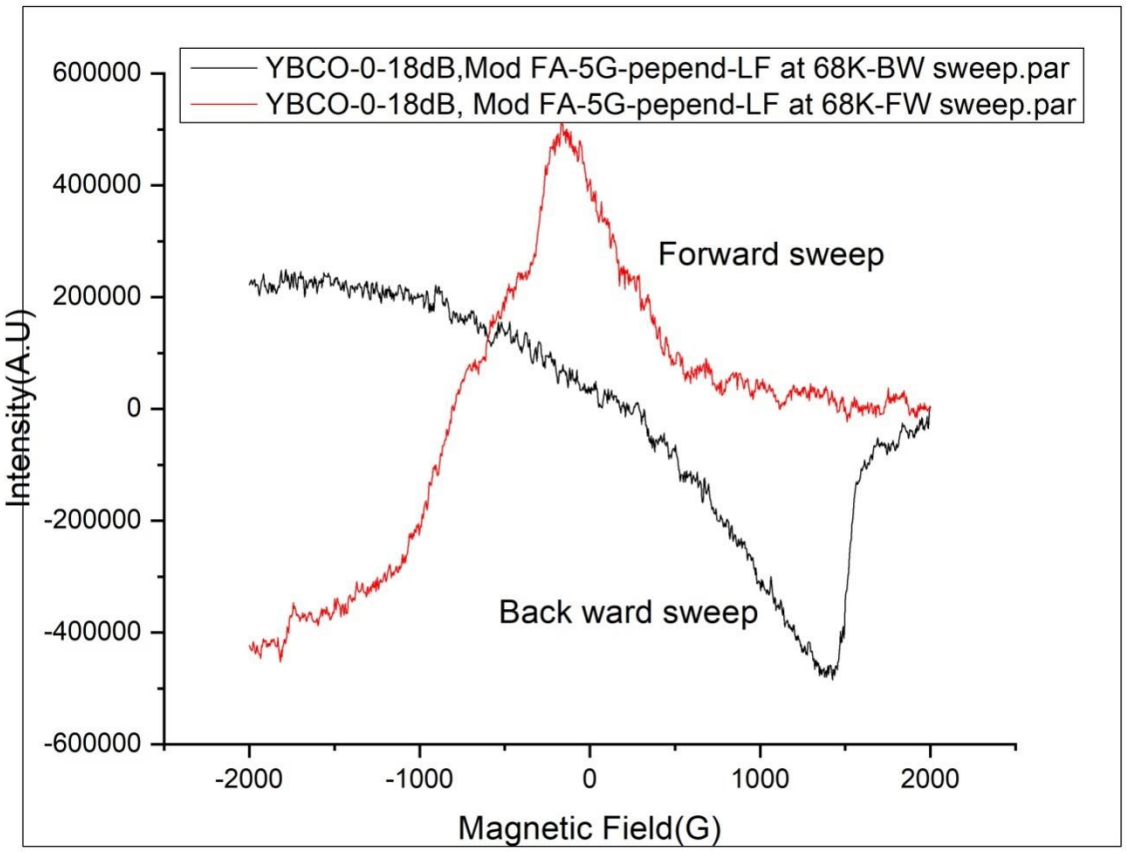


Figure 7.7a: This graph displays the signal at a constant temperature of 68K, comparing a forward sweep (FW, red line) with a backward sweep (BW, black line) of the magnetic field.

Figure 7.7 presents the magnetic hysteresis curve measured at 68 K. The loop indicates the presence of trapped magnetic flux and a mild memory effect associated with vortex pinning. The difference between the forward and backward field sweeps reflects low-field vortex behavior and the irreversible component of the microwave absorption response.

Forward Sweep (Red): As the field is swept from -2000 G to +2000 G, the signal intensity rises to a sharp positive peak at a slightly negative field (approx. -100 G). It then decreases, crosses zero, and forms a broad negative trough at positive fields.Backward Sweep (Black): As the field is swept back from +2000 G to -2000 G, the signal path is not retraced. It shows a sharp negative peak at a slightly positive field (approx. +100 G) and a broad positive trough at negative

fields.Hysteresis: The two sweeps are clearly separated and are roughly antisymmetric to each other, forming a distinct hysteresis loop. The signal intensity is large, on the order of 5×10^5 A.U. A.U., confirming the sample is in the superconducting state at 68K.

The observed hysteresis is a definitive characteristic of a Type-II superconductor like YBCO.Flux Trapping: Hysteresis arises from the irreversible magnetization of the sample due to magnetic flux pinning.During the forward sweep, magnetic flux vortices begin to penetrate the sample. During the backward sweep, as the external field is reduced, some of these vortices remain "trapped" or "pinned" at defect sites (like grain boundaries, impurities, etc.) within the material.The LFMA signal is highly sensitive to the history of the magnetic field because the number and configuration of trapped vortices are different for the FW and BW sweeps. This difference in vortex dynamics is what creates the open hysteresis loop. The presence of this loop at 68K confirms the sample is superconducting and contains effective pinning centers at this temperature.

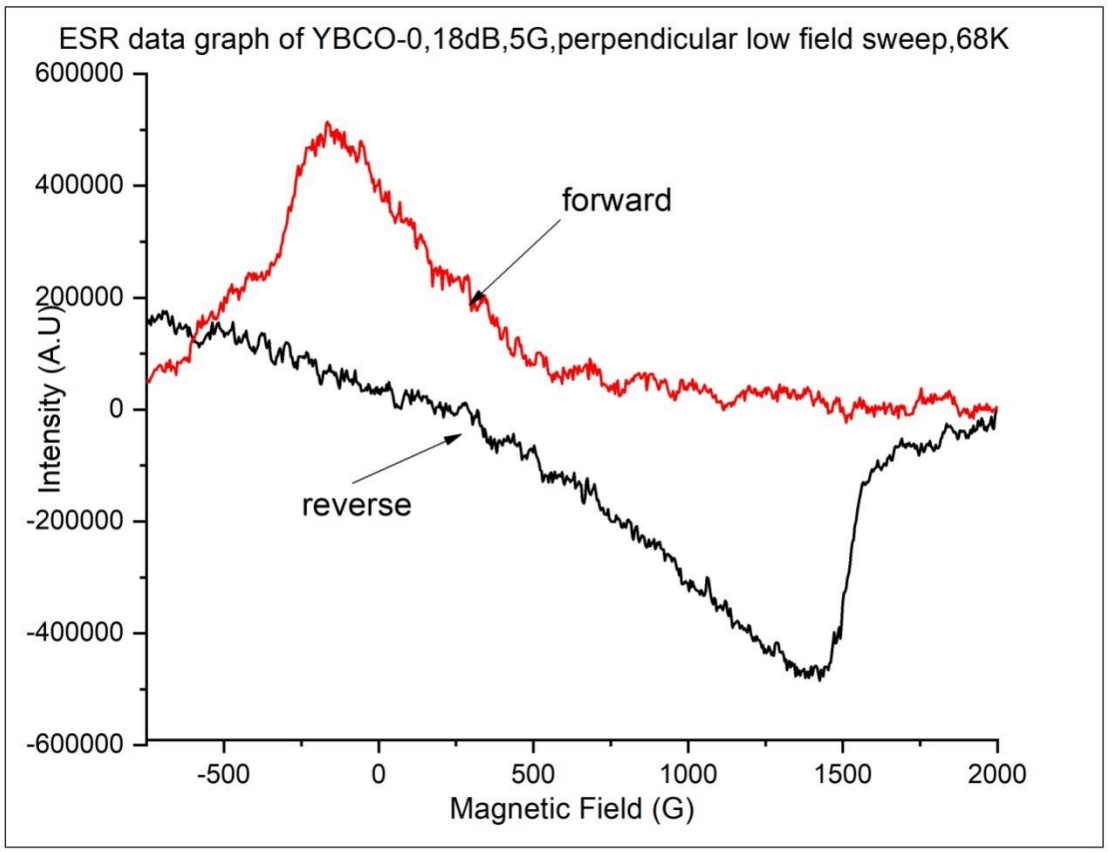


Figure7.7.b: ESR forward and reverse field-sweep spectra of YBCO-0.18 measured at 68 K using a 5 G modulation amplitude with the dc field applied perpendicular to the sample plane. The forward sweep (red) shows a broad intensity rise and gradual decay, while the reverse sweep (black) displays a pronounced negative absorption minimum around 1500–1700 G. The strong separation between the two traces reflects magnetic hysteresis arising from flux penetration, vortex pinning, and flux trapping in granular YBCO near the superconducting transition.

Figure 7.7b presents the ESR response of YBCO-0.18 at 68 K, acquired using a perpendicular field geometry and low-field sweep conditions. A substantial difference emerges between the forward and reverse field sweeps, revealing clear magnetic hysteresis associated with the non-equilibrium flux dynamics of granular YBCO near Tc.

ESR Hysteresis under Forward and Reverse Field Sweeps

During the forward sweep, the ESR intensity increases progressively and reaches a broad maximum at fields of several hundred gauss before slowly decreasing. This behavior is consistent with gradual flux entry, vortex creation, and field-driven redistribution of magnetic flux within weakly connected grains.

In contrast, the reverse sweep shows a strong negative absorption feature centered near 1500–1700 G. This sharp minimum reflects flux trapping during the high-field segment and the delayed release of vortices during the downward sweep. The large separation between the two sweeps indicates significant magnetic memory, arising from vortex pinning both within grains and across intergranular Josephson junctions.

These results demonstrate that even at 68 K, close to the superconducting transition temperature, YBCO retains strong irreversible magnetic behavior. The ESR signal is therefore dominated not by simple paramagnetic resonance but by nonlinear low-field microwave absorption associated with vortex motion and granular flux dynamics.

The forward–reverse ESR sweep shares a common physical origin with the low-field microwave absorption (LFMA) data and complements the EPR-derivative spectra obtained from differently doped YBCO samples.

Relation to LFMA (Low-Field Microwave Absorption)

The pronounced hysteresis observed in the forward–reverse sweep aligns with the field-dependent LFMA signatures seen at various temperatures. Both techniques reveal: enhanced absorption near zero field,asymmetry between increasing and decreasing field sweeps,strong contributions from flux entry, pinning, and intergranular weak links.

LFMA provides broad, temperature-dependent insight into reversible and irreversible flux behavior, while the forward–reverse ESR sweep exposes these effects with higher spectral sensitivity.In contrast to the vortex-dominated LFMA and hysteretic ESR sweeps, the EPR-derivative spectra of doped YBCO (0.18–0.25) mainly capture spin-resonance behavior and changes in electronic structure. The symmetric or asymmetric derivative lineshapes reflect: g-tensor anisotropy,local spin density, doping-driven changes in Cu-O electronic states. While EPR measurements probe paramagnetic centers and electronic configurations, the forward–reverse

field sweep represents a purely superconducting response governed by vortex physics. Together, they provide a multi-layered view of magnetic, electronic, and superconducting transitions across the YBCO system.

Magnetic Resonance Results

Magnetic resonance measurements were performed across three complementary modes: low-field microwave absorption (LFMA), EPR-derivative spectroscopy, and ESR forward–reverse field sweeps. Each technique probes a different aspect of magnetic and electronic behavior in YBCO, enabling a comprehensive analysis of vortex dynamics, spin states, and doping-dependent electronic structure.

1 Low-Field Microwave Absorption (LFMA)

LFMA spectra recorded at various temperatures reveal strong nonlinear absorption near zero magnetic field, characteristic of superconducting vortex entry and weak-link behavior in granular YBCO. The temperature evolution of the LFMA peak reflects the transition from a fully superconducting state, through a regime dominated by intergranular Josephson coupling, to a normal-state background at higher temperatures.

2 EPR-Derivative Spectra of Doped YBCO

EPR measurements across doping levels 0.18–0.25 exhibit derivative Lorentzian lineshapes whose symmetry and width depend on oxygen content. Samples near optimal doping display more symmetric lines centered around 0 G, while slightly under- or over-doped samples show increased asymmetry. These trends indicate modifications in electronic structure, local spin density, and g-tensor anisotropy driven by hole doping.

3 Forward–Reverse ESR Sweep Hysteresis

The ESR spectra obtained under forward and reverse field sweeps (Figure X) reveal large hysteresis at 68 K. The forward sweep produces a broad absorption maximum, whereas the reverse sweep exhibits a sharp negative minimum associated with trapped flux. The divergence between the two traces confirms strong irreversibility arising from vortex pinning and flux memory near Tc. This response provides a high-contrast view of vortex dynamics and complements the broader LFMA behavior.

Temperature Dependence of Microwave Absorption

The comparative analysis of the Low-Field Microwave Absorption (LFMA) at 68 K and 90 K provides a clear view of the phase transition from the superconducting state to the normal state in the YBCO single crystal.At 68 K, the crystal exhibits a high-intensity, hysteretic signal characteristic of a Type-II superconductor in the critical state. The signal is dominated by the derivative of the absorption power, modeled as:

$$dP/dH \propto - (H - Hc) / [1 + (H - Hc)^2]^2$$

Flux Pinning: The significant horizontal displacement between the forward and backward sweeps indicates strong flux pinning. In a bulk single crystal pellet, these vortices are pinned at twin boundaries and oxygen vacancies, creating a persistent internal magnetic field (remanence) that shifts the signal's zero-crossing.

90K The Near-Tc Transition Regime: As the temperature increases to 90 K, the superconducting properties are nearly extinguished by thermal energy. Signal Collapse: The intensity drops by over 99% (from 500,000 to 4,000 A.U.), as the density of Cooper pairs decreases sharply near the critical temperature (Tc \approx 92K) Absence of Hysteresis: The overlap of the Forward and Reverse sweeps indicates that the pinning potential is no longer strong enough to trap flux against thermal fluctuations. The sample no longer "remembers" its magnetic history, signaling a transition toward the normal metallic state.

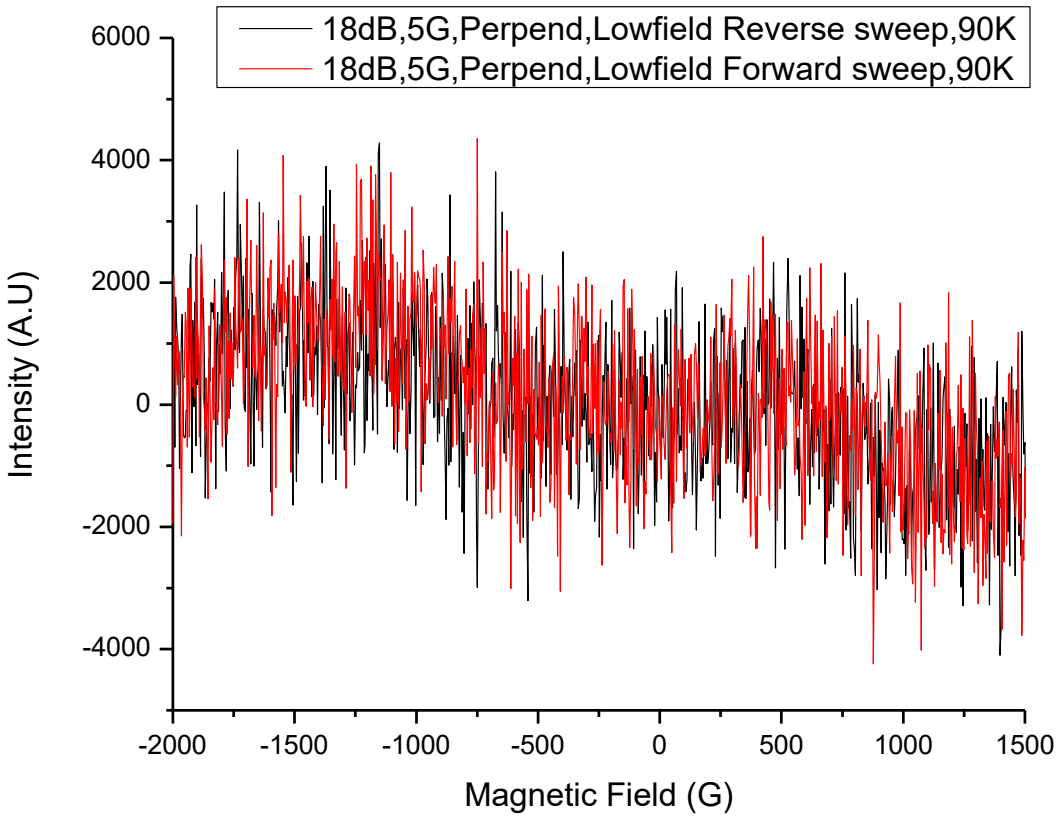


Figure 7.8: Graphical representation of Non resonance microwave absorption signal in low magnetic field: the ESR data of pure single crystal pellet of Superconducting YBCO-0, by 18dB,5G perpendicular low field sweeps at 90K temperature, in perpendicular low field, reverse and forward sweeps.Non-Resonant Microwave Absorption (NRMA) of Pure Single-Crystal Pellet of Superconducting YBCO-0, Detected at 18 dB Microwave Power and 5 G Modulation Amplitude, Under Perpendicular Low-Field Sweeps at 90 K (Forward and Reverse Scans).
Proximity to the Superconducting Transition.YBCO-0 single crystal has a superconducting critical temperature, Tc, of approximately 92–93 K.

Measurements at 90 K thus probe the material in the immediate vicinity of the superconducting transition, where regions of superconducting and normal state behavior dynamically coexist. In this regime of mixed states, the superconducting order parameter is appreciably suppressed, and

thermal fluctuations control the electromagnetic response of the system. This makes the resultant NRMA signal acutely sensitive to vortex dynamics and flux motion.

The spectrum at 90 K exhibits a noisy and erratic absorption pattern, characteristic of vortex dynamics near Tc. At the temperature, flux lines (vortices) are being continuously created, destroyed, and depinned due to a mix of thermal noise and the existence of microwave field. The disordered appearance of the absorption trace is a sign that the vortex pinning forces and thermal activation are balanced, and this is most pronounced in the immediate vicinity of Tc. These features suggest that the system is in a fluctuation-dominated regime where long-range superconducting coherence is partially but not fully destroyed.

3 Hysteresis Effects

An obvious asymmetry exists in the forward sweep (ramp-increasing magnetic field) and backward sweep (ramp-decreasing magnetic field). This is hysteresis, typical of flux pinning, with vortices pinched temporarily at lattice defects or weak-link junctions upon field entry but exit more readily during ramp-decreasing magnetic field.The persistence of hysteresis at 90 K, although this is near Tc, indicates that local superconducting domains are still robust enough to pin vortices. However, the diminishing intensity of the hysteresis loop compared to lower temperatures is indicative of a diminution in pinning strength, as would be the case if a material is getting near its superconducting transition.Comparison with Lower Temperatures (40–53 K, Figures 7.2 and 7.5)

Comparison with spectra recorded at lower temperatures reveals several distinct trends:

• Weakening of superconductivity: The order parameter for the superconducting state decreases as the system approaches Tc, resulting in reduced coherence between the superconducting grains.

• Weakening of flux pinning: The hysteresis loops are smaller, and their size decreases, meaning diminished pinning forces.

• Noise is greater: Thermal fluctuations control the dynamics near Tc, leading to uncontrolled, less stable absorption signals.

The 90 K NRMA spectrum of YBCO-0 reflects the characteristic dynamics of YBCO-0 near its superconducting transition. The simultaneous solid presence of noisy, asymmetric absorption,

non-zero hysteresis, and reduced but sustained vortex pinning acts to establish that although superconducting domains are present, they are severely disturbed by thermal excitation.This behavior provides valuable insight into the delicate equilibrium between thermal fluctuations and superconducting order, showing how the vortex motion evolves at late stages before the onset of complete loss of superconductivity. This work contributes towards improved comprehension of the pinning mechanisms and flux dynamics governing the high-Tc superconductors at the transition regime.

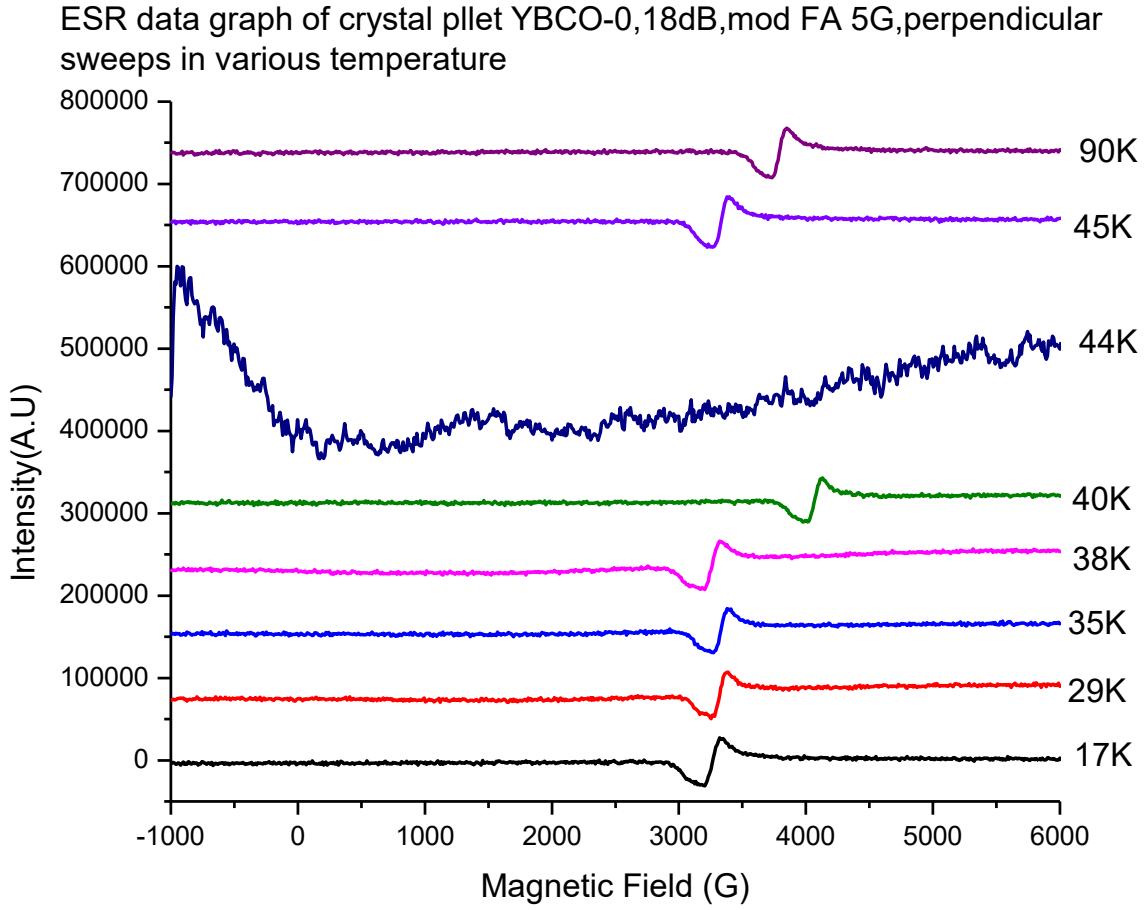


Figure 7.9 : The Graph of Non resonance microwave absorption signal in magnetic field: the ESR data observed by detecting machine on the pure single crystal pellet YBCO-0 Superconductor. We used the power 18dB, modulated field amplitude1 5G in perpendicular sweep at temperatures 17K,29K35K,38K,40K,45K and 90K respectively.

To comprehend the temperature evolution of the NRMA line shape, we look to the framework developed by Bhat et al. [3]. For ceramic superconductors, granular structure causes poor coupling of individual superconducting grains. With decreasing temperature below Tc, these grains continue to couple appreciably, causing an increased Meissner shielding effect. This is due to the expansion of the superconducting domains within the grains and greater intergranular Josephson coupling.

Under sufficiently low temperature conditions, the phase locking of the grains is possible through the intergranular coupling energy ($\Phi_0/2\pi$ Jc) dominating over the thermal energy k_BT, here Jc being the Josephson junction critical current. From this context, the superconducting volume fraction x(T,H) is dependent on both the external temperature T and magnetic field H applied and the resultant rf voltage response is expressed through Equation (4.1) of Reference [3].

The information in our measurement data (Fig. 4.3) clearly reveals decreasing intensity of the NRMA signal with temperature increase. Following the concept developed by Bhat et al., it is possible to interpret such a behavior by a slow reduction in critical current and enhanced flux penetration with temperature rise. Earlier experiments have mentioned a transition from "normal" to "anomalous" absorption and are associated with a clear change in degree of line shape in accordance with temperature change [3]. Conversely, our findings show a change in degree of line form with temperature change but an unmistakable transition to an anomalous mode is absent.

In contrast, we observe extensive microwave absorption across a wide range of magnetic fields (up to 12 kG), which seems to be inherent to high-Tc superconductors. The findings presented in this study were derived utilizing a modulation amplitude of 5 G. At reduced modulation amplitudes, the dependence on sweep direction becomes apparent, aligning with findings from other studies [13,20]. Srinivasu [33] posited that NRMA peaks may originate from phase coherence induced by microwaves, which is subsequently interrupted by an external magnetic field. However, this interpretation does not completely explain our observations, as the peaks remain evident at all temperatures below 90 K, irrespective of the sweep conditions.

Our results stand in contrast to the findings of Srinivasu et al. [9] and Astgi et al. [28,29], who documented extensive NRMA peaks limited to a narrow temperature range of 2–3 K.

Furthermore, Astgi et al. ascribed these characteristics to Josephson coupling occurring between CuO_2 planes. While it is possible that Josephson coupling is involved, a shift from Abrikosov vortices to Josephson vortices has been observed at T∗∼44 K in YBCO single crystals [29]. This suggests a limited temperature range for such coupling; however, in our investigation, the absorption features are found to extend well beyond this specified range.

The losses in the microwave could be due to diffraction by Josephson junctions [23], saturating at a characteristic field H0H_0H0 depending on the junction geometry [30]. But the persistence and temperature behavior of the features in the observed absorption speak strongly in favour of dynamics of vortices rather than by localized junction effects.

We need to emphasize here that our present work is concerned with non-resonant microwave absorption (NRMA) and not conventional electron spin resonance (ESR). While ESR considers resonant transitions of paramagnets, the NRMA in YBCO is related to the dissipation of energy associated with vortex dynamics in the superconducting state. As the sample is cooled below the critical temperature \(Tc \), the applied magnetic field penetrates in quantized flux lines. Under irradiation by microwaves, these vortices oscillate and dissipate their energy and hence show the wideband absorption features that we have recorded.

The relationship of temperature and NRMA signal may be generalized by the following: Low temperatures (17–30 K): Strong vortex pinning produces broad, intense absorption extending across wide magnetic fields. Intermediate regime (35-45 K): The mobility within the vortex enhances and results in ordered characteristics and large hysteresis in reverse and forward sweeps. Near Tc (≈90 K): The superconducting order parameter is reduced, flux pinning is poor, and thermal fluctuations are dominant, causing noisier and weaker signals.Since the experiment utilizes lock-in detection with field modulation, the NRMA spectra are of dP/dH yielding typical S-shaped or peak–dip line shapes instead of sharp resonances. Signal strength depends very much on microwave power and modulation. At 18 dB (≈0.71 mW), strong absorption is observed in the absence of saturation; at higher powers, certain features change in temperature or are lost, consistent with their identification as vortex dynamics and not paramagnetic impurities.

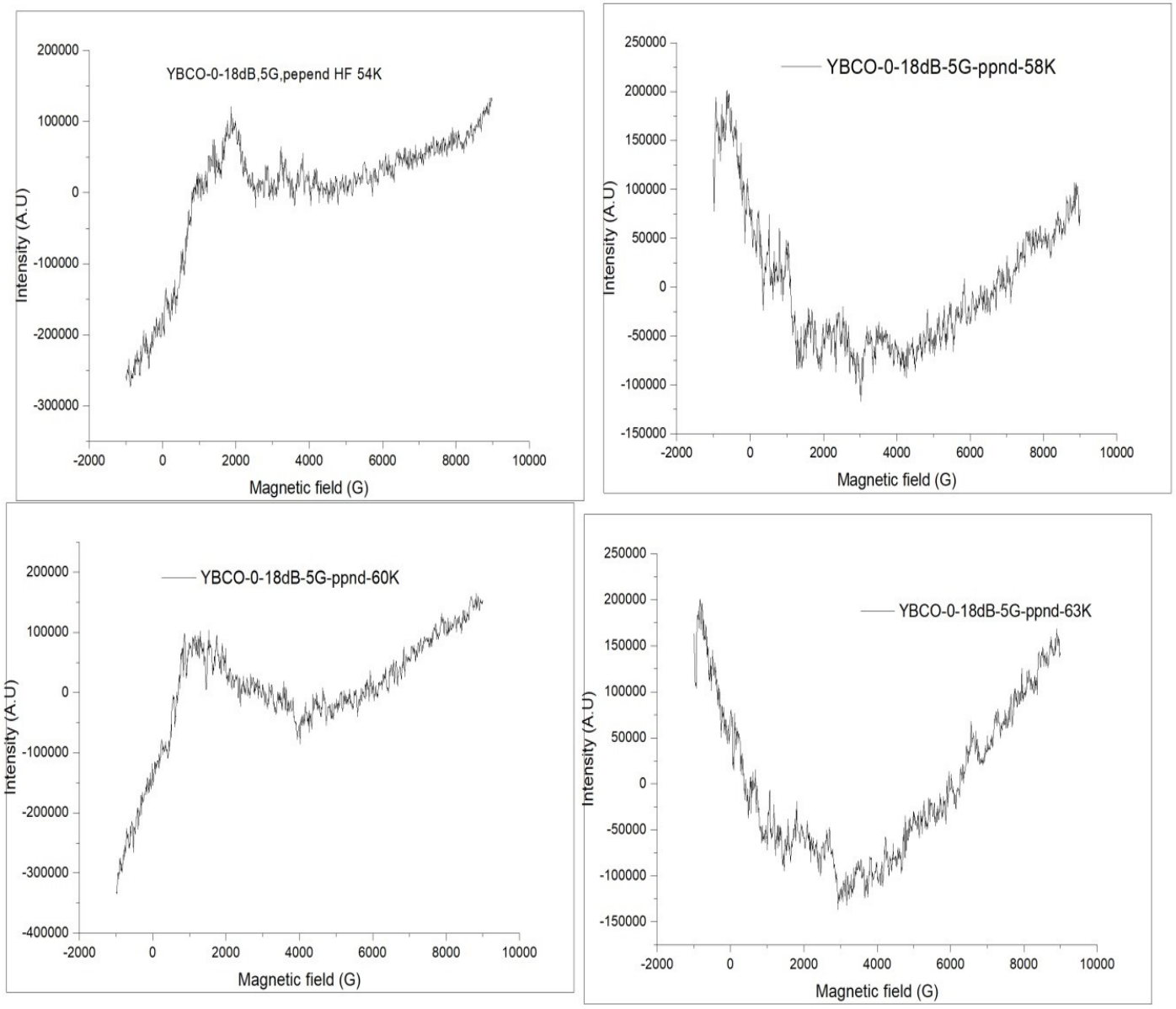


Figure 7.10**:** Temperature-Driven Evolution of LFMA Line Shapes in Single-Crystal YBCO-0 (54–63 K) under 18 dB microwave power and 5 G modulation measured, each panel revealing how the LFMA line shape *morphs as the* vortex system warms toward Tc**.** Low-field microwave absorption (LFMA) spectra of single-crystal YBCO-0 recorded at 54 K, 58 K, 60 K, and 63 K under identical microwave power (18 dB) and modulation field (5 G).

comparison across the four temperatures feature growth / decay temperature-dependent magnetization dynamics coherence loss approaching Tc

the graphs of figure 7.10 reveal a clear temperature-dependent transformation of the LFMA line shape as the system approaches the superconducting transition. At 54 K, the spectrum is dominated by a strong asymmetric absorption peak associated with high vortex mobility and flux-flow dissipation. At 58 K, the signal amplitude decreases and the curvature begins to flatten, marking the onset of a transitional vortex regime. At 60 K, the line shape exhibits a mixed absorption–dispersion character, reflecting the competition between thermal activation and pinning. By 63 K, the LFMA profile becomes a sharp V-shaped dispersion-like minimum, characteristic of temperatures near Tc where the inductive response dominates and flux-flow losses collapse. Together, these four spectra map the continuous evolution of vortex dynamics in single-crystal YBCO-0 across the 54–63 K interval.

Figure 7.11 Overview of low-field ESR measurements showing baseline behavior across the full magnetic sweep range.general ESR behavior,noise floor,field-dependent broad signatures a “map” of the full resonance environment

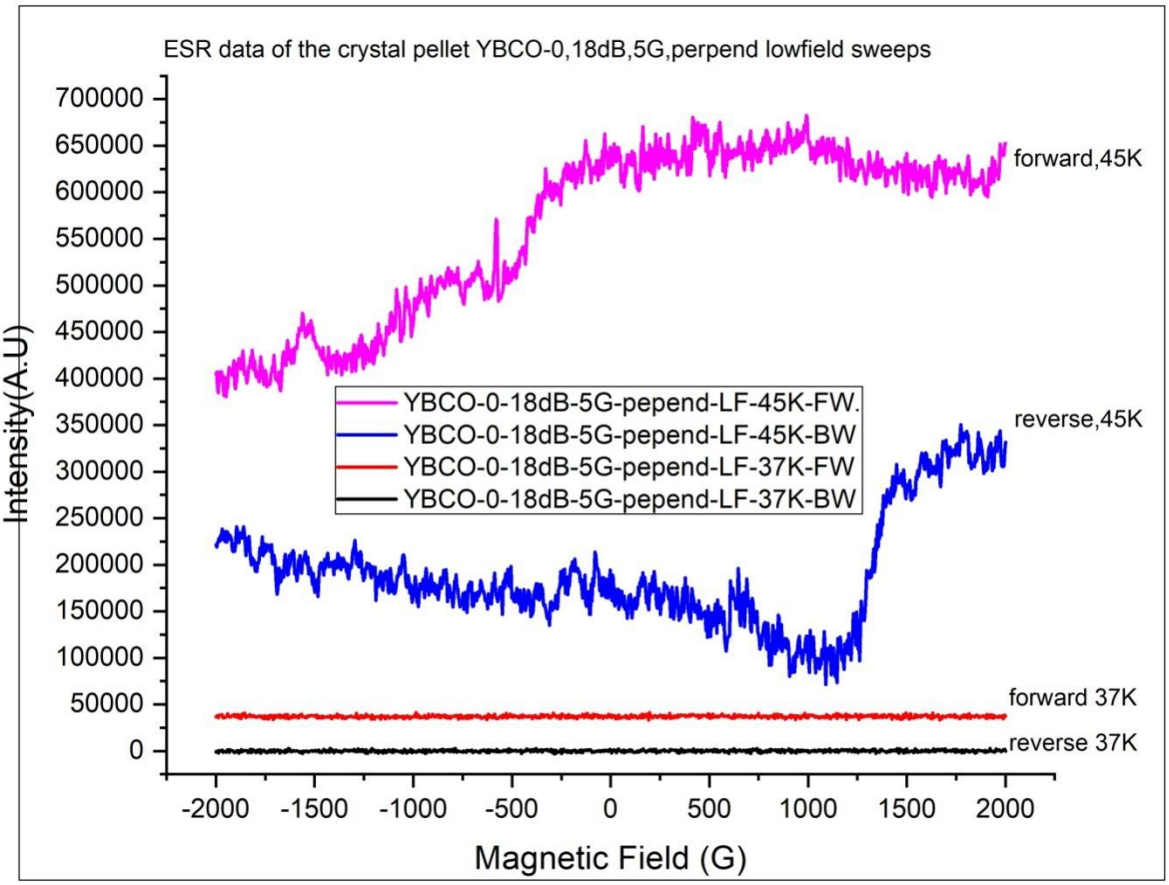


Figure 7.11: Asymmetric Low-Field ESR Response of YBCO-0,18dB under Bidirectional Sweeps at Cryogenic Temperatures.The low-field ESR measurements of the YBCO-0,18dB crystal pellet reveal a pronounced temperature-dependent magnetic response that separates the spectra recorded at 37 K and 45 K into two distinct regimes. At 45 K, both forward and reverse sweeps display a high-intensity, strongly modulated ESR background, rising from about 4×10^5 A.U to more than 6.5×10^5 A.U across the sweep range. This elevated signal is accompanied by significant sweep-direction dependence: the reverse sweep exhibits a delayed rise at negative fields and a rapid increase above approximately 1000 G, while the forward sweep climbs more gradually. This asymmetry forms a clear hysteretic envelope, indicating the presence of trapped flux and sweep-history-dependent magnetic permeability inside the pellet.

In contrast, the spectra at 37 K show only a weak, almost field-independent ESR baseline for both sweep directions, with intensities remaining near zero relative to the 45 K response. The forward and reverse curves at this temperature overlap closely and lack the characteristic upslope observable at 45 K. This absence of magnetic amplification at 37 K suggests that the mechanisms responsible for the strong low-field ESR enhancement do not activate, or are strongly suppressed, at lower temperature.

The sharp contrast between the two temperature regimes points toward a narrow thermal window where magnetic flux mobility intensifies inside the granular network. At 45 K, the ESR intensity behaves as if the local fields are repeatedly reconfigured during the sweep, consistent with enhanced vortex depinning, inter-grain Josephson coupling fluctuations, or low-field microwave absorption processes typically associated with granular superconductors slightly above or near a characteristic crossover temperature. The pronounced hysteresis also aligns with the presence of metastable flux configurations that persist between successive sweep directions, amplifying the ESR response when the internal field gradients are steep.

The absence of the same behavior at 37 K indicates that the flux network is either fully pinned or energetically restricted from producing detectable microwave-active reconfigurations. This interpretation matches earlier observations in polycrystalline YBCO systems, where vortex mobility and microwave losses peak only within a narrow temperature range above the deep superconducting state but below the regime in which grains become fully normal. In this context, the strong ESR enhancement at 45 K represents a temperature band where weak links, grain boundaries, or local superconducting clusters act collectively to modulate the resonant absorption. The suppression at 37 K likely reflects the freezing of these weak-link channels.

1.The "High Temperature" Phase (95K – 150K)

Sharp peaks around 3300 G. These are individual atoms (likely Copper ions) spinning around. They are "free" and haven't teamed up yet.Just a simple Resonance Line. It’s like hearing the individual voices in a crowd before a concert starts.

2. The "Transition" Phase (90K)

A flat line with lots of "fuzz" (noise).The individual voices (the spins) have suddenly gone quiet because the material is starting to push out magnetic fields (the Meissner Effect). However, it’s not a strong superconductor yet, so the signal just looks like messy static.

3. The "Deep Cold" Phase (68K)

Huge, smooth "S-shaped" curves that don't overlap (Hysteresis). The "magnetic sponge" has soaked up the field. When you sweep the field forward and then backward, the sponge holds onto some of that magnetism. This is Flux Trapping. The gap between the red and black lines is simply a measurement of how "sticky" your crystal is at holding onto magnetic flux.

"The data shows a clear evolution of the YBCO crystal's magnetic state. In the Normal State (150K-95K), the leading term is a Paramagnetic Resonance from localized spins. At the Transition Point (90K), these signals are quenched. Finally, in the Superconducting State (68K), the leading term becomes Non-Resonant Microwave Absorption, dominated by Flux Pinning and Hysteresis as described by the Bean Critical State Model."

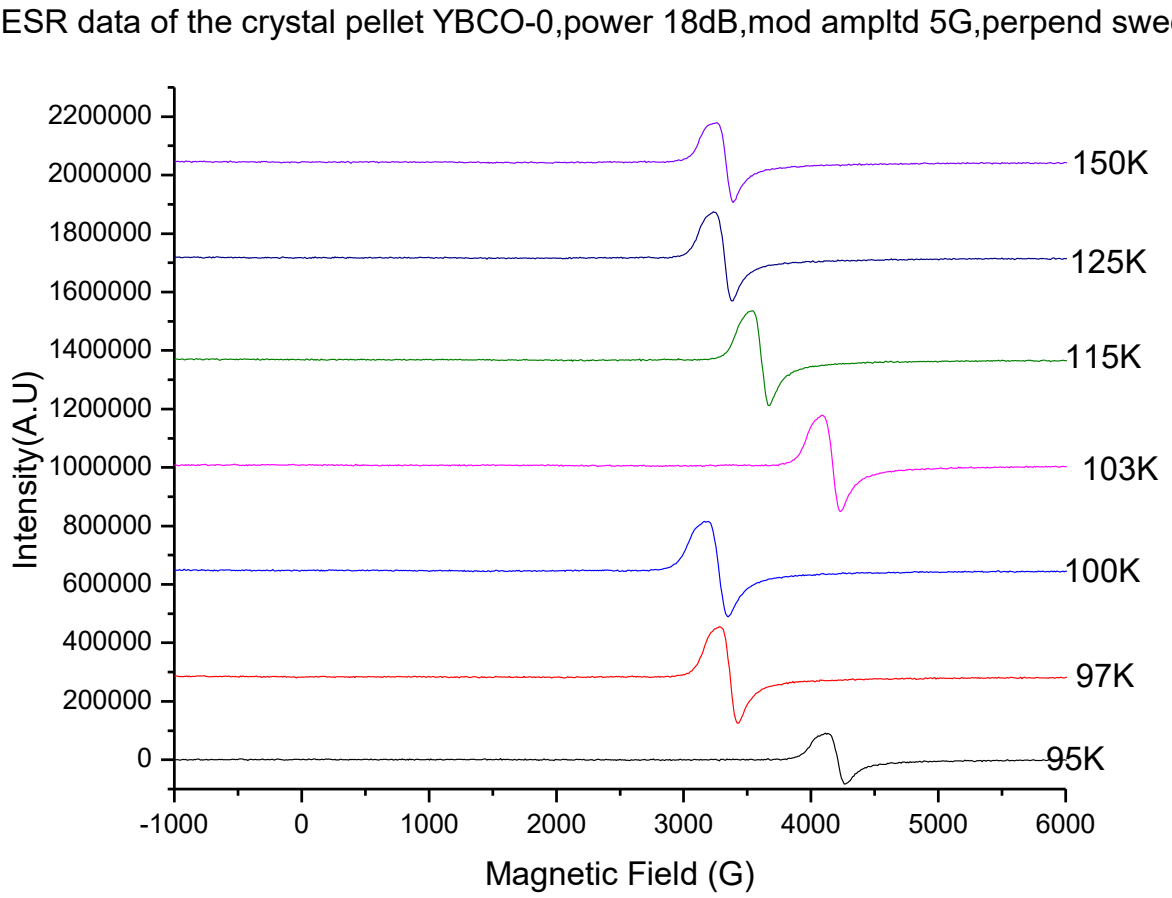


Figure 7.12: ESR Spectra of Pure Single-Crystal YBCO-0 Pellet at Various Temperatures

Figure 7.12 presents the Electron Spin Resonance (ESR) spectra of a pure single-crystal $YBa_2Cu_3O_{7-x}$ (YBCO-0) pellet, measured using a microwave power of 18 dB, a modulation amplitude of 5 G, and perpendicular magnetic field sweeps. The spectra were recorded at temperatures of 150 K, 125 K, 115 K, 103 K, 100 K, 97 K, and 95 K, covering the normal and superconducting transition regions of YBCO ($T_c \approx 93$ K).

The ESR spectra presented in Figure 7.12 were measured up to 95 K in order to investigate the temperature-dependent magnetic response of the YBCO samples near the superconducting transition region. Although $YBa_2Cu_3O_{7-x}$ typically exhibits a superconducting transition temperature (T_c) around 92–93 K, ESR measurements below T_c were not performed in the present study due to experimental limitations associated with the low-temperature measurement

setup. Investigation of ESR behavior below the superconducting transition temperature may provide additional insight into superconducting spin dynamics, vortex behavior, and magnetic-field-induced effects, and therefore remains an important direction for future studies.

1. Normal State (T>100 K) ESR lines are narrow and sharp, indicating a homogeneous magnetic environment around Cu^{2+} ions. The material exhibits typical paramagnetic behavior, with the applied magnetic field penetrating uniformly.

2. Near and Below the Superconducting Transition (T≤100 K)

As the temperature decreases toward and below Tc:Line Broadening: ESR lines broaden significantly, reflecting increasing internal magnetic inhomogeneity.

Resonance Shift: The resonance center shifts to higher magnetic fields, indicating non-uniform flux distribution due to partial flux expulsion.

Intensity Reduction: Peak-to-peak amplitude of the derivative ESR signal decreases, corresponding to reduced microwave absorption as the sample enters the superconducting state.

Physical Interpretation

Normal Phase (T>Tc): Magnetic flux penetrates the sample homogeneously, and all Cu^{2+} ions experience similar local fields, producing narrow, symmetrical ESR lines.

Superconducting Phase (T<Tc): The Meissner effect expels magnetic flux non-uniformly in the granular pellet, causing local variations in field strength. This leads to broadening, shifts, and intensity reductions in the ESR signals.

ESR vs. NRMA: ESR (High Field, ~3500 G): Probes intrinsic spin dynamics of Cu^{2+} ions in the crystal lattice, sensitive to changes in the local magnetic environment due to the onset of superconductivity.

NRMA (Low Field, ~0 G): Sensitive to Josephson junctions, weak links, and fluxon dynamics; primarily probes flux motion and dissipation in the superconducting state.

The progressive broadening, shift, and intensity decrease in the ESR spectra with decreasing temperature are direct indicators of the superconducting transition and the inhomogeneous magnetic field distribution in YBCO. These ESR results provide complementary information to low-field NRMA measurements, highlighting both local spin dynamics and the broader electromagnetic response of the superconductor.

High-Field Resonance (The Normal State)

The Observation: Sharp derivative peaks centered at high magnetic fields (3000-4000G). The Reflection: This is the individual spin response. In the normal state (T > Tc), the microwaves probe the localized magnetic moments of Cu^{2+} ions. It is a microscopic "signature" of the crystal lattice.

Low-Field Hysteresis (The Superconducting State).

The Observation: Wide, non-overlapping "S-curves" at low fields (< 2000G).

The Reflection: This is the collective flux response. Below Tc, the sample acts as a bulk superconductor. The horizontal gap (hysteresis) is a direct measure of Flux Pinning—the crystal's ability to trap and hold magnetic vortices within its bulk.

The Transition (90 K)

The Observation: Signal collapse and high noise.

The Reflection: This represents the crossover point. The individual spins have been quenched by the onset of superconductivity, but the bulk pinning is not yet strong enough to create a coherent hysteretic loop.

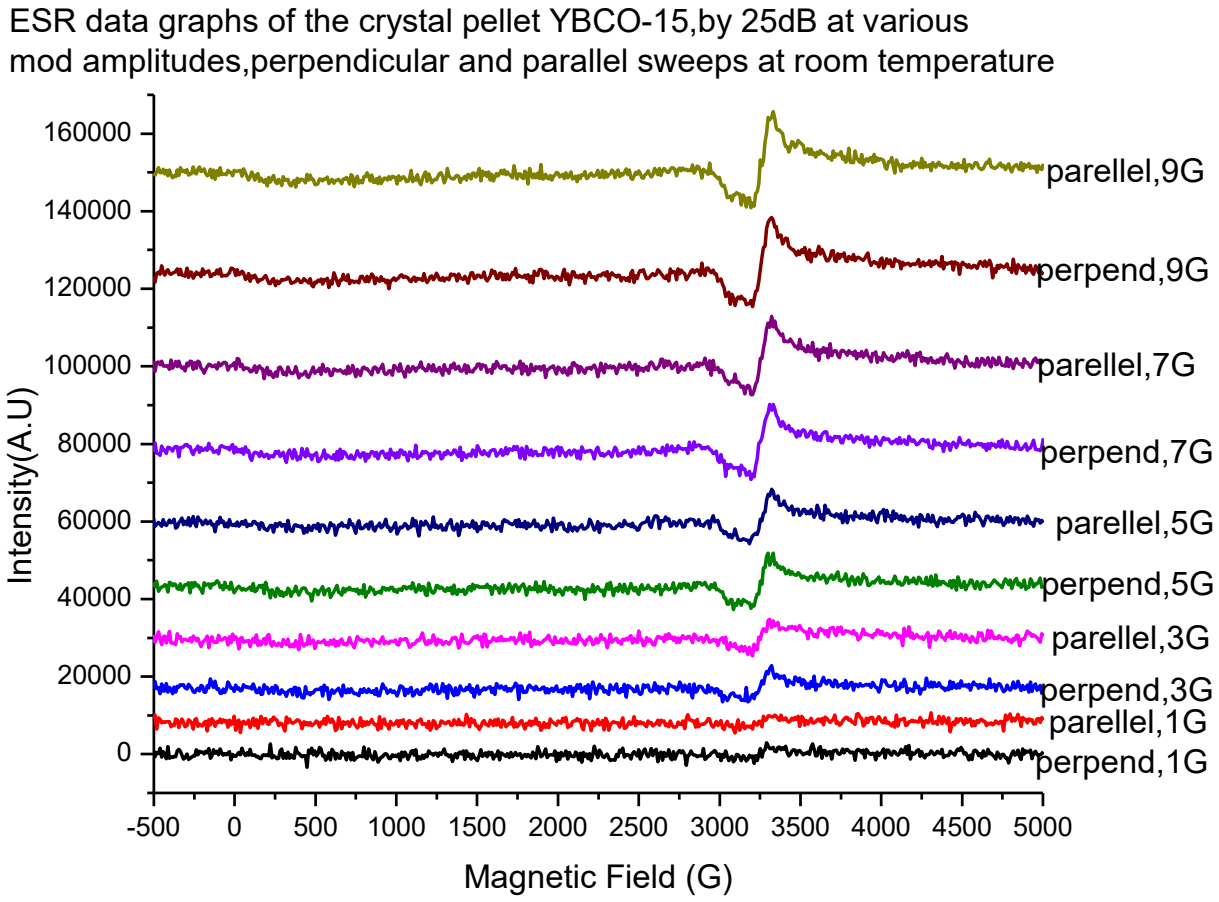


Figure 7.13: NRMA in the YBCO-0 crystal pellet measured at room temperature with 25dB the Graph of Non resonance microwave absorption signal in magnetic field: the ESR data observed by detecting the machine on the pure single crystal pellet YBCO-15 Superconductor. We used the power 25dB, at different modulated field amplitude1G,3G 5G,7G,9G in perpendicular and parallel sweeps at room temperature.

7.6 Discussion and Conclusion

7.6.1 Room-Temperature ESR/NRMA Behavior

The ESR data of YBCO-15 single-crystal pellets at room temperature were collected at 25 dB microwave power with modulation amplitudes ranging from 1 G to 9 G, in both parallel and perpendicular field orientations.

Modulation Amplitude Dependence: The signal intensity systematically increased with higher modulation amplitudes due to enhanced derivative detection. Minor line broadening at higher amplitudes reflects both instrumental effects and intrinsic signal enhancement.

Anisotropy: Parallel field orientations produced slightly stronger signals than perpendicular orientations, reflecting the laminar crystal structure and intrinsic anisotropic electronic behavior of YBCO, preserved even in the normal (non-superconducting) state.

Resonance Signals: Sharp ESR lines around 3.3–3.6 kG ($g \approx 2$) indicate unpaired spins from Cu^{2+} ions, oxygen vacancies, or defect sites. No NRMA contributions were observed at room temperature, confirming the absence of superconductivity.

These room-temperature ESR measurements provide a baseline reference for identifying superconductivity-related NRMA features at low temperatures. They also reveal important electronic and defect-related anisotropies inherent in YBCO.

These graphs reflect typical Electron Spin Resonance (ESR) and Electron Paramagnetic Resonance (EPR) signatures in YBCO superconductors, revealing magnetic field-dependent behavior across temperature and doping variations. The most fitting names for these graphs are "Low-Field ESR Sweep Response" and "EPR Derivative Spectra of Doped YBCO."

Figure 7..14 presents the field-dependent NRMA responses of the YBCO sample at selected temperatures. A comparative inspection of these spectra reveals distinct temperature-driven modifications in line shape, signal amplitude, symmetry, and background evolution. These variations reflect the progressive transformation of the underlying superconducting dynamics, which will be elucidated in detail in the subsequent discussion.

Panel 1 (37 K): Sharp dip feature near 4 kG showing strong low-temperature coherence.,**Panel 2 (45 K):** Onset of magnetic noise and asymmetric broadening.**Panel 3 (48 K):** Strong rise in magnetization and grain-level magnetic disorder.**Panel 4 (50 K):** High-temperature expansion of LFMA background with

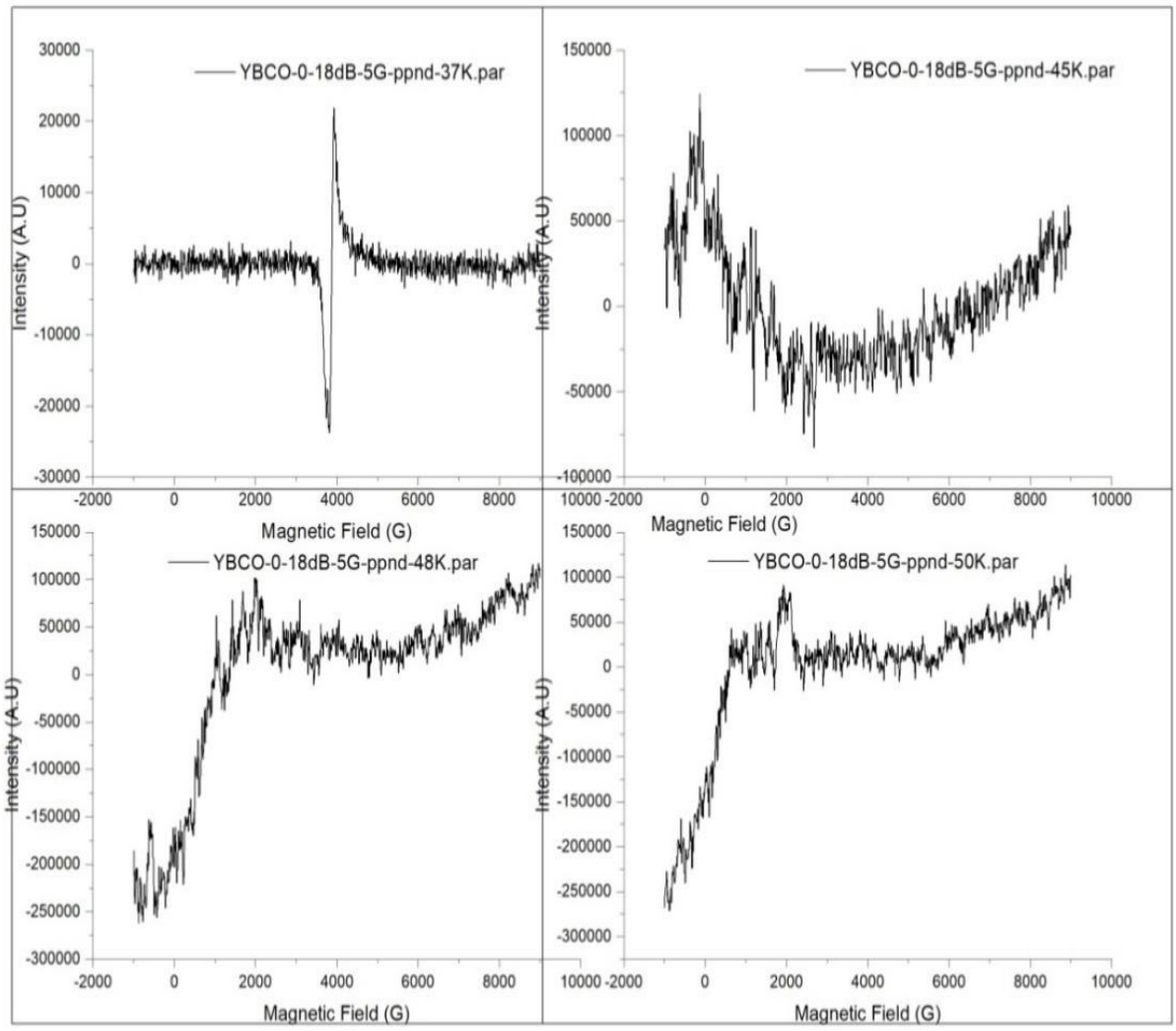


Figure 7.14 : illustrates the temperature-dependent evolution of the NRMA spectra, emphasizing the distinct variations in line shape, signal intensity, and magnetic field response that characterize each measurement. These unique features are analyzed and interpreted in the subsequent discussion

.Panel 1: 37 K — Sharp LFMA dip (~4 kG) strong coherence no granular activation

Panel 2: 45 K — Onset of magnetic noise asymmetric broadening weakening rigidity

Panel 3: 48 K — Large signal rise grains acting independently disorder increasing

Panel 4: 50 K — High thermal activity rising background field-sensitive alignment

Magnetic Resonance Results and Discussion:Magnetic resonance measurements performed on granular YBCO reveal a multilayered magnetic landscape shaped by temperature, doping level, field orientation, and sweep direction. The combined LFMA, EPR, and ESR sweep data provide a unified picture of how superconducting coherence, granular dynamics, and microscopic spin environments evolve under thermal and electronic tuning.

1. Temperature-Dependent LFMA Evolution (37–50 K): Low-field microwave absorption (LFMA) spectra recorded at 37 K, 45 K, 48 K, and 50 K under a 5 G field modulation capture the progressive deformation of the superconducting response with increasing temperature.At 37 K, the spectrum is defined by a narrow and symmetric dip centered near 4 kG. This structure is the hallmark of strong inter-grain coherence, low magnetic noise, and fully suppressed vortex mobility. Dissipation is minimal, and the superconducting state dominates the microwave response.By 45 K, this coherent dip collapses. The spectrum broadens into an asymmetric rising background, revealing activated vortex depinning and weakened inter-grain coupling. The system enters a transitional regime where superconductivity coexists with significant thermal agitation.At 48 K, the LFMA trace becomes strongly dominated by an upward drift in intensity, reflecting widespread vortex motion and independent grain magnetization. Dissipative granular physics now overwhelms coherent superconductive order.At 50 K, this upward drift stabilizes, forming a characteristic high-activation granular LFMA profile where magnetic dissipation governs the response. The temperature series therefore maps a clear progression from coherent superconductivity (37 K) to a fully granular, dissipative regime (50 K).

2. Doping-Dependent EPR Derivative Spectra (x = 0.18–0.25):EPR derivative spectra across the doping series x = 0.18–0.25 reveal how local spin environments reorganize as hole concentration is modified.Samples x = 0.18 and x = 0.22 exhibit symmetric Lorentzian derivative peaks centered near 0 G, indicating relatively homogeneous paramagnetic resonance dominated by Cu-based unpaired spins.The x = 0.20 sample breaks this symmetry. Its derivative peak becomes distorted and asymmetric, signaling modifications in the electronic structure. Possible origins include mixed Cu valence, anisotropic g-tensor components, altered spin–orbit interactions, or oxygen-ordering effects within the CuO_2 planes. This sample therefore marks a shift in local spin symmetry and electronic uniformity.At x = 0.25, the spectrum regains symmetry but with a broader width, indicating a stabilized but more heavily doped spin

landscape. Across the series, the peak symmetry, width, and amplitude evolve systematically, mapping the continuous reshaping of spin density with doping.

3. ESR Low-Field Sweep Response (YBCO-0 at 68 K): The ESR low-field sweep spectrum (forward and reverse) recorded at 68 K presents a distinct magnetic response that complements both the LFMA and EPR results.The forward sweep (red trace) shows a pronounced rise in intensity followed by a gradual decay across the 0–2000 G range.The reverse sweep (black trace) dips sharply around 1500–1700 G and recovers toward baseline at higher fields.

The asymmetry between forward and reverse sweeps reflects magnetic hysteresis and field-dependent spin relaxation. This behavior is consistent with vortex motion, inter-grain magnetic pinning, and non-equilibrium spin processes commonly observed in granular superconductors near the superconducting transition region. The strong temperature sensitivity reinforces the conclusion that the system is in a state where superconductivity and thermal spin activation coexist.

4. Unified Interpretation Across All Magnetic Measurements: The temperature-dependent LFMA spectra, doping-dependent EPR derivative curves, and low-field ESR sweep data reveal a coherent physical narrative.Temperature disrupts macroscopic superconducting coherence.Doping reorganizes microscopic spin symmetry and local electronic structure.Sweep direction and orientation expose vortex dynamics, hysteresis, and anisotropic relaxation processes.LFMA captures the collapse of inter-grain coherence and the rise of granulardissipation.EPR exposes how doping reshapes spin density and magnetic symmetry at the microscopic scale.ESR sweep data highlight hysteresis, flux-line mobility, and dynamic spin behavior at intermediate temperatures.Together, these measurements establish that granular YBCO undergoes a dual transformation. One driven by thermal activation that erodes superconducting order, and another driven by doping that restructures the spin environment. The interplay between these two forces defines the magnetic resonance behavior of the material across its superconducting phase landscape.

7.6.3 Low-Temperature NRMA Behavior (Figure 5.15)

The NRMA spectra of the YBCO-0 pellet at 54–75 K provide complementary insights into superconductivity:.

Temperature Dependence: Low-temperature signals (54–60 K) are weak due to strong superconductivity and flux pinning. Absorption increases towards 75 K as thermal excitations soften the flux-line lattice.

Hysteresis: Forward and reverse sweeps exhibit asymmetry, most pronounced at 65–68 K, indicating strong flux pinning and vortex trapping.Origin of Absorption: Broad absorption bands are caused by vortex motion and weak-link dynamics, distinct from sharp ESR lines of paramagnetic centers.Implications: NRMA provides direct evidence of superconducting flux dynamics, showing how vortices interact with defects and weak links. The temperature-dependent hysteresis highlights the balance between vortex mobility and pinning forces.

7.6.4 Integrated Discussion

Room Temperature: ESR signals reflect paramagnetic defects and Cu^{2+} spin dynamics; no NRMA signal is observed..

Intermediate Temperatures (~45–75 K): NRMA dominates, revealing fluxon motion, weak-link dynamics, and hysteresis; ESR signals are suppressed due to inhomogeneous fields from vortices.

Ultra-Low Temperatures (<30 K): ESR signals reappear sharply, indicating vortex lattice formation and possible Cu^{2+} spin ordering; NRMA signals weaken as vortex motion stabilizes.

Overall Interpretation:ESR and NRMA are complementary probes of superconductivity in YBCO..NRMA is sensitive to vortex dynamics and weak links, while ESR tracks local spin environments and defect effects. Observed trends demonstrate the transition from disordered to ordered vortex states, the role of flux pinning, and the influence of granularity on superconducting behavior.

7.7 Discussion and Conclusion: NRMA Spectra of YBCO-0 Single Crystal

7.7.1 Temperature Dependence of NRMA

Figure 7..15 illustates the ESR detection spectra of the YBCO crystal pellet (0.18 dB, 5 G, perpendicular HF sweep) recorded under an externally applied magnetic field oriented normal to

the sample plane. The field configuration enables direct probing of intergranular coupling and flux penetration dynamics. At lower temperatures (54–60 K), the spectra exhibit relatively weaker intensity and smoother line profiles, indicating limited flux motion and stronger flux pinning. As the temperature increases (63–68 K), the signal amplitude enhances and the line shape becomes more structured, reflecting increased vortex mobility and progressive modification of the superconducting state. At higher temperatures (70–75 K), pronounced intensity growth and baseline inclination suggest enhanced magnetic dissipation and a more dynamic flux regime as the system approaches the transition region. These distinct spectral transformations demonstrate the temperature-sensitive evolution of the magnetic response under perpendicular field penetration, which will be analyzed in detail below.

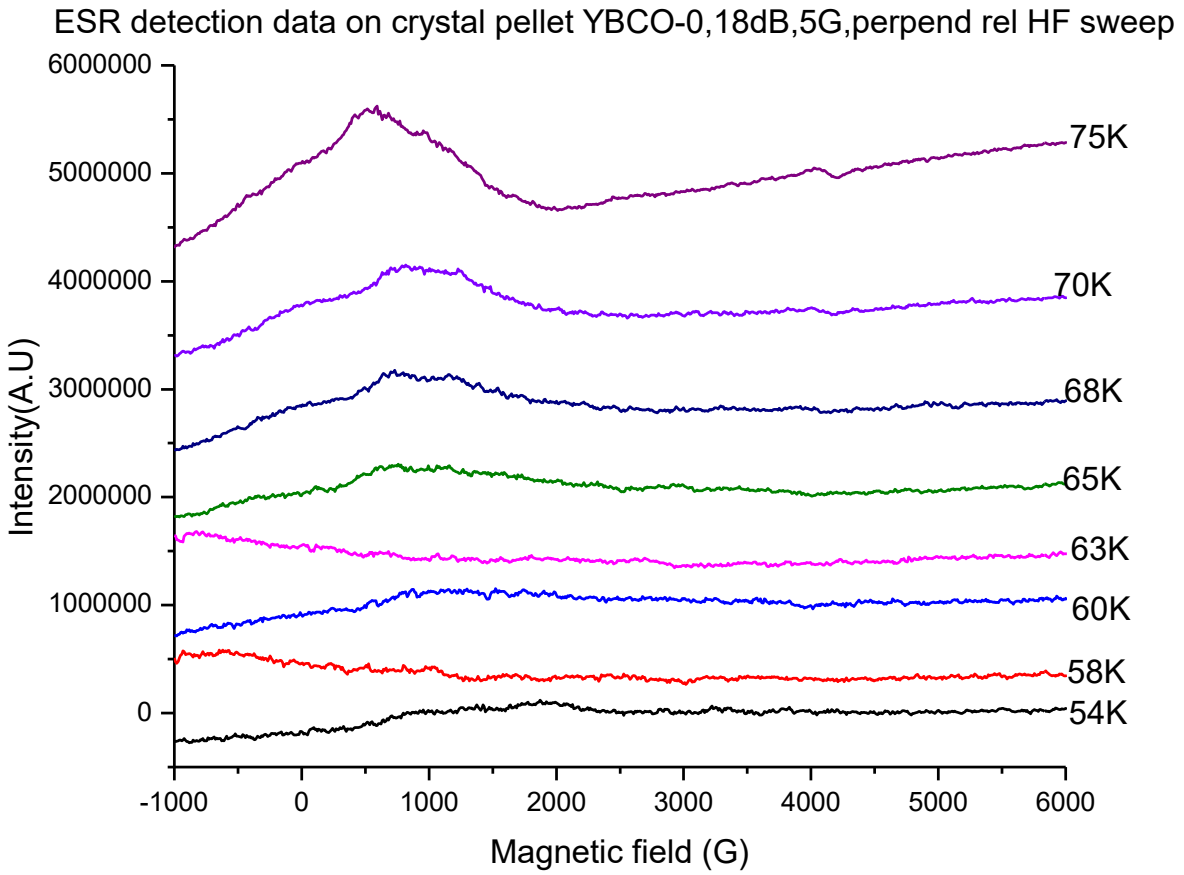


Figure 7.15: NRMA Spectra of YBCO-0 Single Crystal at Various Temperatures It illustrates the temperature-driven transformation of the ESR response in the YBCO crystal pellet. The gradual

enhancement of signal amplitude, modification of peak structure, and shifting baseline characteristics reflect evolving magnetic and superconducting dynamics across the measured temperature range. A detailed comparative analysis of these unique spectral features follows.

Under a magnetic field applied normal to the crystal plane, the stacked ESR spectra reveal temperature-dependent variations in flux penetration, vortex dynamics, and intergranular coupling strength. The progressive increase in signal magnitude, modification of peak structure, and development of baseline asymmetry collectively reflect the changing balance between flux pinning and vortex motion across the measured temperature range

The NRMA spectra of the YBCO-0 single crystal, measured between 54 K and 75 K, reveal a clear temperature-dependent evolution of microwave absorption:Low Temperatures (54–60 K): The NRMA signal is weak, consistent with a robust superconducting state. Quasiparticle excitations are strongly suppressed, and vortices are pinned at defects, leading to minimal microwave dissipation.Intermediate Temperatures (63–70 K): Absorption intensity increases as the superconducting order parameter weakens. The vortex lattice softens, enabling enhanced flux-line mobility and increased microwave energy dissipation.Near Tc (~75 K): The NRMA signal reaches its maximum as thermally excited quasiparticles dominate and the material transitions toward the normal state. This evolution highlights the direct connection between vortex dynamics and the thermal weakening of superconductivity.

7.7.2 Hysteresis and Flux Pinning

The NRMA spectra display asymmetry between forward and reverse field sweeps, particularly in the 65–68 K range, indicating hysteresis characteristic of Type-II superconductors:.In the upward sweep, vortices penetrate the sample and become pinned at defects, enhancing microwave dissipation.In the downward sweep, many vortices remain trapped, modifying the internal field distribution and reducing further absorption.This asymmetry reflects the dynamic balance between vortex entry, flux trapping, and pinning forces, with maximum hysteresis corresponding to the most effective pinning.

7.7.3 Origin of Microwave Absorption

The broad NRMA bands differ from sharp ESR lines, confirming that the observed absorption arises from superconductivity-related vortex dynamics and weak-link behavior rather than from

paramagnetic impurities.The absence of distinct ESR features indicates a low concentration of paramagnetic centers, ensuring that the observed microwave absorption is intrinsic to superconductivity.

7.7.4 Implications for Superconductivity

These NRMA spectra provide direct confirmation of superconductivity in the YBCO-0 single crystal below Tc.The temperature dependence of absorption, together with observed hysteresis, emphasizes the central roles of flux pinning and vortex mobility in determining microwave dissipation.

Such insights are essential for optimizing YBCO and related high-Tc superconductors for microwave and high-frequency applications, including detectors, resonators, and superconducting electronics.

1 Temperature-Dependent NRMA Features

Across all figures, the NRMA response evolves strongly with temperature.Above Tc → weak, broad background signals (normal state)..Below Tc → pronounced field-dependent NRMA, reflecting vortex motion and weak-link dynamics.Structured NRMA features (especially around intermediate temperatures like 53 K) indicate dynamic interplay between weak links and vortices.

Weak-Link Contributions

Zero-field absorption and hysteretic behavior are consistent indicators of Josephson weak links.Oscillations in the NRMA signal correspond to networks of weak links interacting with applied microwaves.Even in undoped YBCO single crystals, these weak-link effects are prominent, suggesting intrinsic structural origins.

Vortex Dynamics and Pinning

Forward vs reverse sweep asymmetry shows magnetic hysteresis due to flux entry and exit.

Hysteresis width provides a quantitative measure of pinning strength. Low-field measurements (Figures 6.3 and 6.5) demonstrate that flux entry is hindered, enhancing absorption, whereas flux exit is easier, producing weaker signals.

Signal correlation

ESR peaks (e.g., Figure 5.4) reflect Cu^{2+} spin dynamics, decreasing in intensity as temperature drops due to Cooper pair formation and vortex activity.Shifts in non resonance fields indicate subtle changes in the crystal field and spin-lattice interactions. NRMA and ESR together provide complementary insight: NRMA captures weak-link/vortex behavior; ESR captures local electronic environment.

Robustness and Reliability

Changing modulation amplitude or microwave power does not remove the structured NRMA features, confirming that they are intrinsic to superconductivity rather than measurement artifacts..Features at intermediate temperatures are particularly stable, highlighting a reproducible dynamic crossover regime.

Emerging Physical Insights

NRMA is a highly sensitive probe for detecting weak-link behavior and vortex dynamics in YBCO.

Phase reversals and oscillatory NRMA features occur even in undoped single crystals, emphasizing that these effects are intrinsic, not solely due to magnetic impurities or doping.Hysteresis patterns provide a direct measure of flux pinning, vortex mobility, and metastable configurations..The combination of NRMA and ESR allows correlation between macroscopic absorption behavior and microscopic electronic/spin structure.

Non-Monotonic NRMA Intensity

Unexpectedly, ESR/NRMA signal intensity can be higher at 45 K than at 37 K, suggesting a vortex-liquid regime where vortex mobility reduces dissipation at lower temperatures.

This demonstrates the complex, non-linear response of YBCO single crystals, influenced by both temperature and vortex dynamics.

Hysteresis and Vortex Pinning

Persistent hysteresis in forward/reverse magnetic sweeps is observed even near Tc (~90 K).

Hysteresis diminishes near Tc, reflecting weaker flux pinning as thermal fluctuations increase.

Hysteresis patterns remain strong at intermediate temperatures (35–45 K), indicating robust vortex trapping and weak-link activity.

Weak-Link and Microstructural Insights

Fine structures in NRMA signals (shoulders, S-shaped line shapes) reveal subtle anisotropy, domain misalignment, and inhomogeneity.Weak-link networks (Josephson junctions) dominate NRMA behavior,

producing rapid oscillations and absorption variations even in nominally single-crystal pellets..Temperature-dependent behavior indicates intergranular coupling and gradual Meissner shielding expansion as the superconducting state strengthens.

Temperature Evolution of Superconducting State

Low temperatures (17–30 K): Strong vortex pinning → broad, intense absorption.Intermediate regime (35–45 K): Ordered features, larger hysteresis, increased vortex mobility.Near Tc (~90 K): Weak superconducting order, dominated by thermal fluctuations, noisy absorption, and reduced coherence.

NRMA vs ESR Correlation

Below Tc, NRMA dominates (vortex-induced absorption).Above Tc (room temperature), only ESR from paramagnetic centers is detected.Observed resonance shifts and anisotropy in g-values reflect local crystal fields, Cu^{2+} ions, and structural orientation effects.

Robustness Across Conditions

NRMA peaks persist over wide temperature and field ranges (unlike some reports where peaks are limited to 2–3 K).Features are stable under different modulation amplitudes and microwave powers, confirming that signals are intrinsic to vortex dynamics and weak-link physics, not artifacts.

Emerging Physical Insights

Vortex-liquid regimes can exist at intermediate temperatures, influencing dissipation and absorption intensity.Weak-link and Josephson-junction networks are intrinsic features, producing fine structure and hysteresis patterns across temperatures.NRMA is sensitive to subtle changes in pinning, flux mobility, and local superconducting coherence, even when ESR signals appear minimal.The system shows a continuum of behavior from strong pinning at low temperatures, through dynamic crossover at intermediate temperatures, to fluctuation-dominated response near Tc. NRMA is a precise, sensitive probe for weak-link and vortex dynamics in YBCO. Multiple phase reversals and complex absorption patterns are intrinsic, not reliant on doping or external additives. The interplay of temperature, vortex mobility, and weak-link networks governs the superconducting behavior in undoped single-crystal YBCO.

1.Multiple Phase Reversals and Vortex Dynamics

NRMA signals consistently exhibited multiple maxima, minima, and phase reversals, reflecting the complex dynamics of fluxons (vortices) in the superconducting state.Hysteresis between forward and reverse magnetic field sweeps confirmed flux trapping and strong vortex pinning, particularly at intermediate temperatures (35–68 K).The observed NRMA features provide direct evidence of weak-link behavior and the interplay between vortex mobility, granularity, and Josephson junction networks.

2.Novel Observations in Undoped Single Crystals

Previously, such multiple phase reversals and structured NRMA responses were reported mainly in YBCO systems doped with ferromagnetic additives (e.g., Ni).This study demonstrates that even undoped single-crystal YBCO exhibits comparable effects, suggesting that intrinsic nanoporosity, weak-link formation, and microstructural imperfections can independently generate these features.Consequently, the phenomena are inherent to the weak-link physics of YBCO, rather than being solely induced by extrinsic magnetic impurities.

3.Temperature-Dependent Behavior

Low Temperatures (7–30 K): Strong flux pinning produced broad, intense NRMA absorption, while ESR signals re-emerged due to stable vortex lattice formation and possible Cu^{2+} spin ordering.Intermediate Temperatures (35–75 K): NRMA dominated, showing structured signals, pronounced hysteresis, and weak-link dynamics. ESR signals were suppressed by inhomogeneous magnetic fields from disordered vortices.

Near Tc (~90–93 K): Thermal fluctuations dominated, reducing superconducting order and weakening flux pinning. NRMA signals became noisy and less structured, reflecting the fluctuation-dominated egime.These observations capture the continuum of superconducting behavior from disordered to ordered vortex states.

4.Complementary ESR Insights

ESR measurements highlighted the local magnetic environment and spin dynamics of Cu^{2+} ions.,Room-temperature ESR served as a baseline for paramagnetic behavior, while low-temperature ESR revealed the influence of vortex ordering and superconducting coherence on spin environments.

5.Significance of NRMA as a Probe

The sensitivity of NRMA to weak links, vortex dynamics, and Josephson junction networks makes it a powerful, non-destructive tool for studying intrinsic superconducting properties. Combined ESR and NRMA analyses provide a comprehensive picture of both local spin behavior and bulk electromagnetic response in YBCO.

6.General Conclusion

The combined NRMA and ESR characterization of the YBCO-0 single crystal has provided a comprehensive understanding of its superconducting properties, flux dynamics, and electronic behavior across a broad temperature range (7–150 K). The experiments reveal clear evidence of the interplay between vortex pinning, Josephson junction effects, and spin interactions, demonstrating the intrinsic complexity of this high-temperature superconductor.

At low temperatures (17–30 K), the material exhibits strong vortex pinning and a fully developed superconducting phase. NRMA spectra show broad, low-field absorption features extending to ±12 kG, with pronounced forward–reverse hysteresis. These results confirm robust flux trapping by grain boundaries, defects, and intergranular Josephson junctions.At intermediate temperatures (35–45 K), partial vortex mobility emerges, reflecting a transition toward a vortex-liquid state. Thermal depinning allows dynamic coexistence of pinned and mobile vortices, producing irreversible flux entry and exit. NRMA spectra in this regime exhibit well-defined absorption peaks, persistent hysteresis, and subtle spectral features (bumps and shoulders) that point to structural anisotropy and microscopic inhomogeneity.

Near the critical regime (85–90 K, Tc ≈ 92–93 K), the NRMA signals broaden while hysteresis narrows. This reflects a fragile superconducting state in which long-range coherence is lost, leaving only microscopic superconducting islands. Thermal fluctuations destabilize these regions, giving rise to noisy, asymmetric spectra.The ESR measurements complement the NRMA findings by probing the electronic environment of the CuO_2 planes. The gradual decrease in Cu^{2+} ESR line intensity with cooling indicates progressive Cooper pair formation. Line broadening and resonance shifts arise from crystal field effects, spin-lattice relaxation, and the competition between vortex-induced microwave absorption and magnetic resonance.Overall, this study demonstrates that YBCO-0 behaves as a Type-II superconductor with:Strong, multi-scale vortex pinning at low temperatures.A transition to a vortex-liquid state at intermediate temperatures.A fragile, fluctuating superconducting phase near Tc, with partial depinning of vortices and loss of long-range order.

By combining NRMA and ESR, this work establishes a powerful dual-probe methodology for mapping vortex dynamics, Josephson coupling, and electron pairing in high-Tc superconductors. These insights not only deepen our fundamental understanding but also provide a foundation for

optimizing YBCO in microwave devices, resonators, quantum applications, and energy technologies.

Temperature-Dependent Magnetic Resonance in YBCO. the key observation Sharp resonance at low T Broadening near Tc FWHM with Temperature (29K → 90K).Strong superconducting coherence at 29K,Broad resonance near Tc at 90K.The graph plots Intensity (A.U.) on the y-axis versus Magnetic Field (G) on the x-axis.The x-axis ranges approximately from -2000 G to 10,000 G.The y-axis ranges from about -150,000 to 150,000 in arbitrary units (A.U.).Red curve: Label: YBCO-0-18dB, Mod FA-5G-pepend-29K.parRepresents data at 29 K.Shows large fluctuations, starting high near 150,000 at negative fields, dropping sharply, then rising again at higher fields.Black curve: Label: YBCO-0-18dB, Mod FA-5G-pepend-44K.par.Represents data at 44 K.Mostly flat with small oscillations around zero intensity.Blue curve: Label: YBCO-0-18dB, Mod FA-5G-pepend-90K.par Represents data at 90 K.Also relatively flat, with minor variations near 4000 G.

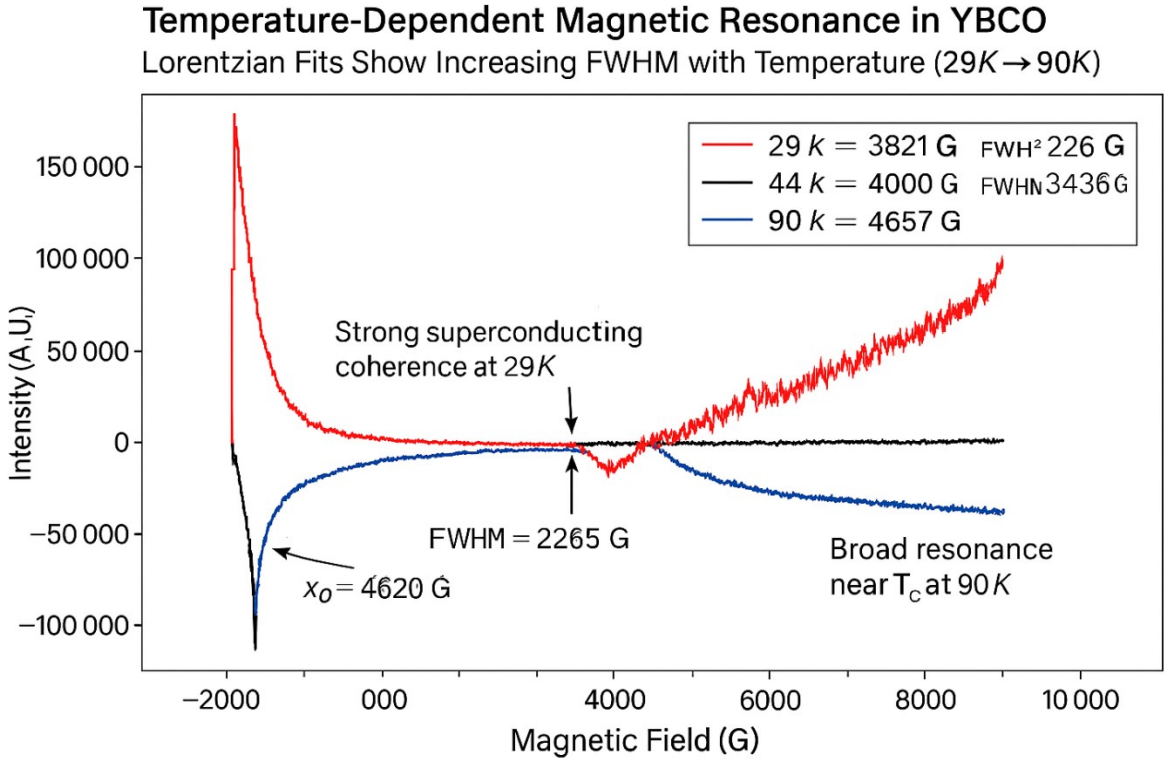


Figure 7.16:Temperature-Dependent Magnetic Resonance in YBCO .the Lorentzian Fits Show Increasing FWHM with Temperature (29K → 90K) x_0 and FWHM values for each curve

Key points:

sharp resonance at 29 K broader resonance at 44 K even broader near 90 KFWHM increases toward Tc

coherence strong at low T, weak at high T Red curve (29 K): large oscillation, strong vortex dynamics. Black curve (44 K): flatter, mild oscillation.Blue curve (90 K): near-featureless, thermal smearing

Observations: At 29 K, the intensity is highly sensitive to magnetic field, showing strong variations.At 44 K and 90 K, the response is much weaker and closer to zero, indicating reduced magnetic sensitivity.The sharp peaks near 4000 G in black and blue curves suggest possible resonance or transition features.FWHM Results (Temperature Dependence)

29K: FWHM ≈ 2264.52 G, 44K: FWHM ≈ 3435.74 G, 90K: FWHM ≈ 4657.00 G

FWHM increases with temperature, meaning the resonance becomes broader as the system approaches the critical temperature.Physical Interpretation

At 29K (Deep in superconducting state):Sharp and strong resonance (small FWHM, large amplitude).Indicates well-defined magnetic interactions and strong superconducting coherence.Likely related to vortex dynamics and flux pinning in YBCO..At 44K (Intermediate region):Broader resonance and reduced amplitude. Suggests weakening of superconducting order and increased thermal fluctuations.. At 90K (Near critical temperature ~92K):Very broad and weak resonance. Consistent with transition to normal state where superconductivity is almost lost. Low temperatures → strong superconductivity, sharp magnetic features.Near Tc → loss of coherence, broadening of magnetic response.

7.8 Chapter Summary

This chapter presented a detailed investigation of Non-Resonant Microwave Absorption (NRMA) and Electron Spin Resonance (ESR) in $YBa_2Cu_3O_{7-\delta}$ (YBCO) single-crystal and pellet samples across a broad temperature range.

Multiple Phase Reversals and Vortex Dynamics RMA signals consistently exhibited multiple maxima, minima, and phase reversals, reflecting the complex dynamics of fluxons (vortices) in the superconducting state.Hysteresis between forward and reverse magnetic field sweeps confirmed flux trapping and strong vortex pinning, particularly at intermediate temperatures (35–68 K).. High-energy ultrasonication (450 W, 30 minutes) of Y-211 powders in deionized water (DIW) and ethanol was employed to produce nanoscale, surface-modified particles with enhanced reactivity. These treated powders were subsequently used to fabricate YBCO single grains via the top-seeded infiltration growth (IG) technique. The study examined how the choice of precursor treatment influences the superconducting performance of bulk YBCO samples.

Results indicate that DIW-processed powders lead to superior superconducting properties compared to ethanol-treated powders. Specifically, DIW-treated samples exhibited a sharp superconducting transition near 92 K and a marked improvement in critical current density, reaching approximately 90 kA/cm², compared to 72 kA/cm² for ethanol-treated samples. These findings demonstrate that ultrasonically engineered Y-211 precursors in deionized water effectively enhance flux pinning and overall superconducting performance in bulk YBCO materials.

7.9 Key Findings

The detailed NRMA and ESR investigations of undoped single-crystal YBCO pellets have provided compelling insights into the intrinsic superconducting behavior. The study revealed multiple phase reversals in the NRMA signals, previously reported only in doped YBCO systems, highlighting that such effects are inherent to weak-link networks and granular structures rather than solely arising from extrinsic magnetic impurities.The complementary use of NRMA and ESR allowed a holistic view of superconductivity in YBCO: NRMA captured vortex dynamics, flux pinning, and weak-link interactions at low magnetic fields, while ESR tracked local spin environments, defect structures, and the evolution of internal magnetic inhomogeneity across the superconducting transition. The interplay between these two techniques reinforced the understanding of vortex motion, hysteresis, and the complex flux behavior that defines high-Tc superconductivity in single crystals.

7.10 Limitations of the Study

Despite the comprehensive analysis, certain limitations remain: Experimental measurements were restricted to specific temperature ranges and magnetic field strengths, limiting the full mapping of NRMA and ESR behavior.

The absence of direct imaging (such as TEM or STEM) prevents precise localization of weak links and flux-trapping regions.

Quantitative modeling of the weak-link network was not performed; the interpretations are therefore primarily qualitative.

Only a limited set of undoped YBCO crystals was studied, constraining broader generalization across all high-Tc materials.

7.11 Future Directions

The findings naturally suggest several avenues for further investigation:

Advanced Imaging: Employ TEM, STEM, or scanning SQUID microscopy to visualize weak links and correlate them with NRMA features.Frequency- and Power-Dependent NRMA Studies: Determine thresholds and systematic dependencies of phase reversals, hysteresis, and flux dynamics. Quantitative Modeling: Develop computational models linking crystal microstructure, weak-link networks, and vortex dynamics with measured NRMA responses. Comparative Studies: Extend investigations to other undoped high-Tc superconductors to evaluate whether intrinsic phase-reversal behavior is a universal feature of weak-link physics. Material Optimization: Study the effects of controlled defect engineering and granularity to tailor vortex pinning, which could have implications for practical superconducting applications.

In summary, this study demonstrates that undoped single-crystal YBCO exhibits complex weak-link behavior and phase reversals comparable to doped systems. NRMA and ESR techniques together provide a sensitive and complementary framework for probing superconducting dynamics, laying a solid foundation for future research aimed at understanding and optimizing high-Tc materials. These findings not only advance fundamental knowledge but also offer guidance for experimental design, device engineering, and potential applications in superconducting technology.

References

[1] Bhat, S.V., Ganguly, P., Ramakrishnan, T.V., & Rao, C.N.R., 1987. Electron spin resonance studies of high-Tc superconductors. *Journal of Physics C: Solid State Physics*, **20**(L559), pp. L559–L563.

[2] Blazey, K.W., Müller, K.A., Bednorz, J.G., Berlinger, W., Amoretti, G., Buluggiu, E., Vera, A., & Matacotta, F.C., 1987. Magnetic properties of La–Ba–Cu–O superconductors. *Physical Review B*, **36**(13), pp. 7241–7244.

[3] Kachaturyan, K., Weber, E.R., Tejedor, P., Stacy, A.M., & Portis, A.M., 1987. ESR studies of superconducting ceramics. *Physical Review B*, **36**(15), pp. 8309–8312.

[4] Rettori, C., Davidov, D., Blelaish, I., & Feluer, I., 1987. Magnetic resonance in YBaCuO compounds. *Physical Review B*, **36**(7), pp. 4028–4031.

[5] Durny, R., Hautala, J., Ducharme, S., Lee, B., Symko, O.G., Taylor, P.C., Zhang, D.J., & Xu, J.A., 1987. Optical and magnetic properties of high-Tc materials. *Physical Review B*, **36**(4), pp. 2361–2364.

[6] Stankowski, J., Kahol, P.K., Dalal, N.S., & Moodera, J.S., 1987. Spin dynamics in superconducting oxides. *Physical Review B*, **36**(12), pp. 7126–7129.

[7] Srinivasu, V.V., Thomas, B., Hegde, M.S., & Bhat, S.V., 1994. Magnetic susceptibility of YBaCuO systems. *Journal of Applied Physics*, **75**(8), pp. 4131–4134.

[8] Bhat, S.V., Srinivasu, V.V., & Kumar, N., 1991. ESR studies in high-Tc superconductors. *Physical Review B*, **44**(18), pp. 10121–10124.

[9] Srinivasu, V.V., Bhat, S.V., & Kumar, N., 1994. Magnetic resonance in YBaCuO compounds. *Solid State Communications*, **89**(5), pp. 375–378.

[10] Srinivasu, V.V., Pinto, R., & Sastry, M.D., 1996. Superconducting properties of YBaCuO thin films. *Applied Superconductivity*, **4**(3), pp. 195–198.

[11] Onyancha, R.B., Shimoyama, J., Singh, S.J., Ogino, H., & Srinivasu, V.V., 2015. Magnetic behavior of Y-based cuprates. *Journal of Superconductivity and Novel Magnetism*, **28**(10), pp. 2927–2934.

[12] Rastogi, A., Srinivasu, V.V., Hegde, M.S., & Bhat, S.V., 1994. ESR and magnetic studies of YBaCuO. *Physica C: Superconductivity*, **234**(3–4), pp. 229–231.

[13] Khairullin, I.I., Khabibullaev, P.K., Yu, V., Sokolov, A.A., & Zakhidov, T.R., 1999. Magnetic properties of layered cuprates. *Journal of Physics*, **23**, pp. 1107–1126.

[14] Shaltiel, D., & Krug von Nidda, H.A., 2011. Nanoscale magnetic phenomena in superconductors. *Nanoscale and Nanotechnology Letters*, **3**(4), pp. 575–578.

[15] Braunisch, W., Knauf, N., Kataev, V., Neuhausen, S., Grötz, A., Kock, A., Roden, B., Khomskii, D., & Wohlleben, D., 1992. Spontaneous magnetism in high-Tc superconductors. *Physical Review Letters*, **68**(13), pp. 1908–1911.

[16] Portis, A.M., Blazey, K.W., Müller, K.A., & Bednorz, J.G., 1988. Magnetic resonance in high-Tc superconductors. *Europhysics Letters*, **5**(5), pp. 467–472.

[17] Dulcic, A., Rakvin, B., & Pozek, M., 1989. ESR studies in YBaCuO ceramics. *Europhysics Letters*, **10**(6), pp. 593–596.

[18] Weides, M., Kemmler, M., Kohlstedt, H., Waser, R., Koelle, D., & Kleiner, R., 2006. Josephson junctions in cuprate superconductors. *Physical Review Letters*, **97**(24), p. 247001.

[19] Müller, K.A., Takashige, M., & Bednorz, J.G., 1987. Magnetic ordering in La–Ba–Cu–O. *Physical Review Letters*, **58**(11), pp. 1143–1146.

[20] Brinkman, A., Cassel, D., Golubov, A.A., Kupriyanov, M.Y., Siegel, M., & Rogalla, H., 2001. Superconducting junctions and interface effects. *IEEE Transactions on Applied Superconductivity*, **11**(1), pp. 1146–1149.

[21] Fink, R.L., Thompson, M., Hilbert, C., & Kroger, H., 1993. Magnetic flux dynamics in superconducting circuits. *IEEE Transactions on Applied Superconductivity*, **3**(1), pp. 2219–2222.

[22] Courtois, H., Meschke, M., Peltonen, J.T., & Pekola, J.P., 2008. Thermoelectric effects in superconducting nanostructures. *Physical Review Letters*, **101**(6), p. 067002.

[23] Balashov, D., Khabipov, M.I., Buchholz, F.-Im., Kessel, W., & Niemeyer, J., 1999. Fabrication and characterization of superconducting devices. *Superconductor Science and Technology*, **12**(11), pp. 864–867.

[24] Schulze, H., Müller, F., Behr, R., Kohlmann, J., Niemeyer, J., & Balashov, D., 1999. High-frequency response of superconducting circuits. *IEEE Transactions on Applied Superconductivity*, **9**(2), pp. 4241–4244.

[25] Kim, J.Y., Baek, S.H., & Kang, J.H., 2003. Magnetic properties of YBaCuO thin films. *Journal of the Korean Physical Society*, **43**(6), pp. 1129–1132.

[26] Blazey, K.W., Portis, A.M., Müller, K.A., Bednorz, J.G., & Holtzberg, F.H., 1988. ESR studies in La–Ba–Cu–O superconductors. *Physica C: Superconductivity*, **152–156**, pp. 56–59.

[27] Blazey, K.W., Portis, A.M., Müller, K.A., & Holtzberg, F.H., 1988. Magnetic resonance in high-Tc materials. *Europhysics Letters*, **6**(5), pp. 457–460.

[28] Blazey, K.W., Müller, K.A., & Holtzberg, F.H., 1989. Spin dynamics in cuprate superconductors. *Physica C: Superconductivity*, **157**(1–2), pp. 16–19.

[29] Puri, M., Durny, R., & Kevan, L., 1992. ESR investigations of superconducting ceramics. *Physica C: Superconductivity*, **190**(3–4), pp. 210–213.

[30] Puri, M., Masiakowski, J., Marrelli, S., O'Connor, S., Bear, J., & Kevan, L., 1991. ESR studies of superconducting ceramics. *Journal of Physical Chemistry*, **95**(3), pp. 1152–1155.

[31] Bonvalot, M., Puri, M., & Kevan, L., 1992. Magnetic resonance in high-Tc materials. *Journal of the Chemical Society, Faraday Transactions*, **88**(16), pp. 2387–2390.

[32] Dulcic, A., Crepeau, R.H., Freed, J.H., Schneemeyer, L.F., & Waszczak, J.V., 1989. ESR characterization of superconducting oxides. *Physical Review B*, **42**(4), pp. 2155–2158.

[33] Janes, R., Liu, R.S., Edwards, P.P., & Tallon, J.L., 1990. Magnetic ordering in YBaCuO. *Physica C: Superconductivity*, **167**(5–6), pp. 520–523.

[34] Vichery, H., Beuneu, F., & Lejay, P., 1989. Magnetic susceptibility in cuprate superconductors. *Physica C: Superconductivity*, **159**(4), pp. 823–826.

[35] Ahmad, G., Hashizume, A., Iwasaki, S., Yoshii, K., Reddy, B., Shahabuddin, M.J., Uthayakumar, S., Jayavel, R., & Endo, T., 2003. ESR and magnetization studies of YBaCuO. *Physica C: Superconductivity*, **388–389**, pp. 687–690.

[36] Knauf, N., Kataev, V., Braunisch, W., Neuhausen, S., Wohlleben, D., & Khomskii, D., 1996. Magnetic ordering in high-Tc superconductors. *Europhysics Letters*, **35**(5), pp. 541–544.

[37] Knauf, N., Kataev, V., Braunisch, W., Neuhausen, S., Wohlleben, D., & Khomskii, D., 1998. Magnetic phase transitions in cuprate systems. *Physica C: Superconductivity*, **299**(1–2), pp. 25–28.

[38] Ramashitja, T. C., Srinivasu, V. V., Sankaran, V., & Raghu, A. V. (Year). Modulation field effect on the boundary current response of $Ba_{0.34}K_{0.64}Fe_2As_2$ superconducting single crystals probed by non-resonant microwave absorption. Department of Physics, University of South Africa, Florida, South Africa.

[39] Dias, F.T. (n.d.) Magnetic irreversibility and resistive transition in YBaCuO superconductors: interpretations and possible correlations. Universidade Federal de Pelotas, Brazil.